MULTIFUNCTIONAL AND PHYSICALLY TRANSIENT SUPERCAPACITORS, TRIBOELECTRIC NANOGENERATORS AND CAPACITIVE SENSORS

A THESIS SUBMITTED TO
THE GRADUATE SCHOOL OF NATURAL AND APPLIED SCIENCES
OF
MIDDLE EAST TECHNICAL UNIVERSITY

BY

METE BATUHAN DURUKAN

IN PARTIAL FULFILLMENT OF THE REQUIREMENTS
FOR
THE DEGREE OF DOCTOR OF PHILOSOPHY
IN
METALLURGICAL AND MATERIALS ENGINEERING

JUNE 2023

Approval of the thesis:

MULTIFUNCTIONAL AND PHYSICALLY TRANSIENT SUPERCAPACITORS, TRIBOELECTRIC NANOGENERATORS AND CAPACITIVE SENSORS

submitted by **METE BATUHAN DURUKAN** in partial fulfillment of the requirements for the degree of **Doctor of Philosophy** in **Metallurgical and Materials Engineering, Middle East Technical University** by,

Prof. Dr. Halil Kalıpçılar
Dean, Graduate School of **Natural and Applied Sciences** _____

Prof. Dr. Ali Kalkanlı
Head of the Department, **Metallurgical and Materials Eng**. _____

Prof. Dr. H. Emrah Ünalan
Supervisor, **Metallurgical and Materials Eng., METU** _____

Assist. Prof. Dr. Yusuf Keleştemur
Co-Supervisor, **Metallurgical and Materials Eng., METU** _____

Examining Committee Members:

Prof. Dr. Kadri Aydınol
Metallurgical and Materials Eng, METU _____

Prof. Dr. H. Emrah Ünalan
Metallurgical and Materials Eng, METU _____

Assoc. Prof. Dr. Simge Çınar Aygün
Metallurgical and Materials Eng, METU _____

Assoc. Prof. Dr. Burak Ülgüt
Chemistry, Bilkent Uni. _____

Assist. Prof. Dr. Şahin Coşkun
Metallurgical and Materials Eng., Eskişehir Osmangazi Uni. _____

Date: 11.07.2023

I hereby declare that all information in this document has been obtained and presented in accordance with academic rules and ethical conduct. I also declare that, as required by these rules and conduct, I have fully cited and referenced all material and results that are not original to this work.

Name Last name : Mete Batuhan Durukan

Signature :

ABSTRACT

MULTIFUNCTIONAL AND PHYSICALLY TRANSIENT SUPERCAPACITORS, TRIBOELECTRIC NANOGENERATORS AND CAPACITIVE SENSORS

Durukan, Mete Batuhan
Doctor of Philosophy, Metallurgical and Materials Engineering
Supervisor: Prof. Dr. H. Emrah Ünalan
Co-Supervisor: Assist. Prof. Dr. Yusuf Keleştemur

July 2023, 216 pages

Electronic waste (e-waste) grows parallel with the increasing need for consumer electronics. This, unfortunately, is leading to pollution and massive ecological problems worldwide. A standing-out solution to this problem is the use of transient electronics. While the transiency of a few components such as transistors and batteries are proposed already, it is crucial to have all elements in electronic devices to be transient. Therefore, the transiency of more electronic components should be demonstrated to alleviate the e-waste problem. Herein, multifunctional nanocomposite electrodes were fabricated using poly(vinyl alcohol) (PVA), carbon black, and activated carbon. These simple electrodes were then used to fabricate physically transient supercapacitors, triboelectric nanogenerators, and capacitive sensors. Transient supercapacitors (T-SUPC) were used numerous times with excellent supercapacitive behavior before being discarded, which showed promise

as an energy storage component for transient systems. Fabricated transient triboelectric nanogenerators (T-TENG) were used to harvest mechanical energy, eliminating the need for an external power supply and paving the way to self-powered devices like a touchpad. Fabricated transient capacitive sensors (T-CAPS), on the other hand, showed extended linear sensitivities and offered waste-free monitoring of physiological signals and body motions. These devices are fabricated using similar materials and layers, proving that multifunctionality is critical to achieve simple transient electronic systems.

Keywords: Transient Electronics, Supercapacitors, Triboelectric Nanogenerators, Capacitive Sensors, Flexible Electronics

ÖZ

ÇOK FONKSİYONLU VE FİZİKSEL OLARAK GEÇİCİ SÜPERKAPASİTÖRLER, TRİBOELEKTRİK NANOJENERATÖRLER VE KAPASİTİF SENSÖRLER

Durukan, Mete Batuhan
Doktora, Metalurji ve Malzeme Mühendisliği
Tez Yöneticisi: Prof. Dr. H. Emrah Ünalan
Ortak Tez Yöneticisi: Dr. Öğr. Üyesi Yusuf Keleştemur

Temmuz 2023, 216 sayfa

Elektronik atık (e-atık), tüketici elektroniğine olan ihtiyacın artmasıyla paralel olarak büyüyor. Bu maalesef dünya çapında kirliliğe ve büyük ekolojik sorunlara yol açıyor. Bu soruna öne çıkan bir çözüm, geçici elektroniklerin kullanılmasıdır. Transistörler ve piller gibi birkaç bileşenin geçiciliği zaten önerilmişken, elektronik cihazlardaki tüm bileşenlerin geçici olması çok önemlidir. Bu nedenle, e-atık sorununu hafifletmek için daha fazla elektronik bileşenin geçiciliği gösterilmelidir. Burada poli(vinil alkol) (PVA), karbon siyahı ve aktif karbon kullanılarak çok işlevli nanokompozit elektrotlar üretilmiştir. Bu basit elektrotlar daha sonra fiziksel olarak geçici süperkapasitörler, triboelektrik nanojeneratörler ve kapasitif sensörler üretmek için kullanılmıştır. Geçici süper kapasitörler (T-SUPC), geçici sistemler için bir enerji depolama bileşeni olarak umut vaat etmekle beraber, atılmadan önce mükemmel süper kapasitif davranışla çoklu döngüde kullanılabilmiştir. Üretilen n geçici triboelektrik nanojeneratörler (T-TENG) mekanik enerjiyi toplamak için

kullanılmış, harici bir güç kaynağına olan ihtiyacı ortadan kaldırmış ve dokunmatik yüzey gibi kendi kendine çalışan cihazların çalışmasını sağlamıştır. Öte yandan üreitlen geçici kapasitif sensörler (T-CAPS), uzun doğrusal hassasiyetler göstermiş ve fizyolojik sinyallerin ve vücut hareketlerinin izlenmesini sağlamıştır. Tüm bu cihazlar, yukarıda belirtilen benzer malzemeler ve katmanlar kullanılarak üretilmiş ve bu da çok işlevliliğin basit geçici elektronik sistemler elde etmenin anahtarı olduğunu kanıtlamıştır.

Anahtar Kelimeler: Geçici Elektronikler, Süperkapasitörler, Triboelektrik Nanojeneratörler, Kapasitif Sensörler, Esnek Elektronikler

Dedicated to my dearest mother and father…

ACKNOWLEDGMENTS

This work was partially funded by The Scientific and Technological Research Council of Türkiye (TÜBİTAK) under grant numbers 220M003 and 120M374.

Doing Ph.D. is a long journey, gradually showing a person how little one knows about how the universe works. Although excellence is awaited at the end, it feels like the beginning of a much bigger world. In this "bigger" world, valued mentors and friends are necessary for pursuing higher knowledge, as humankind continually evolves by working together to achieve their better selves. On this path, I owe my success, knowledge, and never-ending curiosity to my advisor, Prof. Dr. H. Emrah Ünalan. He was the one that sparked my interest in research starting from my undergraduate years and formed a strong bond that I will carry throughout my academic life. I would also thank my thesis committee members Assoc. Prof. Dr. Simge Çınar Aygün and Assoc. Prof. Dr. Burak Ülgüt for their valuable discussions and interest in my progress. I also would like to thank Assist. Prof. Dr. Şahin Coşkun and Assist. Prof. Dr. Recep Yüksel. I am deeply grateful for your leadership in my earliest graduate years.

I owe a huge thanks to Dr. Doğa Doğanay; we almost started the M.Sc. together and formed an unbreakable bond – both for academia and, most importantly, as brothers. We shared our most profound depression as well as our highest happiness. We always dreamt of publishing together in our M.Sc.; look at us now! I would also like to thank Melih Ögeday Çiçek and Mustafa Caner Görür, who started as our juniors but became lifelong friends. I learned a lot from you, and my success (and my mental state) today would not be the same without you.

I would also like to thank all of my labmates and coworkers, Yusuf Tutel, Dr. Ümran Başköse, Dr. Aryan Azad, Yiğithan Tufan, Onuralp Çakır, Tufan Bölükbaşı, Deniz Keskin, Gözde Öztürk, Almila Gözütok, Serkan Koylan, Şensu Tunca, Loay Madbouly, Onur Demircioğlu, Ali Deniz Uçar, Öykü Çetin, Murathan Çuğunlular, Sümeyye Kandur, and Eda Çevik.

I would also like to thank my closest friends Volkan Tümer, Mert Demir, Soner Değirmenci, Berkin Kalay, Ezgi Türkoğlu, Ece Ferizoğlu, Ziya Çağrı Torunoğlu, Mehmet Hazar Şeren, Mustafacan Kutsal, Selin Özkul, Doğancan Tigan, Mehmet Ali Öz, Alptuğ Gür, and Koray Emre Akgöçmen. I know I neglected you a lot, and I will make up to you from now on.

I would also like to thank the love of my life, Irmak Karakaya. She helped me get through hardships with the love she showed and supported me with valuable discussions (thankfully, she is a superb chemist!). I love you. Our cats, Benek and Korsan, played a tremendous role in keeping me calm and loving. Thank you, my little furballs.

Lastly, I thank my father and mother, Mustafa Durukan and Yasemin Durukan, for literally everything. They gave their fullest for me to live a life of my choosing and provided me with everything. I am lucky to be your child. I dedicate this thesis to you. I hope I made you proud. I love you both. Father, I hope you see this someway.

TABLE OF CONTENTS

LIST OF TABLES

LIST OF FIGURES

CHAPTER 1

TRANSIENT ELECTRONICS

1.1 Definition of Transient Electronics

“Transiency” in electronics is a reasonably new adverb/classification that broadly adds the characteristic of physically disappearing to electronic devices. [1] Unlike conventional electronics, which should be functional over an extended period, transient electronics are expected to integrate partially or fully after their purpose of use is at end. As such, they are generally focused on predefined and short-term work.[2] This could be on-demand, triggered via various ways, or can happen at a defined rate – but the main focus is their untraceable disappearance, which is picturized in Figure 1.1. [3]

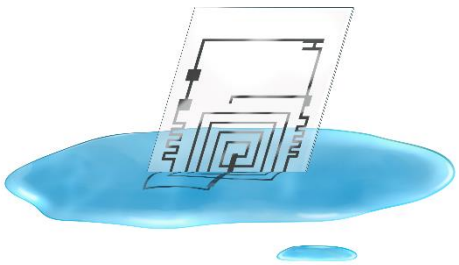

Figure 1.1 Visualized transient electronics (Courtesy of Ayşenur İrfanoğlu).

Transiency means a disintegration in any possible way. Although this did not require to be green, the literature adopted the notion of transient electronics fundamentally requiring green materials, which would cause no environmental harm or leave no trace following their use. It is also possible to "dissolve" transient electronics, which is equally essential in recycling and allows one to easily recollect used materials. [4] Moreover, the electronics could be ingestible or bioabsorbable as well. Since these terms are also consistent with being not harmful or being green, they can also be called as "transient." [3] Therefore, to form a transient electronic device, the system's design should be made with biodegradable, biocompatible, and environmentally friendly materials. [3,5]

1.2 Requirement for Transient Electronics

The rapid progress in electronics and demand for a wide variety of miniaturized, integrated, and wearable devices ranging from intelligent electronics to health-related devices and sensors result in excessive consumption of "newer" and "better" products. This results in tremendous electronic waste (e-waste) across the world [6–8]. According to the 2020 report of United Nation University's (UNU) collaborative Global E-Waste Statistics Partnership (GESP), 21% of increase in e-waste is observed just in 5 years, reaching 53.6 million metric tons worldwide, which is schematically shown in Figure 1.2 [9]. High sum of these e-wastes is from wearable electronics and energy storage devices. E-waste primarily constitutes of lithium, mercury, nickel, cadmium, zinc, lead; most of which are toxic and harmful to both living beings and ecology [7]. In seeking solutions to these problems, a new field has emerged called transient electronics, where at the end of their lives, devices disintegrate with minimal remains that are only eco-friendly residuals. This causes no harm to the environment and produces almost zero waste[10]. Transient electronics can be used in a wide variety of application areas ranging from simple medical

implants to militaristic technologies that can dissolve or degrade in a specific period.[11] In this manner, water-soluble, biofriendly, biocompatible and biodegradable devices that can be used in energy-related applications and sensors are explored to reduce the generated waste [12,13].

Above concepts require the electrode material, encapsulation and/or active material to be biocompatible, biodegradable, and environmentally friendly. In this manner, designs have been made successfully to have environmental sensors [10], biomedical applications[12], soft robotics[14], water soluble energy storage devices[15] and even edible supercapacitors[16,17] and triboelectric nanogenerators[18]. There is a significant increase in demand for smaller energy sources to power electronic devices. Additionally, there is a growing need for health monitoring systems as the population increases. There is also a requirement to continuously monitor patients without the need for any devices or invasive procedures, which necessitates the use of small, biocompatible energy sources. In this manner, emerging field of transient electronics is very promising to satisfy the need for growing demand in electronics without creating any e-waste.

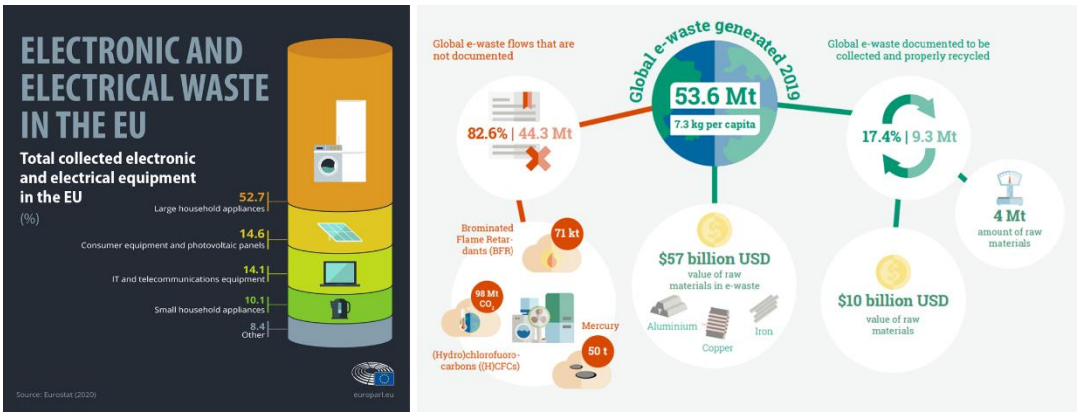

Figure 1.2 Schematic representation of the e-waste generation reported in 2020 by United Nation University's (UNU) collaborative Global E-Waste Statistics Partnership. [9]

1.3 Transient Materials

Transient electronics require to be biodegradable, biocompatible and environmentally friendly, on top of having a pre-defined way to be triggered or have a rate of transiency. In this manner, all of the components of an electronic system or device should be suited to these boundary conditions. If the components of an electronic device are simplified, one could separate them into three. First one is the substrate, where all of the electronic parts are laid on; second being the electronic components, and the third being the encapsulation.

1.3.1 Substrate Materials for Transient Electronics

Substrates are equally important with the electrical components, as they are the first building blocks that allow an electrical system to be built on. In the case of transient electronics, it becomes much more important since the substrate itself should also be transient. [2]

First reported transient electronics study, which actually utilized silk fibroin proteins as a dissolvable and bioabsorbable substrate was conducted in 2009 by Kim et al. [19] Silicon electronics were fabricated on top of silk substrate, which dissolved in water in mere minutes (Figure 1.3 (a)). Apart from silk, the most common substrate for the transient electronics is polyvinyl alcohol (PVA). Çınar et al. [20] employed PVA with the addition of sucrose, which allowed them to control the mechanism of swelling and speed up the dissolution (Figures 1.3 (b) – (d)). Shin et al. [21] introduced bubbling agents inside the already transient gelatin and PLGA to improve their transiency. In the case of gelatin, bubbling agent caused a rapid creation of carbon dioxide (CO_2), resulting in an "explosion" of the system, which is visible in Figure 1.3 (e). A mixture of glycerol and hydroxyethylcellulose (HEC) is also used to construct macromolecular elastomeric gels for transient electronics by introducing aluminum (Al) electrodes on top of it. Besides having healing properties as well, the glycerol/HEC macromolecular films showed transiency inside DI water (Figure 1.3 (f)). [22] All-in-all, it is clear that the polymers and natural substances that are already biodegradable, bioresorbable or even ingestible are great candidates as substrates for transient electronics.

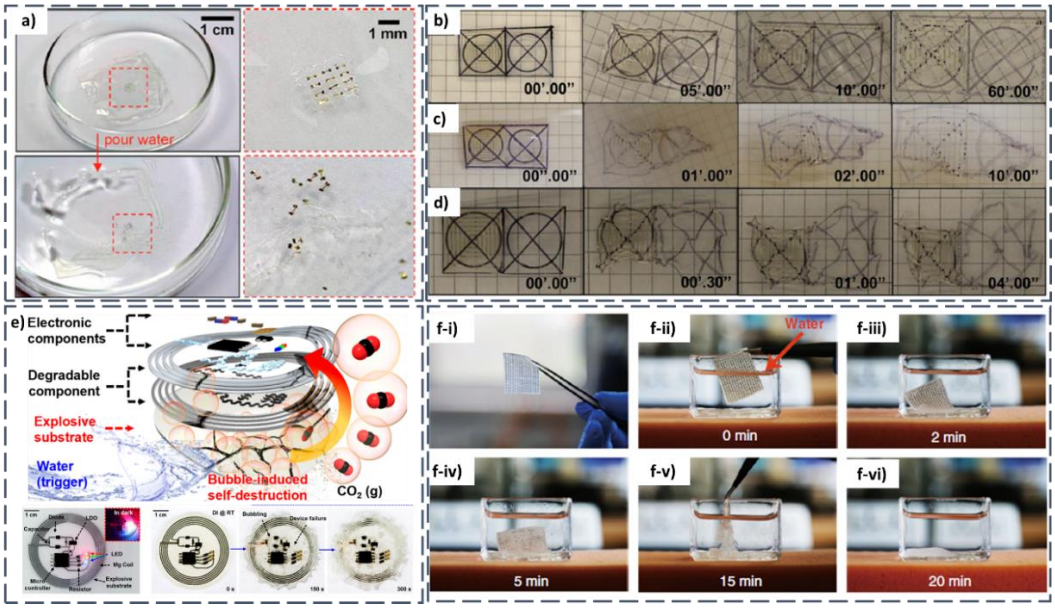

Figure 1.3 a) Dissolution of silicon electronics on silk substrates. [19] b,c,d) Photographs of PVA:sucrose substrates with different ratios of sucrose, 1:0, 2:1, and 1:1, respectively.[20] e) Overall structure of a transient electronic utilizing composite of gelatin and PLGA with the addition of bubbling agents and its dissolution in deionized water [21]. f) Dissolution of glycerol/hydroxyethylcellulose substrates with time [22].

1.3.2 Materials for Electronic Components and Systems in for Transient Electronics

Transient electronics depend on the electronic components being transient as well. Achieving this requires materials that can degrade without leaving any harmful substances behind. Nevertheless, one must use transient components to form a transient electronic system, which may include semiconducting materials, dielectrics, energy storage devices, electrodes and even electrical connections and wiring. The first and foremost idea is to use metals that are already found in the soil

or water as ions, and can even be digested due to the present requirement of human body. [23]

As the prime example of the use of metals, Prof. John A. Rogers' group used magnesium (Mg), zinc (Zn), iron (Fe), tungsten (W), molybdenum (M), and AZ31B Mg alloy to construct n-channel field effect transistors (MOSFETs) to demonstrate their feasibility for use in transient electronics.[24] Thin film patterns constructed with these metals had shown dissolution in deionized water as well as in body fluids. The degradation of the MOSFETs were evaluated via drain current, showing the degradation takes place in hours (Figure 1.4 (a)). Semiconducting polymers can also be used for transient electronics. In such work, Prof. Zhenan Bao's group fabricated totally decomposable conjugated polymer for transient electronics. [25] Group synthesized 5,5'-(2,5-bis(2-octyldodecyl)-3,6-dioxo-2,3,5,6-tetrahydropyrrolo[3,4-c]pyrrole-1,4-diyl)bis(thiophene-2-carbaldehyde), DPP-CHO in short, and polymerized to obtain semiconducting PDPP-PD to be used to fabricate transient CMOS devices. With Fe as the gate and source-drain electrodes, aluminum oxide (Al_2O_3) as the dielectric layer and cellulose as the substrate, a complete disintegration is shown in 30 days (Figure 1.4 (b)). Again, Rogers' group had developed a natural wax composite with tungsten micro/nano particles to obtain conducting composites, which could be used as the electrical pathways for transient electronics (Figure 1.4 (c)). [26] Last but not least, semiconducting amorphous indium-gallium-zinc oxide (a-IGZO) is utilized to fabricate thin film transistors (TFTs). Using a-IGZO, which is shown to have potential for biomedical applications due to its low toxicity. A-IGZO coupled with silicon nitride (SiN_x), silicon oxide (SiO_x), Mo and PVA allowed researchers to obtain fully water-soluble TFTs (Figure 1.4 (d)). [27] Above examples is an indication that a wide variety of materials, from metals to alloys, conjugated polymers to naturally found materials with complex mixtures, and semiconducting materials ranging from oxides to nitrides can be utilized to fabricate transient electronics.

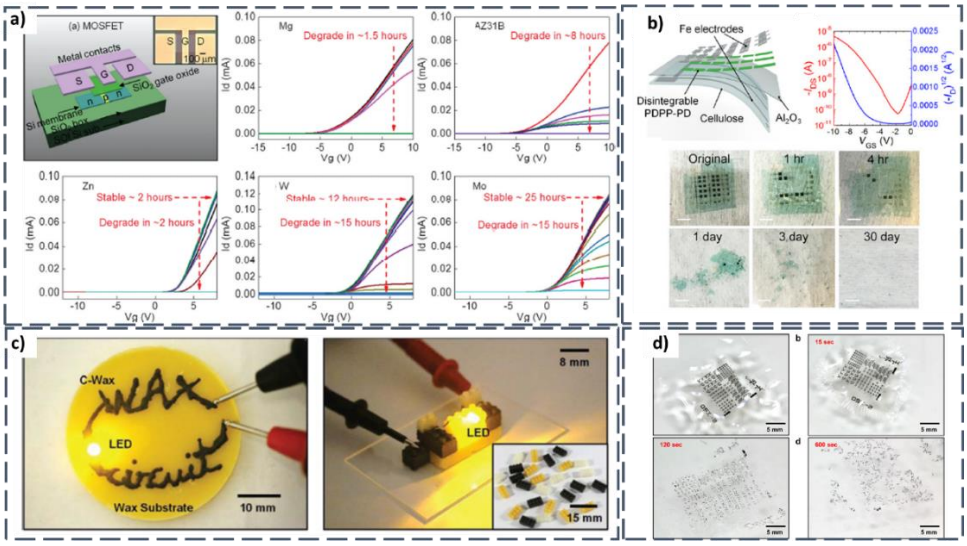

Figure 1.4 a) MOSFET devices fabricated with various metals and alloy patterns and their degradation behavior with respect to gate current. [24] b) Dissolvable and transient semiconducting conjugated PDPP-PD polymer for CMOS devices [25]. c) Natural wax and conducting composite wax for transient applications [26]. d) Transiency of TFT devices configured with a-IGZO, SiN_x, SiO_x, Mo, and PVA in DI water [27].

1.3.3 Encapsulation Materials for Transient Electronics

In transient electronics, encapsulation plays a crucial role in controlling the time of end-use. The trigger mechanism for transiency needs to clear the encapsulation before activation. Thus, usage time and hence the start of the disintegration of transient electronics can be controlled. Transient materials with limited swelling and possibly having different degradation mechanisms than the transient electronic system are promising candidates for encapsulation materials. [28] Nonetheless, materials used as transient substrates are generally used as encapsulation materials.

One of the earliest examples of this is the use of crystallized silk as the encapsulation layer, which allowed the modulation of device degradation. In Figure 1.5 (a), Brenckle et al. improved the stability of the transient electrode in water by adjusting

the number of silk layers outside of it. This also extended the amount of time it took for water to penetrate the encapsulation. [29] Zhong et al. used a more complex polymer that is triggered by UV light in order to achieve transiency on demand. Blend of polystyrene (PS) and [6,6]-phenyl-C_{61}-butyric acid methyl esters (PCBM) to obtain phototriggerable encapsulation layer that is resistant to dissolution. With PS-PCBM encapsulation, resistors and random-access memory (RRAM) devices can withstand water immersion without any faults for prolonged times (Figure 1.5 (b)), yet can be degraded by applying UV light. [30] These two examples show how encapsulation layer could be used to prolong the usage, or control the mechanism of transiency.

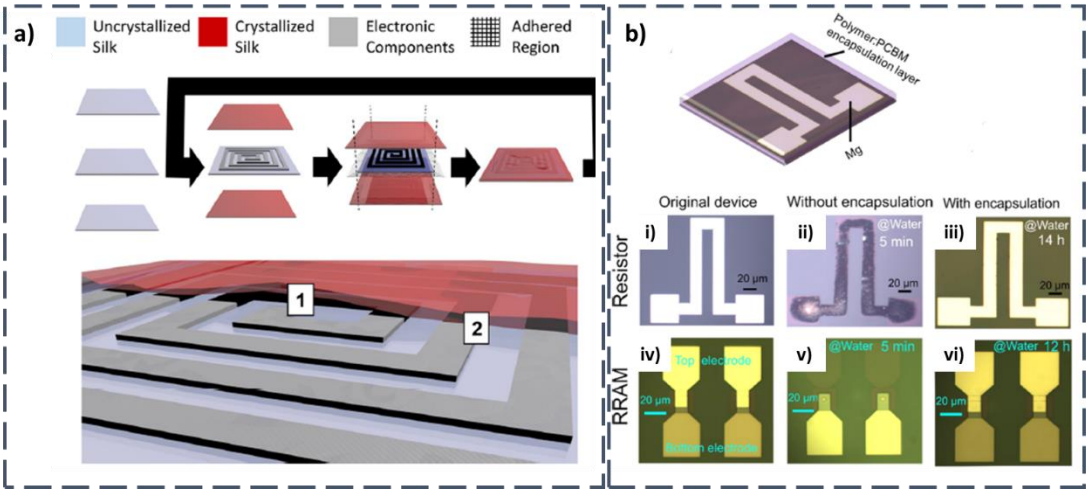

Figure 1.5 a) Encapsulation strategy of electronic components by crystallized silk layer, which is named as pocket strategy. [29] b) Schematic representation of Mg-based devices encapsulated with PS:PCBM polymer blend. b-i,ii,iii) Optical microscope images of a resistor degradation in water immersion without and with encapsulation. Similarly, b-iv,v,vi) shows the optical microscope images of RRAMs in water immersion without and with encapsulation. [30]

1.4 Transiency Mechanism of the Transient Electronics

As discussed above, the transiency mechanism can be controlled via used materials, or encapsulation strategy. Mainly, it is safe to say that the degradation/disintegration mechanisms are either physical or chemical. [31] For both cases, the mechanism could depend on a degradation rate, or triggered via different stimuli such as temperature, light, or solvation. [2]

1.4.1 Transiency via Dissolution

Most common way for the activation of transiency in transient electronics is exposure to various aqueous solutions, which could be as simple as DI water, with different pHs or salts to simulate different conditions. Earliest study on transient electronics firstly explored the transiency with DI water. [32] Although the transiency process is simply dissolving of several different components, the mechanisms for each component can have different triggering mechanism. In the case of Mg electrodes, MgO dielectrics and Si diode, following hydrolysis reactions occur; [32]

$$Mg + 2H_2O \rightarrow Mg(OH)_2 + H_2$$

$$MgO + H_2O \rightarrow Mg(OH)_2$$

$$Si + 4H_2O \rightarrow Si(OH)_4 + 2H_2$$

Similar hydrolysis reactions occur for the similar metals such as Fe, Zn, Mo, and W [24], which makes these metals attractive due to the last product being biocompatible

and environmentally safe. [4] Similarly, Si is a very good candidate for transient electronics due to its hydrolysis reaction leading into orthosilicic acid, which is environmentally benign and very close to neutral pH. [32]

Polymers that are water soluble are great candidates that can be triggered easily with aqueous solutions to induce transiency. In this manner, polymers are used both for substrates and encapsulation layers. [4] Polymers such as PVA [33,34], PLGA [35,36], polycaprolactone (PCL)[35,37], PLA[38,39] and naturally found compounds such as silk[40,41], cellulose[42,43], sodium alginate[44,45], and gelatin[46,47] are widely used for transient electronic systems that can be triggered with water. For example, polymers and naturally found compounds such as PVA and cellulose have hydroxyl groups, making them easily soluble in polar solvents such as water or N-methyl pyrrolidone (NMP). [10] This is due to the permeation of water inside the polymer chains, where water molecules form hydrogen bonds with hydroxyl groups.[48] Aforementioned example in Section 1.3.1 also controlled the rate of transiency in PVA by the addition of sucrose – to make the transiency process much faster than usual (Figures 1.3 (b) – (d)). PLGA; on the other hand, is an actually copolymer of PLA and polyglycolic acid (PGA), and has a hydrophobic characteristic. This hydrophobicity can be improved by controlling PLA:PGA ratio to obtain longer transiency. [10,35]

The only disadvantage of water-soluble transient electronics could be their inevitable susceptibility to moisture [49], which could be very harsh in high-moisture regions in the world. Due to the presence of moisture in atmospheric conditions, it is safe to say that the transiency could begin even in ambient conditions in such places. Water-soluble transient electronics can be triggered by a change in weather, even when moisture levels are low. Therefore, one must always assume their transiency mechanism can be activated in ambient conditions, without even submerging them in water. When designing these devices, it is essential to consider encapsulation in accordance with this factor.

1.4.2 Transiency via Photodegradation

Triggered transiency with light – which in this case is ultraviolet (UV) – is another route to obtain transient electronics. Although most polymers degrade under UV light in prolonged times of exposure, there are also different mechanisms provided by UV exposure. Polymers with photo-acid generators and light-induced phase transition materials are the two examples. [4]

The first and most iconic example is shown by Hernandez et al. [50], where the researchers used metastable Poly(phthalaldehyde) (PPA), where they have combined cyclic PPA (cPPA) with photo-acid generator (PAG) additives. Once the transient electronic on this PAG/cPPA substrate is exposed to UV, PAG additives (which is 2-(4-methoxystyryl)-4,6-bis(trichloromethyl)-1,3,5-triazine – MBTT) release highly reactive $Cl\cdot$ radicals which absorbs the hydrogen from the environment and forms hydrochloric acid (HCl) (Figure 1.6 (a)). The formation of HCl causes rapid depolymerization in cPPA, resulting in a photo-triggered transiency within few hours. The visible degradation of the transient electronics is shown in Figure 1.6 (b). Although not for the transient electronics, similar effect is captured by titanium dioxide (TiO_2) addition. Zhou et al. [51] proposed that with the addition of TiO_2 nanoparticles inside sodium alginate, they have achieved depolymerization under UV light. The UV degradation already happening due to photo-Fenton system, which is the mechanism of the hydroxyl radical generation inside the system. Addition of TiO_2 further improved this generation due to its photocatalytic nature, where the researchers were able to control the rate of depolymerization by controlling the amount of this photocatalytic additives inside the sodium alginate matrix.

Zhong et al. [52] utilized the latter mechanism, which is light-induced phase transition. They have used a hydrogel-oxide bilayer encapsulation, which normally limits water penetration. Under UV-light, the hydrogel undergoes a gel-to-solution transition due to the photoinduced cleavage reaction of azo bonds. This reaction allows water permeation through the MgO oxide layer, which actually triggers the transiency for the RRAM device.

Chen et al. [53] combined the dissolution mechanism with UV radiation to trigger transiency for gold electrodes. While gold is an inert metal and do not dissolve in potassium ferricyanide ($K_3[Fe(CN)_6]$), potassium ferrocyanide ($K_4[Fe(CN)_6]$) irradiated with ambient light enables dissolution of gold. This was attributed to the presence of photoactivity of $K_4[Fe(CN)_6]$, which enables the gold dissolution. The proposed mechanism is electrochemical in nature, which is actually gold cyanidation[53];

$$Au + CN^- \leftrightarrow AuCN_{ads} + e^-$$

$$AuCN_{ads} + CN^- \leftrightarrow Au(CN)_2^-$$

This mechanism is followed by taking optical and SEM images for the gold electrodes, and results are shown in Figure 1.6 (c). With the light exposure, resistance increase was observed (inset of Figure 1.6 (c)), which is by the degradation of gold - both visible in optical and SEM images. This research indicates that the transiency mechanisms could be combined or require one another and open up new tools for the transiency methods for transient electronics.

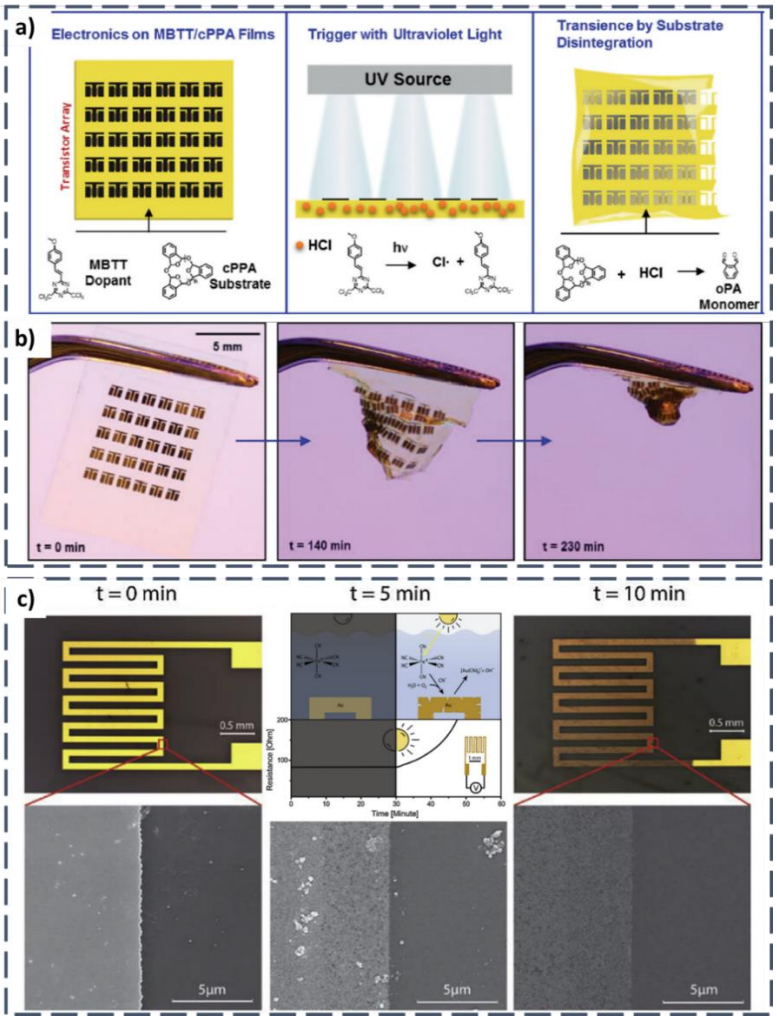

Figure 1.6 a) Schematic representation of transient electronics on MBTT/cPPA films, which underwent degradation due to PAG. b) Optical images of the degradation triggered by the PAG additive in cPPA matrix. [50] c) Optical and SEM images of the dissolution of gold electrodes in potassium ferrocyanide solution irradiated with ambient light. Inset shows the change in resistance before and after irradiation.

1.4.3 Transiency via Thermal Degradation

Thermal degradation of transient electronics is another method for achieving transiency. Thermal degradation, at its core, aims at a complete degradation and destruction of the transient electronics without leaving any trace. [4]

An earlier example done by Park et al. [54] utilized destructive additives in the encapsulant to destroy the transient electronics. For this purpose, encapsulated acid microdroplets were integrated into wax encapsulant, which is schematically shown in Figure 1.7 (a). Upon enough heating, due to the melting of wax, acid microdroplets were released. Upon reaching to cPPA substrate and Mg electrodes, the transient electronics were easily degraded. This is also optically shown while recording the change in resistance for the serpentine-shaped Mg electrodes in Figure 1.7 (a). On the other hand, Liu et al. [54] proposed thermal degradation of substrates for memristors. Using polyoxymethylene (POM) without end-capping resulted in thermally triggerable polymer materials, which allows transient electronics to be built on them. A schematic diagram of the memristor based on chromium (Cr)/Au/SiO_2/Cu built on POM substrate is given in Figure 1.7 (b), with the optical image and typical I-V characteristics. Upon the heat treatment, thermal degradation of the memristor was visible with a naked eye, in less than one hour. Suggested mechanism is the POM releasing a volatile formaldehyde (HCHO) gas with thermal triggering due to depolymerization and induce transiency destructively for the memristor device.

Very recently, research done by Teng et al. [55] obtained fully recyclable liquid-metal-based transient electronic devices, which is unlike most of the thermally triggered ones. [56,57] Researchers utilized liquid metal (LM) based conductors and sodium hydroxide (NaOH) embedded paraffin as a degradation agent. Using room-temperature LM of eutectic gallium-indium (EGaIn) and Galinstan (GaInSn)

allowed a complete recycling of these materials by heating. Optical image of the device is given in Figure 1.7 (c). Upon heating, paraffin wax was melted, which destroyed the LM circuit. Melting of the top layer of NaOH embedded paraffin released the NaOH, which destroyed the whole structure. Yet, recycling was also equally easy, where the representative process of the recycling is given in Figures 1.7 (c-i) to 1.7 /(c-iv). After cutting the device from the corner (Figure 1.7 (c-i)) LM could be easily recollected again by its natural agglomeration (Figure 1.7 (c-iv)), while the paraffin melted down can be recollected again as well Figure 1.7 (c-iii)). All in all, thermally triggered transient electronics also holds lots of potential for the future applications, which may aim the complete destruction of the electronics or recovery of the materials.

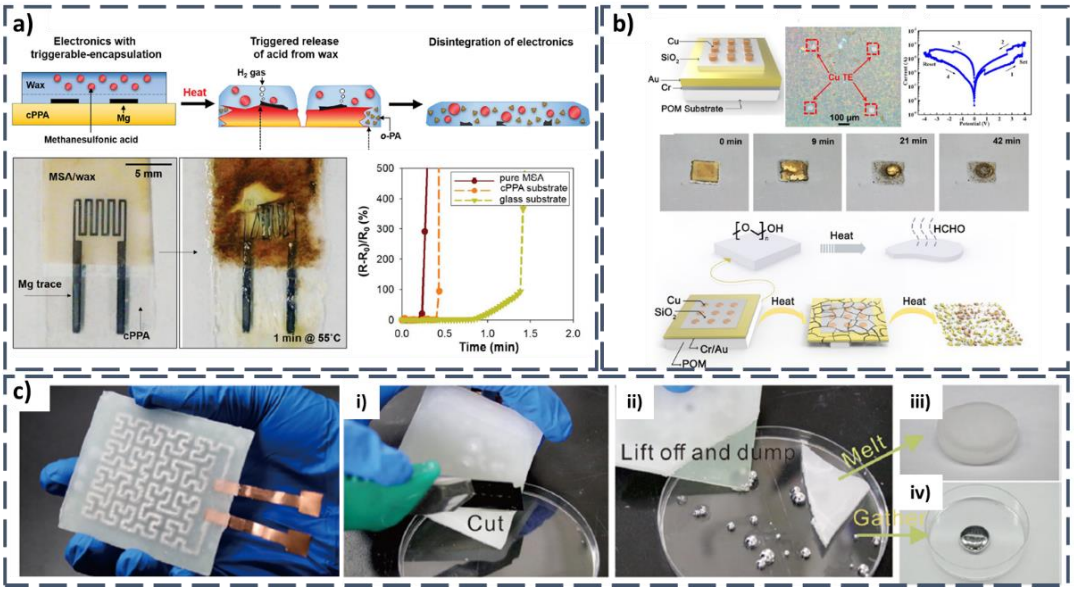

Figure 1.7 a) Schematic representation of the heat-triggerable transient electronics with wax encapsulant embedded with acid microdroplets. Release of the acid leads rapid disintegration of the device due to acid release. Optical images of this disintegration and relevant resistance change are also given. [58] b) Schematic diagram of a memristor on thermally-triggerable POM substrate. Upon heating, due to the depolymerization of POM substrate, HCHO gas is released, destroying the memristor device. [54] c) Transient LM-based heater. i) Recycling can be done simply by cutting the edge of the device, allowing the separation of LM from the wax (ii). Recycled paraffin wax (iii) and LM is (iv) is easily gathered after that.[55]

1.5 Application Areas and Relevant Devices for Transient Electronics

The aim of fabricating transient electronics is to reduce the e-waste caused by the increased use of electronics. Still, the first and foremost area for the transient electronics – being biocompatible, biodegradable, and even implantable and digestible – is biomedical devices. The aforementioned properties, such as its minimal to nonexistent toxicity and on-demand usage, make it highly appealing for the healthcare industry. [59,60] Thus, the usage area for transient electronics can simply be divided into two, biomedical devices and non-biomedical devices. [11]

1.5.1 Biomedical Devices

Transient electronics, which are biocompatible and bioresorbable, are of great interest for biomedical devices. They expand the possibility of implantable devices as well as ingestible devices that can be digested. [59,61] Especially for the ingestible transient device, tracking of various diseases without any intrusive technique can be made possible – which is especially important for gastrointestinal tract.[61] Although not transient, PillCam™ (Figure 1.8) is one of the first examples of ingestible devices to track stomach and colon-related diseases that is commercialized. Yet, it still does not evade being an e-waste after its used, and still needed to be excreted from the human body – which can still have the possibility of some adverse effects. Hence, bioresorbable implantable and ingestible devices hold great potential to reduce most invasive and surgical procedures and also decrease the e-waste generated by the ever-increasing need for health monitoring devices.

Implantable medical devices are one of the cornerstones of modern healthcare systems, as they can be used for diagnosis, treatment, and rehabilitation. [62] The difference between implantable devices and transdermal devices is that the implantable ones are placed directly or close proximity to the target organ – which should be safely removed through surgical methods after their intended use. Transient implantable devices are of great importance in such case, where the placed devices are bioresorbed in an engineered time, without the case of additional surgeries or without the risk of causing infections and side-effects. [62,63] One of the recent works by Boutry et al. [64] present a capacitive pressure sensor which is based on biodegradable materials to measure arterial blood flow, where sensor is operated wirelessly (Figures 1.9 (a) – (d)). The aim is to closely follow a procedure called vessel anastomosis (Figure 1.9 (a)), which is a reconstructive procedure for the veins, which may have post-op complications. In order to follow-up these kinds of procedures, researchers have designed a capacitive sensor that can wrap up veins to follow any change in their diameter (Figure 1.9 (b)). This allows close monitoring or arteries as well as possible complications after surgery. Figure 1.9 (c) shows the structure of the capacitive pressure sensor, which is all built by bioresorbable materials. Figure 1.9 (d) shows an optical image and the SEM images of the capacitive device and its micropatterned PGS layer, which enhances the capacitance reading by its evenly spaced pyramid pattern. Ultimately, researchers have been able to fabricate a short-term device for tracking vessels, which does not require a second surgical process for the removal due to its bioresorbable nature. [64]

Figure 1.8 Photograph of PillCam™ capsule for endoscopy and colonoscopy. Retrieved from medtronic.com

In another work, Choi et al. [65] fabricated a transient closed-loop system which has a bioresorbable pacemaker that is wirelessly connected with skin-integrated devices, which can track the cardiac activity on top of providing multihaptic feedback (Figures 1.9 (e) – (g)). With the wireless closed-loop system, the dependence on the conventional electrical hardware is removed. Moreover, with the transient materials the need for a secondary surgical event is eliminated. As given in the schematic in Figure 1.9 (e), wireless connection made with the transient closed-loop system can provide autonomous therapy and health tracking, which would be terminated by its own with a controlled transiency. The system given in Figure 1.9 (f) is consisted of bioresorbable epicardial pacemaker, bioresorbable steroid-eluting system to reduce the risk of inflammation, bioresorbable power harvesting unit, biocompatible skin sensors for electrocardiogram (ECG) measurements and physiological monitoring, a wireless radio frequency (RF) module to transfer power wirelessly to the power harvester, a haptic actuator, and a handheld device, such as a smartphone, to store and do analysis or visualization of the data. The most important part of this transient and bioresorbable pacemaker (Figure 1.9 (g)) is that it can dissolve in PBS solution completely within 40 days – proving that the use of the device can be terminated without hospitalization. [65]

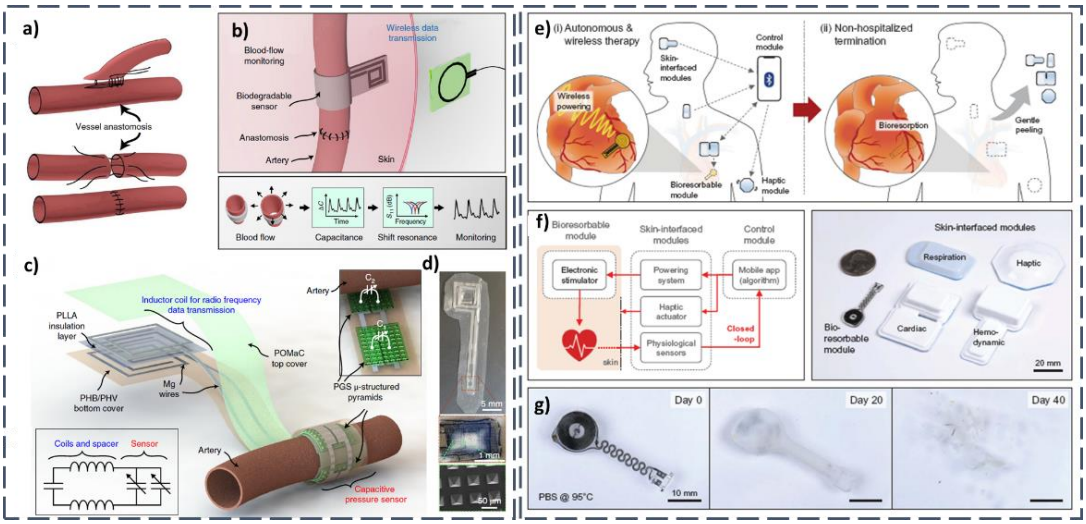

Figure 1.9 a-d) Transient bioresorbable arterial-pulse sensor for post-op tracking. a) Schematic representation of the vessel anastomosis where b) the sensor is placed for post-op monitoring. c) General structure of the sensor including the inductor coil part for data transmission. d) Photos of the fabricated arterial-pulse sensors, and SEM image of the micropatterns for capacitive sensing. [64] e-g) Transient closed-loop system for tracking cardiac pacing and physiological events. e) Schematic and general idea of the working principle of transient closed-loop system, with no requirement of surgical operation for termination. f) Components of the whole device and its operational structure. g) Photos of the bioresorbable module degradation in PBS, which is simulated biofluid. [65]

Apart from bioresorbable and implantable devices, edible and ingestible miniaturized transient electronics also received significant attention.[66] Edible devices are primarily focused on addressing gastrointestinal tract diseases, given the significant market size of nearly one billion dollars associated with these health issues.[67] Conventional ingestible electronics are generally required to be excreted due to their rigid and nondegradable encapsulations, which still carry some risks that may have adverse effects on the patient. Therefore, there is a proposal for transient ingestible devices, known as edible electronics or transient electronics, which can be digested after use, presenting a new form of ingestible devices. [67,68] One of the

earliest examples done by Joseph Wang's group [69] introduced the first completely food-based edible electrochemical sensors by fabricating sensors solely of food materials (Figures 1.10 (a) – (e)). The electrochemical sensors fabricated with food materials are comprised of edible activated charcoal, food sleeves and olive oil (Figure 1.10 (a)). Resulting electrodes which are stuffed with various edible materials are provided in Figure 1.10 (b). These electrodes can be used as electrochemical sensors, which could interact with the saliva (Figure 1.10 (c)), gastric fluid (Figure 1.10 (d)) or intestinal fluid (Figure 1.10 (e)) to give different responses. This proves that the fabricated edible sensors have the potential to detect various diseases throughout the entire digestive system. [69]

Transient electronics with the aim of transiency triggered *in-vivo* rather than *in-vitro* are also studied extensively. In such a recent study, Christopher J. Bettinger's [70] group fabricated a genipin-cross-linked gelatin-based transient ingestible impedance module that can evaluate gastrointestinal diseases. Fabricated capsule measures the impedance with the epithelial barriers in gastrointestinal tract (Figure 1.10 (f)). These epithelial barriers act as membranes and have the duty of absorption of nutrients and water while keeping the waste outside. Thus, the integrity of this barrier is an important parameter to find or cancel-out the possible diseases. Any compromised barrier – which could be related with several diseases, result in a change in impedance measurement (Figure 1.10 (g)), allowing researchers to pinpoint the problematic area in the gastrointestinal tract. Compromised barriers result in lower impedance values, efficiently being a biomarker for detection. The final structure of the device is given in Figure 1.10 (h), with a photo of the thin film electrodes on cross-linked gelatin hydrogels. [70]

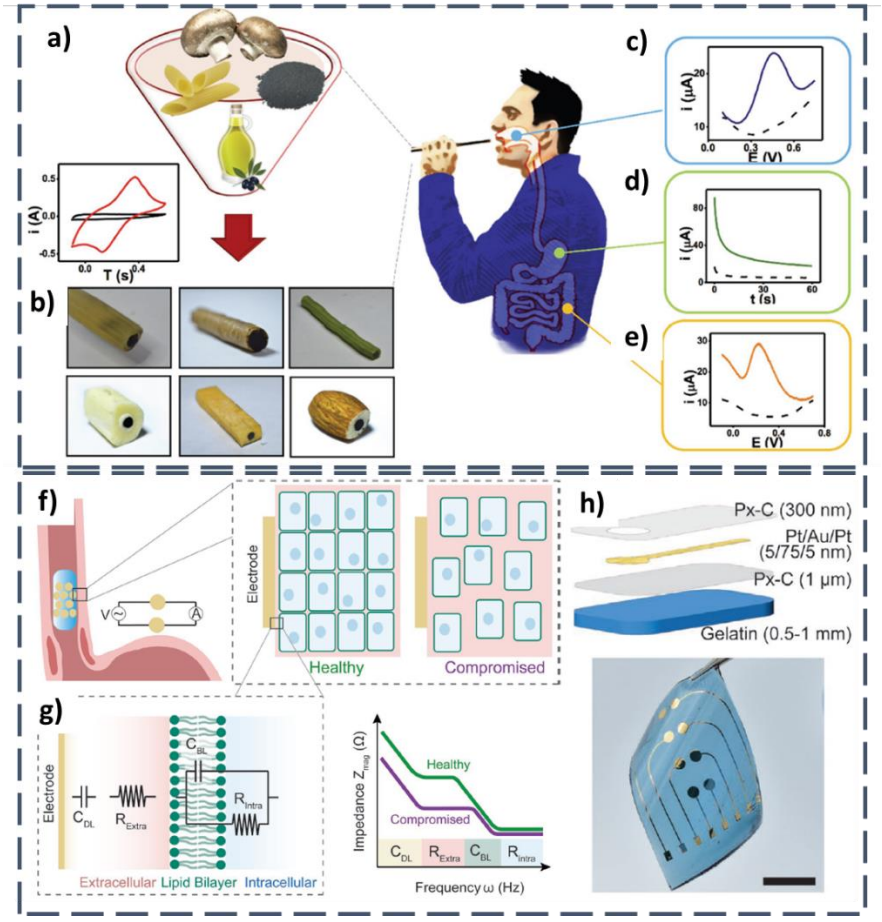

Figure 1.10 a-e) Food-based electrochemical sensors and their signals from different parts of the digestive tract. a) schematic representation of food-based materials and activated charcoal for the fabrication of the edible sensors. b) Photos of the electrodes packed in various types of foods. These electrochemical sensors can give response in c) saliva via differential pulse voltammetry, d) gastric fluid via amperometry or e) intestinal fluid via square wave voltammetry [69] f-h) Conceptual schematics of ingestible transient impedance module that can detect compromised areas in gastrointestinal tract. f) Schematic representation of the module making contact with the epithelial lining in the tract – which can take measurements from the healthy or compromised tracts. g) Representative electrical circuit constructed with the capsule and the epithelial barrier, and representative impedance results. h) Schematic structure of the device with electrodes, and its optical image (scale bar corresponds to 5 mm) [70].

1.5.2 Non-medical Transient Devices

Transient electronics are also important to reduce the general e-waste caused by the ever-growing electronics industry. Although the primary interest with the transient electronics are mostly bio-medical related, transient electronics also hold a great potential for their use in various applications. These include energy storage[71] and energy harvesting[72] devices, electrochemical sensors[73], pressure sensors[74], memristors[75] ,and even soft robotics[46].

Ji et al. [75] fabricated bipolar resistive memory (Figures 1.11 (a)-(c)), which is constructed from transient metals of W and Mg as the electrodes and silk fibroin as the dielectric. Silk fibroin, acting as the switching layer, forms a metal-insulator-metal interface with W and Mg electrodes. Schematic structure and the photos of the device is given in Figure 1.11 (a). Schematics of resistive switching under applied voltage utilizing the silk fibroin is provided in Figure 1.11 (b). The state of ohmic conduction is the initial stage, where silk fibroin has a high -resistance state, and the I-V characteristic is of Ohmic Law. When the applied voltage is increased to the range of 0.2 to 0.5 V, space charges appear inside silk fibroin structure. This state is called space-charge-limited conduction (SCLC). Few generated charges mostly fill the traps inside the dielectric layer. Higher voltages than this increases the due to strong injection of space charges, which changes the characteristic to trap-free SCLC. Pushing beyond, this trap-free SCLC state abruptly converts into a low-resistance stage, where a conductive path is formed between the metal electrodes. This resistive memory device comprised of W/Silk fibroin/Mg was also subjected to transiency in PBS solution (Figure 1.11 (c i-vii)), which was found to dissolve completely in 24 hours. [75]

Tran et al. [76] fabricated a transient semiconductor which is stretchable and fully degradable (Figures 1.11 (d) – (h)). Figure 1.11 (d) shows the schematic representation of the fabricated diketopyrrolopyrrole-based polymer -p(DPP-PPD) for the semiconduction blended with stretchable PCL-based elastomer. This way, two component, fully transient and semiconducting system formed from PCL and p(DPP-PPD) is achieved, which is termed as nanoconfined p(DPP-PPD). As demonstrated in Figure 1.11 (e). The nanoconfined p(DPP-PPD) transferred onto PDMS is stretchable up to 100%. In order to measure the thin-film transistor (TFT) performance under strain, a device shown in Figure 1.11 (f) is fabricated. Nanoconfined p(DPP-PPD) has shown no decrease in mobility under pressure when compared to neat p(DPP-PPD) that does not contain PCL (Figure 1.11 (g)). The obtained nanoconfined polymer is designed to be transient in acidic solutions. In trifluoroacetic acid (TFA), the degradation of both PCL and p(DPP-PPD) is clearly visible, and tracked by the changes in UV-vis spectra (Figure 1.11 (h)).

Molybdenum disulfide (MoS_2), which belongs to transition metal dichalcogenides (TMDs) is also an attractive 2D material for transient electronics. MoS_2, having promising electrical, optical and catalytic properties, is recently studied extensively for biosensors. [77] In thorough research, it was also proven that MoS_2 degrade due to slow hydrolysis reaction in aqueous solutions, and had shown no adverse effect on cell proliferation, indicating that they are biocompatible and non-toxic. [78] Building on this, Yoo et al. [79] used wafer-scale two dimensional MoS_2 layers for the fabrication of environmentally friendly transient electronics, which are photodetectors, pressure sensors and field-effect transistors (Figures 1.11 (i) – (k)). MoS_2 pattern was integrated layer-by-layer onto paper substrate to fabricate a transient pressure sensor, which is shown in Figure 1.11 (i). The difference in the I-V curve with different pressure levels shows that these electronics are viable to be used as pressure sensors. Moreover, field-effect transistors (FETs) were also fabricated by utilizing MoS_2 on PMMA substrates, and again shown a promising

performance under different gate voltages (Figure 1.11 (j)). The transiency of MoS_2 in baking soda buffer (BSB) is also tracked by optical microscopy, images of which are given in Figure 1.11 (k), showing a complete degradation after 180 hours. [79]

In a very interesting study, researchers fabricated soft robotics and soft electronics based on gelatin-biogels, which are surprisingly elastic and resilient, yet have a full transiency (Figures 1.11 (l) – (o)). [46] With the fine tuning by the addition of glycerol and water, excellent mechanical stability is achieved, whereas citric acid is added to prevent the fouling of the gelatin-based device. In ambient conditions, soft actuator (Figure 1.11 (m)) is stable for more than 1 year and can still be used, and can be disposed in wastewater. Soft pneumatic actuators fabricated by gelatin-based biogels have excellent bending performance and can be cycled as many as 330,000 cycles without failure. Soft electronics with the help of flexible and reusable PCB board is also fabricated which had a temperature sensor, humidity sensor, strain sensor, and pressure sensor again based on the biogels (Figure 1.11 (o)). Images of the devices and resulting measurements are provided side-by-side, showing that the gelatin-based biogels enable transient multimodal sensing capability. [46]

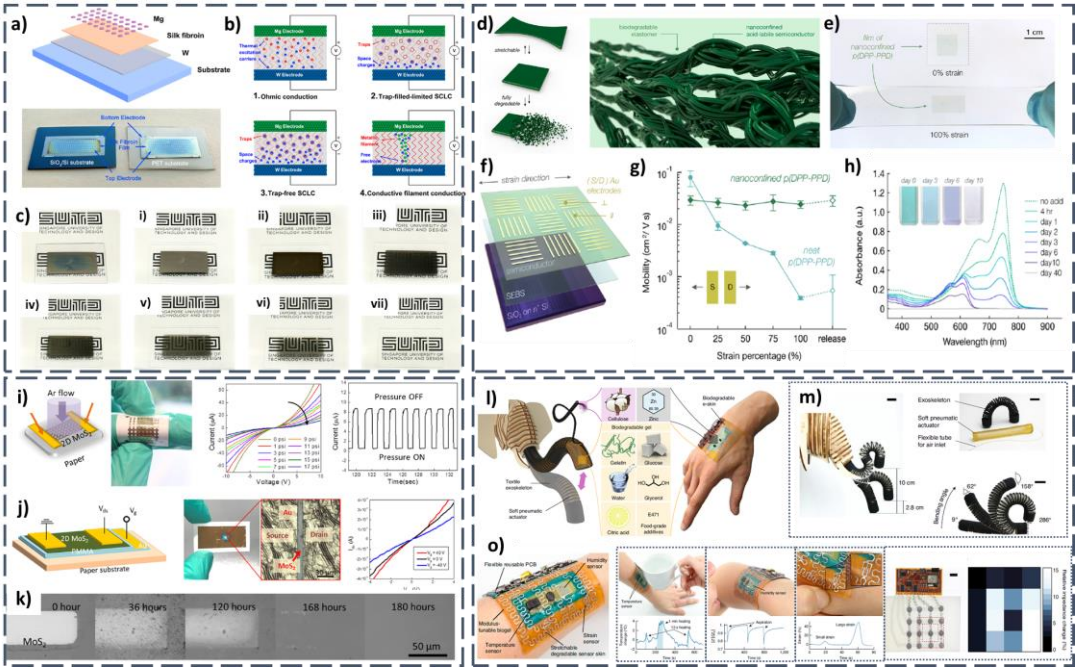

Figure 1.11 a-c) Biodegradable resistive memory. a) Schematic of the resistive memory device utilizing Mg/Silk fibroin/W interface. b) Working mechanism of the device under different voltage bias. c) Transiency of the devices from i) initial submersion to vii) 24 hours. [75] d-h) Design of fully degradable semiconducting polymer films. d) Schematic structure of the PCL – p(DPP-PPD) blend and e) its stretchability. f) Schematic structure of the fabricated device to measure stability under strain. g) The change in saturation mobility under strain conditions. h) UV-Vis spectra of the devices in TFA solution, which shows complete degradation after 40 days. [76] i-k) Transient MoS_2 electronics. i) MoS_2 based pressure sensor on paper substrates and corresponding I-V and current-time graphics under loading conditions. j) MoS_2 based FET devices with optical images of the device showing the magnified version of the components and I-V characteristic under different gate voltage bias. [79] l-o) Gelatin-based soft robotic and soft electronics. l) Schematic representation of the materials used for the actuators and e-skin. m) Soft actuator in s-shape, with the components forming it and the maximum bending that the actuator is capable (Scale bar corresponds to 2 cm). o) Soft electronic patch based on gelatin biogel. Corresponding device photos of temperature sensor, humidity sensor, strain sensor, and pressure sensor are provided with corresponding graphs. [46]

1.6 Motivation of this Thesis

Research efforts on transient electronics mainly focus on the solubility in water or PBS solution at room temperature (RT) or at elevated temperatures [18,75,80]. Different components of transient electronics make use of inert conductors such as carbonaceous materials [81–84], silver [85–87], magnesium [24,88], tungsten [24] or gold [7,17], and safe polymeric materials and biomaterials such as PVA[89,90], poly(lactic acid) (PLA)[89,91], poly(lactic-co-glycolic acid) (PLGA)[85,92], chitosan[93] and agarose[94,95]. Transient electronics concept emerged with frequent demonstrations of transistors and batteries[24,88,96,97] . These are only the two basic components in an electronic device. It is clear that the transiency should be demonstrated in many other electronic components so that the overall electronic product can be claimed as fully transient.

Among the materials, PVA is the most commonly used biocompatible and biodegradable material utilized in biomedical applications[98–100], electronic circuits[101,102], triboelectric nanogenerators[85], nanocomposite fabrication[33,103], and energy storage devices and supercapacitors [104–106]. In supercapacitors, PVA was utilized only as a solid-state electrolyte layer for flexibility and biodegradability [89,104,107]. Transient triboelectric energy harvesters were also a subject of research, which could allow a green energy source with zero waste. Transient triboelectric energy harvesters were also a subject of research, which could allow a green energy source with zero waste. Yet, TENGs utilizing PVA did not explore the transiency aspect. [85,108] PVA was also utilized in capacitive sensing applications for physiological signal monitoring as well as for pressure sensing, but again with limited exploration on transiency. [109,110] It is evident from the literature that multifunctionality of PVA based layers were not explored sufficiently, and most studies fail to address transiency. Moreover, none of these works disclose all PVA-

based (i.e. electrode, electrolyte, insulating layer, and encapsulation layer) physically transient and multifunctional devices.

This dissertation focuses on fabricating multimodal PVA layers to prove an efficient way to obtain different transient electronics with similar layers. As such, simple solution-based approach is adapted to fabricate all PVA-based physically transient supercapacitors (T-SUPC), triboelectric nanogenerators (T-TENG) and transient capacitive sensors (T-CAPS) that are water-soluble, biodegradable, biocompatible. PVA was chosen due to cost effectiveness, modification flexibility, accessibility on top of its inherent biocompatibility and biodegradability. [111] In the light of this, the thesis is divided into 3 sections that explores different application areas and resulting devices:

In Chapter 2 – Transient supercapacitors (T-SUPC) are fabricated by all PVA-based layers to explore their efficient use in energy storage applications;
In Chapter 3 – Transient triboelectric nanogenerators (T-TENG) are fabricated to show the capability of PVA-based layers in energy harvesting and self-powered electronics;
In Chapter 4 – Transient capacitive sensors (T-CAPS) are fabricated to indicate that these layers can also be used for sensing applications, and are sensitive enough to track even the smallest physiological movements.

CHAPTER 2

TRANSIENT SUPERCAPACITORS

2.1 Introduction to Supercapacitors

Electrochemical capacitors (ECs), also known as supercapacitors (SCs), have been known for 60 years. [112] The earliest example, however, traces back before the *Volta's Pile*. Researchers in 18th century relied on *Leyden Jar* for energy storage. Silver foils inside and outside a glass jar which uses the glass jar itself as the dielectric layer; the Leyden jar was the first energy storage device introduced to the world, which worked as a capacitor. [113,114] Earlier and conventional SCs are generally based on high surface area of carbonaceous materials. [115] ECs received significant attention in the recent years due to their very fast discharge rate, long cycling life and capacity retention, and high-power delivery and uptake when compared to the conventional Li-ion batteries. [116,117]

By 2023, there are lots of companies that produces various types of supercapacitors. Figure 2.1 shows the various supercapacitors that are commercial. Companies such as Maxwell Technologies [118,119] (Figure 2.1 (a) and (g)), CAP-XX [120,121] (Figure 2.1 (b) and (f)), Skeleton Technologies [122] (Figure 2 (c)), Capacitech [123] (Figure 2.1 (d)), and Kyocera-AVX [124] (Figure 2.1 (e)) produces all sorts of supercapacitors. The shapes and capacities of these devices vary according to their intended areas of use. Cylindrical small supercapacitors such as in Figure 2.1 (a) and (b) are used in various electronic circuits. Pseudocapacitors in Figure 2.1 (c) are used for start-stop systems of heavy-duty vehicles. Wire-shaped flexible capacitors are particularly

employed in situations where flexibility is required. Supercapacitors can even be designed similar to pouch-type batteries (Figure 2.1 (e)). Big modules such in Figure 2.1 (f) are used in applications ranging from transportation to grid/power correction. [121] Figure 2.1 (g) shows the combination of such modules to be used in combination with the renewable energy sources such as solar or wind energy. [119]

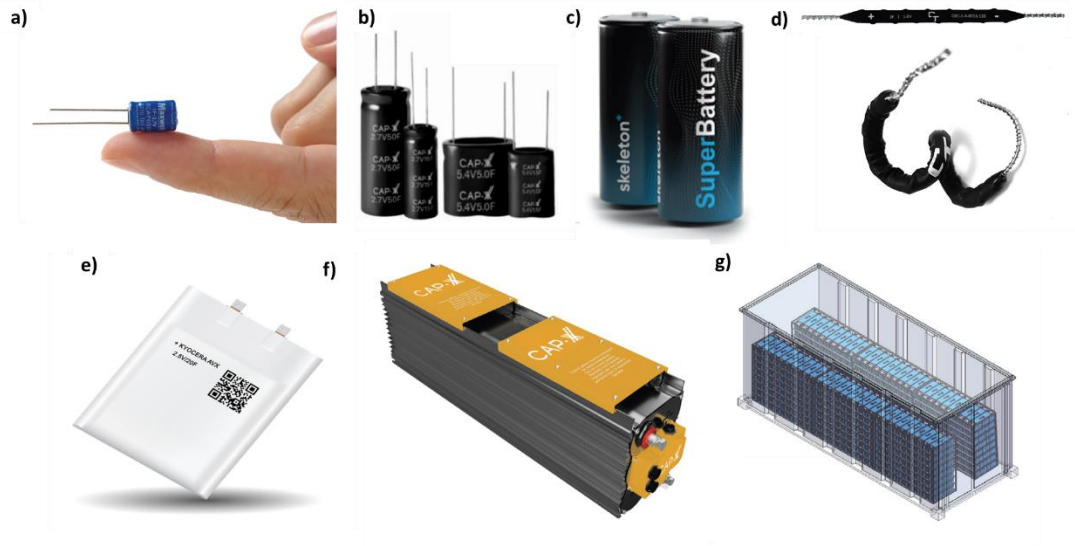

Figure 2.1 Commercial supercapacitor products from a,g) Maxwell Technologies [118] , b,f) CAP-XX [120], c) Skeleton Technologies [122], d) Capacitech Energy [123] , and e) Kyocera-AVX [124].

With the recent advances in technology, there are many application fields in which small powered devices that require high power delivery and fast recharging capability. One such commercialized example is the 'S-Pen' of Samsung S9 (Figure 2.2). This Bluetooth pen can be used 30 minutes with a single charge of 1 minute when it is docked into the smartphone. [125] Apart from the small devices, the use of supercapacitors has also been extended to consumer vehicles. Figure 2.3 (a) shows the supercapacitors (denoted as ultracapacitors – shortly UC) in the various parts of

electric vehicles. The most common use of supercapacitors known to consumers nowadays is the regenerative braking systems, where the lost energy through braking is collected by the supercapacitors to charge the batteries. [126] Apart from this, it is used to significantly increase the acceleration performance by supplying high power output and reduce the costs for hybrid electric vehicles by extending the lifetime of batteries by handling the peak power loads (Figure 2.3 (b)). [127] Supercapacitors are not only used in controlling grid power, they are even used to support the failsafe systems. Such an example is the use of supercapacitor modules for the pitch control of wind turbines to improve safety conditions by replacing Li-ion batteries and efficiency of the turbines (Figure 2.3 (c)). Compared with the previous lead-acid battery systems, supercapacitor modules practically do not require maintenance with a lifetime of 15+ years. This increases the reliability of the wind turbines, as the maintenance fees are highly reduced with much lower downtimes. [128]

Figure 2.2 Photos of Samsung S9 cell phone, which uses a supercapacitor powered 'S-Pen' [125].

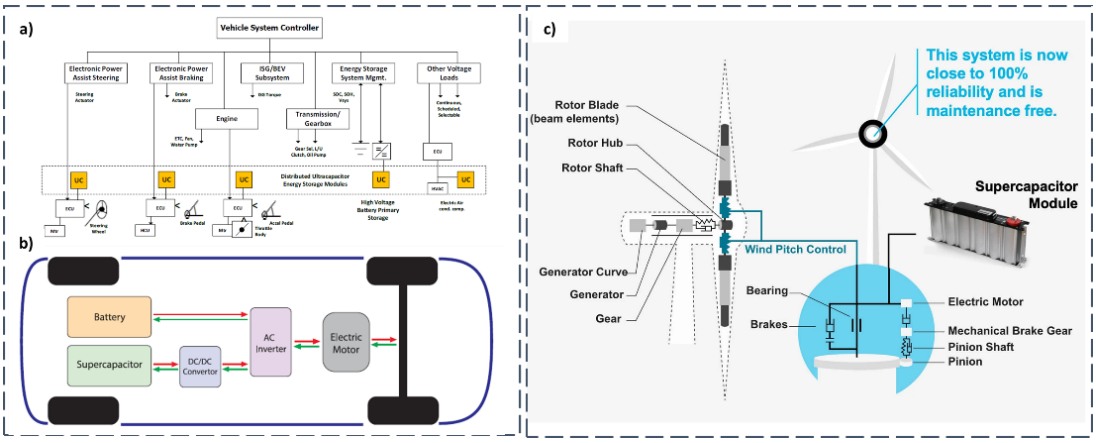

Figure 2.3 a) Various supercapacitor uses on electric vehicles [129]. b) Simplified representation of supercapacitor uses in hybrid electric vehicles [126]. c) Supercapacitor modules used in wind turbines for pitch control [128].

2.2 Working Principles of ECs

Both batteries and SCs rely on electrochemical processes to store energy, but they differ in their energy and power densities. Li-ion batteries store energy by intercalating Li^+ ions into the electrode bulk, which results in slow charge/discharge rates due to diffusion-controlled redox reactions. In contrast, SCs store energy on the electrode surface, which leads to faster reaction rates but lower energy density. [130] Supercapacitors have a charging mechanism that offers a longer cycling life, leading to reduced maintenance costs and less waste compared to batteries. As a result, SCs serve as an effective solution that bridges the gap between batteries and capacitors. [131]

Based on the working principles and types, general classification of the capacitors is given in the Figure 2.4. While the working principle of conventional capacitors and SCs are very alike in terms of utilization of the dielectric mechanism, what differs is that SCs utilize high surface area electrodes with much thinner dielectrics, allowing the SCs to have much higher capacitance and energy density than the conventional ones. [114]

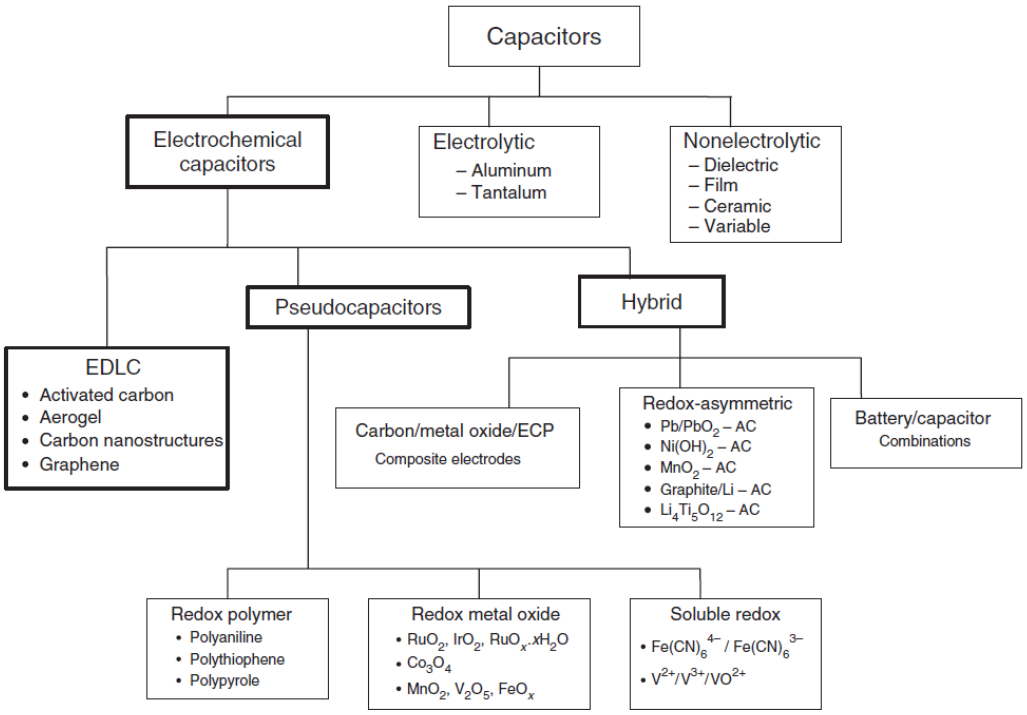

Figure 2.4 General classification of capacitors [114].

Thus, SCs have an exclusive position between the conventional capacitors and lithium-ion batteries due to their capacitances being higher than conventional capacitors and having much faster kinetics than batteries. This relationship is illustrated in Figure 2.5, known as the Ragone Plot, which depicts the energy and power densities of different energy storage devices. As suggested, depending on their mechanisms, batteries are on the high-energy and low-power density region. Typically, batteries have low output power, but they can supply power for many hours. Despite low cycle life, Li-ion batteries are popular because of their high energy density. Scientists put tremendous effort into improving the charging rates and cycle life of batteries. In contrast, electrochemical capacitors have high power; but, low energy density. Charge storage mainly relies on fast, surface-limited processes, which can be electrostatic and/or faradaic in nature. The active material on the electrodes and the chosen electrolyte plays crucial roles in these processes. [132] Depending on these properties, supercapacitors are valuable for a wide-variety of applications ranging from micro-electronics to electric vehicles and energy grid applications, as examples are provided in Section 2.1. It should be noted that the both batteries and supercapacitors have their unique areas of use and are complementary to each other. Using the superior energy densities of pseudocapacitors, it is possible that supercapacitors can replace the batteries in high-power and short-time powering of electronics. However, sometimes the goal is not necessarily to replace one another but to create hybrid systems that extend the lifetime of batteries while providing sufficient power output for applications beyond the capability of batteries alone.

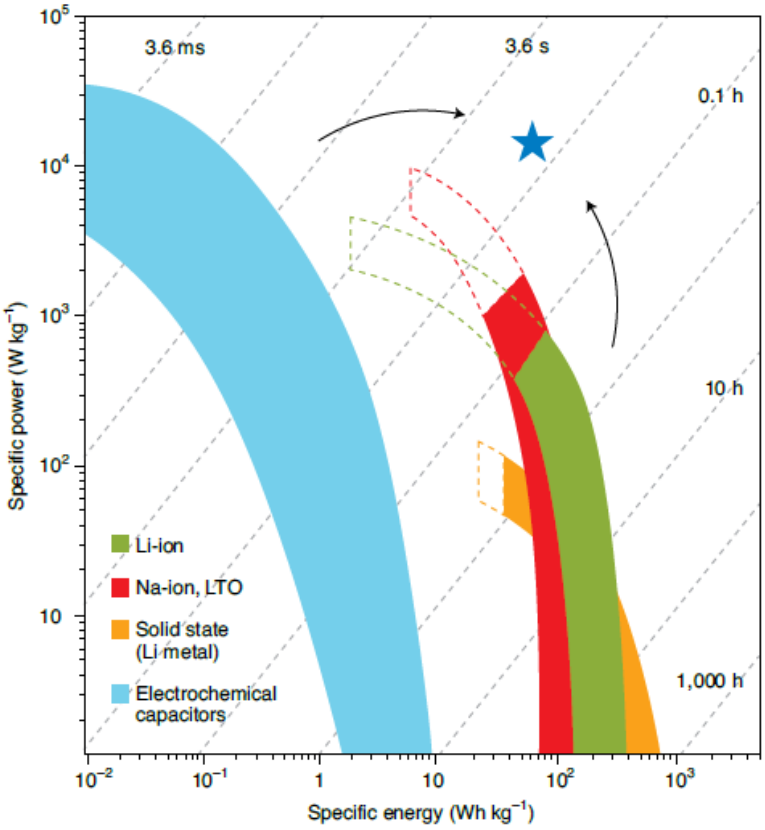

Figure 2.5 Electrochemical capacitors on Ragone Plot. Arrows show the general trend/aim for electrochemical capacitors and batteries [132].

Non-electrolytic capacitors are designed with two parallel plate electrodes and a dielectric material between them, as shown in Figure 2.7. When a potential difference is applied, the positive and negative charges move towards the surface of the electrodes with opposite polarity, storing the charge electrostatically. The capacitance of a capacitor is measured in farads (F) using the equation given below;

$$C = \frac{Q}{V} \quad (2.1)$$

where Q is the electric charge on the electrodes and V is the potential difference between them. The capacitance of a parallel plate capacitor can also be calculated using a specific equation;

$$C = \frac{\varepsilon_0 \varepsilon_r A}{D} \quad (2.2)$$

,where ε_0 and ε_r are permittivity of free space and dielectric constant, respectively. *A* is the area of the electrodes and *D* is the distance between the electrodes. [114]

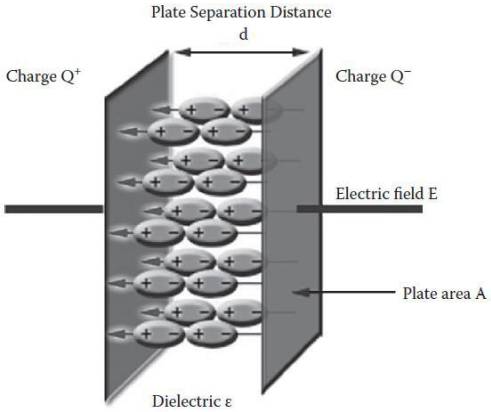

Figure 2.6 Schematic representation of a conventional capacitor device. [113]

A typical supercapacitor device consists of two electrodes separated by a separator. Such an example is given in Figure 2.7 (a). Separator can be glass fiber, polyimide, PTFE or any other porous membranes that allow ions to travel. Separator is wetted with aqueous or organic electrolytes, while solid-state electrolyte act as both separator and ionic conductor. While the structure of the supercapacitors is the same, charge mechanism depends on the active material used in electrodes. Supercapacitors are classified into two groups with respect to that; electrochemical

double layer capacitors (EDLCs) and pseudocapacitors (or redox capacitors). Both types use high surface materials in common, yet electrical double layer phenomena occur at the surface of carbonaceous materials, while fast faradaic reactions happen at the surface of the materials such as transition metal oxides, carbides and sulphides. Such an example of a supercapacitor device is provided in Figure 2.7 (b), which utilizes metal oxide materials for pseudocapacitive energy storage. Pseudocapacitance can also arise from the intercalation of ions into the 2D layered materials such as layered two-dimensional (2D) transition metal carbides and nitrides (MXenes) fabricated from materials such as $Ti_3C_2T_x$. Lately, metal organic frameworks, or MOFs, which have engineered to have desired crystal structure and extreme porosity have also been studied extensively for supercapacitors as active materials.[133] Typical differences between the storage mechanism, energy and power densities, discharge time and cycle life of conventional capacitors, batteries and supercapacitors are given in the Table 2.1 for comparison.

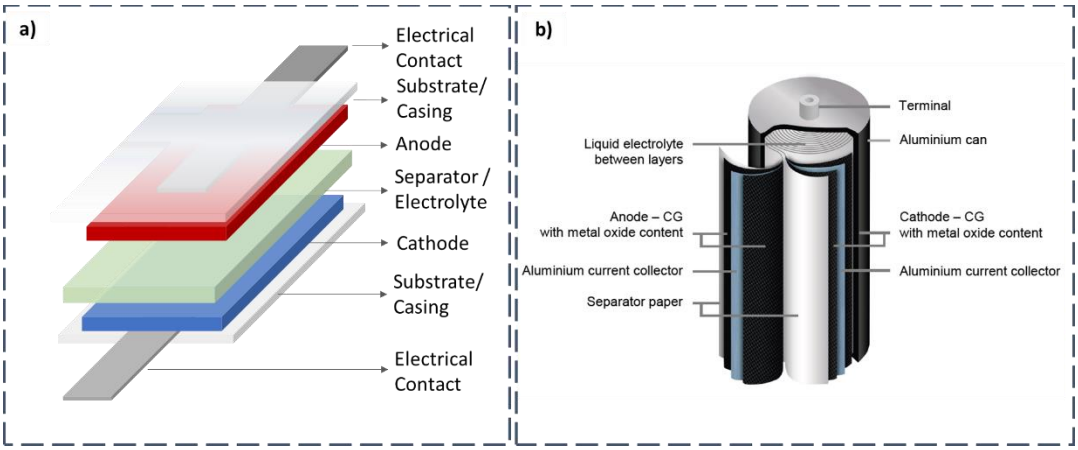

Figure 2. 7 a) Schematic structure of a conventional supercapacitors. b) Schematic structure of a cylindrical supercapacitor by Skeleton Technologies. [122]

Table 2.1 Characteristic properties and performance parameters for conventional capacitors, batteries and supercapacitors. Adapted from [114]

Characteristics	Capacitors	Batteries	Supercapacitors
Storage Mechanism	Electrostatic	Slow intercalation reaction to the bulk	Electrostatic for EDLC Fast Faradaic reactions and intercalation storage for pseudocapacitors
Charge Storage	Charged plates	Entire electrode	Electrode/electrolyte interface
Energy Density (Wh/kg)	<0.1	50 - 500	<10
Power Density (W/kg)	>10 000	<1000	<50000
Cycle Life	$>10^6$	500 - 1000	$>10^5$

2.2.1 Electrical Double Layer Capacitance (EDLC)

Energy storage mechanism in EDLC type materials, mostly carbonaceous ones, purely depend on the active surface area of the materials, in which the charge is stored at the electrode/electrolyte interface. Thus, most important parameters to tune in order to increase the charge storage mechanism are permeability of the electrolyte ions through pores and making use of the surface area.

The charge storage mechanism of double-layer capacitance is outlined in Figure 2.8. The original model was suggested by von Helmholtz (Figure 2.8 (a)), who proposed a quasi-2-dimensional system with oppositely charged layers separated by a small atomic distance. [134] This model was later modified because the original was only for colloidal interfaces, disregarding the electrode interfaces can be affected by the ions that thermally fluctuate and will not remain statically at the electrolyte side of the electrode/electrolyte interface. [135] This model is called “diffuse” double-layer capacitance introduced by Gouy. However, the assumption that ions were point

charges led to an incorrect potential profile at the electrode surface. This incorrect potential profile at the electrode surface resulted in excessively large potential difference prediction that was defined as the rate of change of net ionic charge on the solution side and change of metal solution across the interphase. Chapman [136] modified the Gouy model by combining the diffuse layer mechanism with Boltzmann's energy distribution model (Figure 2.8 (b)), resulting in Poisson-Boltzmann equation. This combination also added the parameter of distance between the active surface area of an electrode and ionic medium. This model was in the interphasial region to the second derivative of electric potential. Later on, Stern[137] improved upon the Gouy-Chapman model by incorporating Langmuir's adsorption isotherm for the inner region of the ion distribution and treating the region beyond the adsorption layer as a diffuse region of distributed ionic charge (Figure 2.8 (c)). Based on the model used, it was possible to calculate the width of the limiting adsorption region of ions by assuming that ions have finite sizes. This allowed Stern to determine the overall capacitance, which was composed of two components: Helmholtz type of double layer having a capacitance C_H, and a diffuse region of double layer having a capacitance C_{diff}. The overall double layer capacitance (C_{dl}) was then calculated as a series relation using an equivalent circuit, in which the overall double layer capacitance is governed by the smaller component of Helmholtz type of capacitance or the diffuse region[116];

$$\frac{1}{C_{dl}} = \frac{1}{C_H} + \frac{1}{C_{diff}} \quad (2.3)$$

According to this equation, the overall double-layer capacitance is controlled by the smaller component. [116]

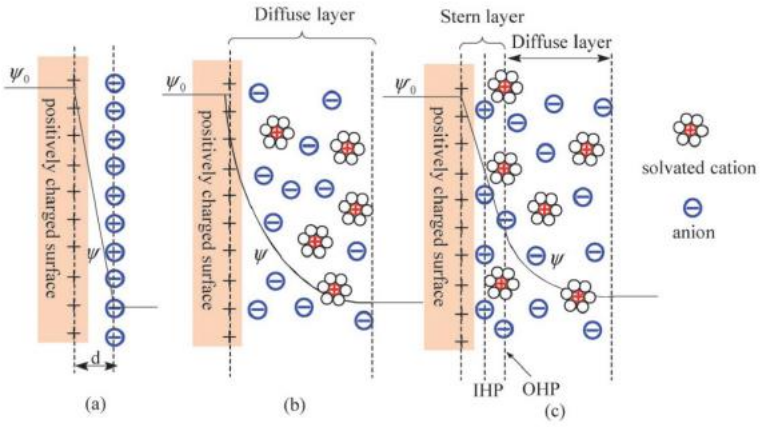

Figure 2.8 Electrical double layer models: (a) Helmholtz model, (b) Gouy-Chapman model, and (c) Stern model. IHP and OHP refers to the inner Helmholtz plane and outer Helmholtz plane, respectively. ψ_0 and ψ refers to the potentials at the electrode surface and the electrode/electrolyte interface, respectively. [138]

Double layer mechanism is generally arisen from carbonaceous materials, as mentioned before, which is extensively used for supercapacitor devices. Carbon source used for commercialized supercapacitors are mainly activated carbon[139], yet different derivatives of carbon such as graphene [140], carbon fibers[141,142], nanotubes [143], and nano-onions [144,145] have garnered significant attention and are currently undergoing extensive research for their potential utilization in supercapacitor devices.

The capacitance value of the carbon electrodes in aqueous electrolytes heavily depends on the pore structure. The basic expectation is an increase in capacitance with increased surface area. Yet, the mechanism is not as such, which was demonstrated back in 2006 by Chmiola et al. [146] A decrease in the capacitance with increased specific surface area was observed. Yet, a critical pore size was found where the trend is reversed and a sharp increase in the capacitance was observed (Figure 2.9 (a)). The behavior was explained in three stages on the graph given in

Figure 2.9 (a). In stage I, where the pores are much larger than the ion size, adjacent pore walls of a structure can contribute to the capacitance. Once the pore size is decreased, which is denoted with region 2, the surface area that can be used by the solvated ions decrease as the ion layers are impinged. Therefore, a decrease in the capacitance in this region II is observed. This behavior is reversed drastically under 1 nm pore size. The solvation shells of the ions are highly distorted and ions are squeezed inside the narrow pore channels that normally cannot contain solvated ions. This distortion allows ion centers to be much closer to the pore walls, increasing the capacitance. [146]

This behavior is not quite the same for the systems with ionic liquids. Absence of the solvent molecules that form the solvation shell, which actually forms a screening between anions and cations, results in a strong ion-ion correlations. It is imperative to explain what is the point of zero charge first. Immersion of a metal surface inside an electrolyte, a double layer is formed at its interface to make the system to maintain electroneutrality. The charge collected on the metal per unit area is;

$$q^m = -F \sum_i \Gamma_i z_i \quad (2.4)$$

where the F is Faraday constant, z_i is the charge of the ionic species i, and Γ_i is the surface excess of that component at the interphase. The summation operator is limited to the solution side of the double layer, which do not take the metal surface into account. To maintain the electroneutrality, it can be thought that the solution side of the double layer is equal to the charge on metal with opposite sign; $q^m = -q^s$. If an ideally polarized electrode is introduced to the system, where charge transfer is not allowed, the Gibbs adsorption isotherm at constant temperature and pressure can be written as;

$$d\sigma = -q^m dE + \sum_i \Gamma_i d\mu_i \qquad (2.5)$$

where the excess charge density due to the ideally polarized electrode can be written as;

$$(\frac{\delta\sigma}{\delta E})_{T,P,\mu_i} = -q^m \qquad (2.6)$$

where the μ_i is the chemical potential of the ionic species, E is the electrode potential, and σ denotes the interfacial tension for adsorption. The potential where $(\frac{\delta\sigma}{\delta E})_{T,P,\mu_i}$ operation is zero is a situation where the metal surface has no excess charge. This potential is defined as the "potential of zero charge" (or PZC in short). [147] This idea is first covered in 1930 by Frumkin while trying to define electrocapillary values for the Cd amalgams. [148]

Figure 2.9 (b) depicts the over-screening effect at the potentials below PZC range, which is attributed to the ion-ion correlations due to the absence of the solvation shell. This forms a counterion layer with an excess charge gathered compared to the polarization level of the electrode. When the potential is much lower, the polarization suppresses the over-screening, resulting in a much closer counterion layer to the inner Helmholtz layer. [149]

Work done by Largeot has shown that the behavior of the carbide derived carbon electrodes are different when an ionic liquid is used. In this case of no solvent, matching pore sizes with the cation and anion sizes are much more important. In the case of ethyl-methylimmidazolium-bis(trifluoro-methane-sulfonyl)imide ionic liquid (EMI-TFSI), both the anion and cation has a dimension over 0.7 nm. When the specific areal capacitance was plotted with respect to pore sizes (Figure 2.9 (c)) it was observed that the capacitance increases up to the point of 0.7 nm, and falls drastically lower than this size. This is attributed to the anion and cation sizes, where that they are unable to get into the smallest pores. [150]

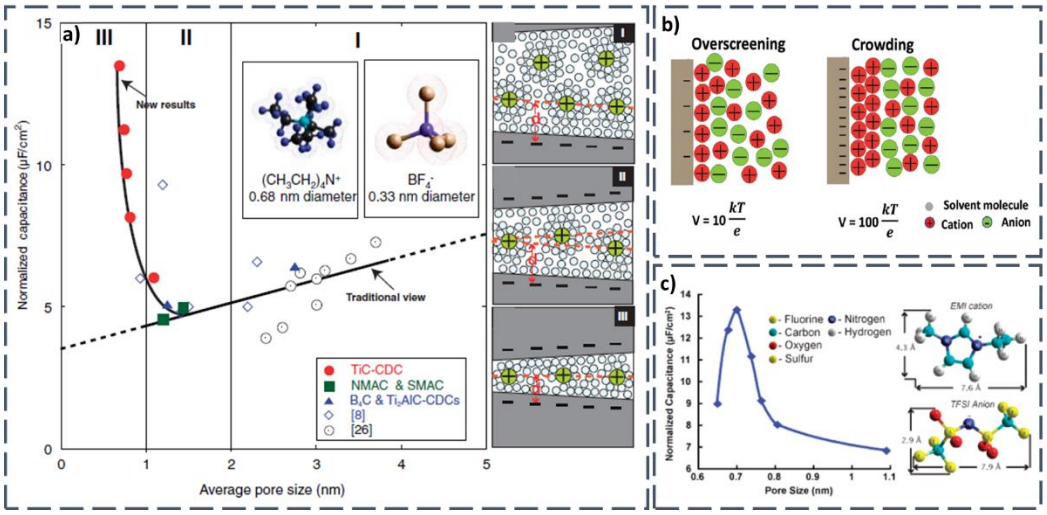

Figure 2.9 a) Plot showing average pore size vs. specific areal capacitance. Compared to the traditional view, titanium carbide-derived carbons having average pore size smaller than 1 nm have a drastic increase in capacitance. [146] b) Overscreening and crowding phenomena with ionic liquids. [149] c) Effect of pore size on the overall capacitance with ionic liquids. [150]

2.2.2 Pseudocapacitance

The energy density of double-layer capacitance is limited because the charge is only stored physically by adsorption onto the carbonaceous materials' surface. Researchers are extensively studying pseudocapacitive materials due to their electrochemical storage mechanism by fast reduction-oxidation reactions. The term 'pseudo' means being almost as, and their electrochemical behavior is similar to EDLC. This term is first used by Conway and Gileadi[151] to find out the dependence of capacitance value to the electrochemical adsorption of ionic species onto electrode surfaces. By 1971, the surface dependence is proven by Trasatti and Buzzanca by experimenting on RuO_2 in perchloric acid, showing that pseudocapacitance can be achieved by changing the material from bulk to a film formation. [152] The storage is done with faradaic reactions, allowing a much higher energy density than carbonaceous materials. [153]

Pseudocapacitive materials store energy with fast, reversible redox reactions at the surface of the active materials, such as transition metal oxides or conducting polymers. Reactions start with mass transfer of reactants towards the electrode interface to have electron transfer at the electrode/electrolyte interface. Afterwards, preceding chemical reactions take place via adsorption or desorption mechanisms at the surface of the electrode. Conducting polymers utilized in SCs such as polyaniline[154] and polypyrrole[155] are examples of conductive polymers utilized in SCs. [156]

A review of how capacitive materials, pseudocapacitive materials and faradaic materials (battery like behavior) is given in Figure 2.10 with respect to their cyclic voltammetry (CV) and discharge profiles. In pseudocapacitive materials, the behavior can have electrochemical behavior of more than one type. In Figures 2.10 (b), (d) and (e), pseudocapacitive materials with an only surface redox reactions such

as MnO_2, intercalation type materials such as Co_3O_4 in organic electrolyte, or materials having both intercalation mechanism and partial redox such as MXene phases (Ti_3C_2 in acidic electrolytes) can be observed, respectively. [157]

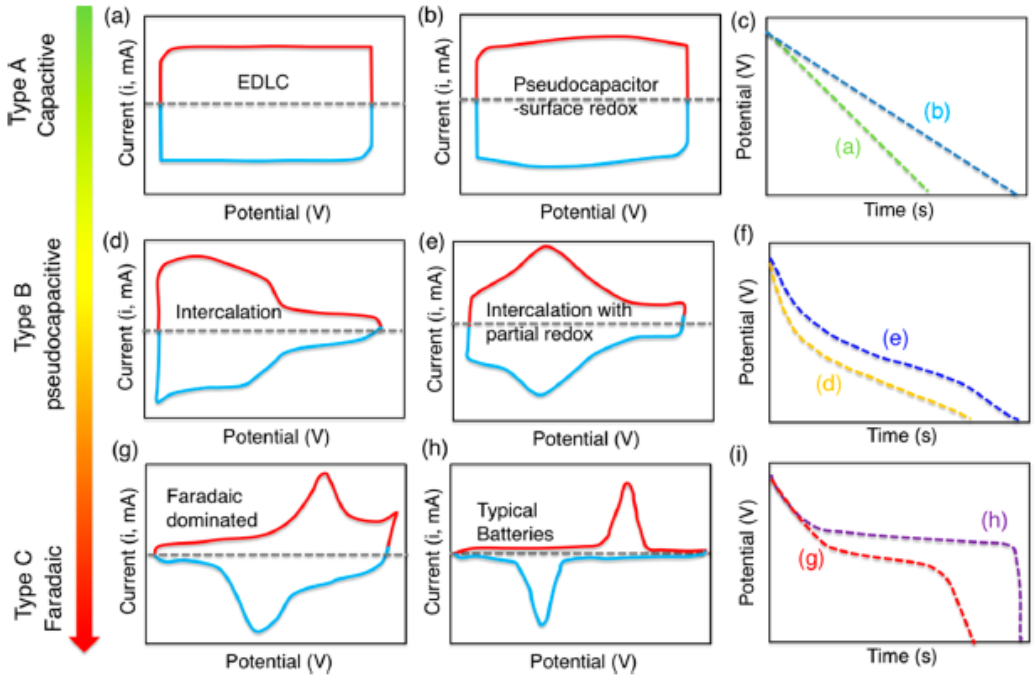

Figure 2.10 (a,b,d,e,g,h) Schematic cyclic voltammograms and their corresponding (c,f,i) galvanostatic discharge curves for different energy storage mechanisms. [157]

2.2.2.1 Metal Oxides

First material to be discovered to have pseudocapacitive properties is RuO_2. Researchers back in 1971 discovered that although the charge storage mechanism is faradaic in nature, the electrochemical behavior is similar to that of electrochemical double layer. [152] In an electrochemical characterization of single crystal RuO_2, only 7% of Ru^{4+} atoms were observed to involve in faradaic reactions, which did not have the "pseudocapacitive" behavior. Continued experiments with the RuO_2 thin films prepared by the thermal decomposition of $RuCl_3.H_2O$, on the other hand; has shown much different properties. Figure 2.11 shows the difference between these two structures. The change in the electrochemical behavior of RuO_2, making it a pseudocapacitive material, is attributed to the improvements below;

i. More accessible redox sites due to film formation,
ii. Inherent high electrical conductivity of RuO_2,
iii. Presence of structural water that facilitates charge transport inside the structure,
iv. Improved surface area resulting in much shorter diffusion lengths [158].

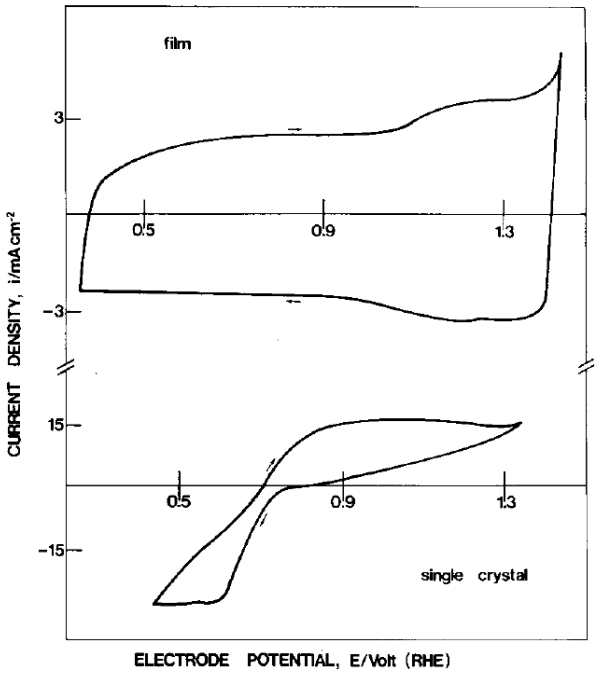

Figure 2.11 Cyclic voltammogram comparison of thin film RuO_2 (top) and single crystal RuO_2 (bottom) in 1 M perchloric acid. [152]

Currently, the situation is considerably more intricate due to the presence of various materials that are classified as pseudocapacitors. The term of pseudocapacitance, as suggested by Brousse[159] should be used more carefully, as most of the materials such as NiO and $Ni(OH)_2$ actually exhibit battery-like behavior. Figure 2.12, adapted from Brousse et al. directly showcases this issue, as $Ni(OH)_2$ and Ni doped cobalt oxides do all exhibit faradaic behavior. The term "pseudocapacitance" should only be used where the behavior is such as MnO_2, as in Figure 2.13 (which is similar with the film behavior of RuO_2 provided in Figure 2.12). [159] It should be noted that the behavior itself is also dependent on ionic species that is adsorbed on the electrode surface. Metal oxides such as iron oxide (Fe_3O_4) [160], manganese oxide (MnO_2) [161,162], cobalt oxide (Co_3O_4) [163] and nickel oxide

(NiO) [164] are examples of some metal oxides that are still labeled as pseudocapacitive materials, although most of the research still contains materials that show battery-like behavior but falsely labeled as pseudocapacitors. According to Fleischmann et al. [165] pseudocapacitors should have;

i. A linear or pseudolinear relationship between the applied potential and state of charge,
ii. Nearly ideal electrochemical reversibility,
iii. Surface controlled kinetics.

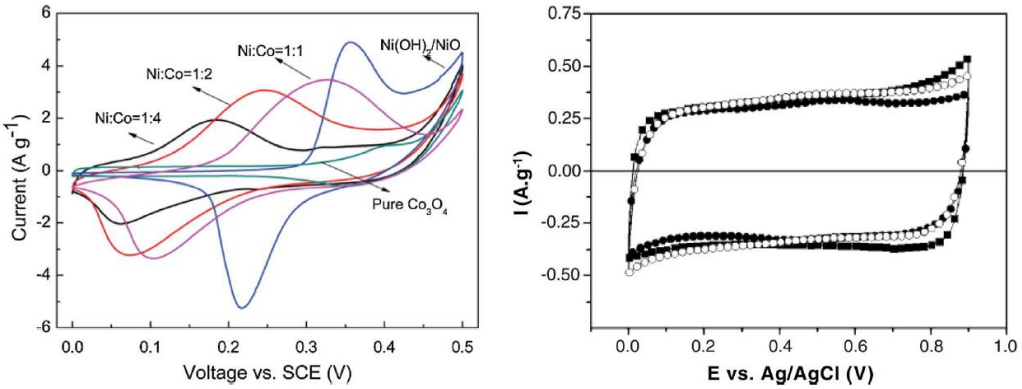

Figure 2.12 (Left) Cyclic voltammograms of nickel oxide, nickel hydroxide, cobalt oxide and nickel doped cobalt oxide, all showing faradaic behavior. (Right) MnO_2 electrode exhibiting a rectangular CV shape, which is typical for pseudocapacitive metal oxides. [159]

2.2.2.2 Transition Metal Dichalcogenides

In recent years, transition metal sulfides, also known as transition metal dichalcogenides (TMDs), have become the focus of attention with their advanced electronic and chemical properties. Especially their 2D form, with strong covalent bonding within the layers and weak van der Waals interaction between the layers, results in unique properties different from their bulk states. Several 2D TMDs based on molybdenum, tungsten, titanium, and vanadium sulfides/selenides/tellurides are researched extensively with their unique semiconducting properties (Figure 2.13 (a)). Their most explored phases, 2H phase and 1T phase, affect their electronic properties. The relevant structures are given in Figure 2.13 (b) and (c). While the H phase is a trigonal prismatic structure, T phase has its one of the tetragons rotated by 180^{o}. This difference in the structure can result in the metallic behavior of 2D TMD, especially due to its 2D form resulting in a quantum confinement. [166,167]

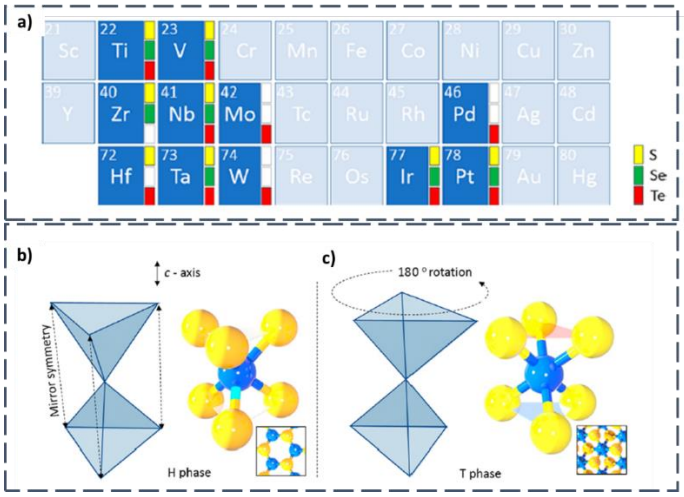

Figure 2.13 a) Possible TMD structures with their available structures of sulfides, selenides and tellurides. b,c) Two primary phases of 2D TMDs. [166]

2D TMDs are very attractive for energy storage applications due to their short electron transport length and efficient ion transport paths. Their advantages include rapid charge transport at the contact of their layered structure, their effective energy storage mechanism dependent on both Faradaic and non-Faradaic processes, and their efficient ion transport between the layers enabling higher charge/discharge rates. [168] The main storage mechanism depends on the intercalation of ions, especially Li^+, which has been known to intercalate between TMD layers since 1975. [169] Primarily if the metallic phase is obtained, the inherent semi-metallic conductivity makes them highly prospective materials for energy storage solutions.

Such an example is demonstrated by Acerce et al. [170] where 1T-MoS_2 phase is achieved through organolithium exfoliation, which resulted in a semi-metallic electrical conduction. Figure 2.14 (a) shows the self-standing film and its cross-sectional SEM image. Cross-sectional image clearly shows the exfoliated and layered 1T-MoS_2. The electrochemical analysis given in Figure 2.14 (b) also shown to differ greatly with the 2H phase, ultimately indicating the prevalence of 1T phase. [170] 2D tungsten sulfide (WS_2) is also a very promising layered TMD for supercapacitor applications. Chen et al. [171] hydrothermally fabricated 2D WS_2 and combined it with graphene to obtain supercapacitor electrodes. TEM images given in Figure 2.14 (c) shows the 2D structure obtained, and its interface with graphene. Different weight ratios were used and 8 wt.% WS_2 with graphene (denoted as M-WGA) was found to perform much better, which also shows great rate capability. [171] H and T phase of the TMDs can also be controlled to improve the electrochemical performance. Simple annealing technique utilized by Ke et al. [172] allowed researchers to control the phase boundary between 2H and 1T phase of MoS_2 (Figure 2.14 (e)). This allowed high charge transfer efficiency in the 2H-1T heterophase boundary, ultimately resulting in a much better electrochemical performance (Figure 2.14 (f)). [172]

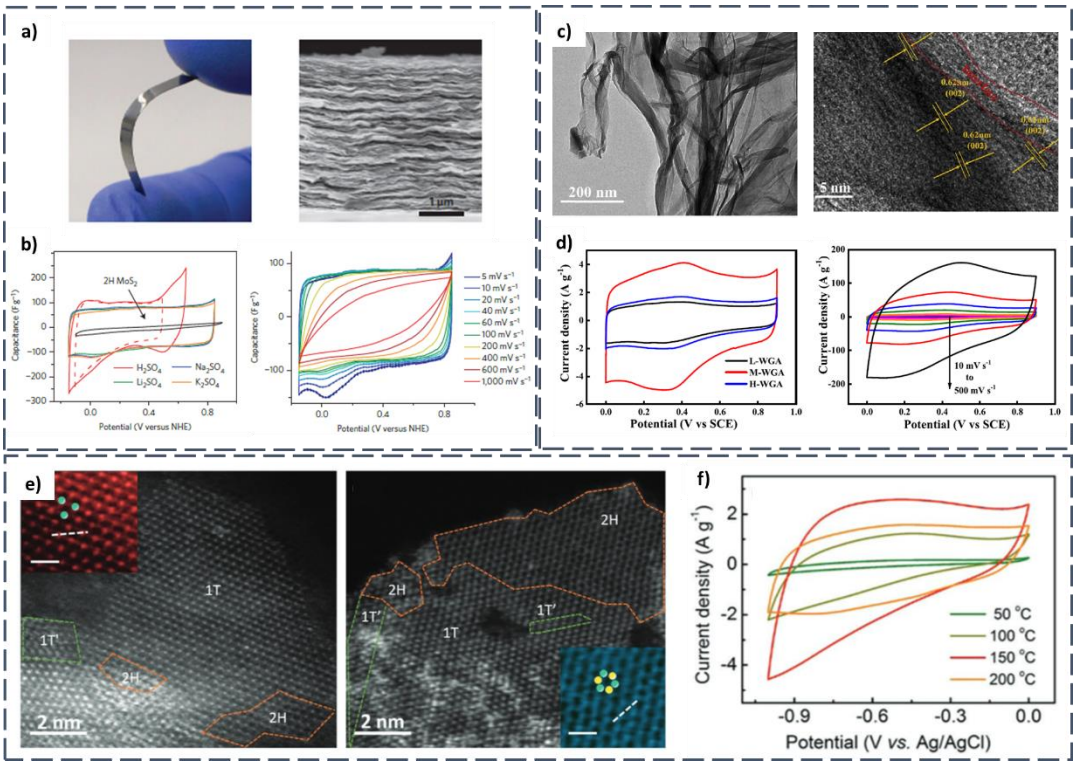

Figure 2.14 a-b) 1T-MoS_2 supercapacitors fabricated by organolithium exfoliation. a) Self-standing 1T-MoS_2 film and its corresponding cross-sectional SEM images. b) Electrochemical characterization with different electrolytes and its rate capability. [170] c-d) 2D WS_2 combined with graphene for supercapacitors. c) Low and high magnification TEM images showing the 2D structure and the interface between WS_2 and graphene. d) Cyclic voltammetry measurements of the supercapacitor electrodes with different WS_2 loadings and rate capability of the best performing one. [171] e-f) Controlling the phase transition of 1T to 2H of MoS_2 for improved performance. e) Shows the regions of 2H after thermal annealing via high resolution TEM. f) Difference in the electrochemical activity of MoS_2 electrodes with thermal annealing. [172]

2.2.2.3 Metal Carbides – MXenes

2D layered transition metal carbides, carbonitrides and nitrides, also called shortly as MXenes, are extensively studied in the last couple of years as newly emerging 2D materials after the first paper published on the fabrication of $Ti_3C_2T_x$ in 2011. The general formula of MXenes is $M_{n+1}X_nT_x$ (n=1-3), where M is a transition metal such as Sc, Ti, Zr, Hf, V, Nb, Ta, Cr, Mo and so on, X is carbon or nitrogen or both, and T is the surface terminations such as hydroxyl bond or fluorine. [173] MXenes can also have more than one transition element and they can be in two different arrangements, a solid solution type or ordered formation. In solid solution type, random arrangement of two transition materials exists in the layers, while in ordered structure, one transition metal is sandwiched between the layers of the second transition metal. [174] MXenes are synthesized by selective etching and delamination from their layered precursors or MAX phases. In 2017, up to 70 different MAX phases including the carbides and nitrides were reported. [174] Figure 2.15 provides a comprehensive overview of both experimental and theoretical types of reported MXenes.

Electrochemical performance of the MXenes for supercapacitors arises from their 2D layered structure. Polar organic molecules and metal ions (Li, Na, K, Mg etc.) can be intercalated spontaneously between the layers chemically or electrochemically. [174] $Ti_3C_2T_x$ is the most typical MXene and its electrochemical behavior as a supercapacitor is shown in Figure 2.16. A similar mechanism to layered TMDs is observed, in which the capacitance is mainly dependent on the intercalation of ions such as K^+, Na^+, Li^+, and even Mg^{2+}.

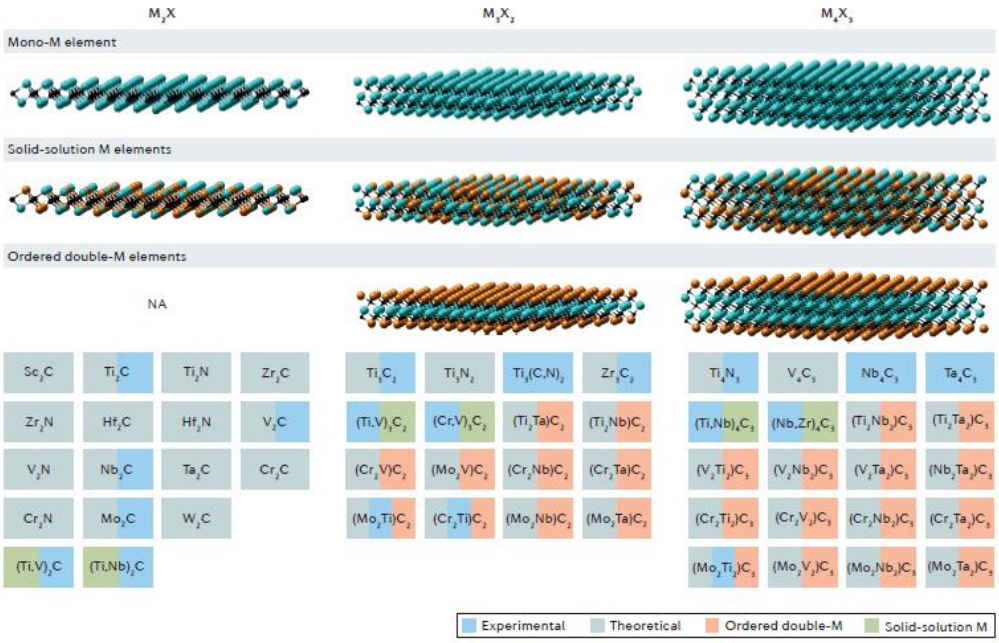

Figure 2.15 In 2017, the number of reported MXene types reached 70, covering both experimental and theoretical variations. [174]

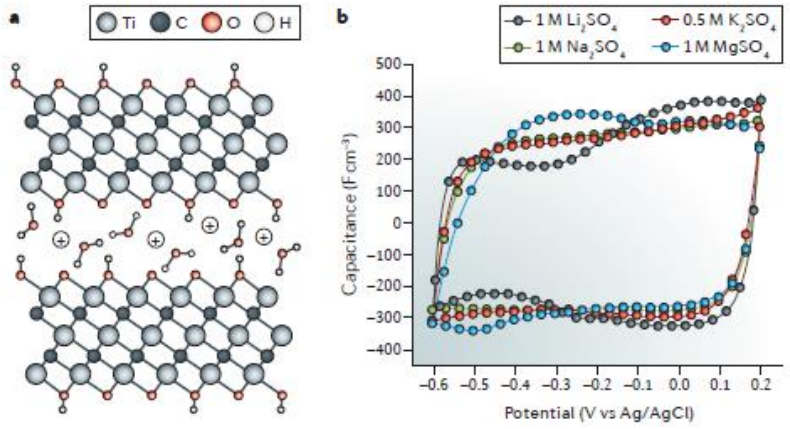

Figure 2.16 a) Schematic representation of cation intercalation between $Ti_3C_2T_x$ layers and b) cyclic voltammograms and representative capacitances with respect to different electrolytes of a 25-micrometer thick free-standing MXene film. [174]

2.2.2.4 Metal-Organic Frameworks

Metal-organic frameworks (MOFs), also called as coordination polymers, assembled via node-spacers in which they have metal centers connected with organic linkers such as imidazolate or carboxylate-based ones. Schematic representation of such combinations is given in Figure 2.17. This structure allows MOFs to be constructed with a desired crystalline structure with extreme porosity, which makes them very good candidates to be used as energy storage materials. [133]

With these unique properties and the absolute engineerable parameters, MOFs can be tailored to have desired properties, such as complementing the low power output of batteries or low energy density of supercapacitors, while keeping the advantages of both type of energy storage devices. [133] First MOF reported in 1999, which was named as MOF-5 had a specific surface area up to 2900 m^2/g, while having a thermal stability up to 300 ℃ and very promising H_2 and CO_2 storage performance, showing good gas adsorption properties.[175] Shortly after, HKUST-1 which is $Cu_3(BTC)_2$ (BTC=1,3,5-Benzenetricarboxylic acid) was fabricated with Cu nodes connected by carboxylate bridges with a three-dimensional paddle wheel unit, creating 0.90 nm side length and 0.50 nm sized one-dimensional pore channels, which are sorption sites for small molecules and contributes to the overall gas sorption ability. [176]

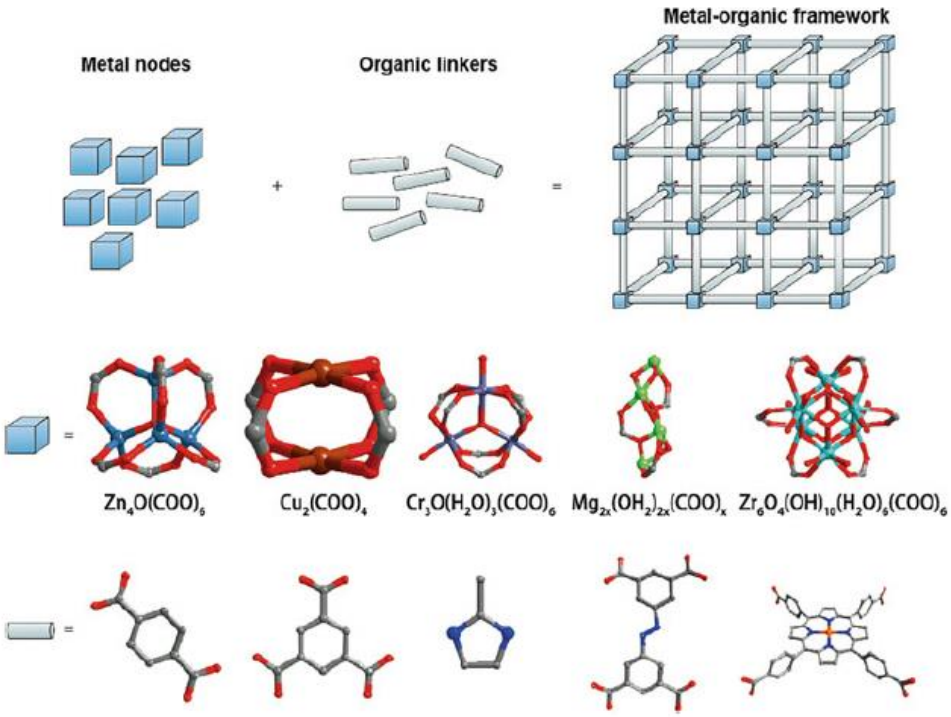

Figure 2.17 Schematic illustration of the shapes and the combination of metal nodes and organic linkers in MOFs [177].

A MOF with Cr as the metal nodes, named as MIL-101, $Cr_3OF(BDC)_3$ was reported in 2005 and had a BET surface area of 4100 m^2/g with its hierarchical tunnels and mesoporous cavities. [178] A much recent one demonstrated in 2012, NU-100E, reached BET surface area of 7140 m^2/g while the computational research shows a theoretical specific surface area of 14000 m^2/g can be reached. [179,180] Figure 2.18 provides schematic representations of both the mentioned MOF structures and additional variations.

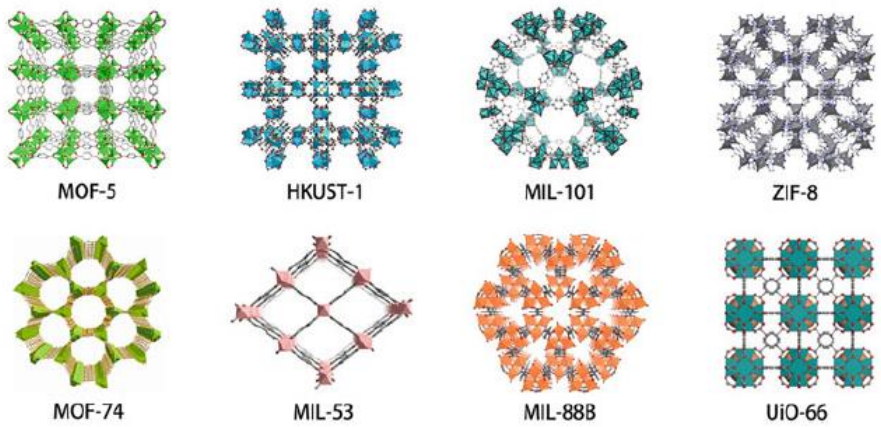

Figure 2.18 Structural representations of example MOFs [179].

2.3 Examples of Transient Energy Devices

As stated in Section 1.2, the exponential growth in consumer electronics not only fuels the consumption but also contributes to the exponential increase in electronic waste. In the case of wearable electronics, ranging from smartwatches to medical implants/sensors, all use conventional energy solutions with harmful and toxic materials. Commonly used battery materials such as cobalt, cadmium, and nickel threaten the environment and health. [181] To alleviate these issues, researchers focused on transient energy solutions that are biodegradable, biocompatible, bioresorbable, and even edible.

2.3.1 Transient Batteries

The concept of transient electronics, starting from first transient silicon electronics[32] brings the need of transient energy storage units. Transient batteries offer a solution for systems that need to operate for extended durations. Although the concept of Li-ion batteries can also be used to fabricate transient batteries [182] , fabrication of transient batteries with safer materials that can be assembled easily with completely transient materials is a must. [183]

The first concept of a fully biodegradable primary battery is suggested by Prof. John. A. Rogers' group, possibly seeing the requirement after their proposal of transient silicon electronics. They replaced the conventional cathode electrodes for Mg primary batteries with Mo metal foils, used Mg as anode, and packaged them with polyanhydrides that are also biodegradable. The schematic structure and photos of the battery are given in Figure 2.19 (a). Fabricated batteries had enough energy density to power up a red LED or a simple antenna (Figure 2.19 (b)). Fabricated transient primary Mg batteries could be triggered with aqueous solutions such as PBS. A complete degradation of the battery was seen after 19 days, showing the promising transient behavior of the fabricated primary Mg batteries. [184]

A similar study conducted by Huang[88] used molybdenum trioxide (MoO_3) as the cathode. MoO3, despite being extensively researched in the field of Li-ion batteries, had not been explored for transient batteries prior to this study. Figure 2.19 (d) shows the structure, where sodium alginate hydrogel with phosphate addition works as an electrolyte. A good discharge behavior (Figure 2.19 (e)) was observed where the batteries can supply 1.6 V for 48 hours with a MoO_3 film thickness of 300 µm. The battery can again light a red LED, which can continue to do so in PBS solution more than 16 hours. [88]

One of the most interesting areas of the transient electronics are the edible ones. The advancements in technology have revolutionized the medical field by introducing edible electronics that enable non-invasive full body diagnostics, which is truly remarkable given that they can be used for both imaging and sensing. [68] To realize these electronics, it is imperative to fabricate edible batteries as well. Ilic et al. [185] fabricated edible and rechargeable batteries depending on redox-active food additives, indigo carmine (E 132) and riboflavin (E 101), on top of two food ingredients, quercetin and ellagic acid. Overall structure is provided in Figure 2.19 (g). Active components were sealed with beeswax, and serially connected edible batteries lighted up the red LED (Figure 2.19 (h)). Capacity and charge discharge curves of the batteries are given in figure 2.19 (i), with a good cycling efficiency over 100 cycles. Although labeled as batteries, the redox active electrodes actually show pseudocapacitive behavior, as the discharge plateau does not stay at constant potential (See Figure 2.10 (f) for clarification). Nevertheless, it is a great addition for the edible energy storage devices. [185]

For the transient batteries, electrolyte/separator layer should also be transient. Seeing the absence of such works, the group of Markus Niederberger fabricated transient separator-electrolyte pair by utilizing cellulose nanocrystals (CNC). Lithiated CNCs are embedded into PVA. CNCs are lithiated in order to enhance the Li^+ transport. The fabricated PVA/CNC-Li electrolytes are also resistant to temperature. In comparison to bare PVA and commercially available Celgard separators, PVA/CNC-Li electrolytes demonstrate high temperature resistance up to 160°C. Relevant images of the electrolytes and their SEM images are given in Figure 2.19 (j). The fabricated electrolytes showed much higher capacity, 94 $mAh.g^{-1}$ in secondary $Li/LiFePO_4$ cells compared to the 18 $mAh.g^{-1}$ obtained from Celgard separators. The fabricated electrolytes can also be dissolved in water, which is demonstrated in Figure 2.19 (k). [186]

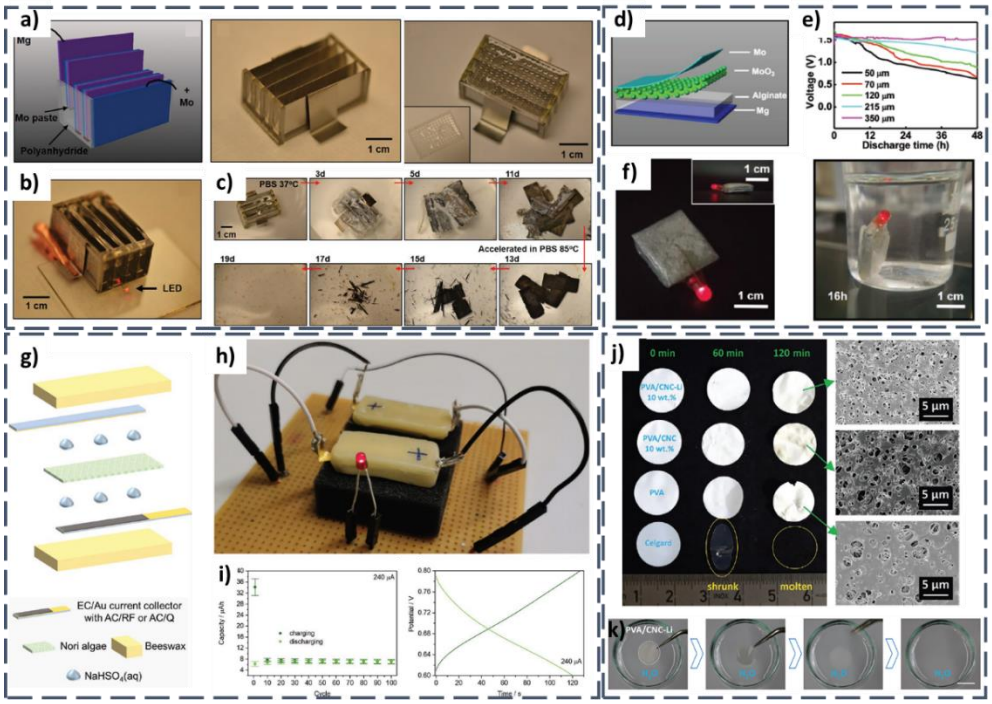

Figure 2.19 a-c) The first conceptualized transient batteries that is a primary Mg battery. a) Schematic representation and optical images of the transient Mg battery. b) Battery lighting up a red LED c) Triggered transiency in PBS solution. [184] d-f) Transient primary Mg batteries based on MoO_3 cathode and alginate hydrogel as the electrolyte. d) Schematic structure of the transient battery. e) Discharge curves depending on the thickness of MoO_3 cathode. f) Transient Mg battery powering up a red LED, even when it is submerged to PBS solution. [88] g-i) An edible rechargeable battery. g) Overall structure of the edible device h) 2 serially connected batteries lighting the red LED. i) Capacity retention and charge-discharge curve of the edible batteries. [185] j,k) Cellulosic transient electrolyte/separator for transient batteries. j) Thermal stability of PVA/CNC-Li electrolytes compared to bare PVA and Celgard at 160 ℃. k) Triggered transiency of the electrolytes in water. [186]

2.3.2 Transient Supercapacitors

Supercapacitors are another interesting energy storage solution for transient electronics. They can supply short bursts of power, which could be used to power up electronics in the required moment, and can be charged much faster than the batteries. Although they can be used to power up sensors, they can also be integrated with batteries in order to supply enough power output for more intricate devices. [181,183]

Lee and coworkers [71] fabricated biodegradable microsupercapacitors based on water-soluble W, Fe, and Mo electrodes. The structure is relatively simple, and it took inspiration from a previous publication dealing with transient electronics using the same metals. [24] Photolithography was used to shape the microsupercapacitors, and metal electrodes were deposited onto glass via magnetron sputtering. Resulting electrodes and their degradation in PBS solution are shown in Figure 2.20 (a). More complex microsupercapacitors with microchannels were also fabricated on PLGA substrates (Figure 2.20 (b)). NaCl/Agarose gels were fabricated as an electrolyte, which are transient in PBS (Figure 2.20 (c)). The microsupercapacitor deposited on PLGA was also soluble in PBS solution (Figure 2.20 (d)); given that the electrolyte was also transient, a fully transient microsupercapacitor was obtained. [71]

Developing transient electrolytes for supercapacitors is essential, as it is also important for the batteries. One such work conducted by Shunsuke Yamada[187] aimed at fabricating water-dissolvable ionic gel. Tris(2-hydroxyethyl)methylammonium methylsulfate, or [MTEOA][$MeOSO_3$], is dispersed in PVA to form ionic gels. Figure 2.20 (h) shows the device structure. The photos of the complete device, and device with ionic gels, membrane and activated carbon paste is given in Figure 2.20 (i). These devices utilize water soluble metals for contacts and activated carbon, an eco-friendly material. (Figure 2.20 (j)). Two

transient supercapacitors utilizing the transient PVA/[MTEOA][$MeOSO_3$] gel can light up three LEDS as long as 100 seconds, showing promise for powering transient electronics. [187]

Transient supercapacitors, as done for the batteries, can be made edible. This is aimed to replace the energy storage devices for temporary implantable electronics and medical procedures such as capsule endoscopy or drug delivery. However, low energy density of the supercapacitors kept them from in vivo demonstrations. Seeing that, Chen et al. [188] fabricated hybrid microsupercapacitors using Zn and activated carbon electrodes. Schematic representation of the fabrication route is given in Figure 2.20 (l). Fabricated microsupercapacitors have much higher energy density due to the use of Zn electrode and $ZnSO_4$ based electrolyte, which is actually a battery-type couple. A photo of the microsupercapacitor is given in Figure 2.20 (m). These devices can be flexed and can power up red LEDs. Moreover, it is suggested by the authors that these zinc-ion microsupercapacitors is actually nutritive, as it can cover the need of daily zinc intake. The transiency of the microsupercapacitors in gastric fluid is also demonstrated (Figure 2.20 (n)), showcasing the promise of such devices for the future of edible and transient electronics.[188]

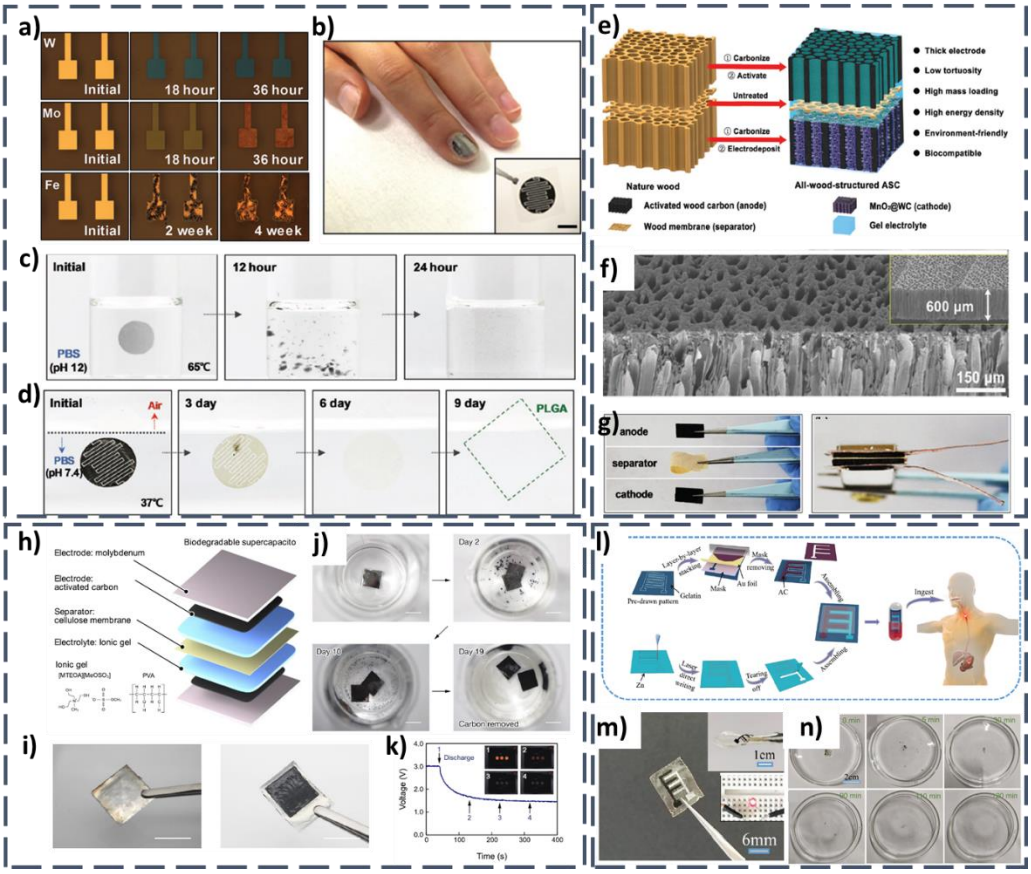

Figure 2.20 a-d) Fully biodegradable microsupercapacitors based on metal electrodes. a) Optical images of the degradation of the metal electrodes in PBS solution. b) Mo-based microsupercapacitors on PLGA. c,d) Triggered transiency of NaCl/agarose gel electrolyte and Mo-based microsupercapacitor in PBS solution, respectively. [71] e-g) Wood based biodegradable supercapacitors. e) Schematic illustration of all-wood-structured supercapacitor. f) Cross-sectional SEM image of wood-based supercapacitor electrode. Inset figure shows the thickness of MnO_2/carbonized wood. g) Photos of the elements of wood-based supercapacitor in separate and in assembled form. [189] l-n) Transient zinc-ion microsupercapacitors. l) Schematic representation of the fabrication of the microsupercapacitors. m) Photo of a transient microsupercapacitor. Inset figures show the demonstration of flexibility and powering of a red LED. n) Transiency of the zinc-ion microsupercapacitors in gastric fluid. [188]

2.4 Experimental Procedure

2.4.1 Fabrication of the Layers

Poly (vinyl alcohol) (PVA) was purchased from Sigma-Aldrich, had a molecular weight of ~ 61,000 with a polymerization degree of ~1,400 and a hydrolysis degree of 98.0 – 98.8 mol%. Sucrose (ACS Reagent), hydrochloric acid (HCl, ACS reagent, 37%) and sodium chloride (ACS Reagent) and glycerol were also obtained from Sigma-Aldrich. Carbon black (CB, 50% compressed) and activated carbon (AC, -20 +40 mesh) were purchased from Alfa Aesar and used without further purification.

2.4.1.1 Preparation of PVA/CB/AC (PCA) Thin Film Electrodes

PCA transient electrodes were prepared via simple solution mixing and doctor blading method adapted from elsewhere. [101] 50 µl of 1 M HCl (to improve the solubility of PVA) and 1 gram of sucrose was added to 20 ml of deionized water (DI) and dissolved. Then, 1 gram of CB and 0.2 gram of AC, which were previously grinded and sieved to 53 – 75 µm were added to the mixing solution, and kept under stirring for 1 hour. Then, obtained suspension was tip sonicated for 5 minutes to obtain agglomeration-free and low viscosity ink. Later, 1 gram of PVA was dissolved in the same suspension at 85°C under stirring. Suspension was heated previously to facilitate PVA dissolution. Lastly, 0.2 grams of glycerol was added dropwise and suspension was left to stir overnight at elevated temperature to completely dissolve PVA. Before casting, obtained ink-like suspension was ultrasonicated for 4 hours to ensure a homogeneous casting, and the suspension was let to stir at 100 rpm for at least 30 minutes to get rid of air bubbles formed during sonication. Afterwards, resulting ink was casted via doctor blading method with a wet thickness of 300 µm

onto glass substrates. Prior to deposition, the substrates underwent a hydrophilic surface modification process. The casted film was dried under ambient conditions overnight, and peeled off to obtain very flexible, thin and transient PCA film electrodes.

2.4.1.2 Preparation of PVA/NaCl (PN) Electrolytes

Solid state PN electrolyte was prepared via simple solution mixing and freeze-thawing method, which was adapted from elsewhere[190]. Typically, 1 gram of PVA was dissolved in 10 ml of DI water at elevated temperature and magnetically stirred for at least 2 hours. Once the clear solution was obtained, 0.8 grams of NaCl was slowly added to ensure a homogeneous dispersion of the salt. After the dissolution of NaCl, 1 gram of glycerol was added and the solution was further mixed at an elevated temperature. Once a clear solution was obtained, the temperature and stirring rpm were reduced to allow air bubbles to disappear. Then the solution was poured into glass petri dishes and freezed at -24°C in a kitchen refrigerator at least for one day.

2.4.1.3 Preparation of Transient PVA/Sucrose/Glycerol (PSG) Encapsulant Films

Transient PSG films were prepared as follows. 50 µl of 1 M HCl (to improve the solubility of PVA) and 1 gram of sucrose was added to 20 ml of deionized water (DI) and dissolved. After stirring for 10 minutes, 1 gram of PVA was added, and solution was kept under heat and stirring at least for 4 hours. After having a clear solution,

0.2 grams of glycerol was added to improve the flexibility and adhesion of the film. Resulting solution was casted onto rectangular plaques with a pastor pipette, and left to dry overnight to obtain transparent and transient encapsulant films, which were used to cover supercapacitors, triboelectric energy harvesters (Chapter 3) and capacitive sensor devices (Chapter 4).

2.4.1.4 Material Characterization

SEM characterizations were done using FEI NOVA NANO SEM 430 at 20 kV of operation voltage. X-Ray diffraction (XRD) analysis of the films were done using Rigaku Ultima-IV system with Cu Kα radiation (0.154 nm) at a scan rate of 1° min^{-1}. Thermogravimetric Analysis (TGA) was conducted via Exstar SII TG/DTA 7300 with a temperature increment of 10 °C.min^{-1} under ambient conditions. Differential scanning calorimetry (DSC) measurements were made via PerkinElmer Diamond with temperature increment of 10 °C min^{-1} from -90 to 300 °C. Fourier transform-infrared (FTIR) spectroscopy analysis were conducted via attenuated total reflectance (ATR) unit of FTIR spectrometer (Bruker Alpha) with a resolution of 4 cm^{-1} within a wavenumber range of 400-4000 cm^{-1}.

2.4.1.5 Device Characterization of T-SUPC

Electrochemical tests were employed using symmetric 2-electrode setup with Swagelok cells, where anode and cathode were PCA electrodes and PN acting as the electrolyte and separator. Biologic VMP3 galvanostat/potentiostat was used for electrochemical characterization. Cyclic voltammetry (CV) and galvanostatic

charge/discharge (GCD) measurements were done at different scan rates and current densities, respectively, at a voltage range of 1 V. Maximum voltage was set as 1 V to avoid water electrolysis in both cathode and anode. Electrochemical impedance spectroscopy (EIS) measurements were conducted within a frequency range of 200 kHz – 50 mHz with employing a sinusoidal AC amplitude of 10 mV and at an open circuit voltage (E_{OC}) and at DC bias of 0.1 V and 0.2 V. DC voltages were applied to observe if there are changes in both high and low frequency regions. Cycling performance were monitored at a scan rate of 200 mV.s^{-1} for 10000 cycles. More than one Swagelok cell were assembled to utilize the supercapacitors in parallel and series configurations. Flexible supercapacitor devices were measured in a similar way, where the contacts were directly taken from the PCA electrodes.

Specific capacitance of the T-SUPC ($C_{sp,cell}$ – F.g^{-1}) was measured from CV analysis using the equation;

$$C_{sp,cell} = {}^{1}/_{Evm} \left(\int_{Ei}^{Ef} idV \right) \quad (2.7)$$

, where E is the voltage range (V), v is the scan rate (mV.s^{-1}), m is the mass of the total active material (g) and i is the current (mA). Specific capacitance of one electrode can directly be calculated from here as:

$$C_{sp} = 4xC_{sp,cell} \quad (2.8)$$

2.4.2 Results and Discussion

2.4.3 Fabrication of the Transient PVA Based Supercapacitor Devices (T-SUPC)

Transient PVA based supercapacitor devices were assembled as follows. First, PCA films were punched to obtain circular electrodes with a diameter of 9 mm. The average weight of the electrodes was found as 1.7 mg per electrode. Electrochemically active carbonaceous materials involved in electrochemical storage in total weighs 0.6 mg for one electrode. Then, freeze thawed PN electrolyte films were also punched at the same diameter, and assembled immediately with PCA electrodes. The assembled electrodes were used without further processing.

Flexible encapsulated electrodes were assembled in a similar way. PCA electrodes were cut into desired shape, and assembled with the hydrogel as explained above. Copper contacts were placed onto PCA electrodes and fabricated devices were covered again with water soluble and transient PSG encapsulant (Figure 2.21). The preparation of this film was the same as the fabrication of PCA electrodes, and amount of sucrose can be manipulated to obtain desired solubility characteristics [101]. Assembled flexible capacitors were also utilized as rolled capacitors. Larger PCA electrodes were combined with PN electrolyte, and metal foils were used to improve contacts in the device. Then, the device was immediately covered with PSG films, and pressed at least overnight to ensure good encapsulation. PSG layer used for encapsulation also acted as an insulating layer when the flexible T-SUPC was rolled.

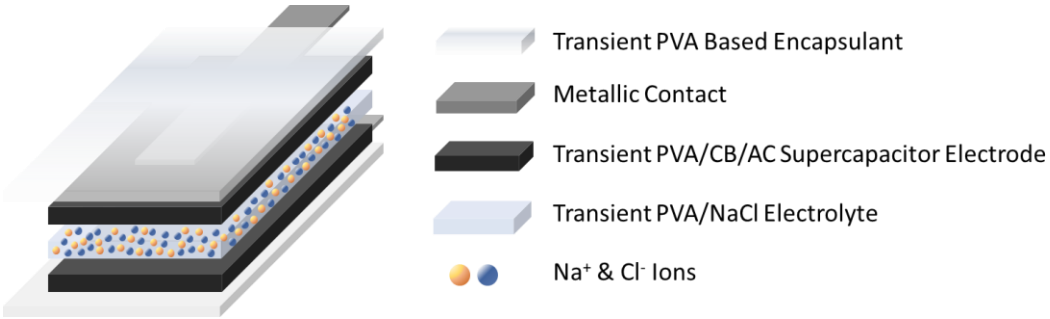

Figure 2.21 Schematic structure of the assembled transient supercapacitor. Reprinted with permission from ref [111], Copyright 2021, Wiley

2.4.4 Optimization of the PCA Films

PVA/Sucrose ratio (1:1) is directly adapted from [191] as explained in the Experimental Section. The CB addition is done in different amounts to make the film conductive. 0.5 g, 1.0 g and 1.5 g of CB is added to the above ratio. First, drop-casting the slurry onto plates and drying is tried. The images of the drop-casted films with and without the glycerol addition is given in Figure 2.22. Without the glycerol, the fabricated composite films were brittle and uneven in both mechanical and electrical properties. With the addition of glycerol, which added the plasticity to the composites, a flexible film could be attained. Still, the conductivities were not enough, as a simple measurement with multimeter yielded resistivities of 800 ohms.cm to 2000 ohms.cm, which could decrease performance in applications. Therefore, doctor blading method was adopted. Doctor blading method allowed reproducible fabrication of homogeneous composites. Suspensions prepared as before doctor bladed onto glass substrates with a wet thickness of 300 µm. The addition of 0.5 g of CB did not yield a satisfactory conductive film (lateral resistance of tens of kohm.cm), 1.5 g of CB addition did not result in a robust and homogeneous film.

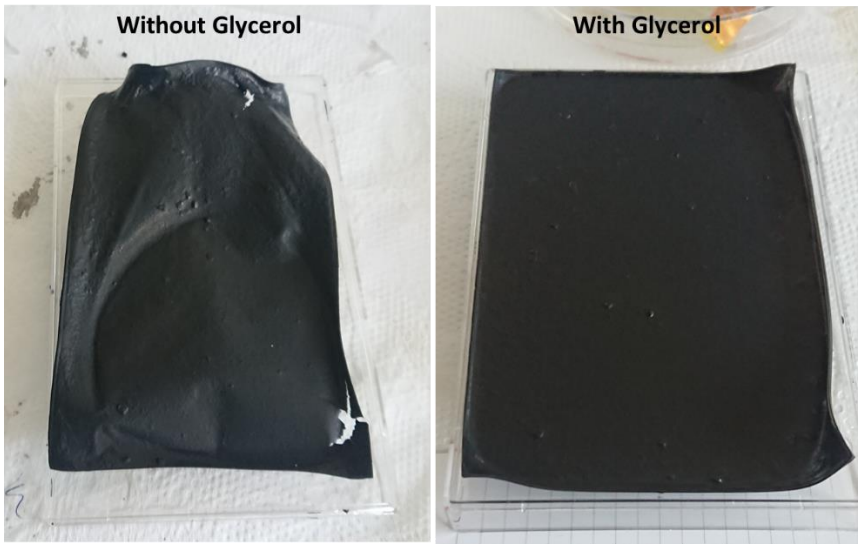

Figure 2.22 Photos of drop-casted PVA/Sucrose/CB films with and without the addition of glycerol.

While 1:1:1 ratio (PVA:Sucrose:CB) resulted the best film in terms of conductivity, the film was brittle. As known from the drop-casted films, glycerol addition was done to plasticize the film in different ratios. 0.2 g, 0.5 g, 1.0 g and 2.0 g of glycerol was added. For all of the cases, PCA film became flexible and robust, yet increased amount of glycerol had a detrimental effect on the conductivity of the film. The resistance increased from approximately 100 ohm.cm to 600 ohm.cm. From these results, the best ratio for a good conducting film was chosen as 1:1:1:0.2 for PVA:Sucrose:CB:Glycerol, respectively. In order to improve the specific capacitance of the PCA films, additional AC was also added in different ratios. Addition above 0.2 grams adversely affected the conductivity of the film. For 0.5 grams and 1 grams of additional AC, resistances were increased up to 1.5 kohm.cm and 1.14 Mohm.cm, respectively. Thus, the last ratio was decided as 1:1:1:0.2:0.2 for PVA:Sucrose:CB:AC:Glycerol, respectively. The parameters and their resulting resistivity values measured with a multimeter is given in Table 2.2.

Table 2.2 Parameters and resulting resistivity values for doctor-bladed PCA electrodes.

Sample (PVA:Sucrose:CB:Glycerol:AC)	Wet Thickness (μm)	PVA (g)	Sucrose (g)	CB (g)	Glycerol (g)	AC (g)	Resistivity (ohm.cm)
1:1:1:0.2:0	300	1	1	1	0.2	0	~150
1:1:1:0.2:0	200	1	1	1	0.2	0	~1000
1:1:1:2:0	300	1	1	1	2	0	~640
1:1:1:2:0	200	1	1	1	2	0	~630
1:1:1:1:0	300	1	1	1	1	0	~500
1:1:1:0.2:0.1	300	1	1	1	0.2	0.1	~200
1:1:1:0.2:0.2	300	1	1	1	0.2	0.1	~100
1:1:1:0.2:0.5	300	1	1	1	0.2	0.5	~1500
1:1:1:0.2:1	300	1	1	1	0.2	1	~1.1 x 10^6

Wet thickness of doctor blade method was also optimized. Thicknesses of 100, 200 and 300 μm was chosen for doctor blading the above ratio. Film prepared with a wet thickness of 100 μm was not robust enough to be removed as a self-standing film. For the film prepared with a wet thickness of 200 μm, the resistance was around 1.0 kohm.cm. The best results were obtained (1:1:1:0.2:0.2) with a wet thickness of 300 μm, which had 95 $\pm$ 10 ohms/square (measured with four-probe) for the selected fabrication route, and resistance across thickness was 6.0 $\pm$ 2.5 ohms. Doctor blade method allowed direct coating of PCA electrodes. This resulted in the formation of mechanically stable, thin and self-standing electrodes with an interconnected structure, offering promising performance in both triboelectric and capacitive applications. Flexibility and mechanical stability of the films were demonstrated through twisting, folding and stretching the film (Figure 2.23).

The supercapacitor device configuration is schematically shown in Figure 2.21. PCA electrodes acted as anode and cathode, PN ionic conducting layer acts as a solid-state electrolyte and separator, and PSG film prepared separately by drop-casting acts as an encapsulant for the supercapacitor devices. Performance-wise, common PVA matrix among the layers enabled excellent adhesion between the layers, promising interfacial behavior between the electrode-electrolyte surfaces, and exceptional adherence of the encapsulant to the whole device. Furthermore, doctor-blading of the PCA electrodes allowed formation of highly porous structure upon drying, leading to an improved performance and high rate-capability in fabricated supercapacitor devices. Related low-magnification and high-magnification SEM images of the PCA electrodes are provided in Figures 2.24 (a) and (b), respectively, showing the aforementioned porous structure. This porous structure was obtained over very thin electrodes (a thickness of 16.5 μm) (Figure 2.24 (c)). With the PN electrolyte layer, the total thickness of the supercapacitor device was around 90 μm**,** as clearly shown in the inset of Figure 2.24 (d). Top-view and cross-sectional SEM images of PCA/PSG electrodes are provided in Figure 2.24 (d). Crystalline nature of PVA in PSG overcoat could be observed clearly. Thickness of the PSG overcoat was about 20 μm, which was found to be efficient for T-TENG and T-CAPS.

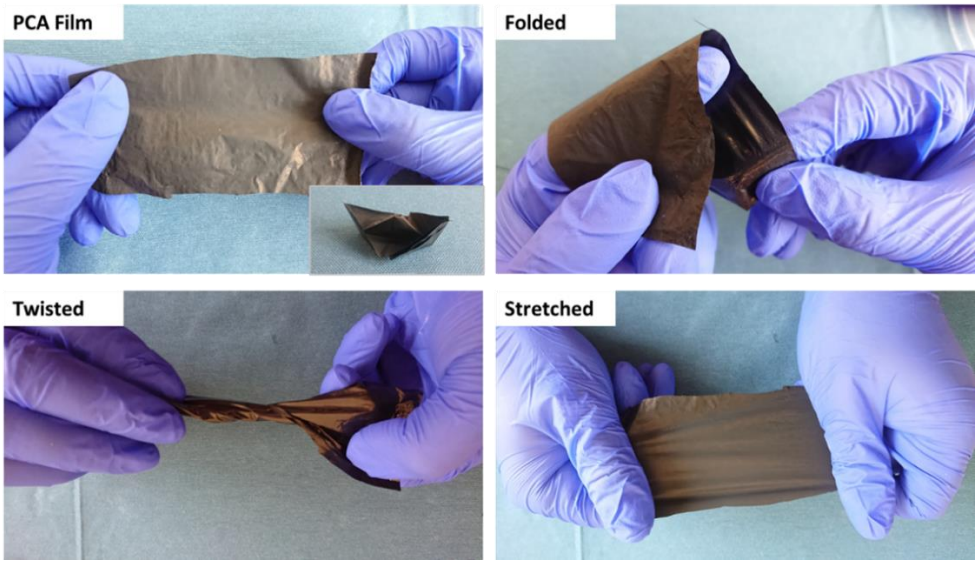

Figure 2.23 Photos demonstrating the flexibility and mechanical strength of the PCA film through twisting, folding and stretching. Inset shows a photo of an origami boat folded with prepared film. Reprinted with permission from ref [111], Copyright 2021, Wiley

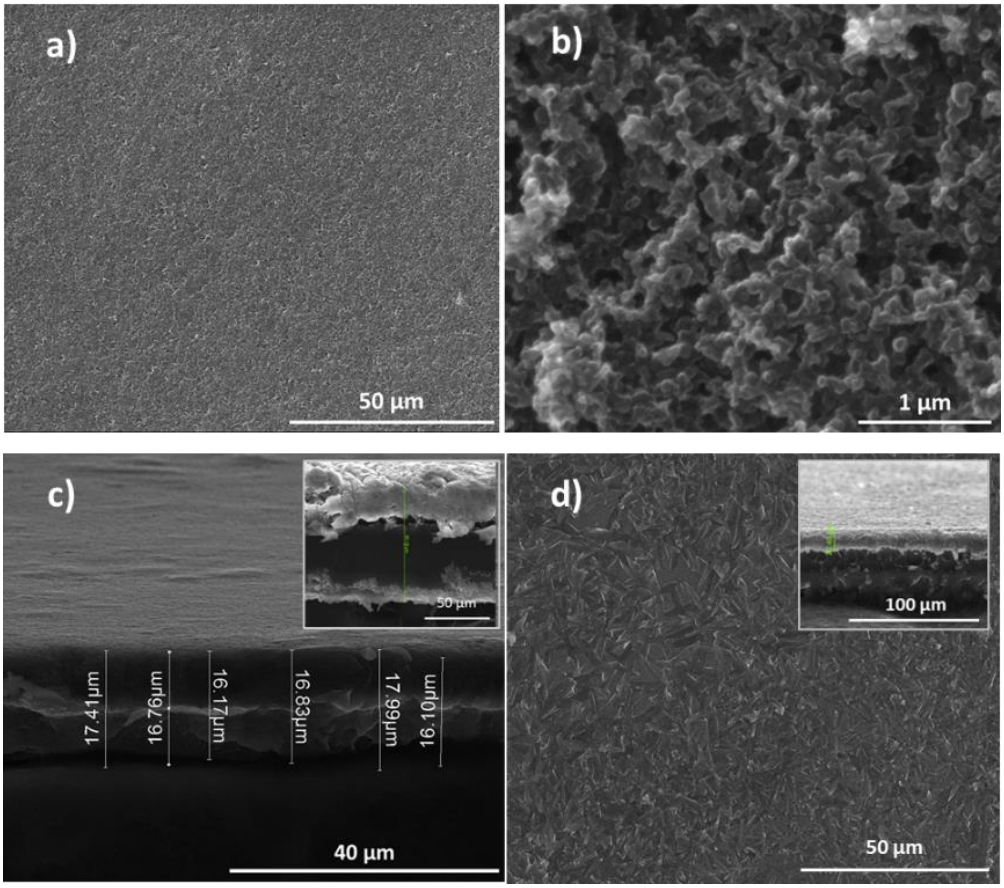

Figure 2.24) Low-magnification, c) high-magnification and d) cross-sectional SEM images of PCA electrodes. Inset shows cross-sectional SEM image of the fabricated supercapacitor device. e) SEM images of PVA/PSG structure used in T-TENG and T-CAPS. Inset shows cross-sectional SEM image of PCA/PSG layer. Reprinted with permission from ref [111], Copyright 2021, Wiley

2.4.5 Chemical Characterization of the Layers

Fabricated PVA-based layers were subjected to detailed materials characterization. X-Ray Diffraction (XRD) pattern, Fourier-Transform Infrared Spectroscopy (FTIR), Differential Scanning Calorimetry (DSC) and Thermogravimetric Analysis (TGA) plots for the characterization of different states of PVA during the fabrication processes are provided in Figure 2.25. Sucrose addition to the PVA matrix enabled control over the transiency of the composites by increasing the water dissolution rate and acting as a plasticizer for PVA and decreasing the viscosity of the matrix. [101,192] The dissolution rate was enhanced due to the increased crystallinity, which caused disentanglement of PVA molecular chains. [193] The effect of crystallinity can be observed from Figures 2.25 (a) – (c). PVA has two characteristic peaks, located at 19.6° and 40.7°. It also includes two low intensity peaks located at 21.5° and 23.8° that describe different sized semi-crystallites. Following sucrose addition, aforementioned peaks were found to lose their intensity due to increased crystallinity of PVA [194]. In support of this claim, a much narrower and sharper melting peak was obtained in DSC (Figure 2.25 (c)) upon sucrose addition, indicating an increase in the crystallinity. [193,195] The effect of the sucrose on PVA matrix can be further explained using FTIR analysis. The band at 1141 cm^{-1} on the bare PVA (Figure 2.25 (b)) shows the C-C stretching mode. When compared with the PVA-sucrose, absorption was found to increase dramatically, suggesting an increase in the crystallinity of PVA. [191] Another change in the FTIR upon sucrose addition took place within 3200-3300 cm^{-1} band. This showed the interaction between the PVA and sucrose through hydrogen bonding. The change in intensity was attributed to the degree of –OH groups. In addition, the number of free –OH groups in the molecule also described the degree of solubility in water. Thus, this increment with sucrose addition evidenced improved solubility. [101]

Glycerol, on the other hand, was used as a plasticizer, which allowed formation of self -standing PCA and PSG electrodes with excellent flexibility. Doctor-bladed films could not be removed from the substrates without the introduction of glycerol. It is expected that the large glycerol molecules enhance the amorphous structure in the polymeric matrix by introducing multiple hydroxyl groups. Therefore, it can create hydrogen bonds with the PVA molecules, resulting in the formation of defective crystallites. [196] This can be clearly observed in the XRD pattern of PSG films (Figure 2.25 (a)). Semi-crystalline peaks (21.5 and 23.8°) that were reduced in intensity with sucrose addition became evident again due to defective crystallite formation by glycerol. [196] DSC analyses showed that glycerol addition results in significant broadening for the melting peak of PVA (Figure 2.25 (c)). This broadening indicated the decrease in the crystallinity.[196,197]

Following the addition of carbon, semi-crystalline region of PVA became broader and semi-crystalline peaks became more intense (Figure 2.25 (a)). A peak at 21.1° was attributed to the residual ash in the added carbonaceous content, which overlaps with a semi-crystalline peak of PVA at 21.5°. It can also be stated that addition of AC into PVA matrix increases the crystallinity of PVA. Thus, after the addition of AC, the semi-crystalline region of PVA at 19.8° became less dominant compared to carbon addition, which is consistent with the literature. [198,199] Broad part around 26° was due to amorphous nature of AC [200] and low crystallinity of CB. [201,202] Carbon addition to PVA resulted in an opaque PCA film, which also reduced FTIR transmittance. Thus, bands attributed to PVA at 1141 cm^{-1} (due to C-C stretching) and at 3200-3300 cm^{-1} (due to hydrogen bonding from -OH groups) became more depressed, which can be observed in Figure 2.14 (b). [192,203]

Thermal degradation behaviors of the bare PVA, PVA/sucrose, PSG and PCA films were investigated via TGA. The weight loss that occurs between 90-150 °C was attributed to the evaporation of absorbed water (Figure 2.25 (d)). Following the removal of absorbed water, degradation step around 220 °C was attributed to the volatilization of glycerol addition, where a sharp increase in degradation can be observed in PSG film (Figure 2.25 (d)). Sucrose addition also changed the degradation mechanics in this temperature range, which could be due to chemical interactions between PVA and sucrose. [192] Characteristic degradation of PVA starts about 250 °C and goes till 360 °C, where the water in PVA chains gets eliminated, followed by the breakdown of the polymer backbone. [204] Degradation beyond 360 °C in Figure 2.25 (d) was attributed to intramolecular cyclization resulted from the remnants of polymer backbone breakdown. [205] After 500 °C, carbonaceous mass was formed due to complete degradation of PVA. Thermal stability of the PCA composite films significantly increased after CB/AC addition as the amount of remaining char was significantly higher than that of bare PVA films.

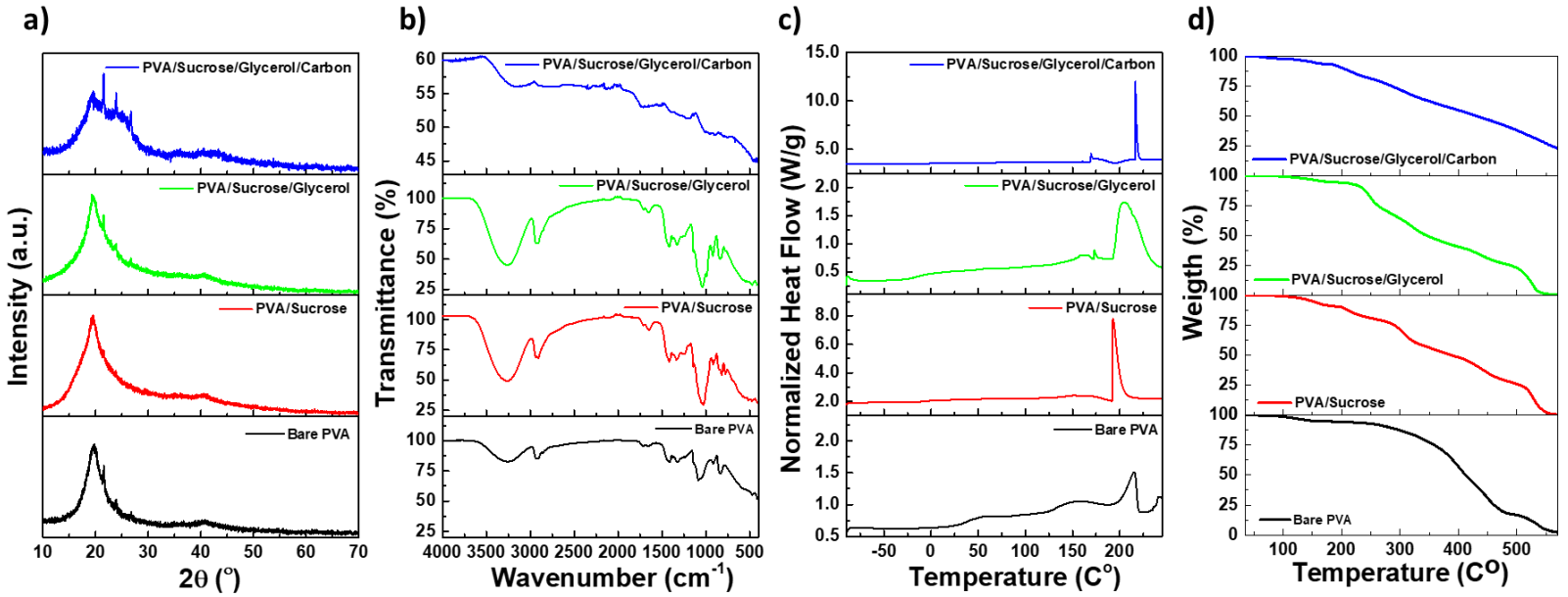

Figure 2.25 a) XRD, b) FTIR, c) DSC and d) TGA results of the bare PVA, PVA/sucrose, PSG and PCA films. Reprinted with permission from ref [111], Copyright 2021, Wiley

2.4.6 Electrochemical Characterization of the Transient Supercapacitor Devices (T-SUPC)

The overall structure of the T-SUPC is provided in Figure 2.21, where PCA electrodes acted as anode and cathode, while solid PN layer was utilized both as electrolyte and separator. As stated before, using both PVA based electrodes and electrolyte improved the adhesion and mating of the surfaces, resulting in better interfacial behavior for energy storage. Results showed close-to-ideal behavior of T-SUPC throughout the measurements. Fabricated supercapacitor cells showed excellent cycling behavior for scan rates extending from 10 $mV.s^{-1}$ up to 1 $V.s^{-1}$, signifying excellent rate capability and stability of the fabricated solid-state supercapacitors (Figures 2.26 (a) and (b)). Almost linear charging and discharging behavior (Figure 2.26 (c)) further supported the ideal behavior of the assembled transient all PVA-based cells. There were no discernible IR drops on the GCD profiles (Figure 2.26 (c)) evidencing remarkable conductivity of the assembled cells. The cycling stability of the transient all PVA-based cells were also explored via CV at a scan rate of 200 $mV.s^{-1}$ for 10000 cycles. Resulting plot for the capacity retention is provided in Figure 2.16 (d). While the initial drop can be attributed to the settling of the electrode/electrolyte interface, transient cell maintained its excellent ideal-like behavior for 10000 cycles with a capacity retention of 93%. The resulting CVs can be observed from the inset graphs in Figure 2.26 (d). The specific capacitance of the transient all PVA-based supercapacitor cell was calculated as 2.62 $F.g^{-1}$ at a scan rate of 10 $mV.s^{-1}$. The capacitance was found to decrease gradually and hit 0.42 $F.g^{-1}$ at a scan rate of 5 $V.s^{-1}$. The gradual decrease in the specific capacitance with an increase in the logarithmic scan rate was close to linear (Figure 2.26 (e)), proving excellent supercapacitive property of the fabricated transient cell. To further analyze the supercapacitive behavior of the transient cell, EIS was employed and resulting Nyquist plots at E_{OC} and at a DC bias of 0.1 and 0.2 V are provided in Figure 2.26

(f). Small semicircle in the high frequency region of the Nyquist plot was due to the interfacial impedance of the PCA electrodes and current collectors (stainless steel rods in Swagelok cell). This was proven by comparing the Nyquist plots of E_{OC} and DC biased ones. No change in the semicircle was observed with DC bias, proving that the transient cell possibly had negligible charge-transfer resistance. This showed that fabricated T-SUPC possess close to ideal supercapacitive behavior. [206] This also suggested that semicircle in PEIS was due to interfacial resistances between electrode/electrolyte and electrode/current collectors. [206] Inset model shows the equivalent circuit of the supercapacitor cell, where R_1, C_2, R_2, C_3 and W_4 corresponds to equivalent series resistance (*Rs*), parasitic capacitance induced by surface resistances, charge transfer resistance (*Rct*), capacitance of the cell and Warburg element, respectively. Rs of the device was as low as 0.54 ohms, while the cell capacitance was found as 2.84 mF ± 7.34 µF. This yielded a specific capacitance of 2.39 $F.g^{-1}$ when divided by the total active material mass, which was consistent with the CV measurements. *Rct* was found to be 13 ± 0.45 ohms, proving that the interfacial resistances caused by metallic conductors-electrodes and electrode-electrolyte interface was low, which was previously proven by bias application during EIS analysis. [206] Capacitance due to interfacial resistances were found to be in the range of µF, which was negligible compared to the overall capacitance.

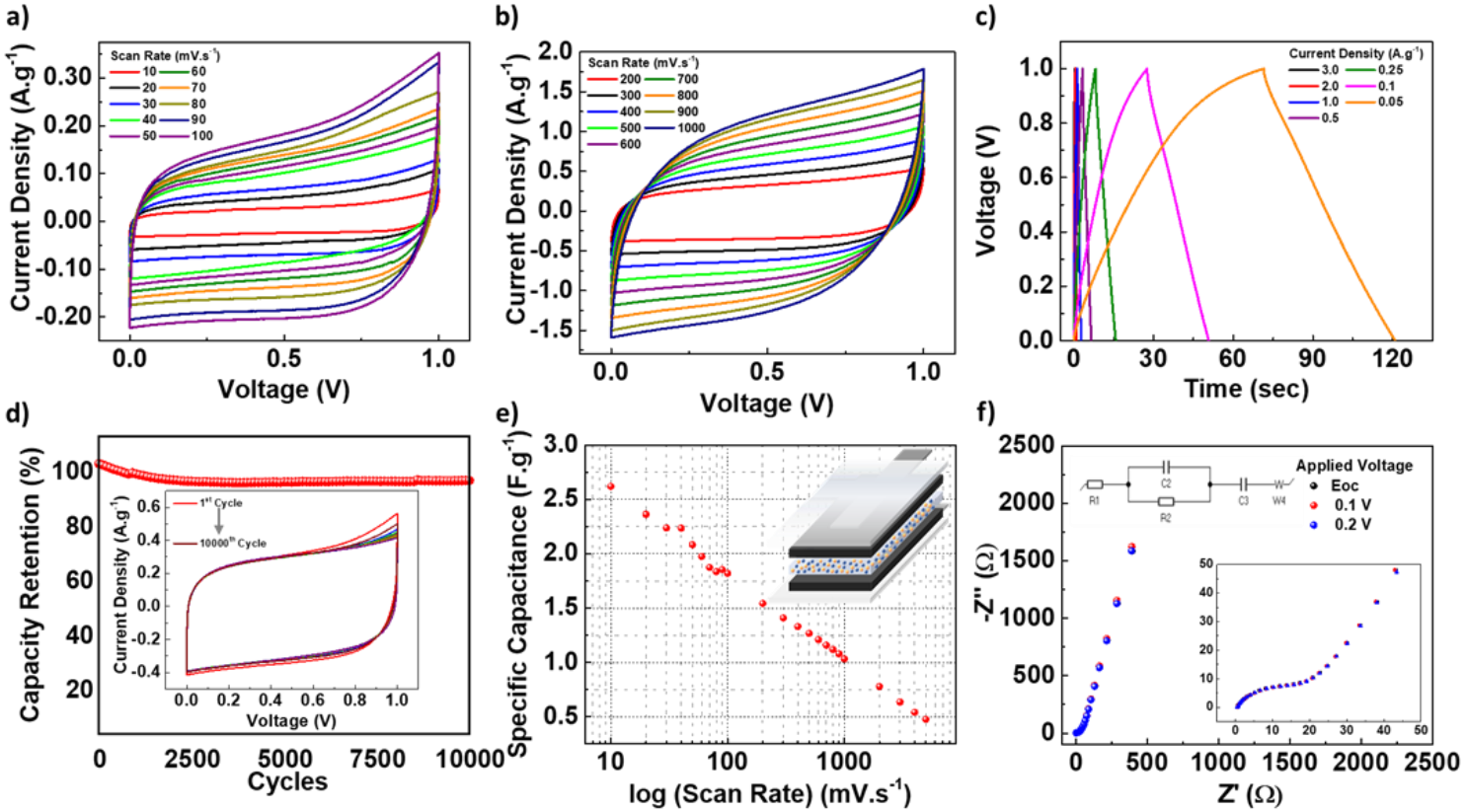

Figure 2. 26 a, b) CVs of the T-SUPC with different scan rates from 10 $mV.s^{-1}$ to 1 $V.s^{-1}$. c) Galvanostatic charge-discharge curves of the T-SUPC. d) Capacity retention plot for 10000 cycles at a scan rate of 200 $mV.\ s^{-1}$. Inset shows the CV shapes from the 1st cycle to 10000th cycle. e) Change in specific capacitance of the transient supercapacitor with scan rate. f) Nyquist plots obtained at different applied DC biases. Insets show enlarged high-frequency region and equivalent circuit of the fabricated supercapacitor device. Reprinted with permission from ref [111], Copyright 2021, Wiley

T-SUPCs were also assembled in series and parallel connections to further demonstrate the ideal performance, with detailed CVs and GCDs provided in Figure 2.27. Larger voltage window at a scan rate of 200 $mV.s^{-1}$ can be easily obtained with the serial connected devices, which is shown in Figure 2.27 (a). Ideal behavior of the serially connected devices can be observed from the GCD curves provided in Figure 2.27 (b). The charge-discharge times stayed the same, while the voltage limit was found to increase linearly with each serially connected cell. Same cells were also assembled in parallel in order to improve the energy density (Figure 2.27 (c)). Finally, the transient devices were assembled as shown by the equivalent circuit given in Figure 2.27 (d), where 2 series and 2 parallel connected devices were compared to devices with different connection configurations. Ideal increase in maximum voltage and energy density in terms of charge-discharge times in each step can be clearly observed, proving an ideal capacitive behavior with little or no harm caused by the connections. Figures 2.27 (a)-(d) demonstrated the potential of T-SUPCs in real applications. Figure 2.27 (e), on the other hand, shows the CVs of the transient supercapacitors at a scan rate of 200 $mV.s^{-1}$ when they were bent to 90° and rolled 360° down to a diameter of 3 mm. CV of a flat supercapacitor is also provided in Figure 2.27 (e)-i. The device perfectly maintained its behavior when bent demonstrating its excellent flexibility (Figure 2.27 (e)-ii). Moreover, fabricated supercapacitor was rolled down to a diameter of 3 mm (which was rolled around itself at least two times) and found to preserve its close to ideal shape (Figure 2.27 (e)-iii), and could be used as a conventional capacitor component in real applications.

It was possible to increase the scan rate up to 10 $V.s^{-1}$ without sacrificing the ideal capacitive behavior, which is highly promising for real-life applications (Figure 2.28). While the equivalent resistance of the device started to be effective after 1 $V.s^{-1}$, the assembled transient device showed promising rate capability and operated up to a scan rate of 5 $V.s^{-1}$ (Figure 2.28 (a)). In Figure 2.28 (a), it is shown that a single device loses its ideal rectangular shape when the scan rate is over 3 $V.s^{-1}$. When multiple T-SUPCs were connected in series and parallel, the potential sweep rate could be increased to 10 $V.s^{-1}$, while preserving the ideal capacitive shape (Figure 2.28 (b)).

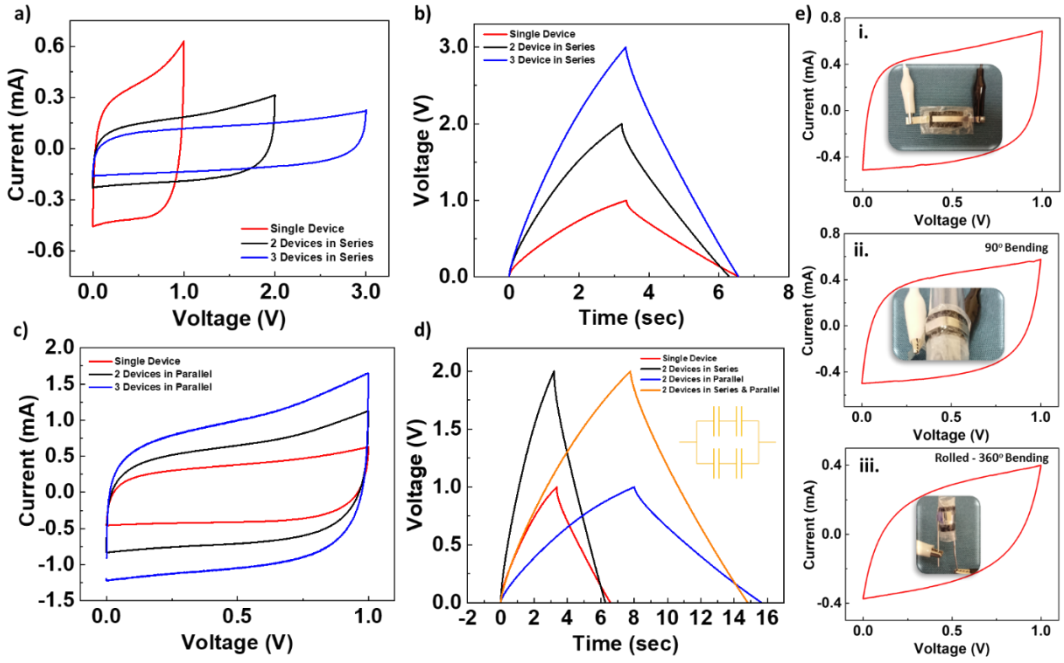

Figure 2.27 CVs and GCDs of serial and parallel connected supercapacitor devices. a,b) CVs and GCDs of serially connected supercapacitor devices. c) CVs of supercapacitor devices connected in parallel. d) Comparison of different combinations of series and parallel connections with GCD. e) CVs of a flexible supercapacitor cell when it was e-i) straight, e-ii) bent at 90°, and e-iii) 360° rolled. Reprinted with permission from ref [111], Copyright 2021, Wiley

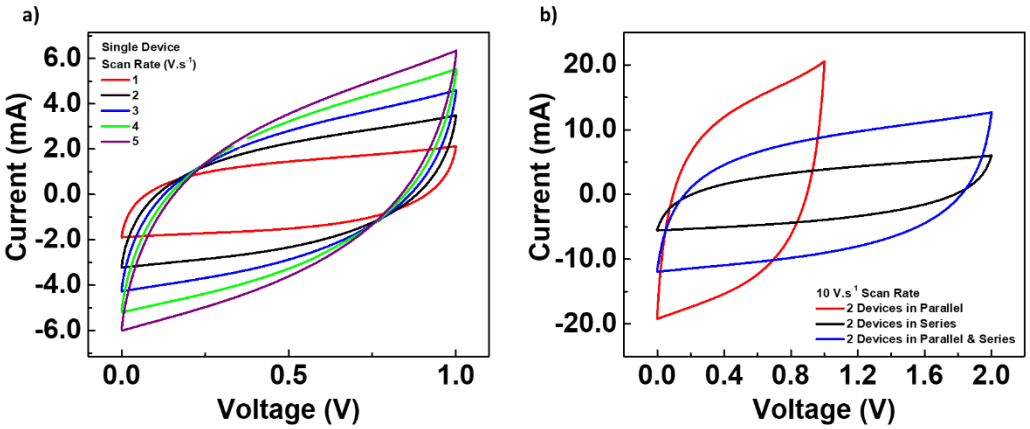

Figure 2.28 CVs of a) a single device up to a scan rate of 5 $V.s^{-1}$ and b) serial and parallel connected devices at a scan rate of 10 $V.s^{-1}$. Reprinted with permission from ref [111], Copyright 2021, Wiley

Comparison of the fabricated T-SUPCs with those supercapacitors in recent literature including carbonaceous materials and transient and non-transient ones are given in Table 2.3. While supercapacitors utilizing pseudocapacitive materials do have better gravimetric capacitances, T-SUPCs have comparable or better areal capacitances in overall. Moreover, T-SUPCs provide one of the best rate capabilities, reaching a scan rate of 10 $V.s^{-1}$, on top of providing the fastest physical transiency. From these results, it is clear that T-SUPCs are promising to be used as energy storage devices in transient electronics.

Table 2.3 Comparison of the fabricated T-SUPCs with those supercapacitors in literature including carbon-based, PVA-based and transient applications.

Materials	**Transiency Mode**	**Energy Storage**	**Maximum Rate**	**Electrochemical Stability**	**Ref.**
W, Fe, Mo metals as electrodes NaCl/agarose as electrolyte	Water-soluble Dissolution in 24 hours at elevated temperature in PBS	Highest achieved – 1.6 mF cm^{-2} at a current density of 0.15 mA cm^{-2}	1 V s^{-1}	10000 cycles – Retention is not provided	[207]
Silk protein, fibroin and sericin protein, PEDOT:PSS and reduced graphene oxide as electrodes NaCl/agarose as electrolyte	Biodegradable Degradation in 21 days in PBS	148.3 F.g^{-1} and 9.85 mF.cm^{-2} at a scan rate of 1 A.g^{-1}	500 mV s^{-1}	500 cycles – Retention is not provided	[208]
Zn-Ti_3C_2 MXene electrodes Gelatin processed in $ZnSO_4$ solution as electrolyte	Degradable in hydrogen peroxide and PBS – 8 days	132 F.g^{-1} and 330 F.cm^{-3} at a current density of 0.5 A.g^{-1}	100 mV s^{-1}	91.6% at a current density of 3 A.g^{-1}	[209]
PLA nanopillars with ZnO layer as electrodes PVA/PBS hydrogel as electrolyte	Bioabsorbable	0.15 mF.cm^{-2}	300 mV s^{-1}	3000 cycles – 70% capacitance retention	[89]
Mo wire as electrodes PVA/NaCl as electrolyte	Water soluble – 15 days with %88 mass retention	4.15 mF.cm^{-2} at a current density of 0.05 mA cm	1 V s^{-1}	5000 cycles – 82% retention	[210]
N-doped graphene microelectrodes PVA-H_3PO_4 as electrolyte	Water soluble – no degradation test	37.5 mF.cm^{-2} at a scan rate of 5 mV.s^{-1}	100 mV s^{-1}	-	[211]
Graphene electrodes MMT/PVA treated with DMSO solution as electrolyte	No transiency	161 F.g^{-1} at a current density of 1 A.g^{-1}	200 mV s^{-1}	10000 cycles – 95% retention	[212]
PPy coated graphene foam as electrodes ACN:PC:PMMA:$LiClO_4$ as gel electrolyte	No transiency	89.6 mF cm^{-2} at a current density of 0.6 mA cm^{-2}	500 mV s^{-1}	10000 cycles - 75% retention at a current density of 5 mA cm^{-2}	[213]
CNT/RuO_2 as electrodes PVA/H_3PO_4 as electrolyte	No transiency	7 mF cm^{-2} at a current density of 0.5 mA.cm^{-2}	500 mV s^{-1}	1000 cycles - close to 100% retention	[214]
Graphene-CNT composite ink as electrodes PVA/H_3PO_4 as electrolyte	No transiency	9.81 mF.cm^{-2} at a current density of 0.05 mA.cm^{-2}	100 mV s^{-1}	10000 cycles – 95.5% retention at a current density of 0.1 mA.cm^{-2}	[215]
PVA/CB/AC as electrodes PVA/NaCl as electrolyte PVA/Sucrose/Glycerol as encapsulant	Water soluble and composed of biodegradable materials - Immediate transiency	2.62 F.g^{-1} and 6 mF.cm^{-2} at a scan rate of 10 mV.s^{-1}	10 V s^{-1}	10000 cycles – 93% retention at a scan rate of 200 mV.s^{-1}	**This Work**

CHAPTER 3

TRANSIENT TRIBOELECTRIC NANOGENERATORS

3.1 Introduction

Rapid technological advancements and industrialization lead to increased demand for power across the globe. This demand is not only created by consumer products (ranging from small consumer electronics to electric cars) but also from the general trend to shift towards sustainable energy sources. As of now, development of such products is hindered by the obsolete energy generation or storage technologies. Conventional solar cells and lithium-ion batteries, in particular, cannot provide enough energy harvesting or storage to get off the grid. [216,217]

Triboelectric nanogenerators (TENGs) was invented by Prof. Zhong Lin Wang and his coworkers. TENGs are used to harvest wasted energy by trivial and low-frequency actions. [218] This energy harvesting is enabled by coupling effect of contact electrification and electrostatic induction. Shortly, this contact electrification on top of the friction of two different surfaces is called as triboelectrification. When two different dielectric solid materials come into contact, triboelectrification occurs, which polarizes the surfaces. [219] These charges can be harvested to realize self-powered systems or charge various small-appliances such as wearable electronics.

The timeline for the study of electrification is given in Figure 3.1. The word triboelectric comes from Greek, where "*ēlektron"* comes from the Greek word "amber," and tribo- prefix is the Greek of "to rub." The first ever triboelectric phenomenon was seen in a dialogue that appeared in Plato's Timaeus, dating back approximately 400. B.C. The dialogue included "the marvels observed about the

attraction of amber," referring to dry hair electrostatically attracting amber. A Chinese philosopher, Pu Guo, described the "amber effect" in his poem, dated around 300 A.D. The poem "Chi Shi Zan (Eulogy of the Magnet)" includes the words below;

"The magnet draws the iron, and the amber attracts mustard seed. There is a breath that penetrates secretly and with velocity and which communicates itself imperceptibly to that which corresponds to it in the other object. It is an inexplicable thing."

Here, the "*breath*" actually refers to the electrostatic attraction between the objects, which the philosopher thought that the objects are "*communicating*" with each other. [220]

The first comprehensive analysis to understand electrification was made much later, in the 1600s, by William Gilbert. He showed that materials such as sulfur, wax, and glass could be electrified when rubbed as amber. Otto von Guericke utilized this in the world's first friction generator. A rotating sulfur globule is constructed, which generates electricity when materials are rubbed to the surface of the globule. Fundamental works on electricity became with Coulomb, where he explained the law for attraction and repulsion between the electrical charges. He also investigated the charges on electrified bodies and found that they are limited to the surface of the materials. Johan Carl Wilcke, a Swedish scientist, suggested the first triboelectric series showing materials' charge affinity in 1757. A similar study was done by Michael Faraday, published in "Experimental Researches in Electricity," which contains the investigations from 1831 to 1855. A series is constructed from the materials most prone to give positive charges to the ones prone to give negative charges, which are subjected to friction. In 1789, Alessandro Volta realized that electrification could happen with contact rather than simply rubbing. From that point,

it was realized that triboelectrification is a complex phenomenon still not completely understood today. [220,221]

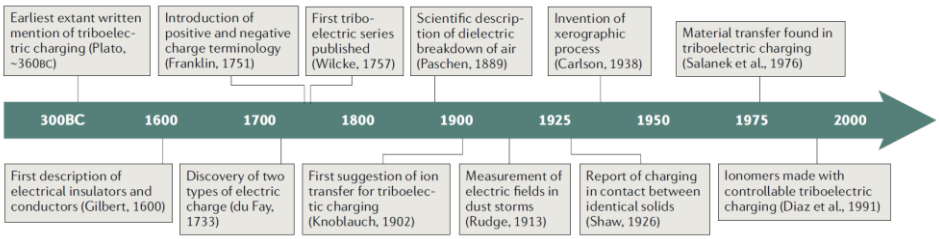

Figure 3.1 Timeline of the study on contact electrification. [222]

3.2 Working Mechanism of TENGs

There are different models proposed for the origin of triboelectrification, and discussed on many levels including electrical engineering, materials science and physics. [222–225] Models are summarized and given in Figure 3.2.

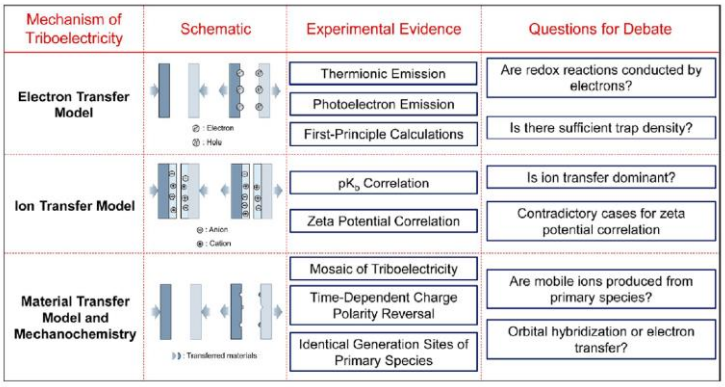

Figure 3.2 Models proposed for triboelectrification and their foundations. [217]

Explained mechanisms all rely on the difference in triboelectric series. Higher the difference between the triboelectric series of the dielectric materials, higher the performance can be achieved. The best quantification with a proposed method for standardized measurement was done by Wang's group in 2019. [226] A linear motor system inside a Faraday cage was built. Liquid metal was used as the electrode of static part of the system. Using liquid metal ensured a complete touching of the triboelectric material and the liquid metal electrode, which eliminated the effect of roughness and elastic/plastic deformations of the triboelectric surface. Resulting quantified triboelectric series is given in Figure 3.3.

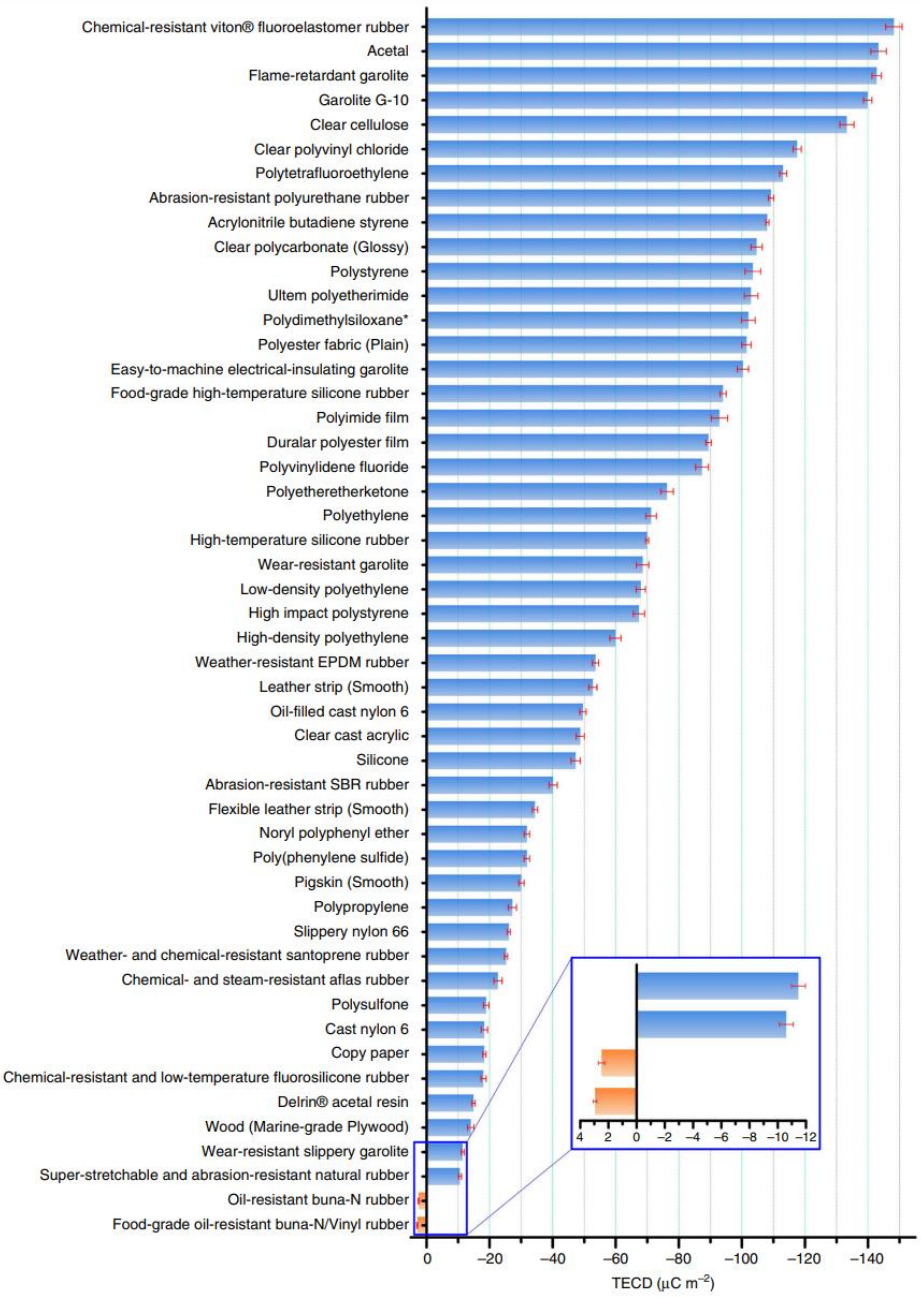

Figure 3.3 Quantified triboelectric series. [226]

3.2.1 Electron Transfer Model

This model relies on the work function difference between solid-solid interfaces. In such insulator-insulator or metal-insulator pairs, an electron transfer mechanism is suggested, which is based on trap states. [227] Visualization of such a transfer is provided in Figure 3.4. While this phenomenon is not completely understood/proven, triboelectric properties were suggested to have a direct relationship with Fermi level of materials and work function. [217] In this model, insulators are expected to have very low performance (in terms of charge generation) due to their high band gaps. If this model is valid, insulators need to overcome a very high energy barrier to transfer electrons. But in contradiction, experimental results have shown that the surface of the insulators is charging much more than semiconductor-metal pairs. [217] This phenomenon is recently explained by the electron transfer triggered by interfacial potential between surface atoms. This phenomenon relies on the interaction between a few angstrom-thick topmost surface atoms and another adjacent pair. With the mechanical contact, overlapping of bands between two materials is suggested, in which the interfacial barrier is overcame because of the superposition principle [217,228]. Yet, studies done by Li et al. by utilizing atomic force microscopy (AFM) and Kelvin probe force microscopy (KPFM) have shown that contact at the nanoscale causes both thermionic emission and photoelectron emission. [229,230] In the thermionic case, it was seen that materials at higher temperature tend to be tribopositive while the latter case, they tend to be tribonegative. This case suggest that charge transfer can also be attributed to the thermal excitation of electrons on the mechanical contact, in which they travel from hotter surface to colder ones. [229] In photon excitation effect; on the other hand, light-induced charge decay on dielectric surfaces were suggested. Moreover, it was found that photons with high energies (4.1 eV for SiO_2, for example) may release triboelectric charges from the surface of the materials. [230]

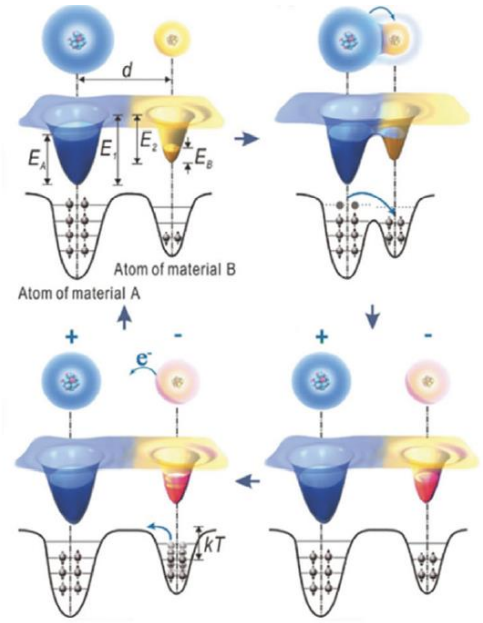

Figure 3.4 Electron charge transfer mechanism explained via electron-cloud model and superposition principle. [223]

3.3 Ion Transfer Model

Electrostatic charging and charge transfer is theorized to happen due to the transfer of ions from contacting surfaces [227]. Yet, a net transfer of charges between one surface to another cannot be distinguished due to neutralization of positive and negative ions. [227] In 1967, Kornfeld suggested a model for frictional electrification for insulators [231];

1) Solid insulators possess their own intrinsic electric field,

2) This intrinsic field is neutralized by the ions from ambient conditions,

3) A surface layer is formed with these attracted ions and other adsorbed species,
4) If this surface is rubbed to another, it mixes with the rubbed one,
5) Thus, intrinsic fields of these surfaces are disturbed and results in electrified surfaces. [231]

Above theory proposed by Kornfeld actually contradicts with the energy requirements for charge transfer between the surfaces. While an electron transfer is surely happening for metal-metal contacts, in insulators, this requires high amount of energy. As an example, when nylon and polyethylene is rubbed, nylon will be negatively charged while polyethylene will be charged positive. Transfer of an electron from negatively charged nylon would require several eVs, while separation across the interface would require around 1 eV, depending on the distance. After the transfer, this electron should be introduced to the alkane ring, which is an endothermic process and again requires additional energy. [232]

McCarty and Whitesides [233] tried to obtain an answer to this insulator-insulator model by investigating ionic polymers which have covalently bound ions and mobile counterions. This allowed them to disregard the mobility difference between anions and cations since one is bound to the polymer chains and thus, immobile. The effect of ions is proved by Diaz as they found an increase in the triboelectrification by increasing the ion concentration in the polymer by utilizing XPS to find the transfer of mobile ions [234]. While this is limited due to the dielectric breakdown of air [233], it still shines light onto the transfer mechanism.

Figure 3.5 (a) shows a suggested mechanism for ion transport model formed from the transport on a single anion. [233] In this case, when two surfaces are in contact with each other, only movement of this anion will be within its single potential well. When the surfaces are separated with an infinitesimal distance, this ion will have a double-well with a very small barrier. Herein, the ion has sufficient energy to freely travel between two surfaces. Yet, this travel is expected to happen with thermal activation, as a tunneling mechanism with large ions such as H^+ is highly unlikely. If the thermal energies are sufficient (this might arise due to local heating because of tribology [229]), one can find the probability of ion being on the surfaces by using Boltzmann distribution. When the distance between two surfaces increases even more, the ion is trapped on one surface. One should note that the final state of ions trapped in one surface or another is not a case of equilibrium distribution of charges. This charging from ion-transfer can be estimated with a simple calculation from Boltzmann distribution by assuming a model such as Figure 3.5 (b). The equation for this case is given below; [233]

$$\frac{n}{N-n} = \exp\left(-\frac{n\,d\,e^2}{\varepsilon_0\,k\,T}\right) \qquad (3.1)$$

,where *N* is the number of ionic functional groups per unit area, which is separated by a distance *d* from the unfunctionalized surface. *n* is the number of mobile anions transferred from one surface to another, *e* is the magnitude of charge on a single ion. Thus, electrostatic work needed for the anion to go from functional surface to unfunctionalized one is $\frac{n\,d\,e^2}{\varepsilon_0}$.

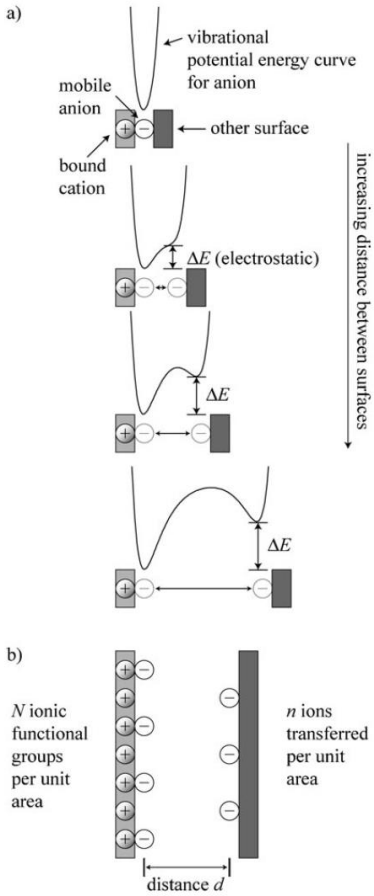

Figure 3.5 a) Representation of the ion transfer model and b) model used to calculate the amount of charge separation due to ion transport mechanism. [233]

3.3.1 Material Transfer Model and Mechanochemistry

While the material transfer model is suggested in earlier studies [217,227], this model was disregarded due to the expectation of a very small contribution to triboelectrification. [235] Yet, in 2011, Baytekin et al. [236] discovered that contact electrification between two polymers arise from nanoscopic mosaic charging because of material transfer. Relevant schematic can be seen in Figure 3.6. In short,

Baytekin et al. proved that triboelectrification is also caused by material transfer through the use of KPFM, confocal Raman spectroscopy (CRS) and X-ray photoelectron spectroscopy (XPS). In these methods, it is proven that triboelectrification does not occur traditionally by two different surfaces, but a single surface consists of mosaic pattern of differently charged regions. [236]

Triboelectrification between polymers is accompanied by bond cleavage and suggested that the mechanical deformations on the surface of the polymers give rise to mechanoradicals that are even capable of driving chemical reactions. [237] Moreover, Sakaguchi et al. [238] observed that for polyvinyl chloride (PVC) and polyvinyl fluoride (PVF) produces mechano-radicals, which are actually neutral free radicals from chain-ends of homogeneous scission of carbon-carbon bonds by utilizing electron spin resonance (ESR) spectroscopy. Likewise, they observed mechano-anions, which are from heterogeneous scission of the carbon-carbon bonds. These mechano-radicals and mechano-ions also contributes to the triboelectrification of polymer surfaces by mechanical fracture.

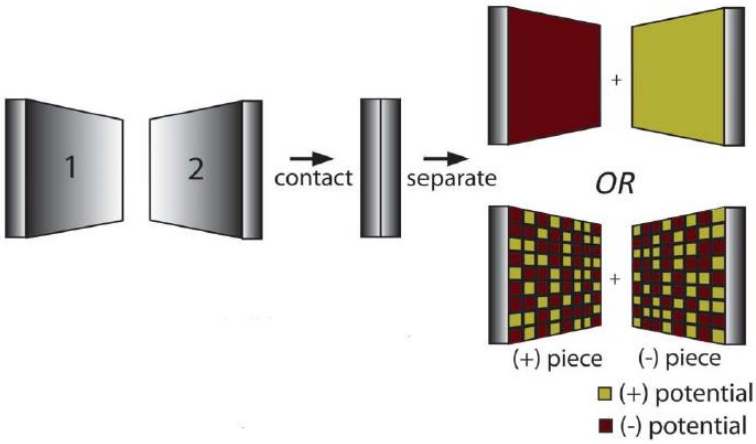

Figure 3.6 Schematic representation of contact electrification investigated by KPFM surface potential maps. Above is the traditional theory, while mosaic surface charge is observed with KPFM and confocal Raman microscopy. [236]

3.4 Materials and Methods for the Output Performance of TENGs

The output performance of TENGs can be improved via various modifications made to the triboelectric layer. This involves the surface modifications – including both physical and chemical structuring, chemical modifications of the dielectric layer to obtain different mechanisms such as changing dielectric properties or adding ionic characteristics to improve the conductivity, and adding filler materials to the dielectric layer to form composites to improve the charge generation.

3.4.1 Surface Modifications

Surface modifications include physical modifications made to the triboelectric layer – such as adding roughness/nanoarchitecture or chemical modifications – such as adding chemical groups or chemical grafting. Both methods, which alter the surface properties of the triboelectric layers, aim to increase the charge generation at the contact surface.

3.4.1.1 Physical modifications on triboelectric layer

Physical modification of the triboelectric layer is one of the most fundamental ways to improve the charge generation. Main idea is to create a micro/nanostructured surface to improve the contact area, thus improving the effective surface area or creating a 3D structure to increase the available surfaces that can generate charges upon triboelectrification. [239–242] Tremendous efforts have been made since then, to obtain a patterned triboelectric layer – mainly via templating, etching, inducing

wrinkles or crumples and adding nanostructures onto triboelectric layers through deposition.

Texturing, especially adding specific structures such as pyramid structure to the triboelectric layers are widely used to increase the triboelectrification. [239,243–245] Yang et al. [246] recently tried to explain this phenomenon via simulation and compared the texture sizes of the pyramids and its effect on the triboelectrification. Effective dimensions are presented in Figure 3.7 (a). PDMS patterns are fabricated with respect to these, and optical microscopy images were taken under different loadings to show the change in area (Figure 3.7 (b)). They have found that especially under lighter loadings, there is a change in the open-circuit voltage due to changing contact area, while it became constant at higher loadings due to unchanged contact area. However, a decrease in the output performance of the TENGs was observed when the texturing is very close and frequent, which ultimately decreases the superficial area (Figure 3.7 (c)). In the light of this, a simple texturing done by Tantraviwat et al. compared three different PDMS surface structures, which are highly porous, micropillars and flat surfaces (Figure 3.7 (d)). [247] Highly randomized and porous surface with random cavities obtained via dry-etching technique had better V_{oc} and I_{sc} than micropillared and flat surfaces – indicating that instead of having periodic architectures, it is much better to have randomized small cavities (Figure 3.7 (e)). However, researchers have observed that the implementation of micro-pillars yields superior results compared to using a flat PDMS surface, indicating that surface texturing is still a feasible way to improve TENG output performance.

It is also possible to improve the triboelectrification by simply adding nanomaterials onto the triboelectric surface. Bhavya et al. [248] simply used liquid-phase exfoliated 2D hexagonal boron nitride nanosheets (BNNS) to modify the triboelectric layer. BNNS are spin coated on biaxially-oriented polyethylene terephthalate (BoPET). By

using polyvinyl butyral as the binder, deposited BNNS on BoPET improved the triboelectrification for at least 70 times – which changes the surface properties as the BNNS are triboelectrically more negative. This also shows a feasible and cost-effective way to improve the triboelectrification by simply depositing nanomaterials onto triboelectric layer.

Ahn et al. in 2021 [249] introduced wrinkled structures coexisting with micropillars to improve the TENG performance by both utilizing the regularly arranged microstructures with randomly distributed nano-texturing (Figure 3.7 (f)). To obtain this structure, typical methods that were used for surface texturing were combined, namely nanotransfer, molding, and buckling. A typical SU-8 was used for the molding, yet treated with photolithography to obtain a microstructure for the elastomeric substrate. In the side, nanopatterned PVA was prepared via KrF lithography of a Si master, where polyurethane resin was used to obtain the nanopatterned mold. Subsequent Au deposition using e-beam evaporator and transfer onto PVA films are made to deposit nanopatterns on PVA films. The elastomer used for micropatterns, on the other hand, treated with (3-aminopropyl) triethoxysilane (APTES) and coated with UV-curable adhesive to transfer nanostructures on PVA. After PVA was dissolved in water, authors achieved morphology-controllable wrinkled micro/nano hierarchical structure (WHS) on a single substrate, which is normally very challenging to achieve. Nanostructures provided by wrinkled surface enabled them to have superhydrophobicity – which is also essential for TENG devices. It is worth noting that triboelectrification is highly affected by humidity. All in all, with the WHS structure, the output performance of TENGs is increased by 608% when compared to simple flat surface. The effect on the pre-stretching and dimensions of the nanopattern in terms of output voltage, showing the micro/nano pattern and its effect on the output performance is controllable (Figure 3.7 (g)). This proves the significant impact of surface morphology and/or alterations on the output performance of TENGs.

3.4.1.2 Chemical Modification of the Surface of Triboelectric Layer

In addition to physical modifications that can be made to the triboelectric layer, the performance of TENGs can also be enhanced through chemical modifications specifically applied to the surface [250–253]. While the route to alter the properties of the triboelectric surface, particularly to enhance charge efficiency, holds promise, there has been relatively limited research conducted in recent years.

Byun and coworkers in 2016 [254] explored the concept of chemical functionalization of the surface of triboelectric layer by thoroughly controlling the surface dipoles and surface electronic states. To realize that, they have used electron-donating and -withdrawing functional groups, which were self-assembled as monolayers (SAM) on SiO_2 surfaces (Figure 3.8 (a)). By completely controlling the surface properties, they have shown that it is possible to alter the conventional triboelectric series. Alteration of the surface of the indium tin oxide (ITO) directly shown huge improvement on the voltage and current output (Figure 3.8 (b)). SAM addition to typical substrates such as SiO_2, Al_2O_3 and ITO shown to alter in a great deal – where NH_2 groups tend to behave as an electron-donating layer, resulting in a more positive triboelectricity, whereas CF_3 behave as electron-withdrawing layer, resulting in a more negative triboelectricity (Figure 3.8 (c)). [254]

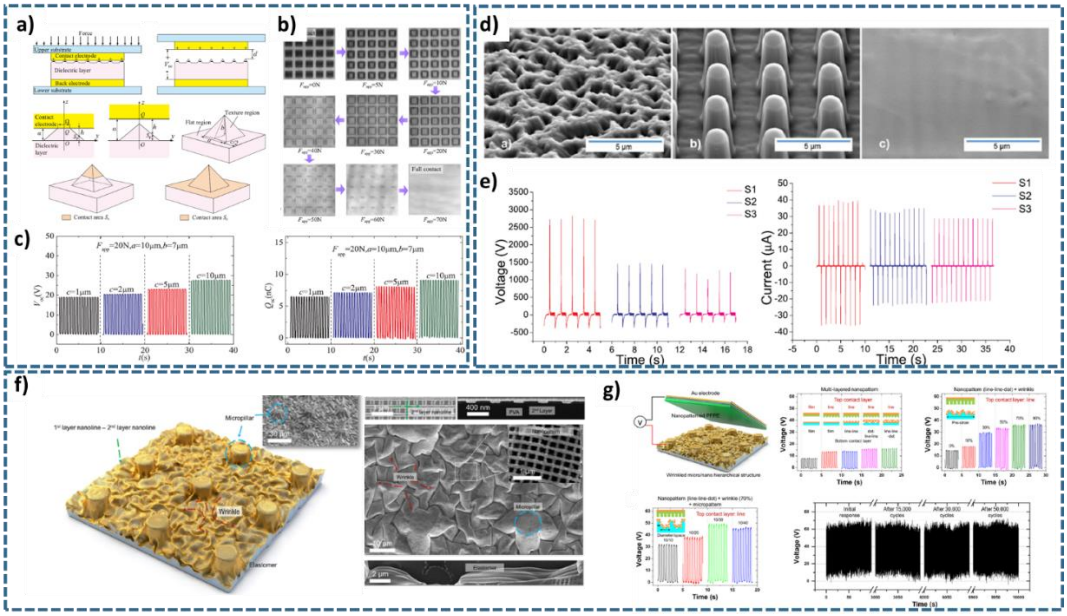

Figure 3.7 TENGs with surface modifications for improved output performances. a) Schematic diagrams of pyramid texture in contact and separation state. b) Contact images of textured PDMS under different applied forces. c) Variations of open circuit voltage and short-circuit charge with different texture spacings. [246] d) SEM images of patterned PDMS with porous morphologies such as nanograss (S1) and micropillars (S2) and flat PDMS (S3). e) Difference in open circuit voltage and short circuit current outputs of different morphologies. [247] f) Schematic image of wrinkled micro/nano hierarchical structure and SEM images of inclined surface, cross-sectional images, top-view and side-view of fabricated structure on elastomer substrate. g) Schematic representation of TENG developed with the wrinkled structure and its performance with respect to wrinkled structure, its pre-stretching effect on the output performance, nanopattern dimensions and its effect on the output performance, and stability. [249]

With this knowledge, researchers modified various surfaces, and used it even in textile-based TENGs. As an example, Sun and coworkers in 2022 [255] modified silk-based fabrics with different functional groups, organo-siloxanes such as n-Butyltrimethoxysilane (BTMS), (3-amonopropyl)trimethoxysilane (APTMS), (3-bromopropyl)trimethoxysilane (BPTS), and (3-mercaptopropyl)trimethoyxsilane (MPTMS). Fabrics are treated with oxygen plasma to graft hydroxyl groups, then immersed into organo-siloxane containing ethanol solution for 12 hours. Schematic representation final TENG structure and the grafting procedure is given in Figure 3.8 (d). Here, researchers again observed that the electronegativity variation of the whole TENG device can be regulated by the functional groups that are grafted onto silk fabrics. This chemical grafting also changed the hydrophilicity of the fabric surfaces, which is also given in Figure 3.8 (d). In a simple combination of original silk/modified silk pair, the output voltage and the short-circuit current can be regulated from 5.38 to 36.6 V and from 0.12 to 0.52 μA, respectively (Figure 3.8 (e)). This not only proves that the chemical functionalization of the surface can yield much better output performance, but also shows that the surfaces can be tailored for a specific end-usage.[255]

Both physical and chemical modifications of the triboelectric layer can be utilized to improve the performance in a significant manner. Feng and coworkers, in 2022,[256] used this idea to amplify the TENG performance compared to flat and un-modified surfaces. They have used direct image lithography (DIL) method to fabricate polyurethane layers with surface microcones, then chemically functionalized it with trichloro (1 H, 1 H, 2 H, 2 H-perfluorooctyl) silane (FOTS) vapor to obtain increased roughness with surface fluorine groups (Figure 3.8 (f)). TENG device is formed with microcones treated with FOTS and untreated one, as schematically shown in Figure 3.8 (f). Having microcone structures resulted in a much better current and charge output compared to the flat surfaces (Figure 3.8 (f)). Moreover, with respect to original cone structure, polyurethane (PU) treated with FOTS yielded much higher

current and charge output (Figure 3.8 (g)) – showing the promise of chemical functionalization combined with traditional physical modifications. [256]

Ion implantation is another interesting technique used to improve the triboelectrification on the surface. [257–259] This technique puts an advance over the simple chemical grafting methods as the distribution of implanted ions in a varied thickness can be controlled precisely. [260] In order to explore such concept, Fan et al. [260] used ion implantation to create polar bonds and found that they significantly improve the polarization, which is schematically provided in Figure 3.8 (h). N ions are chosen to be implanted into PTFE and FEP as it provides the most electronegativity. With the ion implantation technique, they have observed a stronger polar bonding formation such as $C \equiv N$ or $C = N$ bonds. While the best performing ion implanted PTFE and FEP is seen to have 7.8-fold and FEP 4.6-fold increase in their charge density when compared to their original structures, it is also observed that with the ion implantation PTFE has now a polar polymer structure with increased dielectric constant (Figure 3.8 (i)). These are correlated with a higher surface charge accumulation, hence, has a huge impact on the output performance of the triboelectric layer (Figure 3.8 (i)). [260]

3.4.2 Modification of the Chemical Structure of Triboelectric Layers

Apart from the chemical modifications that are done as a post-process to functionalize, graft or implant ions onto the surface of the triboelectric layer, one can also start from scratch and modify the triboelectric layer. As the choice of material selection is crucial for TENGs for high performance output, it is also tailorable by the processing techniques. [261] As such, what is proposed for the modification of the chemical structure is to modify the widely known polymer materials such as PTFE, FEP, PVDF, nylon, PVA or cellulose to obtain better mechanical properties or lower impedance/higher electrical conductivities, and even change their polarity in terms of triboelectrification. [262] In this manner, the most common technique is to introduce ionic groups to the polymeric triboelectric layers or increasing the inherent conductivity of the polymers with doping. [250,263]

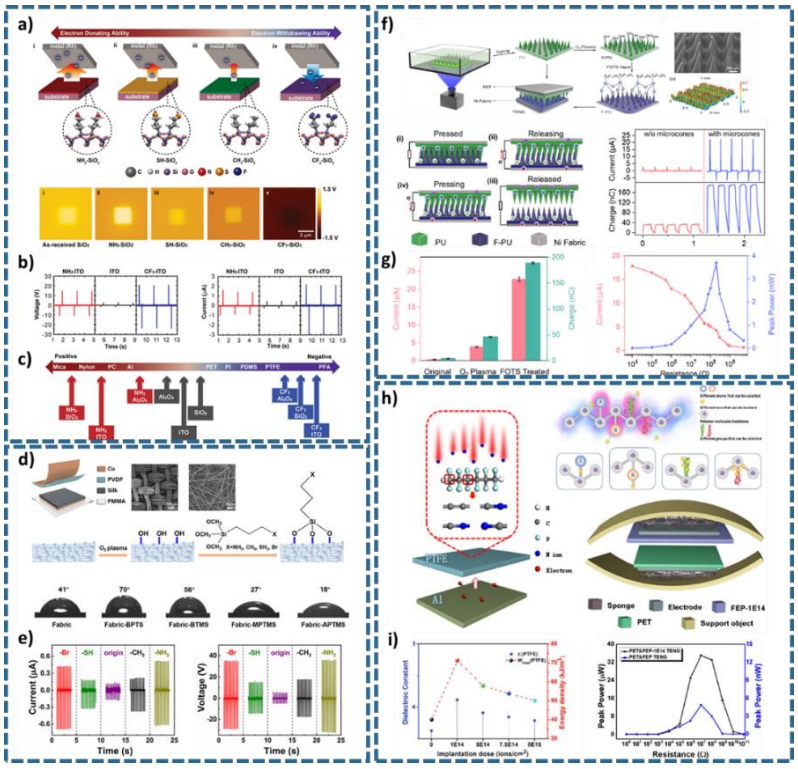

Figure 3.8 Examples of the chemical modifications on the surface of triboelectric layers. a) Schematic of controlling surface dipoles and via SAM and their triboelectrification with electron-donating and withdrawing groups. b) Triboelectric performances of SAM-modified ITO coupled with PI. c) Effect of SAM modification on the triboelectric series of ITO, AI_2O_3 and SiO_2. [254] d) Schematic representation of the TENG device with functional-group-modified fabric, and the schematic representation of the modification process and the SEM images of modified silk and PVDF nanofibers. Below images show the contact angle images with respect to different modification groups. e) I_{sc} and E_{oc} of TENG devices with PVDF and modified silk triboelectric pair with different modification groups. [255] f) Schematic representation of the fabrication of fluorinated PU microcones and its mechanism of triboelectrification with unfluorinated one. Graph shows the performance difference between microcones and flat PU. g) Current density and charge density difference between FOTS treated microcones and O_2 plasma treated one. Load resistance matching test showing peak power is also given. [256] h) Schematic figure of ion implantation into the polymers with the diagram of molecular chain modification via ion pairing. Resulting schematic TENG device containing ion implanted PTFE is also given. i) Dielectric constant with respect to implantation dose, with the results of peak power with respect to load for the sample with highest dielectric constant. [260]

3.4.2.1 Addition of ionic species

The main idea of introducing ionic groups – cations, anions or ionic liquids – is to induce Hofmeister effect and synergistically increase the electrostatic interaction at the same time. Mainly, identity of ions specific ion effects (shortly SIE) is much more important than the number of ionic charges or concentrations as suggested by Debye-Hückel theory. [264] This Hofmeister effect, coupled with the electrostatic induction caused by the ionic species, is very widely applied route to improve TENG performance. In a very simple manner, Ryu et al. [265] explored the addition of ionic species to PVA to change its triboelectric properties, which is confirmed with KPFM and enhanced output (Figures 3.9 (a) and (b)). With the addition of calcium chloride ($CaCl_2$) and phosphoric acid (H_3PO_4), they have been able to obtain the most positive and most negative triboelectric materials, respectively (Figure 3.9 (c)). The output performance increase in these were attributed to asymmetric ion pairing. [265] To build on that, Cheong et al. 2021 [266] introduced different ionic species to see both anion and cation effect. They have explored the molarity, the effect of cation species while the anion is fixed, and vice versa to find the best performing combination. Interestingly, the best performing ones, which are PVA-$CaCl_2$ and PVA-$NaNO_3$, have the highest dielectric constant and dielectric losses, in which they attributed to the increase in ionic polarization due to migration of ionic species (Figure 3.9 (d)). Moreover, they systematically explored the triboelectric performance metrics with fixed electrolyte concentration, fixed anion concentration, and fixed cation concentration (Figure 3.9 (e)). Although significant achievements have been made by simply adding ionic species to the PVA matrix, no relation was made with the Hofmeister effect. Wu et al [267] explored this effect to understand the mechanism behind the ionic additions on triboelectrification. Polyacrylamide/PVA organohydrogels were prepared with the Na^+ based salts using a glycerol immersion process. Schematic summary of the findings on the synergistic effects on the

conductivity of Polyacrylamide/PVA organohydrogels is given in Figure 3.9 (f). It is seen that that the Hofmeister effect influences the conductivity, and although the cations are generally disregarded in Hofmeister effect in terms of conductivity, anions such as lithium and sodium are very important due to their electrostatic interactions. They have seen the "salting-out" phenomenon positively effecting the output performance of the organohydrogels. This is due to the formation of lithium or sodium bonds by electrostatic interactions and provide stable charge channels and higher conductivity than other pairs. A TENG is assembled to see how these affect the output performance of the triboelectric layer (Figure 3.9 (g)). Ultimately, in Figure 3.9 (g), it is observed that the electrostatic interaction plays a much higher role in determining the output performance, as LiCl or NaCl performs much better than the Na_2SO_4 or $NaNO_3$. [267]

3.4.2.2 Modification of polymer structure

Different bottom-up modifications other than ionic integration is also made to modify polymeric triboelectric layers, not only to obtain performance but also transparency. Park et al. 2022 [268] used adipate-based plasticizer on polyvinyl chloride (PVC) to obtain transparent and stretchable TENGs. As the plasticizer is added, both transparency and dielectric constant is improved as well as the tribonegativity of the PVC. They have achieved nearly 20 times the output performance when compared to the native PVC. [268] In a similar manner, Wu et al. [269] controlled the degree of cross-linking and ionic conductivity to find an optimum point for highest TENG performance. They have used 1-butyl-3-metyhyimidazoium hexafluorophosphate ([BMIM]PF_6) as the ionic liquid and polyethylene glycol dimethacrylate (PEGDMA) as the monomer for polymerization to obtain polyethylene glycol (PEG) with different molecular weights. They have seen that

increase in molecular weight after some point decreased the conductivity, while the increase in the ratio of ionic liquid increased both the ionic conductivity and transmittance. [269] Both works indicated that controlling the structure of the polymers enable transparent and possibly stretchable triboelectric layers with improved triboelectrification.

Bottom-up fabrications combined with top-down processes to modify the triboelectric layer are named as nanoarchitectronics. [270] Although it achieves the advantages of fast reproduction and applicability to the large areas, a rapid and one-step nanoporous structures can be obtained. Park et al. [271] achieved this one-step fabrication via ternary polymer solution blend with supramolecular assembly. Sulfonic-acid-terminated poly(styrene) (SPS), poly(2-vinylpyridine) (P2VP), and amine terminated poly(ethylene oxide) (APEO) are used to obtain triboelectric layer (Figure 3.9h). Competition between APEO-SPS and P2VP-SPS interaction causes the formation of spontaneous nanopores with an average diameter of 33 nm, which leads to formation of surface-conformal triboelectric nanoporous films with power density of almost 2 times higher than that of planar surfaces. [271]

3.4.3 Composite Structures

Another common way to improve the overall TENG performance is the fabrication of composite structures. Incorporation of materials ranging from micron to nano sizes, and ranging from inorganic materials to polymeric materials has shown a very effective way to improve the output performance. [262,272,273] Ultimate motive for the fabrication of composite structures is the modulation the dielectric constant, providing new charge generating surfaces, improving the conductivity/lowering the impedance of the dielectric layer or even improve the mechanical or frictional properties of the dielectric layer. [273,274] Moreover, the composite structure can be a hierarchical assembly or simply an addition of another layer for the purpose of improved charge generation or charge trapping. [275–277] Herein, rather than focusing on the type of materials, the focus is given to the type of composite structure and its ultimate purpose.

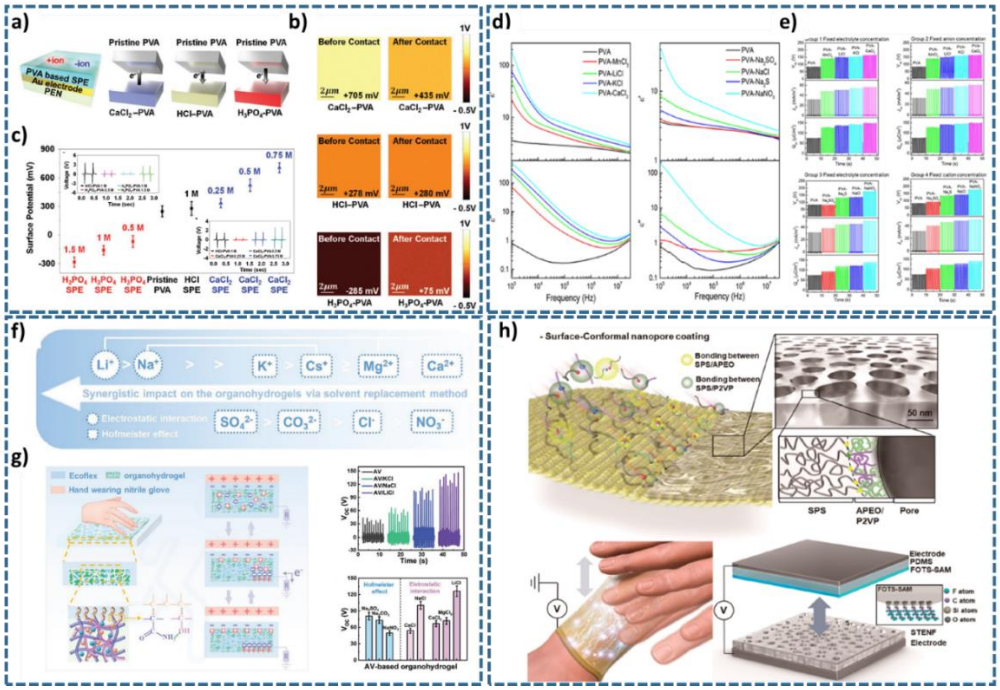

Figure 3.9 Modification of the chemical structure of triboelectric layers. a) Schematic representation of an ionically modified PVA triboelectric layers assembled as TENGs. b) Shows the modified surfaces via KPFM in terms of polarization. c) Change in the surface polarization with respect to ion addition. Inset graphs shows the triboelectric performance of the modified PVA layers. [265] d) Dielectric constant and dielectric loss graphs of PVA layers with different ionic additions. e) Performance metrics of PVA triboelectric layers modified with different ions with respect to fixed electrolyte, fixed anion, and fixed cation concentration. [266] f) Schematic representation of Hofmeister effect in organogels. g) TENG measurements comparing electrostatic and Hofmeister effect. [267] h) Schematic of conformal coating of nanoporous structure due to competitive hydrogen bonding between SPS and P2VP. Conceptual schematics of this cloth utilized as wearable TENG application, and its device structure. [271]

3.4.3.1 Microadditives

As mentioned before, one of the simplest ways to improve the overall performance is the incorporation of nanomaterials to the dielectric matrix. Mostly, the aim is to modify the dielectric constant, with the side benefits of increasing surface-charge density and reduction of the triboelectric loss. [278] Yet, incorporation of micron-sized particles has also shown to improve the output performance of TENGs. Kim et al. 2019 [279] used bulk molybdenum disulfide (MoS_2) to form composites with triboelectrically positive ferroelectric Nylon-11 and triboelectrically negative ferroelectric PVDF-TrFE (Figure 3.10 (a)). By dipolar polarization, and adding MoS_2 structures, they have obtained 500% increase in current density and 220% increase in output voltage, which is attributed to the change in surface polarization imaged with KPFM (Figure 3.10 (a)). [279] Similarly, Kim et al. 2020 [280] used high permittivity $CaCu_3Ti_4O_{12}$ dielectric particles and formed a composite with butylated melamine formaldehyde (BMF). Compared with the typical aluminum oxide (Al_2O_3) and titanium dioxide (TiO_2), they have seen that high permittivity $CaCu_3Ti_4O_{12}$ material also enhances triboelectric output voltage and current density. Compared with the pure BMF, even 1 wt.% addition of $CaCu_3Ti_4O_{12}$ increased both the voltage and current output at least two times. [280]

3.4.3.2 Nanoadditives

Nanomaterials are commonly used to improve the performance of triboelectric layers for TENGs. The effect of nanomaterials can vary depending on their material properties. The main focus is to improve the dielectric constant to improve the electrostatic induction, change or improve the charge affinity, and increase the surface charge density with the possible side benefits of increasing mechanical

stability or resistance to wear. [274] To achieve all of these, various nanostructures such as nanoparticles[281–283], nanowires [284,285], and nanosheets [286–288] are employed for the fabrication of nanocomposite structures.

As an example, for nanoparticle additives, barium titanate ($BaTiO_3$) is one of the most common materials that is used to form composites for TENGs. [289,290] Wang et al. 2022 [291] fabricated a PVDF/ $BaTiO_3$ nanocomposite to increase the permittivity of the film, hence increase the TENG performance. They fabricate a self-polarized TENG with floating metal at the middle of two $BaTiO_3$ filled PVDF composites. Through the addition of $BaTiO_3$, researchers increased the dielectric permittivity of the nanocomposite layer, thus improving the output performance. [291] Metal nanoparticles, such as Au or Ag, are also used to facilitate higher performance in TENGs. [282,283,292] In a particular example, Zhang and coworkers [293] introduced Ag NPs with varying sizes to silica gel in order to observe its effect on triboelectric performance (Figure 3.10 (b)). They have seen that the particle size directly effects the output performance of the silica gels, with the smallest being 20 nm in size showing the best results. These results were again attributed to improved dielectric constant on top of increased contact area between the Ag NPs and silica gel, which resulted in increased charge generation (Figure 3.10 (b)). [293]

1D nanostructures, such as nanowires[284,294] are also used to form nanocomposites. Moreover, composite nanofibers [295,296] are also formed by various techniques to improve the performance of TENGs. For example, Doganay et al. 2021 [285] used Ag NWs to impart conductivity to textiles, then used a TPU lamination to obtain a TPU/Ag NW fabric (Figure 3.10 (c)). Composite fabrics obtained from TPUs performed much better without sacrificing the electronic conductivity, which is also resistant to mechanical bending and washing. Compared with PDMS, PI, Ecoflex and PLA, best triboelectric pair is formed with PLA, in which composite fabrics with higher loading of TPU performed much better than the lighter one (Figure 3.10 (d)).

[285] Kang et al. 2019 [297] also used Ag NWs to form an Ag NW/Polymer hybrid system with PMMA and PVC spin coated onto Ag NW coated substrates (Figure 3.10 (e)). Mesh structure formed by Ag NWs on the top of PMMA or PVC polymer changes the surface potential, making PMMA more tribonegative and PVC more tribopositive. Mechanisms for different triboelectric pairs such as nylon and PFA is given, where AgNW-polymer hybrid can be paired with both tribopositive and tribonegative materials and perform equally good due to the interface created by Ag NWs (Figure 3.10 (f)) [297] Another example of 1D nanostructure is carbon nanotubes (CNT). Kim et al. [298] fabricated PDMS/CNT composite triboelectrification layer, which has increased mechanical and electrical properties due to the addition of CNT. With the additional fluorocarbon plasma etching applied to reveal CNT structures on top of PDMS layer, the triboelectrification is further improved. [298] Last but not least, Pu et al. 2020 [299] introduced aligned zinc oxide (ZnO) NWs into electrospun PVDF and Nylon-11 nanofibers to obtain TENGs. ZnO NW addition to polymeric nanofibers again increased the output performance, on top of increasing the mechanical and thermal stability. [299]

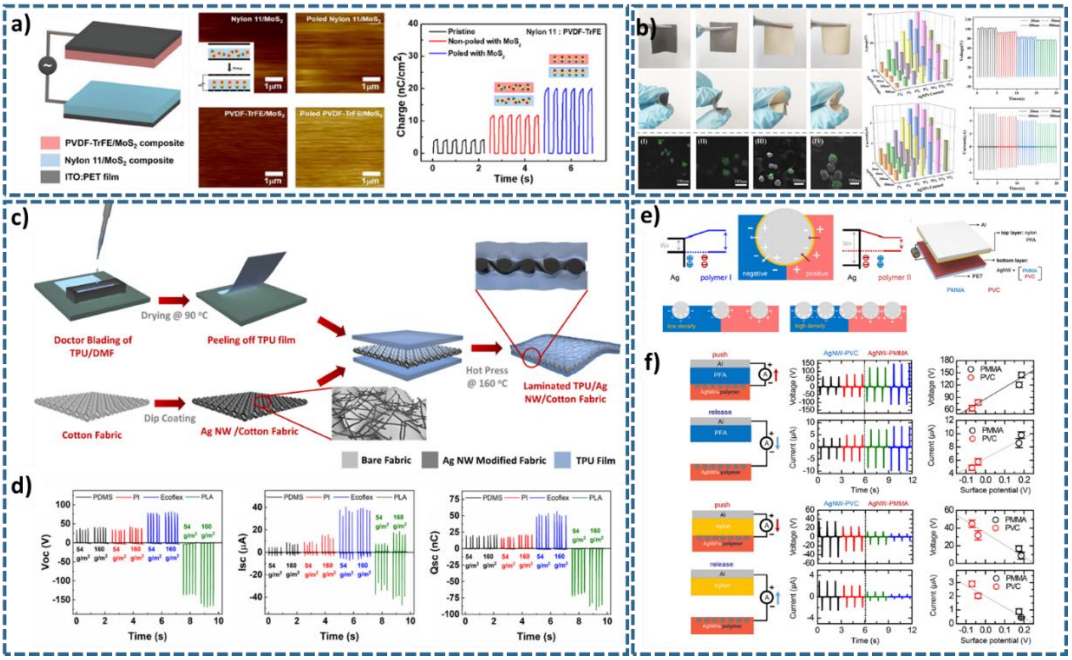

Figure 3.10 Examples of composite structures for TENGs. a) MoS_2 as a microadditive for PVDF-TrFE and Nylon 11, which is paired for TENG. KPFM images of unpoled and poled MoS_2 composites, where poled composites have increased charge generation due to modified surface polarization. [279] b) Introduction of Ag NPs with different sizes and their effect on the triboelectric performance [293] c) Schematic representation of the fabrication of Ag NW-TPU fabric composite. d) Performance metrics of the Ag NW-TPU fabric composite with different triboelectric pairs. [285] e) Schematic representation of charge transfer between PVC and PMMA facilitated by the Ag NWs, where blue region is tribonegative and red region is tribopositive. f) Schematic illustration of the operation mode with different triboelectric pairs and their corresponding performance analysis in terms of output voltage and current. [297]

Lately, the use of 2D nanomaterials for the modification of TENG layers are also on the rise. [272] These include graphene [300,301] , transition metal dichalcogenides (TMDs) [302–304], and titanium carbide, or MXene [305,306]. For example, Shi et al. 2021 [287] introduced graphene nanosheets into electrospun PVDF fibers to improve triboelectrification (Figure 3.11 (a)). Authors found out that graphene nanosheets improve the triboelectric performance due to enhancement of surface potential as determined through KPFM measurements (Figure 3.11 (b)). The surface potential according to the graphene content was optimized that would correspond to the best output performance from PVDF fibers loaded with graphene nanosheets (Figures 3.11 (c) and (d)). Similarly, Hedau et al. 2022 [304] used liquid-phase exfoliated MoS_2 to enhance the surface potential of PVDF. They have seen that the incorporation of MoS_2 sheets promoted the β-phase of PVDF, which have nonzero dipole moments. These newly formed β-phase PVDF was said to increase potential difference between positive and negative charges, resulting in a repressed recombination of these two charges after triboelectrification. This "self-poled" structure was observed via KPFM, which had shown unique distribution of surface charges (Figure 3.11 (e)). According to the loading content and the heat treatment, best performing sample was deduced according to the KPFM (Figures 3.11 (e) and (f)). Most negative surface charge was obtained from MoS_2/PVDF composite heat treated at 170℃. This is attributed to the formation of β- phase of PVDF due to the addition of MoS_2, which has the highest degree of polarization per unit cell. [304] Apart from these general examples, Chen et al. 2022 [307] introduced metal-organic framework (MOF) nanoflakes into silk fibroin for enhanced triboelectrification. It is noted that the MOF nanoflakes increase the capacitive performance of the composite film due to their high aspect ratio – which is possibly forming nanoscale capacitors across the composite, which yielded 9 times better output performance that its bare counterpart. [307]

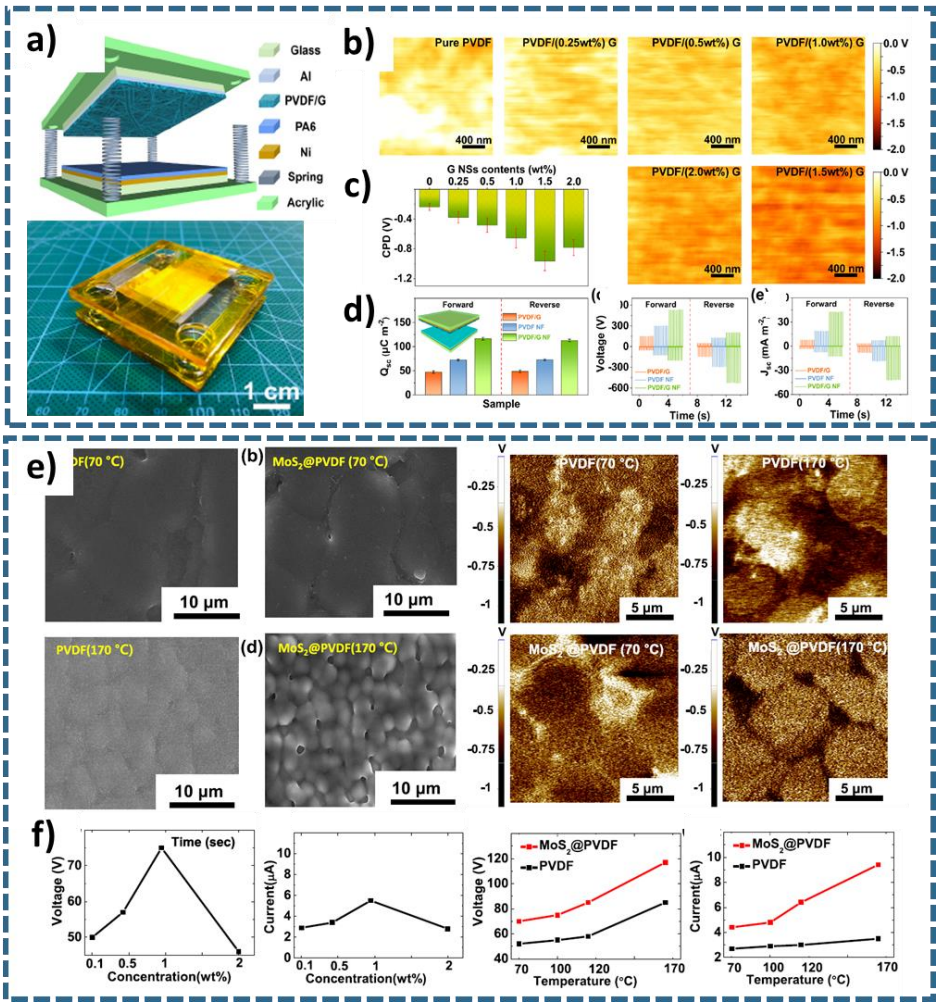

Figure 3.11 Examples of composite structures for TENGs. a) Schematic representation of a TENG device utilizing PVDF fibers loaded with graphene nanosheets. b) KPFM images showing the alteration of surface potentials due to graphene loading. c) Graph corresponding to the surface potentials and graphene loading to PVDF. d) Output metrics of best performing PVDF fiber/graphene nanosheet composites. [287] e) SEM and KPFM images of bare PVDF and liquid exfoliated MoS_2/PVDF nanocomposite layers. f) Performance metrics for the assembled TENGs with respect to different concentrations of MoS_2 and different postannealing temperatures. [304]

3.5 Transient Triboelectric Nanogenerators in Literature

As with the general work done on transient electronics, research on transient TENG devices is also on the rise. Figure 3.12 summarizes some of the latest developments on transient TENGs. Figure 3.12 (a) shows a biodegradable TENG for in-vivo biomechanical energy harvesting. Schematic structure, its triboelectric performance and cell viability analysis is given in the same figure, potentially showing that these TENGs can be a power source for transient implantable medical devices. Biocompatibility of the devices were proven by cell viability tests, where no distinct change from the control group is seen after 7 days. TENG devices were degradable in PBS especially after 60 days, indicating their on-demand transiency (Figure 3.12 (b)). [308] To demonstrate a different transiency mechanism, sunlight triggerable TENGs are also fabricated.[309] Researchers used acid-sensitive poly(phthalaldehyde) (PPHA), and introduced PAGs and photosensitizers (PS). When a UV irradiation was done, PS transfers electrons to PAGs, which released acid that depolymerizes the PPHA. The change in triboelectric performance under UV irradiation is given in Figure 3.12 (c). The degradation is rather fast, and degradation of PPHA films happen under 5 minutes (Figure 3.12 (d)). [309]

TENGs can also be used to promote wound healing and elimination of harmful microorganisms. In such research, Imani et al. [310] designed a transient implantable TENG providing electrical stimulation to eliminate deep tissue microorganisms. The TENGs could be eliminated via ultrasound (US) under the skin. Schematic representation of the implantable TENG and its structure is given in Figure 3.12 (e). *Escherichia coli* and *Staphylococcus aureus* could be eliminated 99% with the fabricated TENGs. Moreover, transiency of the components of the TENG in PBS solution and elimination of the poly(3-hydroxybutyrate-co-3-hydroxyvalerate) (PHBV) under US was shown (Figure 3.12 (f)). Last but not least, Lee et al. [311] designed transient TENG devices that generates electricity at low intensity US, and

disintegrate at high intensities. Schematic illustration of such devices is given in Figure 3.12 (g). The degradation is only triggered at high intensity US (HIS), which allowed a continuous generation at lower intensities. Schematic of the degradation mechanism is also given in the same figure. HIU triggers the mechanical disintegration of the PHBV, which allows the hydrolytic degradation of the devices. Figure 3.12 (h) shows the optical images of the degradation of the membrane when HIU is applied. [311]

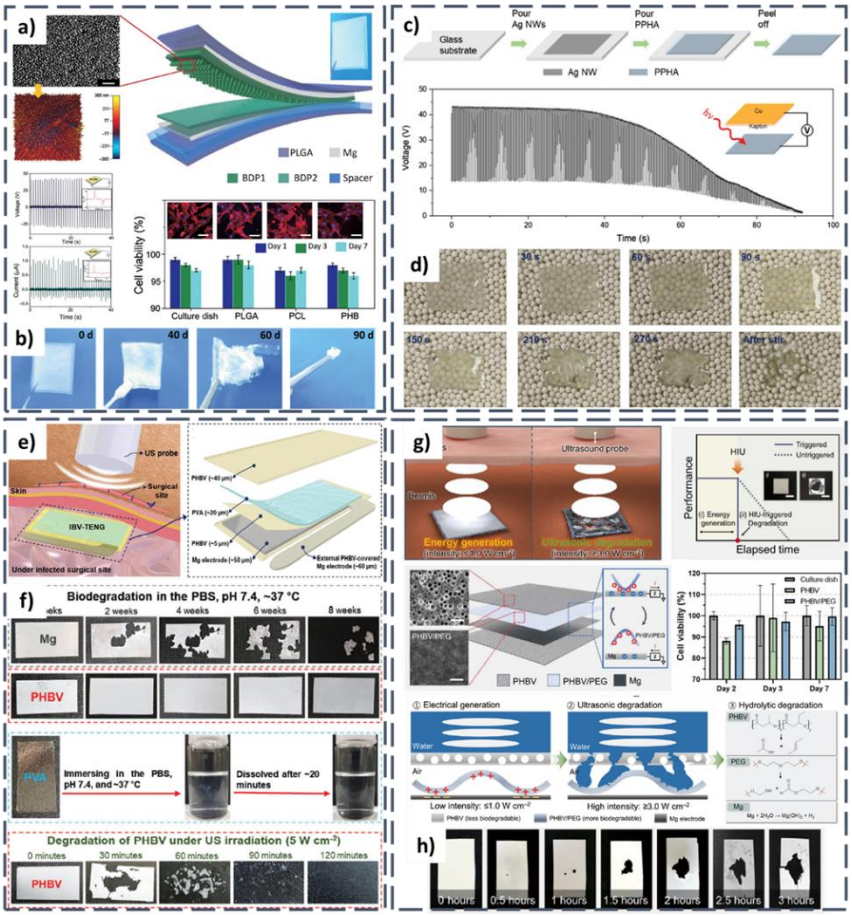

Figure 3.12 a,b) Biodegrable TENGs. a) Schematic structure, performance analysis and cell viability of the biodegradable TENGs. b) Degradation of the TENGs in PBS solution. [308] c,d) Sunlight-triggerable transient TENGs. c) Schematic steps of the fabrication steps and photodegradation of the TENGs with respect to time under UV irradiation. d) Photos showing the photodegradation. [309] e,f) Implantable ultrasound triggerable TENG for subcutaneous antibacterial activity. e) Schematic representation of the subcutaneous activity of TENG for microorganism elimination. f) Biodegradation of the components of TENG in PBS solution and PHBV degradation under US irradiation. [310] g,h) Ultrasound-mediated energy generation for implantable devices. g) Schematic representation of the devices and their performance and degradation under different intensities of US. Cell viability of the devices are also provided. Schematic of electrification shows the electrical generation and degradation at low intensity and high intensity US, respectively. h) US degradation of PHBV layer used for encapsulation. [311]

3.6 Experimental Procedure

3.6.1 Fabrication of the Transient PVA/PSG Based Triboelectric Energy Harvesters (T-TENG).

The PCA electrodes were prepared following the same procedure described in Section 2 and casted using doctor blading method. Electrodes were left to dry overnight. Then, PVA/sucrose/glycerol solution was prepared and casted onto PCA electrodes again with doctor blading method to ensure a thin coating with insulation on the one side of the PCA film. Wet thickness of the overcoat with PSG was 300 µm. Resulting PCA/PSG layer (60 cm^2) was utilized as a single T-TENG electrode. Smaller pieces from the same layer were cut (2.5 cm x 2.5 cm) and encapsulated with additional PSG layer to fabricate self-powered touchpad.

3.6.2 Measurement of the TENG

Performance of the fabricated triboelectric device was measured through hand tapping using a nitrile glove. Open circuit voltage (V_{OC}) and short circuit current (I_{SC}) of the T-TENGs with varying resistances were measured via Keithley 6514/E-Electrometer with a LabView code. The preparation of the electrodes and the respective measurements were made in an air-conditioned room kept at 20 °C and 25% relative humidity.

3.7 Results and Discussion

3.7.1 Characterization of PCA/PSG Single Electrode Transient Triboelectric Nanogenerators (T-TENG)

Harvesting the energy created by human body in motion can be used to power-up small, miniaturized, wearable devices[312–314]. Triboelectrification, defined as electrification due to contact of dissimilar materials, might be very useful in that regard [226,313,314]. Mechanism of charge accumulation and energy harvesting from triboelectricity can be explained using the structure provided in Figure 3.13.

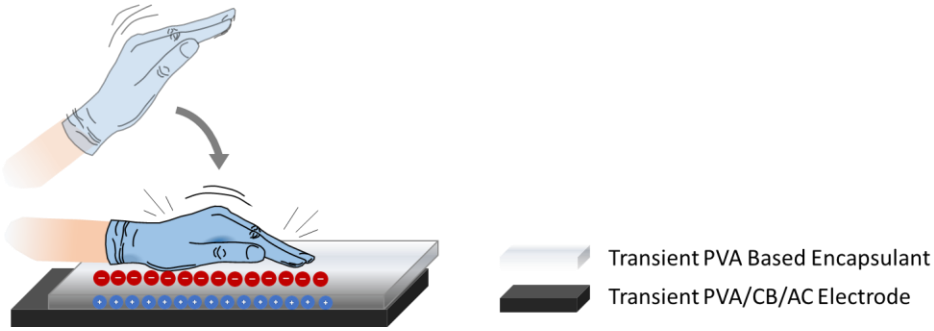

Figure 3.13 Schematic representation and structure of T-TENGs. Reprinted with permission from ref [111], Copyright 2021, Wiley

As explained in the Section 3.6.1, PCA electrodes were overcoated with PSG to obtain a very thin and uniform coating, which effectively insulated the top layer of the electrodes. In this single electrode device, triboelectrification was obtained between this insulating PSG layer and hand, which simply enabled the conversion of mechanical energy into electrical energy [217,315]. The related mechanism is

schematically illustrated in Figure 3.14 (a). Initially, surfaces of the nitrile glove and PCA/PSG layer had zero charges. The surfaces of the nitrile glove and PSG overcoat become oppositely charged upon contact during hand tapping. Following the elevation upon coming into contact with T-TENG, potential difference starts to increase, and the difference reach a maximum when the surfaces are separated by a considerable distance. This change in the potential leads to an electron flow from the electrode to the ground. The electrons start to flow back from the ground to PCA electrode when the nitrile glove approaches to PSG overcoat again, resulting in an alternating current due to reversed potential. This alternating current is regularly generated upon repetitive tapping and separating processes. Based on this mechanism, open circuit voltage (V_{OC}) and short circuit current (I_{SC}) of the fabricated TENG electrodes were collected via hand-tapping and obtained values are shown in Figures 3.14 (b) and (c), respectively. A maximum V_{OC} and I_{SC} of 21.6 V and 4.6 µA, respectively, were obtained from the fabricated electrodes with a size of 60 cm^2, proving that transient PCA/PSG layers are highly promising for energy harvesting and self-powered applications. Respective voltage and current plots in varying loads are provided in Figure 3.14 (d), which were used to calculate output power with respect to different loads. A maximum output power of 2.2 $mW.m^{-2}$ was obtained at a resistance of 50 Mohm. Fabricated PSG/PCA layers were used to light up serially connected white LEDs arranged to show “METU”, and associated images are provided in Figures 3.14 (f)-(i). Fabricated T-TENG single electrode device allowed 86 LEDs to light up at the same time through simple hand-tapping.

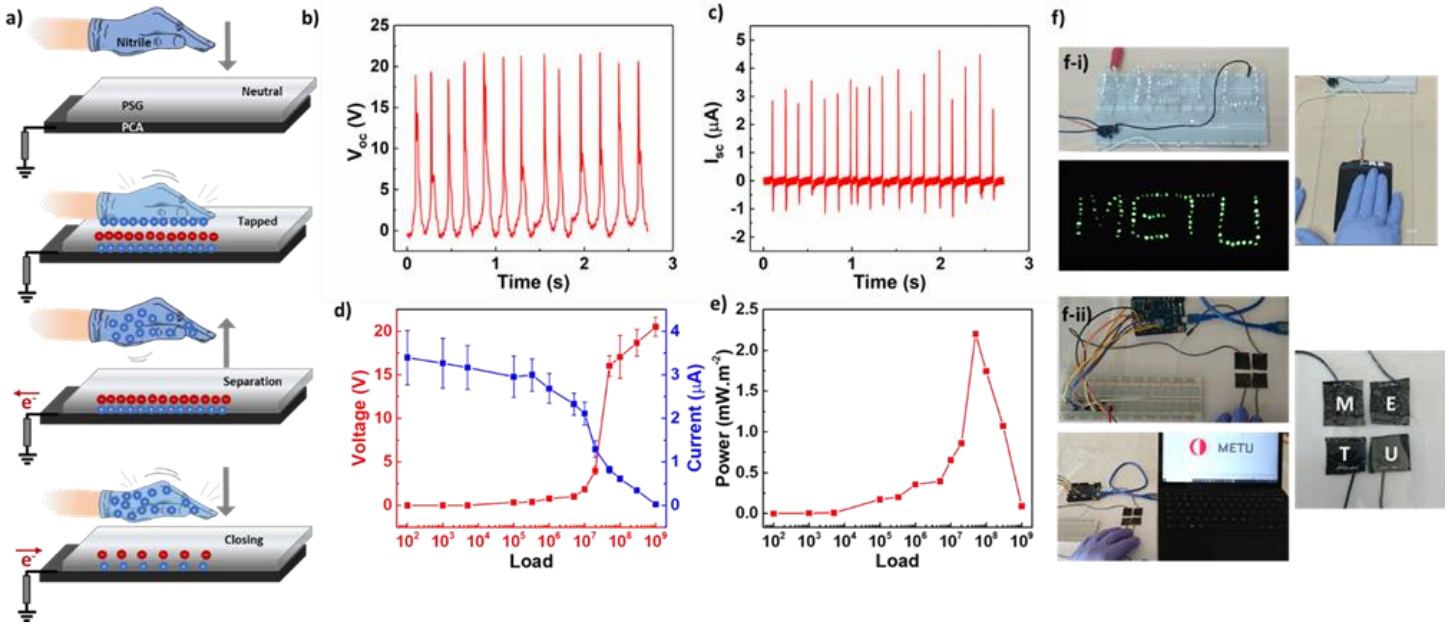

Figure 3.14 a) Mechanism of single-electrode triboelectrification via hand-tapping. b) Open circuit voltage and c) short-circuit current of PCA/PSG layers in operation. d) Output voltage and current values obtained using different load resistors and e) the resulting power generated. f-i) Photos of serially connected 86 white LEDs lit with hand-tapping the PCA/PSG layers. f-ii) Triboelectric self-powered keyboard demonstration with PCA/PSG layers where each electrode is assigned to one letter to write “METU”. Reprinted with permission from ref [111], Copyright 2021, Wiley

The output performance of T-TENG was also explored under different separation frequencies, and corresponding Isc and Voc values of the devices are provided in Figures 3.15 (a) and (b), respectively. I_{SC} roughly increased from 0.6 µA to 4 µA upon increasing the frequency from 1 Hz to 5 Hz, respectively. The deviations in the maximum currents are due to uneven hand tapping, especially at higher frequencies. V_{OC}, on the other hand, increased from 10 to 20 V upon increasing the frequency from 1 to 4 Hz, respectively, and reached a saturation point at 4 Hz. Although the variation in V_{OC} is not expected theoretically [85], increased frequency inevitably increased the force applied to T-TENGs during hand-tapping. Figure 3.15 (c) shows that the short circuit charge at a hand-tapping frequency of 4 Hz is roughly 10 nC. The robustness of the T-TENG was measured by monitoring changes in V_{OC} under continuous hand-tapping at 4 Hz for 4 minutes. The resulting data are plotted and provided in Figure 3.15 (d). No significant decrease in V_{OC} was observed during the 4 minutes of measurements, showing the mechanical robustness of the fabricated T-TENGs. To further investigate the robustness of T-TENGs, the changes in V_{OC} was monitored for the same T-TENG sample after 3 months of fabrication. Results are compared in Figure 3.15 (e). No obvious change in V_{OC} was observed, indicating the chemical robustness of the fabricated T-TENGs.

With the same T-TENG, it was possible to charge capacitors with capacitance values ranging from 1.0 to 4.7 µF. The charging curves are provided in Figure 3.16 (a). In order to demonstrate another use of T-TENGs, fabricated PCA/PSG layers were used as a self-powered keyboard. Fabrication was done through cutting the T-TENGs into small pieces followed by the contact formation, simply practiced by an office stapler and copper wire. A simple Arduino code was used to detect the voltage spikes resulted from touching the electrodes, and each electrode was assigned to a single letter (either M or E or T or U). Photos of this proof-of-concept transient and self-powered T-TENG device are provided in Figures 3.14. The voltage response for touch detection is given in Figure 3.16 (b). The constructed Arduino system enabled

the detection of voltage change, and puts down the related letter that is affiliated with the button via coding. These results revealed the potential of transient electronics fabricated using simple and all PVA-based structures.

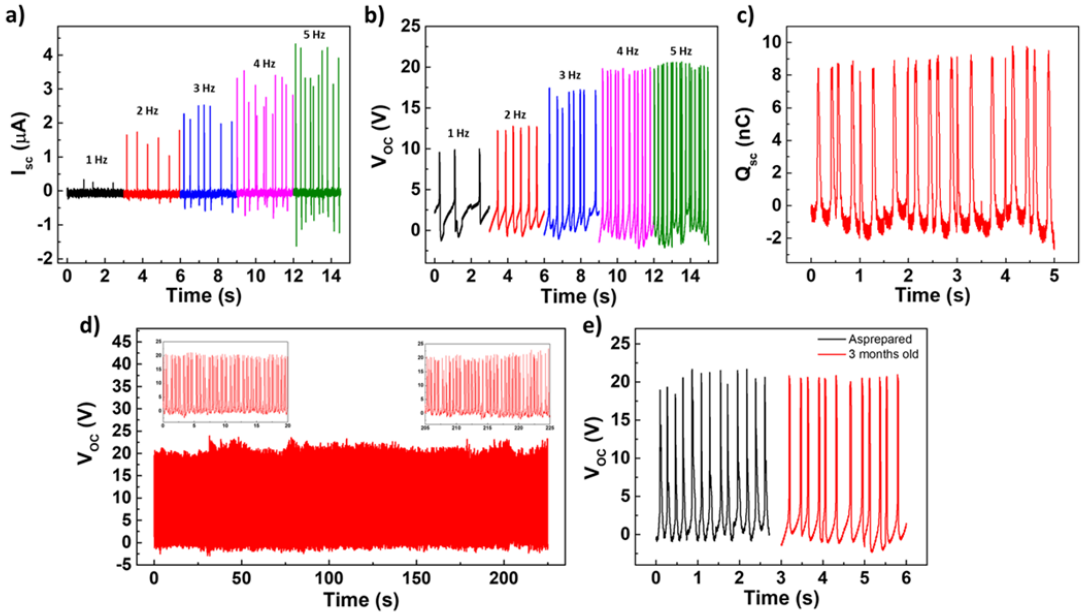

Figure 3.15 a) Short circuit current and b) open circuit voltage of T-TENG with respect to hand-tapping frequency. c) Short circuit charges (Q_{sc}) of T-TENG. d) Robustness of T-TENG via continuous hand-tapping at a frequency of 4 Hz. Insets show the first and last 20 measurements. e) T-TENG performance change in means of open circuit voltage after 3 months of fabrication. Reprinted with permission from ref [111], Copyright 2021, Wiley

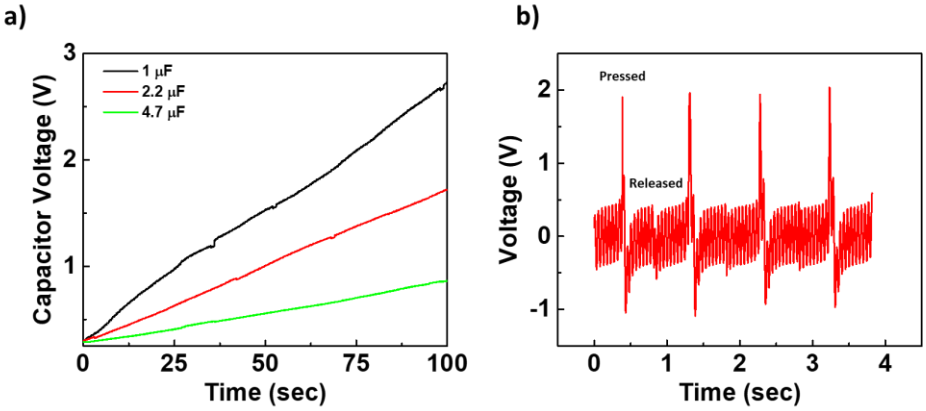

Figure 3.16 a) Charging curves of different sized capacitors. b) Voltage response curve of self-powered touchpad upon pressing and releasing a button. Reprinted with permission from ref [111], Copyright 2021, Wiley

Comparison of the fabricated T-TENGs with those triboelectric nanogenerators in literature including carbon-based, PVA-based and transient ones are provided in Table 3.1. While the output performance of most TENG articles in literature are better, they do not offer any transiency. Among the transient TENGs; however, T-TENG provides one of the best performances on top of immediate transiency when triggered with aqueous solutions. Moreover, despite its immediate transiency in water, it is proven that the TENG stable over 3 months in the ambient conditions (Figure 3.15 (e)), which shows a promising on-demand transiency use case. All in all, reported performance of T-TENGs allowed fabrication of self-powered transient devices that can be readily used in transient electronics.

Table 3.1 Comparison of the fabricated T-TENGs with those triboelectric nanogenerators in literature including carbon-based, PVA-based and transient applications.

Materials	**Triboelectric Mode**	**Transiency Mode**	**Open Circuit Voltage (V)**	**Short Circuit Current (µA)**	**Charge (nC)**	**Power Density**	**Ref.**
PVDF and PVA as negatively and positively polarized triboelectric materials Al foil as current collector	Contact Separation – Two Electrodes	No transiency	230 V	6 µA	-	3.1 W m^{-2}	[316]
Cellulose/PVA hydrogel as triboelectric layers VHB films as spacer Copper foil as current collector	Contact Separation – Single Electrode	No transiency proposed	41 V	500 nA	15 nC	-	[317]
PVA combined with PPA-PEI and PVDF as triboelectric layers	Contact Separation – Two Electrodes	No transiency	28.8 V	62.3 µA	-	112.3 mW m^{-2}	[108]
AgNWs as current collector Silk protein as the triboelectric layer	Contact Separation – Single Electrode	Biocompatible No transiency proposed	110 V	0.1 µA	-	2 mW m^{-2}	[318]
AgNW and CNT current collectors Sodium lauroyl glutamate as dielectric layer PMMA/PTFE as the triboelectric layer	Contact Separation – Single Electrode	Dissolvable in water and oil in 1 minute	13.8 V	425 nA	-	250 µW m^{-2}	[319]
Bacterial cellulose as dielectric layer Bacterial cellulose/CNT/PPy layers as electrodes	Contact Separation – Sandwich Structured Single Electrode	Recyclable yet no transiency is shown	29 V	0.6 µA	-	3 µW	[43]
Mg foil as current collectors Electrospun PLA and nanostructured gelatin as triboelectric layers	Contact Separation – Two electrodes	Biodegradable and dissolvable in water in 20 days	500 V	10 mA cm^{-2}	-	5 W cm^{-2}	[320]
PVA and PLGA as triboelectric layers AgNW as current collector	Contact Separation – Single electrode	Biodegradable and dissolvable in PBS in 40 days	~95 V	~ 1.5 µA	~30 nC	130 mW m^{-2}	[321]
PCA layer as current collector PSG layer as triboelectric layer Additional PSG layer as encapsulant	Contact Separation – Single electrode	Biodegradable and water soluble Immediate transiency	21.6 V	4.6 µA	10 nC	2.2 mW m^{-2}	**This Work**

CHAPTER 4

TRANSIENT CAPACITIVE SENSORS

4.1 Introduction to Wearable Electronics and Pressure Sensors

Mankind is always fascinated by the prospect of wearable electronics, ranging back to the 1950s with comics and movies such as The Jetsons or James Bond. The best known is presented in Star Trek series back in the 1960s, where the characters wore communicators that had sensors and allowed communication. Note that handheld tablets and virtual reality rooms were also commonly used in Star Trek series. Such as these, there are lots of visionary concepts both in literature and entertainment that pushes the progression of humankind. In the case of wearable electronics, the first realization was done with Z-Glove and DataGlove (Figure 4.1 (a)). [322] Inventors Thomas Zimmerman and Jaron Lanier were able to fabricate what they call a "hand to machine interface device", where they could capture the hand gestures and position of the hand in real-time. Z-Glove employed ultrasonic positioning and orientation system that worked with Commodore 64 systems, while DataGlove used magnetic positioning that worked with Apple Macintosh. [322] Nintendo's Power Glove, released in 1989, was developed on the patent of DataGlove for the hand gestures but added functionalities to be an entertainment system. Images in Figure 4.1 (b) show the structure and example gestures for the input commands. [323] Although visionary, the system was very complex to control especially back then, and the games that can be played were very limited. With a similar futuristic dream, Ivan Sutherland [324] proposed a "head-mounted three-dimensional display" (later called as *The Sword of Damocles*). It is recognized as one of the first virtual reality

(VR) systems that use miniature cathode ray tube (CRT) with display optics (Figure 4.1 (c)). The optic system enabled the CRT displays to be magnified. Moreover, head motions were also tracked via mechanical arm and ultrasonic head position sensor. [324] After approximately 50-60 years from these cornerstones, VR systems such as Oculus Rift, with augmented VR capabilities for both head and hand movements that can receive commands, are among the consumer electronics. [325]

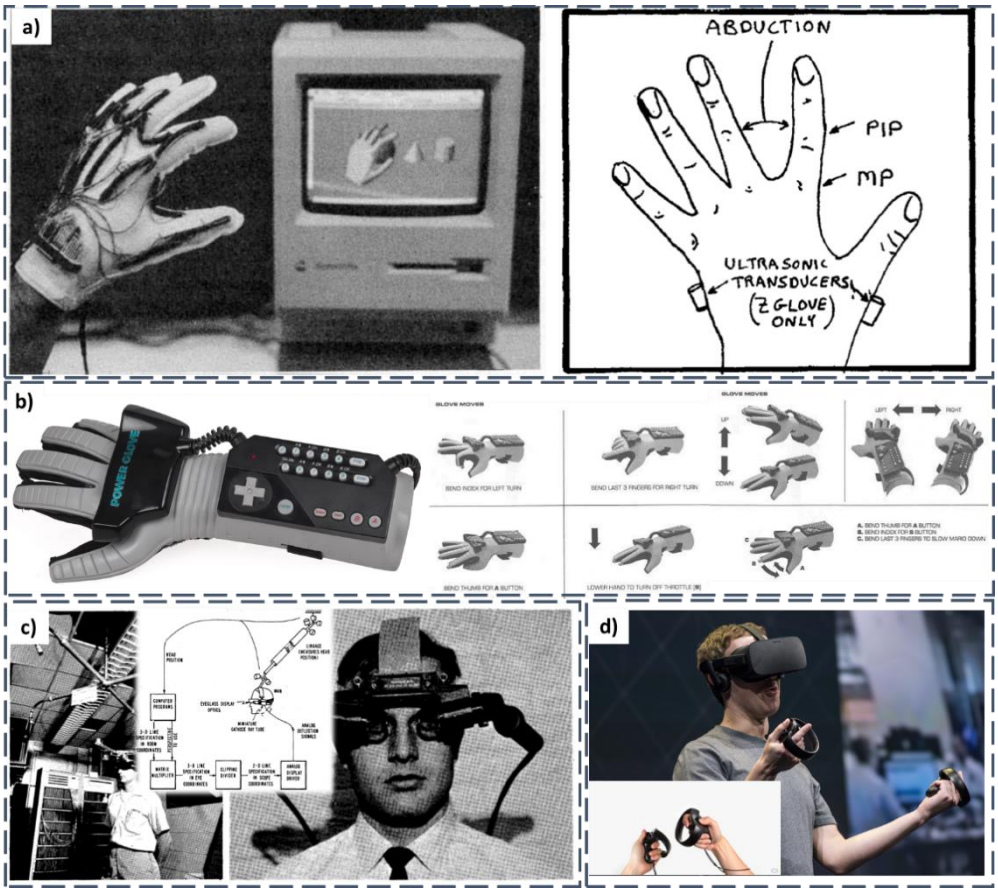

Figure 4.1 Technological advancement of wearable electronics from then to now. a) Structure of the DataGlove that can sense the hand gesture movements.[322] b) Power Glove produced for Nintendo Entertainment systems and typical hand gestures to input different commands. c) One of the earliest examples of VR system and its mechanism. [324] d) Oculus Rift. [325]

Wearable pressure sensors are part of this progression. Tactile sensors, which cover pressure and strain sensors alike, allow mechanical inputs into digital information. This can be used to process environmental sources such as pressure, strain, distortion, and acceleration [326] With the advancements shared in Figure 4.1, pressure sensing has been an active field of research. The research is diversified into many regions, from designing new systems to integrating with other devices, improving sensitivities, and developing new materials and fabrication techniques. Therefore, the research field for tactile sensing requires an interdisciplinary approach, including electronics, materials science, system engineering, and even robotics. [327]

The interdisciplinary nature of the pressure sensors can be understood more easily with the given schematic in Figure 4.2. Wearable pressure sensors find applications in three main areas: human-machine interfaces, robotics, and physiological signal monitoring. However, due to their interdisciplinary nature, these distinctions between the different areas are not sharply defined. Human-machine interface (Figure 4.2 (a)) can actually be coupled with robotics (Figure 4.2 (c)) to obtain gesture-mimicking robotics (Figure 4.2 (b)). Robotics can be coupled with physiological sensors (Figure 4.2 (e)) to obtain applications such as prosthetic robotic arms that move regarding to body signals (Figure 4.2 (d)). Physiological signal sensors can be used with human-machine interaction tools to fabricate bimodal sensors (Figure 4.2 (f)). As it can be understood here, the future of pressure sensors is an amalgamation of disciplines, fostering groundbreaking advancements that can surpass conventional means.

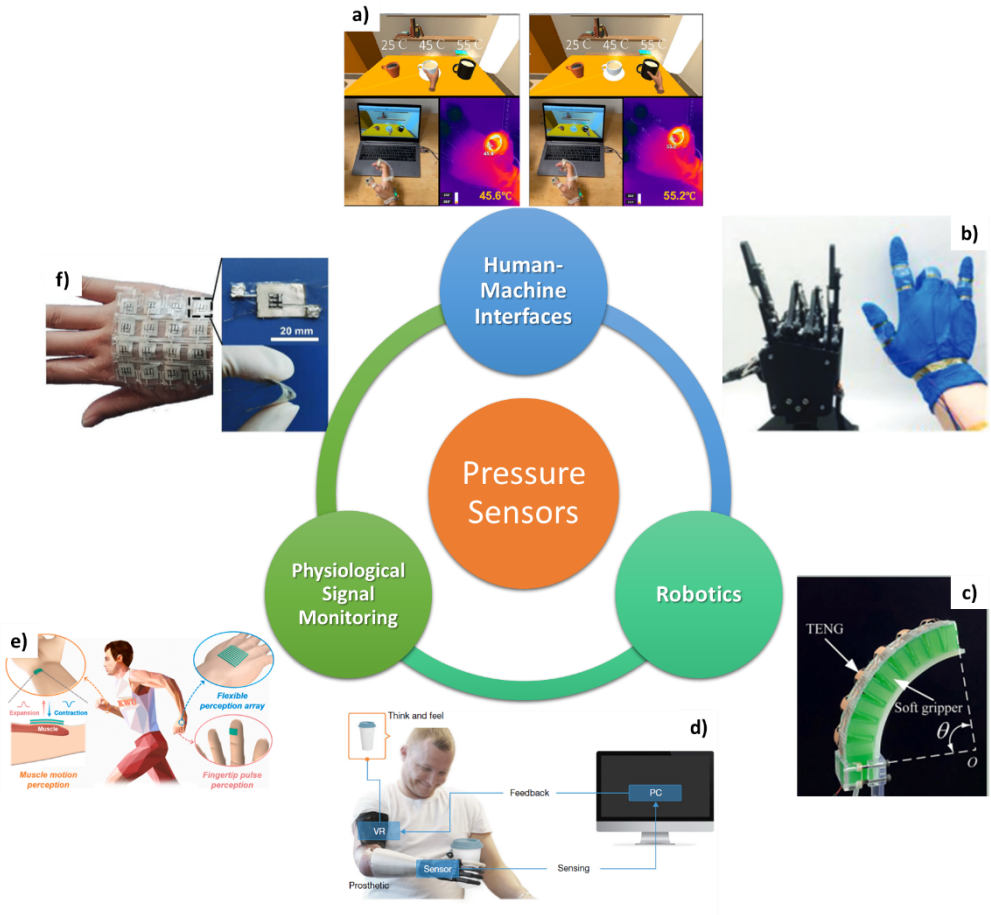

Figure 4.2 Main usage areas of pressure sensors and their related applications. a) Thermo-haptic feedback. [328] b) Controlling robotic arm using hand gestures. [329] c) Robotic gripper grasping system sensor. [330]. d) Prosthetic arm with an epidermal VR [331]. e) Tactile sensor for physiological signal sensing. [332] f) Bimodal sensor array attached on hand [333].

4.2 Mechanisms used in Pressure Sensors

Pressure sensing can be practiced using different mechanisms. Piezoresistive, piezoelectric, triboelectric, and capacitive are the four main mechanisms used in pressure sensors. The following sections will cover all mechanisms, while capacitive will be more detailed to align with this chapter's subject. The effect of selected mechanisms on different aspects of the pressure sensors are provided in Table 4.1. Although iontronics are primarily utilized in capacitive sensing, it is worth noting that they have diverse applications beyond this field. Therefore, iontronics will be integrated into the other four main mechanisms.

Table 4.1 Pressure sensing mechanisms and their performance in related aspects. Adapted from [334].

Aspects	**Piezoresistive**	**Piezoelectric**	**Triboelectric**	**Capacitive**	***Iontronic***
Sensitivity	Medium	High	Medium	Low	*High*
Noise	High	Low	Low	Low	*Low*
Anti-interference	High	High	High	Low	*High*
Static Force Response	Yes	No	No	Yes	*Yes*

4.2.1 Piezoresistive Pressure Sensors

Among other working principles, piezoresistive behavior is the simplest mechanism to achieve and has the easiest fabrication. [335] Piezoresistive sensors simply convert the change in resistance value as an output signal under different mechanical distortions to realize the sensing mechanism. [336] For composite structures with conductive fillers, when the pressure is applied, percolation of the conductive filler network increases – hence the piezoresistive mechanism is achieved. When pressure is applied to ionic polymers, the effective thickness of the polymer decreases, leading to increased conductivity and reduced resistance.

One of the earliest and great examples is the study done by Paradiso et al. [337] in 2005, which used simple stainless steel (SS) wires that were twisted around viscose yarn, and use hydrogel membranes to improve the signal quality. Figure 4.3 (a) shows the "WEALTHY" system on the human body, with placements and internal structure. The fabricated textiles were excellent at collecting body signals such as ECG, Einthoven, precordial, respiration, and movement (Figure 4.3 (b)). [337]

Sponge systems are quite popular with piezoresistive systems. A polyurethane/graphene sponge demonstrated by Yao et al.[338] in 2013 also used as a piezoresistive sensor, to detect the spatial distribution of the applied pressure. The expected mechanism was given schematically and observed via SEM images, showing the increased percolation in the sponge system (Figure 4.3 (c)). Inset shows the simulated conditions where red dots show the percolation points, which increases substantially with applied pressure. Figure 4.3 (d) shows the fabricated artificial skin, which can detect the distribution of applied pressure. [338] Even though it was conducted 8 years later, a remarkably similar study showed that it still relies on the same percolation theory for piezoresistive sensing. A polyimide nanofiber/MXene composite aerogel is fabricated which can be compressed, flexed, and twisted easily

with no damage (Figure 4.3 (e)). The working mechanism given in Figure 4.3 (f) is a simplified version of the mechanism of the simulation shared in Figure 4.3 (c). The aerogel sponge had an excellent sensitivity to the applied strain and was stable through different rates of compression-relaxation (Figure 4.3 (g)). [339]

Iontronic systems, as mentioned at the beginning of this section, got very popular over the last decade. [334] Although mostly worked in capacitive mode, it is possible to construct a piezoresistive sensor through ionic hydrogels. One such example fabricated chemically crosslinked methacrylated carboxymethyl cellulose (CMC) with the addition of NaCl to obtain pressure sensors. [340] A schematic representation of the fabrication process, which involves photopolymerization, is provided in Figure 4.3 (h). Figure 4.3 (k) shows the fabricated hydrogel which can be stretched up to 100% of its original length. These flexible and stretchable hydrogels can be used to monitor pulse with great accuracy, showing that ionic hydrogels are very promising as piezoresistive sensing. [340]

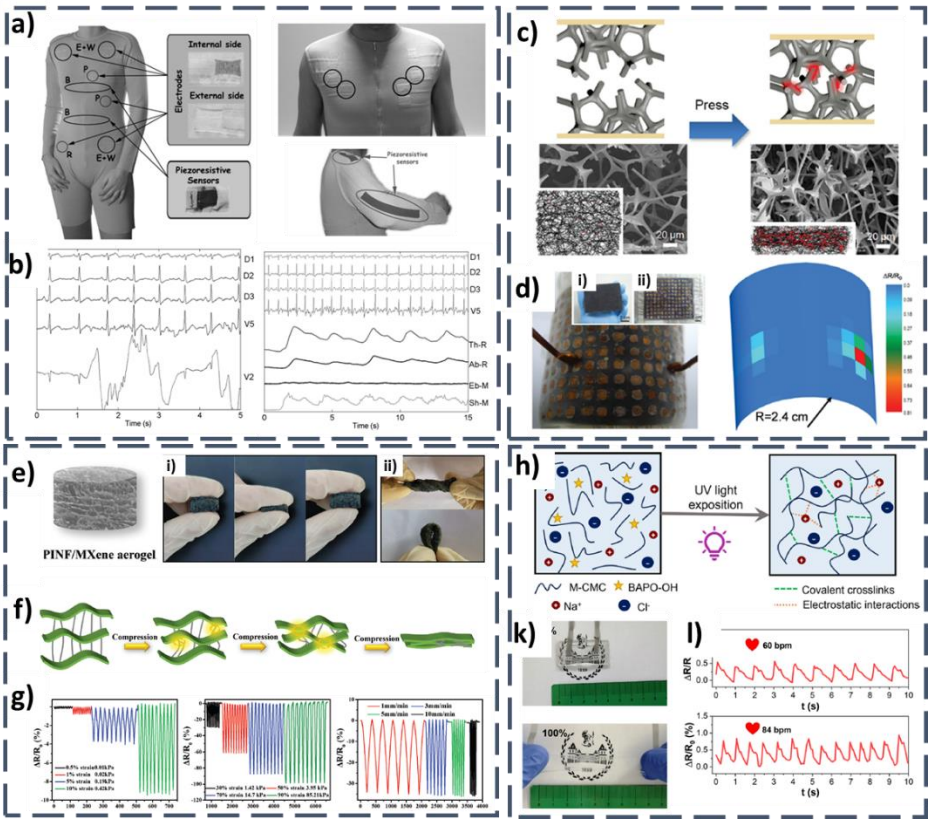

Figure 4.3 Piezoresistive sensors a-b) Wearable full-body health care system based on knitted textiles. a) Prototype model of E+W, Einthoven and Wilson; R, reference; P, precordial leads, B, breathing sensors. Inset shows the knitted piezoresistive sensors. Sensors can be attached to the chest for impedance pneumography and arms for motion sensing. b) (Left) ECG signals from the left shoulder (Right) Body signals including Einthoven, precordial, respiration, and movement. [337] c-d) Pressure-sensitive graphene-polyurethane sponge. C) Schematic of the working mechanism of the sponge and its relative SEM images. Insets show the simulation of the resting and pressed conditions, where red dots show the percolation points. d) Artificial skin made from the foam in flexed condition and its mapping profile. Inset i) shows the large area of sponge used ii) shows the as-fabricated state. [338] e-g) Polyimide fiber/MXene composite aerogel as a piezoresistive sensor. e) Schematic structure and mechanical demonstrations of the aerogel. i) under pressure, ii) twisting and bending. f) Mechanism of compression and change in the structure g) Response of the aerogel under different pressures. [339] h-l) Piezoresistive ionic hydrogels. h) Schematic illustration of CMC-based hydrogel structure. k) Photos of hydrogels without and with stretching. l) Pulse monitoring with the hydrogels. [340]

4.2.2 Piezoelectric Pressure Sensors

Compared to other sensing mechanisms, piezoelectric pressure sensors offer superior energy conversion efficiency and simpler architectural requirements. [341] First discovered by Curie brothers in 1880, piezoelectric materials separate positive and negative charges under applied mechanical stress. [342] This phenomenon is originated from the ionic structure in certain materials, where the applied mechanical force changes the equilibrium in the system, which causes polarization in the crystalline structure.[341] The biggest disadvantage of the piezoelectric sensors, as given in Table 4.1, is that there is no static sensing. The charge separation and hence the voltage/current output solely depends on mechanical perturbation, which does provide a static signal in relaxed conditions. [334,342]

One of the earliest examples of piezoelectric pressure sensors is shown by Professor Zhong Lin Wang's group in 2008. A pressure sensor based on an individual ZnO piezoelectric wire is fabricated. An ultralong ZnO wire is fabricated via a high-temperature thermal evaporation process. ZnO wire is bonded to a polystyrene (PS) substrate and contacts are taken from two ends (Figure 4.4 (a)). Photos of the sensor and the schematic of the measurement system are also provided in Figure 4.4 (a). The sensor worked both in compression and stretching modes under a fixed bias of 2 V with excellent stability and fast response. [343] Dagdeviren et al. [344] used lead zirconate titanate (PZT), which is a ferroelectric/piezoelectric material, for cutaneous pressure monitoring. The PZT array is fabricated and connected to silicon nanomembrane (SiNM) n-MOSFET to amplify the signals. Schematic of the device structure and its photograph are given in Figures 4.4 (c) and (d). The monitoring of blood pressure and pulse exhibited exceptional accuracy and high levels of sensitivity (around 0.005 Pa) and very fast response times (around 0.1 ms). Combination with the MOSFET allowed very clear signals, which actually enabled the researchers to collect even the subtlest effect on the surface of the skin. [344]

The morphology can also be controlled to improve the pressure-sensing capability of piezoelectric materials. One such example was demonstrated by Ha et al. [345] included bioinspired micro and nanostructured ZnO NW arrays. The schematic structure of the piezoelectric pressure sensor with interlocked hierarchical structure, and its SEM images are given in Figures 4.4 (f) and (g). The interlocked hierarchical structure resulted in increased piezoelectric generation as every ZnO nanowire flexed against the others (Figure 4.4 (h)). Figure 4.4 (k) illustrates the contrast between a basic planar piezoelectric current generation and a hierarchical structure. The latter demonstrates a nearly two-fold improvement in performance under identical pressures. [345]

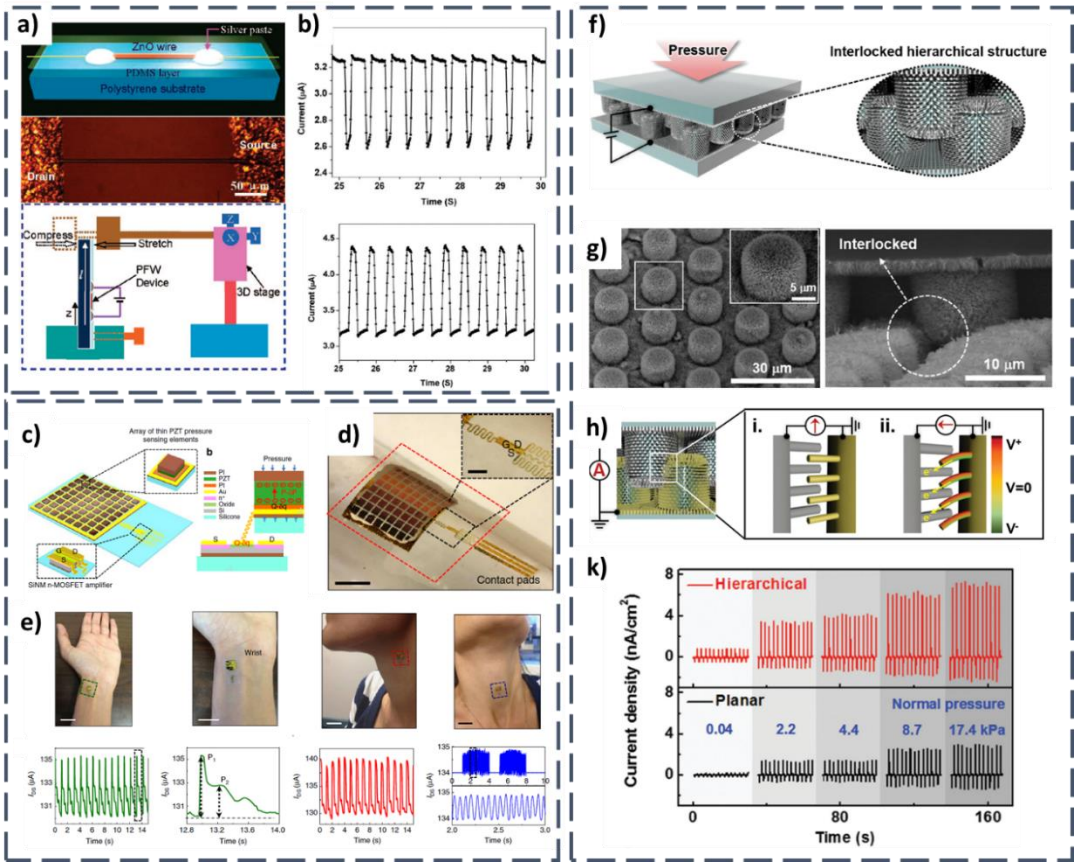

Figure 4.4 a-b) Piezoelectric sensor based on a single ZnO wire. a) Schematic structure of the device, its photo, and schematic representation of the measurement system. b) Current response under (top) compression and (bottom) strain. [343] c-e) PZT based piezoelectric pressure sensor for pulse and blood pressure monitoring. c) Schematic structure of PZT array. d) Photo of the PZT array. e) Various placements of the PZT array and its relevant signals. [344] f-k) Hierarchical micro-nano structured ZnO nanowires for pressure sensing. f) Schematic representation of the interlocked hierarchical structure. g) SEM images of the micro-nano structured ZnO nanowires and their pressed state. h) Mechanism of piezoelectric generation based on the hierarchical structure. k) Output current density in the case of planar and hierarchical structures. [345]

4.2.3 Triboelectric Pressure Sensors

Triboelectric nanogenerators are one of the latest additions to pressure sensing applications. The working mechanism of TENGs is explained in detail in Section 3.2. Simply put, the triboelectrification's current or voltage output can be linked to mechanical stress, with the output's magnitude serving as an indicator of stress level. The most common mechanisms to realize triboelectric pressure sensing are contact separation and single electrode modes. [346] Although promising, the required architecture is rather complex compared to the other sensing mechanisms. In addition, triboelectric pressure sensors share the same drawback as piezoelectric pressure sensors, as electrification only occurs upon impact, resulting in the unavailability of static force response. [334]

The most iconic triboelectric pressure sensor study that has been subject to many review articles was conducted by Fan et al.[347] in 2012 where PDMS is patterned with different Si molds. Microstructures of lines, cubics, and pyramids were achieved via molding. In Figure 4.5 (a), the micropatterning process and corresponding SEM images are displayed, showcasing the lines, cubics, and pyramid shapes that were produced. Interestingly, the pyramid shapes demonstrated the most impressive triboelectric performance when sensing liquid droplets. In fact, they were capable of detecting even the slightest feather drop, as illustrated in Figure 4.5 (b). [347] Figure 4.5 (c) shows a novel way of femtosecond laser patterning to obtain varying patterns on PDMS. Schematic shows how gaussian pulses can have different shapes with different depths. Figure 4.5 (d) gives the depth profile and the gradual change in the microstructure. These structures could easily detect different pressures of airflow as well as pulse detection (Figure 4.5 (e)). [348]

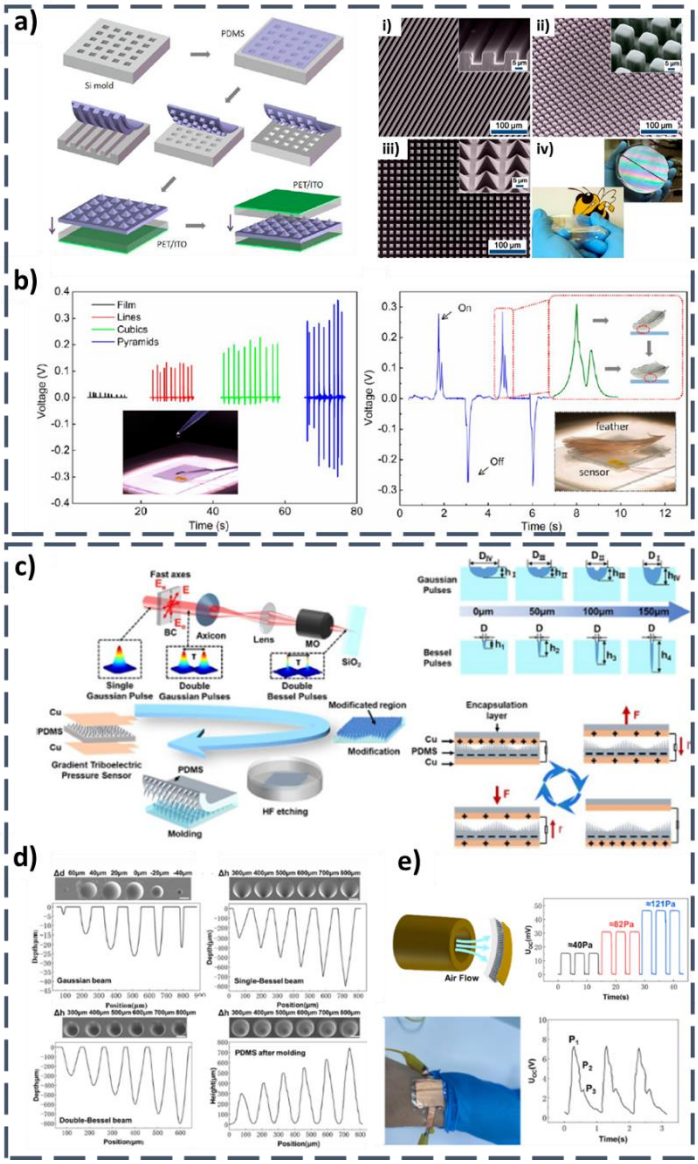

Figure 4.5 a-b) Micropatterned PDMS layers for triboelectric pressure sensing. a) Schematic of the fabrication route for micropatterned PDMS. SEM images of i) lines, ii) cubics, iii) pyramids obtained on the PDMS surface. iv) Shows the stretchability of the PDMS layers. b) Triboelectric performance of pressure sensing with the micro patterns. [347] c-e) Varying pattern obtained through femtosecond laser and its pressure sensing. c) Schematic representation of the fabrication route and the schematic representation of the shapes that can be achieved via this route. d) Micropatterns and their variation that can be achieved with different techniques. e) Pressure sensing performance under airflow and pulse monitoring. [348]

4.2.4 Capacitive Pressure Sensors

Capacitive pressure sensing is one of the most commonly used mechanism for pressure sensing. Compared to other mechanisms, it is very easy to obtain high sensitivity in this method. One major drawback of capacitive sensors is their sensitivity to ambient conditions which may result in high noise or change in the sensitivity. [334,342]

4.2.4.1 Working Mechanism of Capacitive Sensors

Capacitive sensors for pressure sensing rely on simple parallel-plate capacitor structure, which is shown in Figure 4.6 (a). When a voltage v is applied, the parallel metal plates are charged with +q and -q, respectively (Figure 4.6 (b)). The amount of the charge is proportional to the applied voltage. *Capacitor* is said to store this electrical charge, which is

$$q = Cv \quad (4.1)$$

,where C, the constant of the relation between electrical charge and v, is known as *capacitance*. The unit is farads (F), which is coulomb/volt. Although q and v are dependent on each other, C does not simply depend on them. The capacitance value depends on the physical dimensions and the dielectric permittivity;

$$C = \varepsilon_0 \varepsilon_r \frac{A}{d} \quad (4.2)$$

,where ε_0 is the permittivity of space, ε_r is relative permittivity, A is the area of electrodes, d is the distance between the plates, and C is the capacitance.

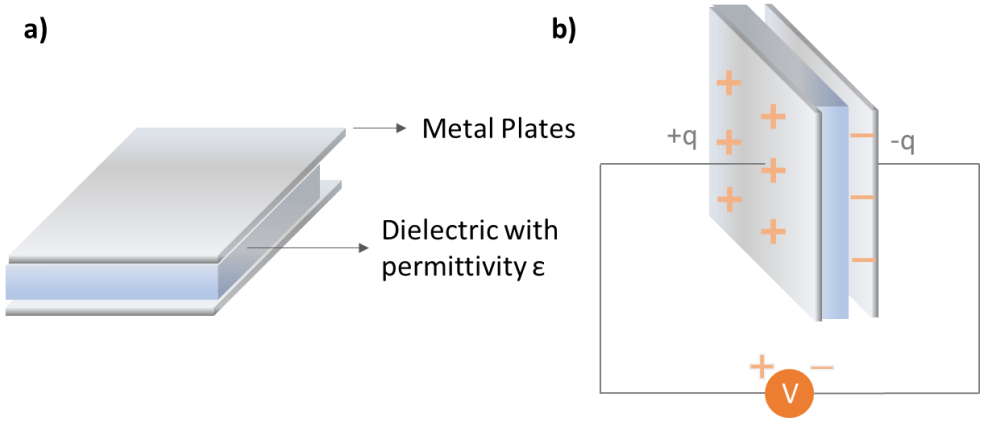

Figure 4.6 a) A typical capacitor structure. b) A polarized capacitor with an applied voltage.

When the dielectric becomes an ionic medium, the material chosen for electrodes can also alter the capacitance. If EDLC is the mechanism, utilizing high surface area electrodes, like activated carbon, increases the capacity for ionic charges to be adsorbed onto the electrode surface, effectively enhancing the capacitance. Thus, adsorption on the surface of the electrode and ionic species can change the capacitance values – which is effectively called a supercapacitor. If the ionic species-electrode couple has surface-limited faradaic reactions under applied voltage, which is called pseudocapacitors, capacitance is effectively increased even more compared to EDLC but starts to be a diffusion-limited process. The working mechanisms are explained in detail in Section 3.2.

Depending on the supercapacitive working mechanisms, the electrode becomes very important for capacitive sensors. This is especially correct for the subsection that emerged, which is called *iontronics*. [334] The choice of the electrode material is an aspect that is often overlooked but holds significant importance, particularly when working with ionic dielectrics.

4.2.4.2 Materials for Capacitive Sensors and Improvement Strategies

Overall strategies to improve the sensitivity values of capacitive sensors are given in Figure 4.7. Micro-nano structuring of electrodes and dielectrics, using porous or ionic dielectric layers, obtaining composite dielectrics, and choosing appropriate electrode materials are the general routes for obtaining better sensitivities. These will be explained in the following sections under “Dielectrics” and “Electrodes”.

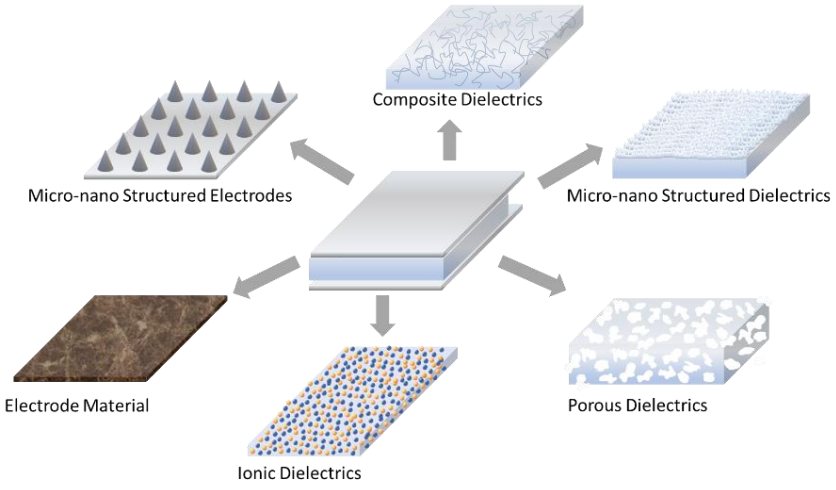

Figure 4.7 Strategies to improve the sensitivity of capacitive pressure sensors.

4.2.4.2.1 Dielectrics for Capacitive Pressure Sensors

The initial idea to manipulate the sensitivity mechanism for the capacitive pressure sensors is the modification of the dielectrics. Apart from using thin layers of ceramics or polymeric layers, one can have porous and compressible dielectrics, add nanostructuring, or use ionic polymeric layers to enhance the sensitivity. Improving the dielectric permittivity by itself is not a solution, since the sensitivity of a capacitive pressure sensor is;

$$S = \frac{\Delta C/C_0}{\Delta P} \quad (4.3)$$

where S is the sensitivity and C_0 is the initial capacitance of the device. The change in capacitance, ΔC, with respect to change in loading, ΔP, is measured. [349] This mechanism can easily be controlled by adding micro-nano structuring on the dielectric layer or using porous dielectric such as aerogels or foam structures. In this way, initial dielectric permittivity becomes dependent on the volume of air between the electrode and the dielectric layer;

$$\varepsilon_{eff} = \varepsilon_{air} V_{air} + \varepsilon_{dielectric} V_{dielectric} \quad (4.4)$$

With the addition of air permittivity, the initial capacitance of the sensors becomes very small, generally in pF range. When it is under compression, the volume of the air drastically decreases, resulting in a sharp increase in the efficient permittivity. This results in a very high sensitivity in higher loadings.

Second enhancement is to use composite dielectric layers, where the resulting capacitance is affected by the percolation theory. Relationship with the dielectric constant of the composite dielectric and the filler can be predicted as [350];

$$\varepsilon_r \propto (P_c - P)^{-s} \ , \ P < P_c \quad (4.5)$$

, where P_c is the percolation threshold of the filler, P is the filler content, and s is the critical exponent of dielectric constant. From the formula, it is expected that dielectric constant of the composite is directly proportional to filler concentration when the content is lower than the percolation threshold [350].

Example of a micropatterned dielectric layer for improved sensitivity is given in Figure 4.8 (a). A bioinspired pattern made from lotus leaf mold creates unique micropatterned PDMS dielectrics. Interestingly, the micropatterned PDMS is used outside of the tactile sensor; while microspheres of PS are used as the dielectric layer. Using microspheres also added the feature of having a micropatterned dielectric layer. The utilization of micropatterned PDMS-based electrodes enables the PS microspheres to effectively occupy the cavities within the electrodes, thereby enhancing sensitivity (Figure 4.8 (b)).[351] Foam-based capacitive sensors also offer increased sensitivity. Researchers fabricated a conductive porous nanocomposite; while taking advantage of both foam-type dielectrics and having a composite structure. An Ecoflex-CNT foam composite is achieved and CNT amount is controlled to achieve better sensitivity. Figure 4.8 (c) shows the device schematics, SEM image of the final structure and optical images of the dielectric layer in different states. It was seen that having a partially conducting Ecoflex-CNT foam results in much better sensitivities, with an ability to detect even small water droplets. [352] Another aspect of having foam type structure with increased dielectrics is shown by

Chhetry et al. [353] PU foams are coated with calcium copper titanate ($CaCu_3Ti_4O_{12}$ – CCTO) to improve the dielectric permittivity (Figure 4.8 (e)). Incorporating a controlled amount of CCTO onto pristine PU resulted in a minimum three-fold increase in capacitance change, attributed to the additional dielectric permittivity introduced by CCTO. [353]

In recent years, the use of ionic dielectric layers for capacitive sensors have been extensively studied. These are known as interfacial supercapacitive sensing or iontronic sensing, which utilize electrochemical double layer (EDL) provided by electrolytic-electrode interface [354]. 'Iontronics' is used to name the mechanism, which involves variety of devices that are using ions as charge carriers (as a counterpart of the term electronics). The use of ionic layers immediately increased unit area capacitance (UAC), which is order of several μF, which are at least 1000 times higher than conventional parallel-plate capacitors which offers capacitance in pF range. Increased UAC also eliminates the parasitic effect since the capacitance is on micro-farad levels, on top of increasing sensitivities even more.

The drastic effect of iontronics on capacitance can be explained by Gouy-Chapman-Stern model. Here, excess ionic charge carriers which are at the surface of ionic layer led to strong electrostatic interaction. Due to this interaction, counter-ions are attracted to the electrode surface, which gives rise to a region at electrode-electrolyte interface. This interface layer, which is also named as Helmholtz layer, is assumed to have a thickness of the 1-2 solvated ions [334,355]. Next adjacent layer to the Helmholtz is called diffuse layer, and controlled via Poisson-Boltzmann relationship. The electrical behavior of this diffuse layer also affects the overall capacitance since it has an effect on dielectric property of the ionic layer. This is related to the Debye length of the electrolyte and thus, the effect of screening just outside the Stern layer [355].Thus, these two components effecting the capacitance of the iontronic layer can

be deduced as C_H and C_D, respectively, for Helmholtz and diffuse layer. Depending on this mechanism, below equation can be written for EDL[334];

$$C_{EDL} = \left(\frac{1}{C_H} + \frac{1}{C_D}\right)^{-1} = \eta_A \,.\, \varphi(d, \varepsilon, C, \phi, T) \,.\, A = UAC.A \quad (4.6)$$

,where $\varphi(d, \varepsilon, C, \phi, T)$ is a parameter which is influenced by;

1. Dielectric constant
2. Thickness of Helmholtz layer
3. Concentration and type of ionic species
4. Surface potential (both related to electrode and electrolyte)
5. Temperature.

Also, η_A is defined as the roughness ratio, which also has an effect on the contacting surfaces.

The effect of the addition of ionic species are extensively explored by Cicek et al. [356]. Textured cellulose based supramolecular bio-polymer gels (SBPG) were fabricated with different concentrations of NaCl added, and assembled as a capacitive sensor with carbon-cellulose composite electrodes (Figure 4.8 (g)). Here, several strategies were combined; a textured dielectric layer, addition of ionic species to the dielectric layer, and choosing appropriate carbon-based electrode (which will be explained in next section.). The ionic conductivity was greatly enhanced with the addition of NaCl species (Figure 4.8 (h)), which directly increased the areal capacitance values (Figure 4.8 (k)). The SBPG layers exhibiting the highest ionic conductivity demonstrated the most significant changes in capacitance, making them

excellent candidates for pressure sensing applications. An ultra-high sensitivity of 1 475 000 kPa^{-1} was obtained. [357] This is an excellent indication that combining several strategies for sensitivity can significantly influence the output of the sensing devices.

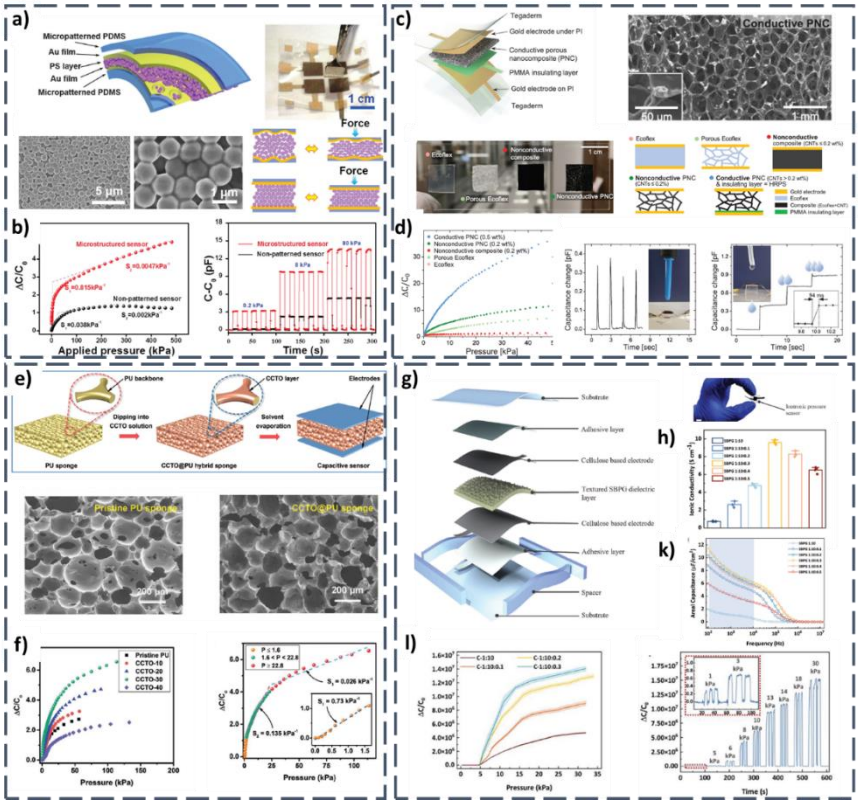

Figure 4.8 a-b) Micropatterned PDMS/Au electrodes with PS microspheres as dielectric layer for capacitive sensors. a) Device structure and working mechanism b) Change in sensitivity with respect to micropatterning.[351] c-d) A conductive foam as dielectric layer for capacitive sensors. c) Schematic structure, SEM image of the conductive foam, and its step-by-step fabrication steps. d) Capacitance change with respect to applied pressure. [352] e-f) PU sponge-CCTO composite for enhanced sensitivity. e) Fabrication steps and respective SEM images. f) Capacitance measurements and resulting sensitivity with the composite foam. [353] g-l) Iontronic SPBG layer for ultra-high sensitivity. g) Schematic structure of the capacitive pressure sensor. h) Ionic conductivities and k) areal capacitance values of SPBG layers with different ionic concentrations. l) Relative capacitance changes. [357]

4.2.4.2.2 Electrodes for Capacitive Pressure Sensors

As mentioned in the previous section, electrode design and selection are very important. Especially the interaction between the dielectric layer and the electrode material, due to the formation of EDL, affects the initial capacitance levels, hence the sensitivities. One of the clearest examples is given in the thesis work of Cicek[326], with the work related with SBPGs [356] with the details given in Section 1.2.4.2.1 and in Figure 4.8. Figure 4.9 (a) shows the sensitivity of the best performing SBPG layer with cellulose-carbon composite electrodes. When the identical SBPG layer was employed in conjunction with aluminum electrodes, the change in capacitance levels decreased by as much as a factor of 1000. This is due to the synergy between Na^+ and Cl^- ions with carbon particles in the composite electrode, which enhanced the EDL behavior and thus, the sensitivity of the capacitive sensor. [326]

Microstructuring the electrodes as well as the dielectric layer can help in enhancing the sensitivity. This is again similar with the effective dielectrics – the microstructure on the electrode creates air gaps inside the system, effectively reducing the capacitance. With increased pressures, the gap decreases, resulting in the sharp increase of the effective dielectricity. One such research done by Li et al.[358] explored the effect of the microstructure distribution. Figure 4.9 (b) shows the pyramid structures with different spacings through the Figure 4.9 (b)-i to Figure 4.9 (b)-iv. The pyramids are then Ti/Au coated (Figure 4.9 (b)-v and 4.9 (b)-vi), which are able to be flexed (Figure 4.9 (b)-viii). Researchers found the microstructuring of the electrode increases the sensitivity especially in the low-pressure region, mostly due to the effective dielectric change. Furthermore, a sparser distribution of the micro pyramids was observed to significantly enhance the sensitivity. [358]

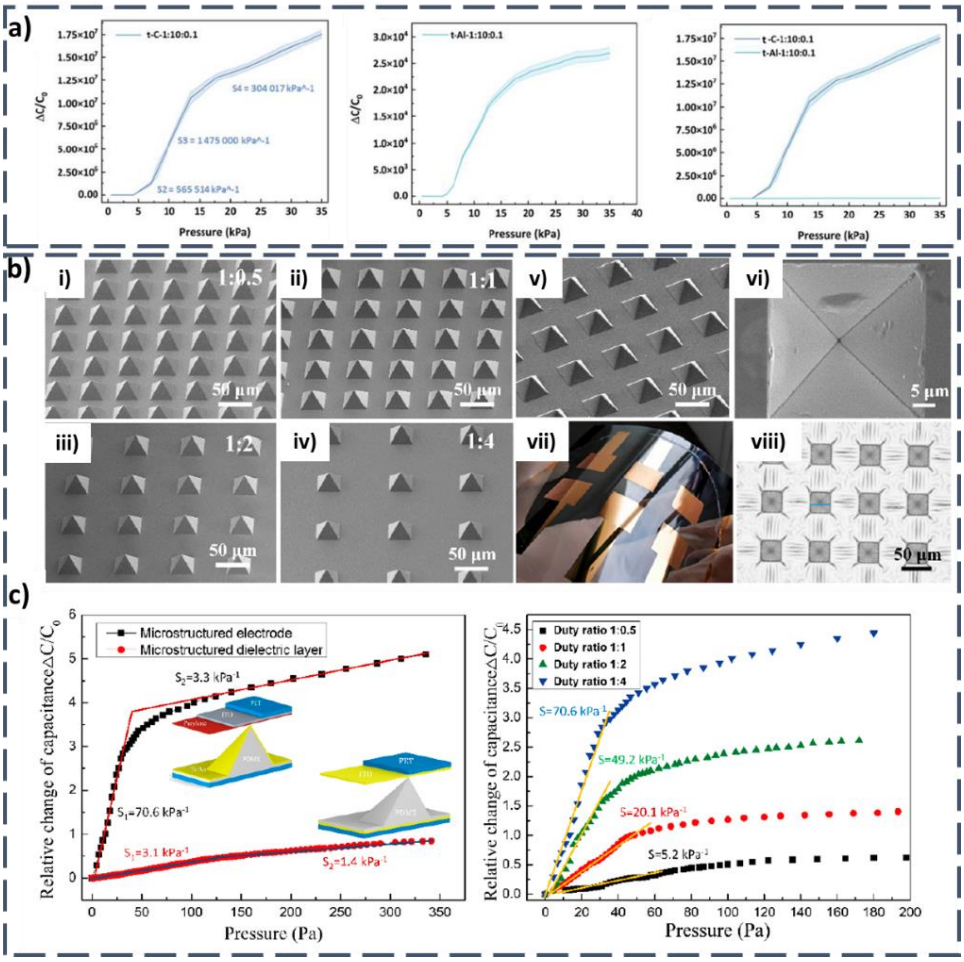

Figure 4.9 a) The effect of electrode material on sensitivity with an ionic dielectric layer. [326,356] b-c) Effect of microstructured electrodes on sensitivity of the capacitive pressure sensor. b) SEM images of i-iv) Micro pyramid structures with different spacings v,vi) Ti/Au coated pyramids as electrodes. vii) Photo of the electrodes on PET substrate. viii) Photo of the wrinkled structure after deposition if PET substrate is not used. c) Relative capacitance changes of microstructured electrodes and their comparison. [358]

4.3 Transient Capacitive Pressure Sensors

One of the most fascinating applications of transient capacitive pressure sensors is their use in physiological monitoring, both in vivo and in vitro. Two excellent examples are already provided in Figure 1.9, where transient bioresorbable arterial-pulse sensor[64] and transient closed-loop system for tracking cardiac pacing and physiological events. [65] In a similar vision, Boutry et al. [359] fabricated a bimodal sensor for strain and pressure sensing with only biodegradable materials. Figure 4.10 (a) shows this bimodal sensor, its potential areas of use and its structure. This sensor was bioresorbable, which eliminates the need for a second surgery to extract the implant from the body. Two biodegradable polymers, which are poly(glycerol sebacate) (PGS) and poly(octamethylene maleate (anhydride) citrate) (POMaC) were used to fabricate the stretchable sensor, while Mg electrodes were used as the transient metal conductors. Pressure signals were recorded from the sensor implanted on the back of a Sprague–Dawley rat. From in vivo tests, the pressure sensor acted perfectly up to 2 weeks, and was even usable after 3.5 weeks (Figure 4.10 (b)). [359] Novel electrode materials are also usable for transient systems. In a specific case, researchers used room-temperature liquid metal (RTLM), GaInSn, on micro channeled PVA to fabricate transient electronics. The simple structure of the electronic circuits can be used as transient antennas and capacitive touch sensors. Photos of the fabricated flexible sensors are given in Figure 4.10 (c). The structure of the capacitive touch sensor and its response to a touch is shown in Figure 4.10 (d). The PVA micro channeled substrate can be dissolved in water, where the liquid metal can be collected. [360] This research shows how transient capacitive sensors can be used in different applications and how transient electronics can be different in terms of their transiency mechanism.

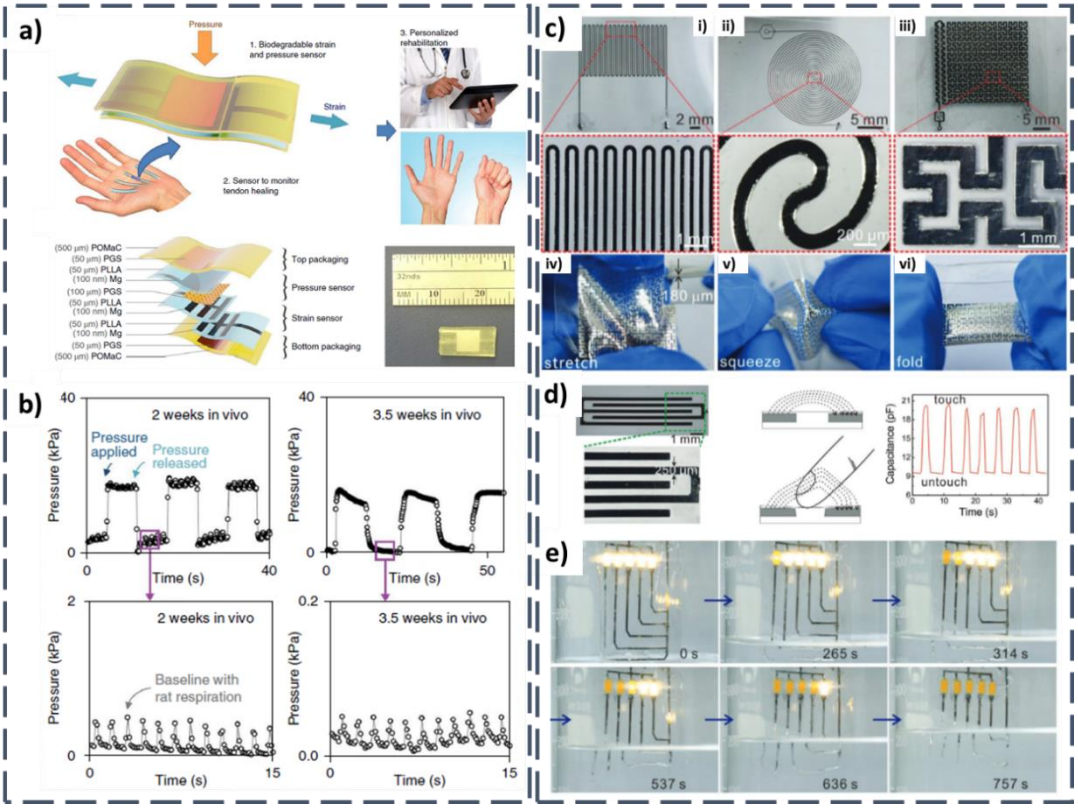

Figure 4.10 a-b) Bimodal transient pressure and strain sensor. a) Schematic structure of the sensor with its possible usage areas. b) Pressure sensing done in-vivo, after 2 weeks and 3.5 weeks of implanting. [359] c-e) RTLM based transient electronics. c) Photos of the transient RTLM based sensors. i-iii) Photos of the different structures and iv-vi) their mechanical stability under stretching, squeezing and folding, respectively. d) Shows the structure for capacitive touch sensor. e) Controlled transiency of the sensor in water. [360]

4.4 Experimental Procedure

4.4.1 Fabrication of the Transient PVA/PSG Based Capacitive Sensors (T-CAPS)

Same PCA/PSG layers utilized in T-TENG explained in Section 3.6.1 was used here. The contacts for PCA/PSG electrodes were taken simply by using a stapler and connecting it with a copper wire to reduce the possible noise and additional capacitance change from sensor-metallic foil interface. Fabricated electrodes were divided by an additional PSG film, and again covered with PSG film to obtain a parallel plate capacitive pressure sensor.

4.4.2 Characterization of the T-CAPS

Capacitive measurements of the fabricated sensor with different loads were made by a hand-made apparatus and Twintex LCR-7200 precision LCR meter. Same apparatus was used to determine the sensitivity. Physiological signals and joint movements were detected by Arduino Leonardo with a simple RC circuit code. Sensitivity of the T-CAPS is defined as *S* and calculated as below,

$$S = \frac{(\Delta C/C_0)}{\Delta P} \qquad (4.7)$$

,where C_0 is the initial capacitance, ΔC is the capacitance change, and ΔP is the change in applied pressure (kPa).

4.5 Results and Discussion

Substitution of bulky and rigid materials with flexible and transient counterparts is very important in achieving "green" sensors that can be easily utilized in wearable and biomedical technologies. Furthermore, these devices can be easily recycled at the end of their life cycle. [361,362]. Herein, we encapsulated two PCA/PSG layers used for TENG devices shown in Figure 3.13 with an additional PSG layer to obtain T-CAPS for the real time physiological monitoring and joint movement detection. The final structure is given in Figure 4.11. For the assembly, double sided very high bond (VHB) bands are used to close down the structure as well as introducing a gap between the electrodes in their relaxed state.

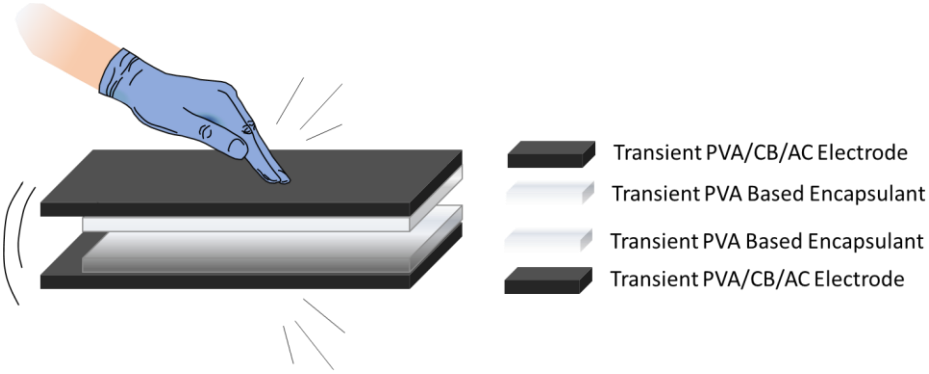

Figure 4.11 Schematic representation of the T-CAPS. Reprinted with permission from ref [111], Copyright 2021, Wiley

All results with relevant locations on human body and representative inset photos are provided in Figure 4.12. The same sensor was used throughout the data collection process to demonstrate the flexibility and functionality of the sensor. Sensitivity of the transient capacitive sensor was measured through monitoring the capacitance change under a variety of pressures up to 44.1 kPa (Figures 4.12 (a) and Figure 4.13 (a)). Sensitivity of the PCA/PSG films were found to be 0.69 kPa^{-1} up to 22 kPa, and 0.48 kPa^{-1} from 24.5 kPa up to 44 kPa, offering a solid performance with a long linear sensitivity range. Response and recovery times of the fabricated sensors were measured as 22 and 49 ms, respectively. These values are highly ideal for such a sensors utilized in a wide variety of applications as demonstrated herein (Figure 4.13 (b)). In order to demonstrate their stability, T-CAPS were subjected to cyclic loading/releasing test for 1000 cycles, results of which are provided in Figure 4.13 (c). No obvious change was observed in the relative capacitance, indicating excellent mechanical robustness for T-CAPS.

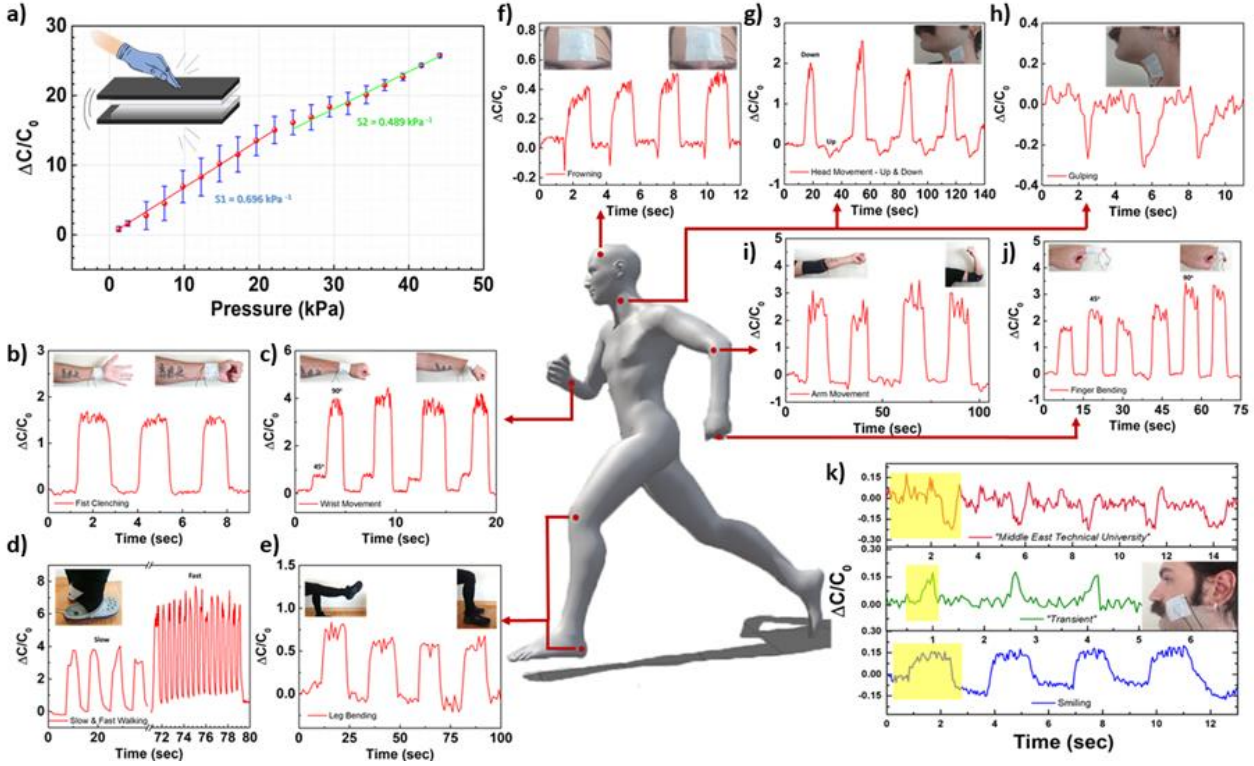

Figure 4.12 Physiological signal and movement detection with the T-CAPS. a) Sensitivity of the fabricated sensor and its performance under different loads. b) Detection of clenching and c) wrist movement by attaching the sensor onto inner side of the wrist. d) Relative capacitance changes between slow and fast walking. e) Monitoring of joint movement by stretching the leg and sitting position by attaching the sensor on kneecap. f) Transient sensor placed onto forehead to detect frowning. Sensor attached to the side of the neck to monitor g) head movement and even h) gulping. i,j) Transient sensor attached to elbow and finger to monitor both large and small muscle and joint movements. k) Relative capacitance changes upon talking and smiling when the transient sensor is attached to the cheek, detecting different muscle movements. Highlighted regions show the first signals of four repeats. Reprinted with permission from ref [111], Copyright 2021, Wiley

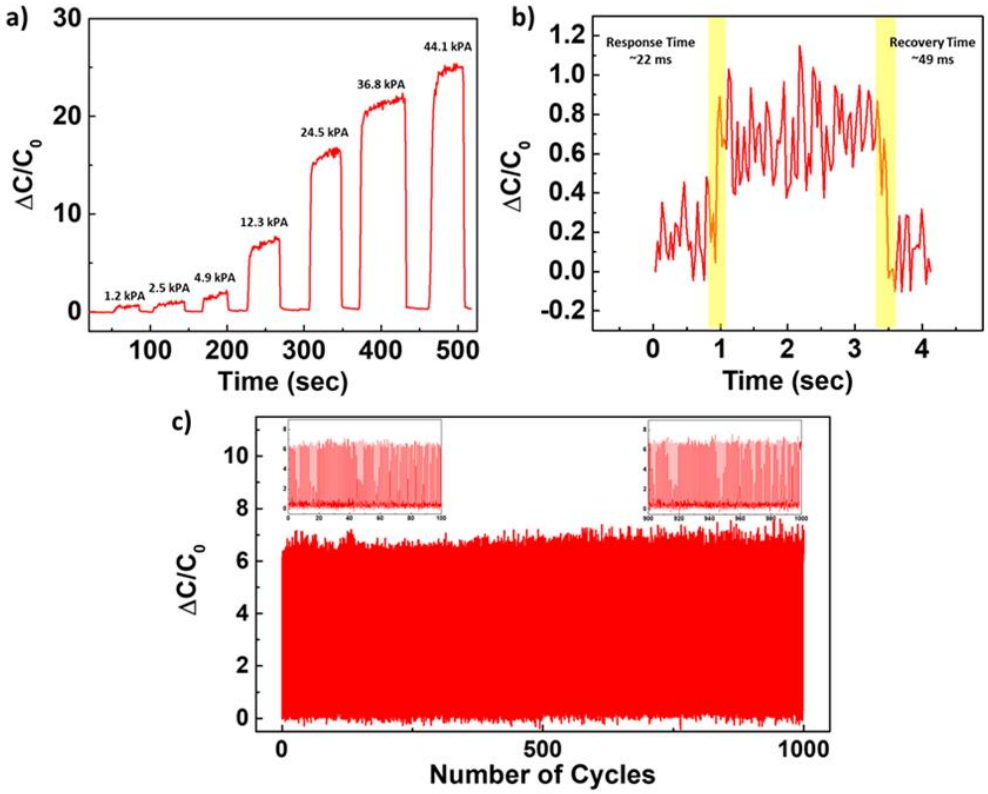

Figure 4.13 a) Relative capacitance changes under different loads. b) Response and recovery times of the sensor under a load of 1.2 kPa. c) Stability of the T-CAPS under constant load-release cycles. Reprinted with permission from ref [111], Copyright 2021, Wiley

Capacitance change occurs when the electrodes are pressed onto each other or flexed so that compressive stresses are formed on the dielectric/dielectric interface. This results in a change in dielectric layer geometry and thickness [87,363]. Here, PSG overcoat layers offer high sensitivity due to electrical double-layer formation between the layers. When the electrodes are compressed, the first thing to happen is the full contact of the dielectric layer surfaces, which eliminates the empty spaces and reduces the distance between the electrodes. Effective dielectric constant of the system increases under compression due to the elimination of the air gap between

two adjacent electrodes, resulting in an increase in the overall capacitance of the pressure sensor. At the same time, the decreased distance between the PCA electrodes further improves the overall capacitance. Due to both of these mechanisms in the first stage, electrical double-layer formation is enhanced, resulting in very high sensitivity. Secondly, after obtaining full contact between dielectric layers, further applied compressive stresses cause a reduction in the thickness of the dielectric layer. In this second stage, the behavior of the capacitance change is altered. With the increased pressure, the distance between the electrode decreases even further. This decrease in the distance is dominated by the elastic deformation of the dielectric PSG layers. This results in a more efficient ionic conduction, which further increases the overall capacitance of the pressure sensor. Overall structure of the capacitive pressure sensor and ionically conductive dielectric layers enabled sensors to show favorable sensitivity in a long linear range.

T-CAPS was used in different locations on the human body to demonstrate their potential for the transient wearable electronics. During the joint movements, the PCA/PSG layers were compressed onto each other in different geometries and angles leading to a change in capacitance. On small muscle movements, T-CAPS was either flexed or relaxed, which again resulted in a capacitance change. Figures 4.12 (b) and (c) demonstrate how the T-CAPS behave when it was attached to the inner side of the wrist. Clenching of the fist created a muscle contraction around the wrist, causing the bending of the capacitive device. This resulted in an increase in capacitance, which is clearly shown in Figure 4.12 (b). In Figure 4.12 (c), the wrist was moved at different angles to demonstrate the sensitivity of the transient capacitive sensor. Fabricated sensors can also be used to monitor walking frequency and intensity by observing the extent of the capacitance change and repetitions. This is demonstrated by placing the T-CAPS on the foam clogs and walking both slowly and fast. The intensity and frequency of the walking can be easily observed from the magnitude of relative capacitance change and the onset of the capacitance changes given in Figure

4.12 (d). Capacitive sensors can also be used to detect joint movements. For this purpose, it was placed on the kneecap. When the stretched leg was changed into a sitting position, bending at the kneecap change the geometry of the capacitive cell. Thus, an increase in capacitance was observed allowing the detection of the motion. T-CAPS was also attached to the forehead and neck to monitor physiological signals and movement from smaller muscle groups. Figure 4.12 (f) shows how the capacitance changes if a person frowns, evidencing the high sensitivity of the fabricated T-CAPS. This could allow the monitoring of a person's mood, which is important for stress management and mental health monitoring. When the sensor was attached to the side of the neck, it can also detect the head movement fairly easily. Even the gulping action was detected, suggesting that the fabricated sensors can be used to monitor eating habits (Figures 4.12 (g) and (h), respectively). Figures 4.12 (i) and (j) show that the T-CAPS can be used to detect both large and small movements in the human body by placing the sensor on elbows and fingers, respectively, indicating the applicability of the sensor for different cases. Lastly, the transient sensor was demonstrated to detect talking through the movement of the muscle groups on the cheeks. These results of real-time measurements are provided in Figure 4.12 (k). "Middle East Technical University" and "Transient" words were spoken several times, during which the change in the capacitance was monitored. An increase in the relative capacitance was observed upon pronouncing "Middle East Technical", while a drop-in capacitance was observed upon pronouncing "University". This clearly demonstrated that the word detection or movement detection of different muscle groups using the fabricated sensors is possible. As another single word, "Transient" caused an increase in the relative capacitance. It was also possible to monitor smiling of a person, which further proved that the transient all PVA-based capacitive sensors can be used for mood tracking. All results provided in Figure 4.12 clearly demonstrated the potential of the physically transient PCA/PSG layers for future sensing applications with great flexibility and versatility.

A comparison of T-CAPS with other, recently reported capacitive sensors is provided in Table 4.2. Except for the iontronic capacitive sensors, our work showed one of the best sensitivities with a long linear range, and excellent response time when compared to articles utilizing similar materials. T-CAPS is mechanically robust, and provide the most rapid physical transiency when compared to other reported transient capacitive sensors.

Table 4.2 Comparison of T-CAPS with those in recent literature on capacitive pressure sensors including carbon-based, PVA-based and transient applications.

Materials	**Transiency Mode**	**Operating Pressure Range (kPa)**	**Sensitivity**	**Response Time (ms)**	**Stability**	**Ref.**
Cellulose/PVA composite hydrogel	Environmentally friendly with zero wastage – no transiency proposed	0.036 - ~2.50	13.91 kPa^{-1} (0.036 – 1.5 kPA) 0.76 kPa^{-1} (1.5 kPA – 2.5 kPA)	-	-	[317]
PVA/H_3PO_4 intrafillable structure as dielectric material Au coated Pt as electrodes	No transiency	0 – 100	3302.9 kPa^{-1} (<10 kPa) 671.7 kPa^{-1} (10-100 kPa) 229.9 kPa^{-1} (>100 kPa)	9	5000 cycles	[364]
PVA/Sodium Alginate/Bacterial Cellulose/Modified carbon nanotube	No transiency proposed	0 – 337	0.033 kPa^{-1} (0-29 kPa) 0.009 kPa^{-1} (29-172 kPa) 0.004 kPa^{-1} (172-337 kPa)	230	-	[365]
PVA/cellulose nanofibril hydrogel	Biocompatible – no transiency proposed	0 - 4	0.75 kPa^{-1}	-	-	[366]
Graphene oxide foam as dielectric rGO on PET substrates as electrodes	No transiency	0.24 – 4	0.8 kPa^{-1} (0.24-1.0 kPa) 0.15 kPa^{-1} (1 – 4 kPa)	100	1000 cycles	[367]
Graphene/PDMS sponge as dielectric layer	No transiency	0 – 500	0.12 kPa^{-1} (0-10 kPa) 0.042 kPa^{-1} (10-100 kPa) 0.004 kPa^{-1} (100-500 kPa)	7	5000 cycles	[368]
Silver nanofiber/silk fibroin as electrodes Ecoflex as dielectric layer	Decomposition in 5% papain solution in 24 hours	0 – 700	0.019 kPa^{-1} (<45 kPa) 5.50e-4 kPa^{-1} (45-700 kPa)	-	7200 cycles	[369]
Sebabic Acid/Glycerol as dielectric layer PVA as adhesive layer PHB/PHV film coated with iron and magnesium as electrodes	Degradable in PBS solution after 7 weeks	0 - 10	0.76 kPa^{-1} (<2 kPa) 0.11 kPa^{-1} (2-10 kPa)	-	-	[370]
Freeze-dried rose petals as dielectric layer AgNW loaded leaf skeleton as electrodes	Biodegradable in water and PBS (75 days)	0.1 – 56.1	0.08 kPa^{-1}	-	5000 cycles	[371]
PCA layer as current collector PSG layer as dielectric layer Additional PSG layer as encapsulant	Biodegradable and water soluble Immediate transiency	0 - 44	0.69 kPa^{-1} (<24.5 kPa) 0.48 kPa^{-1} (24.5 – 44 kPa)	22	1000	**Our Work**

4.6 Transiency of the T-SUPC, T-TENG, and T-CAPS

The rapid advancements and increasing demand for wearable technologies and small electronics have resulted in a significant rise in electronic waste (e-waste) like never before [10,372]. Thus, it is prudent to think about the future of the environment by designing transient energy storage devices, energy harvesters, and electronics. In this manner, fabricated PCA electrodes and PCA/PSG layers were tested for transiency, and obtained results are provided in Figure 4.14. The photo in Figure 4.14 (a) demonstrates the aforementioned flexibility and conductivity of PCA electrodes, where an origami boat was used to complete the circuit to light up a LED. When the boat was left on the water, gradual disintegration was observed in 4 minutes. At the end of 4 hours, a carbon film was found to survive on the surface of the water, suggesting the necessity for a mechanical disturbance. Instant structural disintegration in the PCA electrode is observed in Figure 4.14 (b), upon pouring a small amount of water. When it was rubbed with the other hand, the structure was found to break down instantly. This proved the physical transiency of the PCA electrodes and rapid disintegration with some mechanical action and water. A very simple way to apply this mechanical action was by shaking. This was done with a used-up T-SUPC, which included a PCA electrode and PN layers. The resulting photos are provided in Figure 4.14 (c). The used supercapacitor cell was placed into a vial and shaken up by 30 times. The disintegration can be observed in the provided photographs. With only 5 shakes, the disintegration of the cell started, and after 30 shakes, total disintegration occurred and a homogeneous black solution was obtained. This proved that the electrode materials can be easily recycled or collected as a solution to be used again. The transiency of PCA/PSG layers used in T-TENG and T-CAPS were also explored and associated photos are provided in Figure 4.14 (d). By dipping the electrode into the water and shaking it inside, it was possible to disintegrate the electrodes and easy to recover the metallic contact for reuse. Overall,

having a simplified structure with similar materials also make recycling easier for the devices. Easy recollection of the device parts as a solution to collect the materials again, and recollecting materials used for assembly and contacts by just dissolving the attached devices make all PVA-based devices promising for transient electronics.

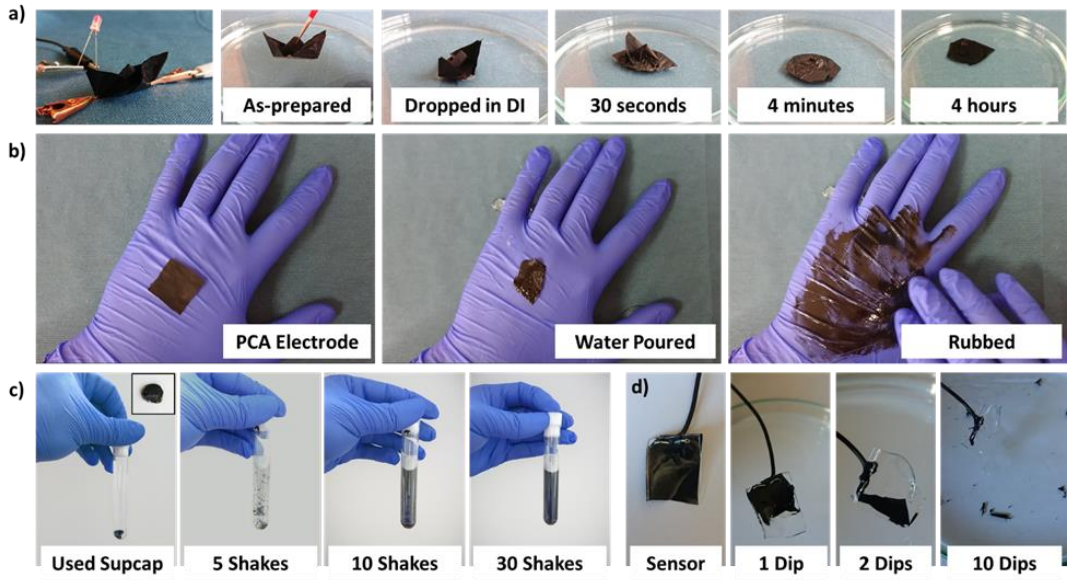

Figure 4.14 a) Photos demonstrating the flexibility and aqueous transiency of the fabricated electrode by forming an origami boat with PCA and its disintegration in DI water. b) A full physical transiency is achieved by a small amount of water and mechanical action. c) Demonstration of the transiency of a T-SUPC cell in a water-filled vial by simply shaking. d) Disintegration of a PCA/PSG electrode used in T-TENG and T-CAPS through dipping into water and simply shaking. Reprinted with permission from ref [111], Copyright 2021, Wiley

Physical transiency of the PCA/PSG layers was further explored using simple solutions that can be prepared at home (hot water, vinegar, and drain clog remover) to observe how easily these electrodes degrade in different aqueous conditions. Related photos are provided in Figure 4.15. When the transient electrodes were placed into hot water (boiled), the disintegration process gets significantly accelerated compared to water at RT. The disintegration was achieved just in 5 minutes without the need of mechanical action (Figure 4.15 (a)). A home-grade vinegar (3% acetic acid) was also used for disintegration. The breakdown of the electrode was observed just in 10 minutes, photos of which are provided in Figure 4.15 (b). As another example, a teaspoon of drain clog opener (sodium hydroxide - NaOH) was also used to create a basic environment. Very fast disintegration (under 3 minutes) of the electrode was observed that was comparable to that in hot water (Figure 4.15 (c)). These results suggested that the disintegration of the fabricated PCA/PSG electrodes is fairly easy, which clearly shows the promise of using the fabricated electrodes in transient electronics applications.

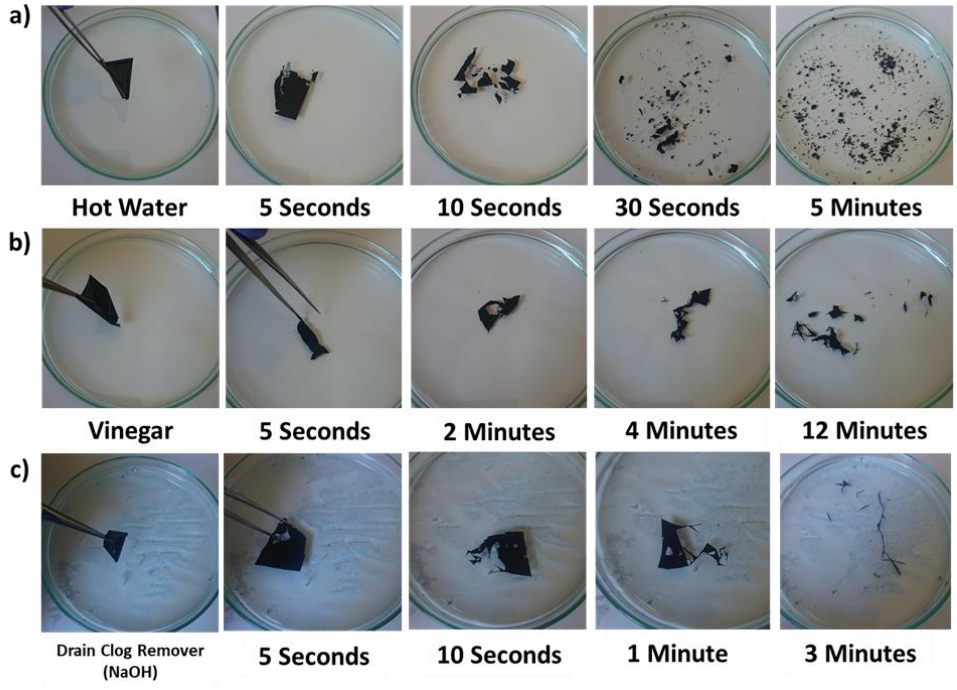

Figure 4.15 Demonstration of the transiency of PCA/PSG layer in home-based solutions utilizing a) hot water, b) vinegar and c) drain clog remover. Reprinted with permission from ref [111], Copyright 2021, Wiley

CHAPTER 5

CONCLUSIONS AND FUTURE REMARKS

5.1 Conclusions

To conclude, all PVA-based (i.e. electrode, electrolyte, insulating layer, and encapsulation layer) transient and multifunctional devices were prepared and characterized in this thesis. Simple solution-based methods were used for their fabrication. Devices of interest included supercapacitors, triboelectric nanogenerators and capacitive sensors. Fabricated solid state T-SUPC showed excellent EDLC behavior and was subjected to 10000 charge/discharge cycles without significant loss in its performance. A large-sized supercapacitor encapsulated with PSG layer was rolled 360° without any significant loss in its performance. Fabricated TENG allowed lighting of 86 serially connected white LEDs and produced a maximum power output of 2.2 $mW.m^{-2}$. T-TENGs were also assembled as a self-powered touchpad. Fabricated T-CAPS were used to monitor physiological signals and joint movement with long linear sensing ranges. A sensitivity of 0.69 kPa^{-1} was achieved up to 24 kPa followed by 0.49 kPa^{-1} for loads up to 44 kPa. Other than walking, head movement and joint movements, very small muscle group movements could as well be monitored using the fabricated T-CAPS, suggesting that the fabricated T-CAPS can be used to detect even mood changes or habits. Rapid physical transiency of the fabricated devices was also demonstrated in simple home-based solutions. All of these results showed that all PVA-based structures are highly promising for the replacement of several components in electronic systems including T-SUPC as the energy storage, T-TENG as the mechanical energy harvesting and self-powering, and T-CAPS as the sensing components.

5.2 Future Recommendations,

This thesis showcases a practical way to fabricate transient electronics using similar materials. The possibility of using the same PVA-based structures from energy storage to energy harvesting and sensing provides a route for integrating transient electronics without the complexity of several different fabrication routes. Already abundant in the industry, PVA is an excellent choice for low-cost transient electronics. Yet, transiency triggered in water always has an adverse side-effect – susceptibility to moisture. Encapsulation of the devices and different triggering mechanisms concerning the encapsulation should be explored. Moreover, performance metrics were on-par with the transient electronics but mostly fell below the conventional non-transient solutions. Thus, it is imperative to fabricate transient electronics with performance levels competitive with conventional solutions to transition to transient electronics.

In Chapter 2, transient supercapacitors, T-SUPCs, are fabricated with PCA-based electrodes and PVA-based hydrogel electrolyte, PN. Although the behavior is very close to ideal EDLC behavior, the specific capacitance levels can be improved. Transient 2D materials such as MoS_2 or MXenes can be involved with the composite PCA layers to increase the capacitance levels. The inherent conductivity of these materials would not hinder the conductivity of the PCA films and can even increase their mechanical integrity. This improvement would increase the overall cost, yet the devices would still be environmentally friendly, biodegradable, and biocompatible. Moreover, PNs are prone to drying and should be encapsulated immediately – in this thesis, a PVA layer without the addition of sucrose was used to encapsulate the capacitors. Still, PVA can be affected by moisture and can even draw water molecules from the PN layer, which would decrease the lifetime of the supercapacitors. All in all, it is necessary to improve the capacitance levels to improve the flexibility of the fabricated transient supercapacitors for different usage areas and applications.

In Chapter 3, transient triboelectric nanogenerators, T-TENGs, were fabricated, and their performance was analyzed. The biggest issue in the TENG community, the effect of moisture, could not be analyzed with the fabricated single-electrode TENGs. This issue should be explored to see the effect of moisture, in the long run, to completely understand the stability of the T-TENGs. Moreover, the performance could be increased by using the ionic PSG layer. Multilayered structures of TENGs, where each layer can be engineered to improve the overall charge collection efficiency. For example, a thin PVA layer, followed by an ionic PVA layer with the current collector at the bottom, could improve triboelectrification and charge collection. Even more, the single-electrode could be converted into a complete device by manipulating the triboelectric series of PVA layers by ionic additions. Several experimentations were done with sulfuric acid and sodium chloride, but changing the mechanical aspects of the PVA resulted in inconclusive results. A parametric study to obtain such structures could be done to achieve a transient PVA-based T-TENG device. Last, the electrode could be again modified with 2D materials such as in T-SUPC to improve triboelectrification.

In Chapter 4, transient capacitive pressure sensors, T-CAPs, were fabricated and used for physiological monitoring. Overall sensitivity levels and physiological monitoring are quite good, compared to non-transient and conventional solutions. Yet, it could be increased even more with the use of iontronics. An ionic PSG layer could be doctor-bladed onto PCA electrodes to explore the ionic layer's effect on the capacitive sensor's sensitivity performance. Moreover, the 2D material addition to the PCA electrodes here and the other applications could change the sensitivity of the devices.

REFERENCES

[1] M. Irimia-Vladu, E. D. Glowacki, N. S. Sariciftci, S. Bauer, *Green Materials for Electronics*, Wiley-VCH Verlag GmbH & Co. KGaA, Weinheim, Germany, **2017**.

[2] R. Jamshidi, M. Taghavimehr, Y. Chen, N. Hashemi, R. Montazami, *Adv Sustain Syst* **2022**, *6*, 2100057.

[3] K. K. Fu, Z. Wang, J. Dai, M. Carter, L. Hu, *Chemistry of Materials* **2016**, *28*, 3527.

[4] G. Lee, Y. S. Choi, H.-J. Yoon, J. A. Rogers, *Matter* **2020**, *3*, 1031.

[5] S. K. Kang, L. Yin, C. Bettinger, *MRS Bull* **2020**, *45*, 87.

[6] Y. Gao, L. Ge, S. Shi, Y. Sun, M. Liu, B. Wang, Y. Shang, J. Wu, J. Tian, *Environmental Science and Pollution Research* **2019**, *26*, 17809.

[7] R. Akram, Natasha, S. Fahad, M. Z. Hashmi, A. Wahid, M. Adnan, M. Mubeen, N. Khan, M. I. A. Rehmani, M. Awais, M. Abbas, K. Shahzad, S. Ahmad, H. M. Hammad, W. Nasim, *Environmental Science and Pollution Research* **2019**, *26*, 16923.

[8] R. Nithya, C. Sivasankari, A. Thirunavukkarasu, *Environ Chem Lett* **2021**, *19*, 1347.

[9] V. Forti, C. P. Baldé, R. Kuehr, G. Bel, *The Global E-Waste Monitor 2020*, **2020**.

[10] K. K. Fu, Z. Wang, J. Dai, M. Carter, L. Hu, *Chemistry of Materials* **2016**, *28*, 3527.

[11] W. B. Han, J. H. Lee, J. W. Shin, S. W. Hwang, *Advanced Materials* **2020**, *32*, 1.

[12] S. K. Kang, L. Yin, C. Bettinger, *MRS Bull* **2020**, *45*, 87.

[13] S. Huang, X. Zhu, S. Sarkar, Y. Zhao, *APL Mater* **2019**, *7*, DOI 10.1063/1.5116146.

[14] J. Shintake, H. Sonar, E. Piskarev, J. Paik, D. Floreano, in *2017 IEEE/RSJ International Conference on Intelligent Robots and Systems (IROS)*, IEEE, **2017**, pp. 6221–6226.

[15] G. Lee, S. K. Kang, S. M. Won, P. Gutruf, Y. R. Jeong, J. Koo, S. S. Lee, J. A. Rogers, J. S. Ha, *Adv Energy Mater* **2017**, *7*, 1.

[16] X. Wang, W. Xu, P. Chatterjee, C. Lv, J. Popovich, Z. Song, L. Dai, M. Y. S. Kalani, S. E. Haydel, H. Jiang, *Adv Mater Technol* **2016**, *1*, 1.

[17] C. Gao, C. Bai, J. Gao, Y. Xiao, Y. Han, A. Shaista, Y. Zhao, L. Qu, *J Mater Chem A Mater* **2020**, *8*, 4055.

[18] G. Khandelwal, T. Minocha, S. K. Yadav, A. Chandrasekhar, N. P. Maria Joseph Raj, S. C. Gupta, S. J. Kim, *Nano Energy* **2019**, *65*, 104016.

[19] D. H. Kim, Y. S. Kim, J. Amsden, B. Panilaitis, D. L. Kaplan, F. G. Omenetto, M. R. Zakin, J. A. Rogers, *Appl Phys Lett* **2009**, *95*, DOI 10.1063/1.3238552.

[20] S. Çinar, R. Jamshidi, Y. Chen, N. Hashemi, R. Montazami, *J Polym Sci B Polym Phys* **2016**, *54*, 517.

[21] J. W. Shin, J. Chan Choe, J. H. Lee, W. B. Han, T. M. Jang, G. J. Ko, S. M. Yang, Y. G. Kim, J. Joo, B. H. Lim, E. Park, S. W. Hwang, *ACS Nano* **2021**, *15*, 19310.

[22] M. Hao, L. Li, S. Wang, F. Sun, Y. Bai, Z. Cao, C. Qu, T. Zhang, *Microsyst Nanoeng* **2019**, *5*, DOI 10.1038/s41378-019-0047-4.

[23] W. Li, Q. Liu, Y. Zhang, C. Li, Z. He, W. C. H. Choy, P. J. Low, P. Sonar, A. K. K. Kyaw, *Advanced Materials* **2020**, *32*, 2001591.

[24] L. Yin, H. Cheng, S. Mao, R. Haasch, Y. Liu, X. Xie, S. W. Hwang, H. Jain, S. K. Kang, Y. Su, R. Li, Y. Huang, J. A. Rogers, *Adv Funct Mater* **2014**, *24*, 645.

[25] T. Lei, M. Guan, J. Liu, H. C. Lin, R. Pfattner, L. Shaw, A. F. McGuire, T. C. Huang, L. Shao, K. T. Cheng, J. B. H. Tok, Z. Bao, *Proc Natl Acad Sci U S A* **2017**, *114*, 5107.

[26] S. M. Won, J. Koo, K. E. Crawford, A. D. Mickle, Y. Xue, S. Min, L. A. McIlvried, Y. Yan, S. B. Kim, S. M. Lee, B. H. Kim, H. Jang, M. R. MacEwan, Y. Huang, R. W. Gereau, J. A. Rogers, *Adv Funct Mater* **2018**, *28*, DOI 10.1002/adfm.201801819.

[27] S. H. Jin, S. K. Kang, I. T. Cho, S. Y. Han, H. U. Chung, D. J. Lee, J. Shin, G. W. Baek, T. Il Kim, J. H. Lee, J. A. Rogers, *ACS Appl Mater Interfaces* **2015**, *7*, 8268.

[28] Y. Chen, *Transient Electronics: Materials, Mechanics, and Applications*, **n.d.**

[29] M. A. Brenckle, H. Cheng, S. Hwang, H. Tao, M. Paquette, D. L. Kaplan, J. A. Rogers, Y. Huang, F. G. Omenetto, *ACS Appl Mater Interfaces* **2015**, *7*, 19870.

[30] S. Zhong, H. C. Wong, H. Y. Low, R. Zhao, *ACS Appl Mater Interfaces* **2021**, *13*, 904.

[31] A. Uva, A. Lin, J. Babi, H. Tran, *Journal of Chemical Technology & Biotechnology* **2022**, *97*, 801.

[32] S. K. Hwang, H. Tao, D. H. Kim, H. Cheng, J. K. Song, E. Rill, M. A. Brenckle, B. Panilaitis, S. M. Won, Y. S. Kim, Y. M. Song, K. J. Yu, A. Ameen, R. Li, Y. Su, M. Yang, D. L. Kaplan, M. R. Zakin, M. J. Slepian, Y. Huang, F. G. Omenetto, J. A. Rogers, *Science (1979)* **2012**, *337*, 1640.

[33] Z. W. Abdullah, Y. Dong, I. J. Davies, S. Barbhuiya, *Polymer - Plastics Technology and Engineering* **2017**, *56*, 1307.

[34] M. Julinová, L. Vaňharová, M. Jurča, *J Environ Manage* **2018**, *228*, 213.

[35] S. W. Hwang, J. K. Song, X. Huang, H. Cheng, S. K. Kang, B. H. Kim, J. H. Kim, S. Yu, Y. Huang, J. A. Rogers, *Advanced Materials* **2014**, *26*, 3905.

[36] J. K. Chang, H. P. Chang, Q. Guo, J. Koo, C. I. Wu, J. A. Rogers, *Advanced Materials* **2018**, *30*, DOI 10.1002/adma.201704955.

[37] S. Parandeh, M. Kharaziha, F. Karimzadeh, *Nano Energy* **2019**, *59*, 412.

[38] Y. Guo, M. Zhong, Z. Fang, P. Wan, G. Yu, *Nano Lett* **2019**, *19*, 1143.

[39] G. Li, L. Wang, X. Lei, Z. Peng, T. Wan, S. Maganti, M. Huang, V. Murugadoss, I. Seok, Q. Jiang, D. Cui, A. Alhadhrami, M. M. Ibrahim, H. Wei, *Adv Compos Hybrid Mater* **2022**, *5*, 853.

[40] C. Wang, K. Xia, Y. Zhang, D. L. Kaplan, *Acc Chem Res* **2019**, *52*, 2916.

[41] H. Tao, M. A. Brenckle, M. Yang, J. Zhang, M. Liu, S. M. Siebert, R. D. Averitt, M. S. Mannoor, M. C. McAlpine, J. A. Rogers, D. L. Kaplan, F. G. Omenetto, *Advanced Materials* **2012**, *24*, 1067.

[42] P. Singh, S. Magalhães, L. Alves, F. Antunes, M. Miguel, B. Lindman, B. Medronho, *Food Hydrocoll* **2019**, *88*, 68.

[43] J. Zhang, S. Hu, Z. Shi, Y. Wang, Y. Lei, J. Han, Y. Xiong, J. Sun, L. Zheng, Q. Sun, G. Yang, Z. L. Wang, *Nano Energy* **2021**, *89*, 106354.

[44] Y. Pang, F. Xi, J. Luo, G. Liu, T. Guo, C. Zhang, *RSC Adv* **2018**, *8*, 6719.

[45] S. Alesaeidi, M. S. Kahrizi, A. Ghorbani Tajani, H. Hajipour, M. Ghorbani, *J Polym Environ* **2023**, *31*, 396.

[46] M. Baumgartner, F. Hartmann, M. Drack, D. Preninger, D. Wirthl, R. Gerstmayr, L. Lehner, G. Mao, R. Pruckner, S. Demchyshyn, L. Reiter, M.

Strobel, T. Stockinger, D. Schiller, S. Kimeswenger, F. Greibich, G. Buchberger, E. Bradt, S. Hild, S. Bauer, M. Kaltenbrunner, *Nat Mater* **2020**, *19*, 1102.

[47] S. K. Ghosh, J. Park, S. Na, M. P. Kim, H. Ko, *Advanced Science* **2021**, *8*, DOI 10.1002/advs.202005010.

[48] H. Acar, S. Çinar, M. Thunga, M. R. Kessler, N. Hashemi, R. Montazami, *Adv Funct Mater* **2014**, *24*, 4135.

[49] Y. Gao, Y. Zhang, X. Wang, K. Sim, J. Liu, J. Chen, X. Feng, H. Xu, C. Yu, *Sci Adv* **2017**, *3*, DOI 10.1126/sciadv.1701222.

[50] H. Lopez Hernandez, S. K. Kang, O. P. Lee, S. W. Hwang, J. A. Kaitz, B. Inci, C. W. Park, S. Chung, N. R. Sottos, J. S. Moore, J. A. Rogers, S. R. White, *Advanced Materials* **2014**, *26*, 7637.

[51] Q. Zhou, Y. Liu, G. Yu, F. He, K. Chen, D. Xiao, X. Zhao, Y. Feng, J. Li, *Polym Degrad Stab* **2017**, *135*, 111.

[52] S. Zhong, X. Ji, L. Song, Y. Zhang, R. Zhao, *ACS Appl Mater Interfaces* **2018**, *10*, 36171.

[53] W. D. Chen, S. K. Kang, W. J. Stark, J. A. Rogers, R. N. Grass, *Sens Actuators B Chem* **2019**, *282*, 52.

[54] D. Liu, S. Zhang, H. Cheng, R. Peng, Z. Luo, *Sci Rep* **2019**, *9*, DOI 10.1038/s41598-019-54565-5.

[55] L. Teng, L. Li, J. Huang, S. Li, R. Hu, X. Zhou, H. Wang, *Adv Mater Technol* **2023**, *8*, DOI 10.1002/admt.202201031.

[56] J. Yoon, J. Lee, B. Choi, D. Lee, D. H. Kim, D. M. Kim, D. Il Moon, M. Lim, S. Kim, S. J. Choi, *Nano Res* **2017**, *10*, 87.

[57] G. Li, E. Song, G. Huang, Q. Guo, F. Ma, B. Zhou, Y. Mei, *Adv Funct Mater* **2018**, *28*, DOI 10.1002/adfm.201801448.

[58] C. W. Park, S. K. Kang, H. L. Hernandez, J. A. Kaitz, D. S. Wie, J. Shin, O. P. Lee, N. R. Sottos, J. S. Moore, J. A. Rogers, S. R. White, *Advanced Materials* **2015**, *27*, 3783.

[59] S. Lee, S. M. Silva, L. M. Caballero Aguilar, T. Eom, S. E. Moulton, B. S. Shim, *J Mater Chem B* **2022**, *10*, 8575.

[60] A. Dutta, H. Cheng, *Nanoscale* **2023**, *15*, 4236.

[61] C. Steiger, A. Abramson, P. Nadeau, A. P. Chandrakasan, R. Langer, G. Traverso, *Nat Rev Mater* **2018**, *4*, 83.

[62] R. Singh, M. J. Bathaei, E. Istif, L. Beker, *Adv Healthc Mater* **2020**, *9*, 2000790.

[63] A. Fanelli, D. Ghezzi, *Curr Opin Biotechnol* **2021**, *72*, 22.

[64] C. M. Boutry, L. Beker, Y. Kaizawa, C. Vassos, H. Tran, A. C. Hinckley, R. Pfattner, S. Niu, J. Li, J. Claverie, Z. Wang, J. Chang, P. M. Fox, Z. Bao, *Nat Biomed Eng* **2019**, *3*, 47.

[65] Y. S. Choi, H. Jeong, R. T. Yin, R. Avila, A. Pfenniger, J. Yoo, J. Y. Lee, A. Tzavelis, Y. J. Lee, S. W. Chen, H. S. Knight, S. Kim, H.-Y. Ahn, G. Wickerson, A. Vázquez-Guardado, E. Higbee-Dempsey, B. A. Russo, M. A. Napolitano, T. J. Holleran, L. A. Razzak, A. N. Miniovich, G. Lee, B. Geist, B. Kim, S. Han, J. A. Brennan, K. Aras, S. S. Kwak, J. Kim, E. A. Waters, X. Yang, A. Burrell, K. San Chun, C. Liu, C. Wu, A. Y. Rwei, A. N. Spann, A. Banks, D. Johnson, Z. J. Zhang, C. R. Haney, S. H. Jin, A. V. Sahakian, Y. Huang, G. D. Trachiotis, B. P. Knight, R. K. Arora, I. R. Efimov, J. A. Rogers, *Science (1979)* **2022**, *376*, 1006.

[66] W. Xu, H. Yang, W. Zeng, T. Houghton, X. Wang, R. Murthy, H. Kim, Y. Lin, M. Mignolet, H. Duan, H. Yu, M. Slepian, H. Jiang, *Adv Mater Technol* **2017**, *2*, DOI 10.1002/admt.201700181.

[67] Y. Wu, D. Ye, Y. Shan, S. He, Z. Su, J. Liang, J. Zheng, Z. Yang, H. Yang, W. Xu, H. Jiang, *Adv Mater Technol* **2020**, *5*, 2000100.

[68] A. S. Sharova, F. Melloni, G. Lanzani, C. J. Bettinger, M. Caironi, *Adv Mater Technol* **2021**, *6*, 2000757.

[69] J. Kim, I. Jeerapan, B. Ciui, M. C. Hartel, A. Martin, J. Wang, *Adv Healthc Mater* **2017**, *6*, DOI 10.1002/adhm.201700770.

[70] G. Balakrishnan, A. Bhat, D. Naik, J. S. Kim, S. Marukyan, L. Gido, M. Ritter, A. S. Khair, C. J. Bettinger, *Advanced Materials* **2023**, *35*, 2211581.

[71] G. Lee, S. K. Kang, S. M. Won, P. Gutruf, Y. R. Jeong, J. Koo, S. S. Lee, J. A. Rogers, J. S. Ha, *Adv Energy Mater* **2017**, *7*, DOI 10.1002/aenm.201700157.

[72] A. A. Mathew, A. Chandrasekhar, S. Vivekanandan, *Nano Energy* **2021**, *80*, 105566.

[73] P. Cataldi, L. Lamanna, C. Bertei, F. Arena, P. Rossi, M. Liu, F. Di Fonzo, D. G. Papageorgiou, A. Luzio, M. Caironi, *Adv Funct Mater* **2022**, *32*, DOI 10.1002/adfm.202113417.

[74] Y. Zhu, W. Lu, Y. Guo, Y. Chen, Y. Wu, H. Lu, *RSC Adv* **2018**, *8*, 36999.

[75] X. Ji, L. Song, S. Zhong, Y. Jiang, K. G. Lim, C. Wang, R. Zhao, *Journal of Physical Chemistry C* **2018**, *122*, 16909.

[76] H. Tran, V. R. Feig, K. Liu, H. C. Wu, R. Chen, J. Xu, K. Deisseroth, Z. Bao, *ACS Cent Sci* **2019**, *5*, 1884.

[77] S. Barua, H. S. Dutta, S. Gogoi, R. Devi, R. Khan, *ACS Appl Nano Mater* **2018**, *1*, 2.

[78] X. Chen, Y. J. Park, M. Kang, S. K. Kang, J. Koo, S. M. Shinde, J. Shin, S. Jeon, G. Park, Y. Yan, M. R. MacEwan, W. Z. Ray, K. M. Lee, J. A. Rogers, J. H. Ahn, *Nat Commun* **2018**, *9*, DOI 10.1038/s41467-018-03956-9.

[79] C. Yoo, M. G. Kaium, L. Hurtado, H. Li, H. Li, S. Rassay, J. Ma, T. J. Ko, S. S. Han, S. S. Han, M. S. Shawkat, M. S. Shawkat, K. H. Oh, H. S. Chung, Y. Jung, Y. Jung, Y. Jung, *ACS Appl Mater Interfaces* **2020**, *12*, 25200.

[80] Q. Chang, L. Li, L. Sai, W. Shi, L. Huang, *Adv Electron Mater* **2018**, *4*, 1.

[81] T. Tu, B. Liang, Q. Cao, L. Fang, Q. Zhu, Y. Cai, X. Ye, *RSC Adv* **2020**, *10*, 7241.

[82] A. Pullanchiyodan, L. Manjakkal, S. Dervin, D. Shakthivel, R. Dahiya, *Adv Mater Technol* **2020**, *5*, DOI 10.1002/admt.201901107.

[83] M. B. Durukan, R. Yuksel, H. E. Unalan, *Electrochim Acta* **2016**, *222*, 1475.

[84] I. B. Dogru, M. B. Durukan, O. Turel, H. E. Unalan, *Progress in Natural Science: Materials International* **2016**, *26*, 232.

[85] X. Peng, K. Dong, C. Ye, Y. Jiang, S. Zhai, R. Cheng, D. Liu, X. Gao, J. Wang, Z. L. Wang, *Sci Adv* **2020**, *6*, DOI 10.1126/sciadv.aba9624.

[86] A. Elsayes, V. Sharma, K. Yiannacou, A. Koivikko, A. Rasheed, V. Sariola, *Adv Sustain Syst* **2020**, *2000056*, DOI 10.1002/adsu.202000056.

[87] M. O. Cicek, D. Doganay, M. B. Durukan, M. C. Gorur, H. E. Unalan, *Adv Mater Technol* **2021**, *2001168*, 1.

[88] X. Huang, D. Wang, Z. Yuan, W. Xie, Y. Wu, R. Li, Y. Zhao, D. Luo, L. Cen, B. Chen, H. Wu, H. Xu, X. Sheng, M. Zhang, L. Zhao, L. Yin, *Small* **2018**, *14*, 1.

[89] H. Li, C. Zhao, X. Wang, J. Meng, Y. Zou, S. Noreen, L. Zhao, Z. Liu, H. Ouyang, P. Tan, M. Yu, Y. Fan, Z. L. Wang, Z. Li, *Advanced Science* **2019**, *6*, DOI 10.1002/advs.201801625.

[90] L. Liu, H. Liang, J. Zhang, P. Zhang, Q. Xu, Q. Lu, C. Zhang, *J Clean Prod* **2018**, *195*, 786.

[91] I. Bayraktar, D. Doganay, S. Coskun, C. Kaynak, G. Akca, H. E. Unalan, *Compos B Eng* **2019**, *172*, 671.

[92] S. W. Hwang, J. K. Song, X. Huang, H. Cheng, S. K. Kang, B. H. Kim, J. H. Kim, S. Yu, Y. Huang, J. A. Rogers, *Advanced Materials* **2014**, *26*, 3905.

[93] L. Liu, H. Liang, J. Zhang, P. Zhang, Q. Xu, Q. Lu, C. Zhang, *J Clean Prod* **2018**, *195*, 786.

[94] S. Verma, Gaganjot, J. Tripathi, M. Katiyar, V. Verma, *Appl Mater Today* **2018**, *13*, 83.

[95] G. Lee, S. K. Kang, S. M. Won, P. Gutruf, Y. R. Jeong, J. Koo, S. S. Lee, J. A. Rogers, J. S. Ha, *Adv Energy Mater* **2017**, *7*, 1.

[96] K. Fu, Z. Wang, C. Yan, Z. Liu, Y. Yao, J. Dai, E. Hitz, Y. Wang, W. Luo, Y. Chen, M. Kim, L. Hu, *Adv Energy Mater* **2016**, *6*, 1.

[97] S. W. Hwang, D. H. Kim, H. Tao, T. Il Kim, S. Kim, K. J. Yu, B. Panilaitis, J. W. Jeong, J. K. Song, F. G. Omenetto, J. A. Rogers, *Adv Funct Mater* **2013**, *23*, 4087.

[98] M. S. B. Husain, A. Gupta, B. Y. Alashwal, S. Sharma, *Energy Sources, Part A: Recovery, Utilization and Environmental Effects* **2018**, *40*, 2388.

[99] A. Kumar, S. S. Han, *International Journal of Polymeric Materials and Polymeric Biomaterials* **2017**, *66*, 159.

[100] M. Liao, H. Liao, J. Ye, P. Wan, L. Zhang, *ACS Appl Mater Interfaces* **2019**, *11*, 47358.

[101] S. Çinar, R. Jamshidi, Y. Chen, N. Hashemi, R. Montazami, *J Polym Sci B Polym Phys* **2016**, *54*, 517.

[102] W. B. Han, J. H. Lee, J. W. Shin, S. W. Hwang, *Advanced Materials* **2020**, *32*, 1.

[103] A. Das, R. Uppaluri, C. Das, *Int J Biol Macromol* **2019**, *131*, 998.

[104] S. Peng, X. Jiang, X. Xiang, K. Chen, G. Chen, X. Jiang, L. Hou, *Electrochim Acta* **2019**, *324*, DOI 10.1016/j.electacta.2019.134874.

[105] H. N. Fard, G. B. Pour, M. N. Sarvi, P. Esmaili, *Ionics (Kiel)* **2019**, *25*, 2951.

[106] S. Alipoori, S. Mazinani, S. H. Aboutalebi, F. Sharif, *J Energy Storage* **2020**, *27*, 101072.

[107] K. Sun, E. Feng, G. Zhao, H. Peng, G. Wei, Y. Lv, G. Ma, *ACS Sustain Chem Eng* **2019**, *7*, 165.

[108] X. Chen, A. Yusuf, J. S. del Rio, D. Y. Wang, *Nano Energy* **2021**, *81*, 105656.

[109] X. Jing, H. Li, H. Mi, Y. Liu, P. Feng, Y. Tan, *Sens Actuators B Chem* **2019**, *295*, 159.

[110] J. Huang, M. Zhao, Y. Cai, M. Zimniewska, D. Li, Q. Wei, **2020**, *1900934*, 1.

[111] M. B. Durukan, M. O. Cicek, D. Doganay, M. C. Gorur, S. Çınar, H. E. Unalan, *Adv Funct Mater* **2022**, *32*, 1.

[112] H. I. Becker, *Low Voltage Electrolytic Capacitor*, **1957**.

[113] B. K. Kim, S. Sy, A. Yu, J. Zhang, in *Handbook of Clean Energy Systems*, John Wiley & Sons, Ltd, Chichester, UK, **2015**, pp. 1–25.

[114] F. Beguin, E. Frackowiak, *Supercapacitors*, Wiley, **2013**.

[115] R. Kotz, M. Carlen, *Electrochim Acta* **2000**, *45*, 2483.

[116] B. E. Conway, *Electrochemical Supercapacitors*, Springer US, Boston, MA, **1999**.

[117] P. Simon, Y. Gogotsi, *Nat Mater* **2008**, *7*, 845.

[118] "Maxwell Technologies," can be found under https://maxwell.com/, **n.d.**

[119] *Energy Storage Application Brief*, **n.d.**

[120] "Cap-XX," can be found under https://www.cap-xx.com/, **n.d.**

[121] *CAPMOD Data Sheet*, **2022**.

[122] *SuperBattery-Sustainable and Safe*, **2022**.

[123] "Capacitech Energy," can be found under https://www.capacitechenergy.com/, **n.d.**

[124] *SCP Series PrizmaCap^{TM} 2.5V Series*, **n.d.**

[125] K. Welch, "Samsung announces Galaxy Note 9 with bigger screen, huge battery, and more powerful S Pen," can be found under https://www.theverge.com/circuitbreaker/2018/8/9/17658576/samsung-galaxy-note-9-specs-price-release-date-camera-screen-battery-2018, **2018**.

[126] M. Horn, J. MacLeod, M. Liu, J. Webb, N. Motta, *Econ Anal Policy* **2019**, *61*, 93.

[127] *Automotive Applications for Skeleton's Energy Storage Solutions*, **n.d.**

[128] J. Pikkarainen, "Wind Turbine Pitch Control - Ultracapacitors solving unreliability & unpredictability with the lowest TCO," can be found under https://www.skeletontech.com/skeleton-blog/wind-turbine-pitch-control-ultracapacitors-solving-unreliability-unpredictability, **2019**.

[129] *Ultracapacitor Solutions to Adress Energy Storage Needs of Vehicles*, **n.d.**

[130] P. Simon, Y. Gogotsi, B. Dunn, *Science (1979)* **2014**, *343*, 1210.

[131] S. M. Benoy, M. Pandey, D. Bhattacharjya, B. K. Saikia, *J Energy Storage* **2022**, *52*, 104938.

[132] P. Simon, Y. Gogotsi, *Nat Mater* **2020**, *19*, 1151.

[133] B. Xu, H. Zhang, H. Mei, D. Sun, *Coord Chem Rev* **2020**, *420*, 213438.

[134] Helmholtz, *Ann Phys* **1853**, *165*, 211.

[135] M. Gouy, *Journal de Physique Théorique et Appliquée* **1910**, *9*, 457.

[136] D. L. Chapman, *Philosophical Magazine Series 6* **1913**, *25*, 475.

[137] O. Stern, *Zeitschrift fur Elektrochemie* **1924**, *30*, 508.

[138] L. L. Zhang, X. S. Zhao, *Chem Soc Rev* **2009**, *38*, 2520.

[139] A. G. Pandolfo, A. F. Hollenkamp, *J Power Sources* **2006**, *157*, 11.

[140] Y. Zhu, S. Murali, W. Cai, X. Li, J. W. Suk, J. R. Potts, R. S. Ruoff, *Advanced Materials* **2010**, *22*, 3906.

[141] C. Kim, K. S. Yang, *Appl Phys Lett* **2003**, *83*, 1216.

[142] M. Kim, Y. Kim, K. M. Lee, S. Y. Jeong, E. Lee, S. H. Baeck, S. E. Shim, *Carbon N Y* **2016**, *99*, 607.

[143] E. Frackowiak, F. Béguin, *Carbon N Y* **2002**, *40*, 1775.

[144] D. Pech, M. Brunet, H. Durou, P. Huang, V. Mochalin, Y. Gogotsi, P.-L. Taberna, P. Simon, *Nat Nanotechnol* **2010**, *5*, 651.

[145] M. Zeiger, N. Jäckel, V. N. Mochalin, V. Presser, *J. Mater. Chem. A* **2016**, *4*, 3172.

[146] J. Chmiola, G. Yushin, Y. Gogotsi, C. Portet, P. Simon, P. L. Taberna, *Science (1979)* **2006**, *313*, 1760.

[147] S. D. Argade, E. Gileadi, *The Potential of Zero Charge*, **1967**.

[148] A. Frumkin, F. J. Cirves, *J Phys Chem* **1930**, *34*, 74.

[149] H. Shao, Y.-C. Wu, Z. Lin, P.-L. Taberna, P. Simon, *Chem Soc Rev* **2020**, *49*, 3005.

[150] C. Largeot, C. Portet, J. Chmiola, P. L. Taberna, Y. Gogotsi, P. Simon, *J Am Chem Soc* **2008**, *130*, 2730.

[151] B. E. Conway, E. Gileadi, *Transactions of the Faraday Society* **1962**, *58*, 2493.

[152] S. Trasatti, G. Buzzanca, *J Electroanal Chem Interfacial Electrochem* **1971**, *29*, A1.

[153] T. Brousse, D. Belanger, J. W. Long, *J. Electrochemical Soc.* **2015**, *162*, A5185.

[154] P. Kumari, K. Khawas, S. Nandy, B. K. Kuila, *Electrochim Acta* **2016**, *190*, 596.

[155] H. Park, J. W. Kim, S. Y. Hong, G. Lee, D. S. Kim, J. hyun Oh, S. W. Jin, Y. R. Jeong, S. Y. Oh, J. Y. Yun, J. S. Ha, *Adv Funct Mater* **2018**, *28*, 1.

[156] G. A. Snook, P. Kao, A. S. Best, *J Power Sources* **2011**, *196*, 1.

[157] Y. Gogotsi, R. M. Penner, *ACS Nano* **2018**, *12*, 2081.

[158] V. Augustyn, P. Simon, B. Dunn, *Energy Environ Sci* **2014**, *7*, 1597.

[159] T. Brousse, D. Bélanger, J. W. Long, *J Electrochem Soc* **2015**, *162*, A5185.

[160] D. Xuan, W. Chengyang, C. Mingming, J. Yang, W. Jin, *Journal of Physical Chemistry C* **2009**, *113*, 2643.

[161] W. Wei, X. Cui, W. Chen, D. G. Ivey, *Chem. Soc. Rev.* **2011**, *40*, 1697.

[162] M. Aghazadeh, M. Asadi, M. G. Maragheh, M. R. Ganjali, P. Norouzi, F. Faridbod, *Appl Surf Sci* **2016**, *364*, 726.

[163] M. B. Durukan, R. Yuksel, H. E. Unalan, *Electrochim Acta* **2016**, *222*, 1475.

[164] R. Kumar, R. K. Singh, R. Savu, P. K. Dubey, P. Kumar, S. A. Moshkalev, *RSC Adv* **2016**, *6*, 26612.

[165] S. Fleischmann, J. B. Mitchell, R. Wang, C. Zhan, D. Jiang, V. Presser, V. Augustyn, *Chem Rev* **2020**, *120*, 6738.

[166] G. H. Han, D. L. Duong, D. H. Keum, S. J. Yun, Y. H. Lee, *Chem Rev* **2018**, *118*, 6297.

[167] W. Choi, N. Choudhary, G. H. Han, J. Park, D. Akinwande, Y. H. Lee, *Materials Today* **2017**, *20*, 116.

[168] N. S. Arul, V. D. Nithya, *Two Dimensional Transition Metal Dichalcogenides: Synthesis, Properties, and Applications*, Springer Singapore, Singapore, **2019**.

[169] M. S. Whittingham, F. R. Gamble, *THE LITHIUM INTERCALATES OF THE TRANSITION METAL DICHALCOGENIDES*, Pergamon, **1975**.

[170] M. Acerce, D. Voiry, M. Chhowalla, *Nat Nanotechnol* **2015**, *10*, 313.

[171] W. Chen, X. Yu, Z. Zhao, S. Ji, L. Feng, *Electrochim Acta* **2019**, *298*, 313.

[172] Q. Ke, X. Zhang, W. Zang, A. M. Elshahawy, Y. Hu, Q. He, S. J. Pennycook, Y. Cai, J. Wang, *Small* **2019**, *15*, DOI 10.1002/smll.201900131.

[173] M. Naguib, V. N. Mochalin, M. W. Barsoum, Y. Gogotsi, *Advanced Materials* **2014**, *26*, 992.

[174] B. Anasori, M. R. Lukatskaya, Y. Gogotsi, *Nat Rev Mater* **2017**, *2*, 16098.

[175] H. Li, M. Eddaoudi, M. O'Keeffe, O. M. Yaghi, *Nature* **1999**, *402*, 276.

[176] S. S.-Y. Chui, S. M.-F. Lo, J. P. H. Charmant, A. G. Orpen, I. D. Williams, *Science (1979)* **1999**, *283*, 1148.

[177] A. J. Howarth, Y. Liu, P. Li, Z. Li, T. C. Wang, J. T. Hupp, O. K. Farha, *Nat Rev Mater* **2016**, *1*, 15018.

[178] C. Férey, C. Mellot-Draznieks, C. Serre, F. Millange, J. Dutour, S. Surblé, I. Margiolaki, *Science (1979)* **2005**, *309*, 2040.

[179] W. Xia, *Fabrication of Metal–Organic Framework Derived Nanomaterials and Their Electrochemical Applications*, Springer Singapore, Singapore, **2018**.

[180] O. K. Farha, I. Eryazici, N. C. Jeong, B. G. Hauser, C. E. Wilmer, A. A. Sarjeant, R. Q. Snurr, S. T. Nguyen, A. Ö. Yazaydin, J. T. Hupp, *J Am Chem Soc* **2012**, *134*, 15016.

[181] K. Rajaram, S. M. Yang, S.-W. Hwang, *Advanced Energy and Sustainability Research* **2022**, *3*, 2100223.

[182] Z. Wang, K. K. Fu, Z. Liu, Y. Yao, J. Dai, Y. Wang, B. Liu, L. Hu, *Adv Funct Mater* **2017**, *27*, DOI 10.1002/adfm.201605724.

[183] L. A. Wehner, N. Mittal, T. Liu, M. Niederberger, *ACS Cent Sci* **2021**, *7*, 231.

[184] L. Yin, X. Huang, H. Xu, Y. Zhang, J. Lam, J. Cheng, J. A. Rogers, *Advanced Materials* **2014**, *26*, 3879.

[185] I. K. Ilic, V. Galli, L. Lamanna, P. Cataldi, L. Pasquale, V. F. Annese, A. Athanassiou, M. Caironi, *Advanced Materials* **2023**, *35*, 2211400.

[186] N. Mittal, A. Ojanguren, N. Cavasin, E. Lizundia, M. Niederberger, *Adv Funct Mater* **2021**, *31*, DOI 10.1002/adfm.202101827.

[187] S. Yamada, *ACS Appl Mater Interfaces* **2022**, *14*, 26595.

[188] K. Chen, L. Yan, Y. Sheng, Y. Ma, L. Qu, Y. Zhao, *ACS Nano* **2022**, *16*, 15261.

[189] C. Chen, Y. Zhang, Y. Li, J. Dai, J. Song, Y. Yao, Y. Gong, I. Kierzewski, J. Xie, L. Hu, *Energy Environ Sci* **2017**, *10*, 538.

[190] S. Peng, S. Liu, Y. Sun, N. Xiang, X. Jiang, L. Hou, *Eur Polym J* **2018**, *106*, 206.

[191] S. Çinar, R. Jamshidi, Y. Chen, N. Hashemi, R. Montazami, *J Polym Sci B Polym Phys* **2016**, *54*, 517.

[192] H. Acar, S. Çinar, M. Thunga, M. R. Kessler, N. Hashemi, R. Montazami, *Adv Funct Mater* **2014**, *24*, 4135.

[193] S. K. Mallapragada, N. A. Peppas, *J Polym Sci B Polym Phys* **1996**, *34*, 1339.

[194] B. Electrolytes, S. B. Aziz, A. S. Marf, E. M. A. Dannoun, M. A. Brza, *Polymers (Basel)* **2020**, *12*, 1.

[195] J. Jang, D. K. Lee, *Polymer (Guildf)* **2003**, *44*, 8139.

[196] L. Y. Lim, L. S. C. Wan, *Drug Dev Ind Pharm* **1994**, *20*, 1007.

[197] F. Reguieg, L. Ricci, N. Bouyacoub, M. Belbachir, M. Bertoldo, *Polymer Bulletin* **2020**, *77*, 929.

[198] N. S. Alghunaim, *Results Phys* **2016**, *6*, 456.

[199] E. Y. Malikov, M. B. Muradov, O. H. Akperov, G. M. Eyvazova, R. Puskás, D. Madarász, L. Nagy, Á. Kukovecz, Z. Kónya, *Physica E Low Dimens Syst Nanostruct* **2014**, *61*, 129.

[200] J. Xu, L. Chen, H. Qu, Y. Jiao, J. Xie, G. Xing, *Appl Surf Sci* **2014**, *320*, 674.

[201] S. Lu, H. Wang, J. Zhou, X. Wu, W. Qin, *Nanoscale* **2017**, *9*, 1184.

[202] S. M. Lyth, W. Ma, J. Liu, T. Daio, K. Sasaki, A. Takahara, B. Ameduri, *Nanoscale* **2015**, *7*, 16087.

[203] M. J. Rampe, B. Setiaji, W. Trisunaryanti, T. Triyono, *Indonesian Journal of Chemistry* **2011**, *11*, 124.

[204] M. T. Taghizadeh, N. Sabouri, **2013**, *1*, 21.

[205] K. Gulati, S. Lal, P. K. Diwan, S. Arora, *International Journal of Applied Engineering Research* **2019**, *14*, 170.

[206] T. S. Mathis, N. Kurra, X. Wang, D. Pinto, P. Simon, Y. Gogotsi, *Adv Energy Mater* **2019**, *9*, 1.

[207] G. Lee, S. K. Kang, S. M. Won, P. Gutruf, Y. R. Jeong, J. Koo, S. S. Lee, J. A. Rogers, J. S. Ha, *Adv Energy Mater* **2017**, *7*, 1.

[208] R. K. Pal, S. C. Kundu, V. K. Yadavalli, *ACS Appl Mater Interfaces* **2018**, *10*, 9620.

[209] Q. Yang, Z. Huang, X. Li, Z. Liu, H. Li, G. Liang, D. Wang, Q. Huang, S. Zhang, S. Chen, C. Zhi, *ACS Nano* **2019**, *13*, 8275.

[210] H. Lee, G. Lee, J. Yun, K. Keum, S. Y. Hong, C. Song, J. W. Kim, J. H. Lee, S. Y. Oh, D. S. Kim, M. S. Kim, J. S. Ha, *Chemical Engineering Journal* **2019**, *366*, 62.

[211] Q. Chang, L. Li, L. Sai, W. Shi, L. Huang, *Adv Electron Mater* **2018**, *4*, 1.

[212] C. Lu, X. Chen, *Nano Lett* **2020**, *20*, 1907.

[213] H. Park, J. W. Kim, S. Y. Hong, G. Lee, D. S. Kim, J. hyun Oh, S. W. Jin, Y. R. Jeong, S. Y. Oh, J. Y. Yun, J. S. Ha, *Adv Funct Mater* **2018**, *28*, 1.

[214] S. Hong, J. Lee, K. Do, M. Lee, J. H. Kim, S. Lee, D. H. Kim, *Adv Funct Mater* **2017**, *27*, 1.

[215] Y. Wang, Y. Zhang, G. Wang, X. Shi, Y. Qiao, J. Liu, H. Liu, A. Ganesh, L. Li, *Adv Funct Mater* **2020**, *30*, 1.

[216] H. Sun, Y. Zhang, J. Zhang, X. Sun, H. Peng, *Nat Rev Mater* **2017**, *2*, 1.

[217] W. G. Kim, D. W. Kim, I. W. Tcho, J. K. Kim, M. S. Kim, Y. K. Choi, *ACS Nano* **2021**, *15*, 258.

[218] Z. L. Wang, *Adv Energy Mater* **2020**, *10*, 1.

[219] J. Luo, W. Gao, Z. L. Wang, *Advanced Materials* **2021**, *2004178*, 1.

[220] R. Zhang, M. Hummelgård, J. Örtegren, M. Olsen, H. Andersson, Y. Yang, H. Zheng, H. Olin, *Nano Energy* **2021**, *86*, 106041.

[221] S. Hellström, *ESD — The Scourge of Electronics*, Springer Berlin Heidelberg, **1998**.

[222] D. J. Lacks, T. Shinbrot, *Nat Rev Chem* **2019**, *3*, 465.

[223] Q. Lu, M. Sun, B. Huang, Z. L. Wang, *Advanced Energy and Sustainability Research* **2021**, *2*, 2000087.

[224] C. Xu, Y. Zi, A. C. Wang, H. Zou, Y. Dai, X. He, P. Wang, Y. C. Wang, P. Feng, D. Li, Z. L. Wang, *Advanced Materials* **2018**, *30*, 1.

[225] J. Shao, M. Willatzen, Z. L. Wang, *J Appl Phys* **2020**, *128*, DOI 10.1063/5.0020961.

[226] H. Zou, Y. Zhang, L. Guo, P. Wang, X. He, G. Dai, H. Zheng, C. Chen, A. C. Wang, C. Xu, Z. L. Wang, *Nat Commun* **2019**, *10*, 1.

[227] J. Lowell, A. C. Rose-Innes, *Adv Phys* **1980**, *29*, 947.

[228] Z. L. Wang, A. C. Wang, *Materials Today* **2019**, *30*, 34.

[229] S. Lin, L. Xu, C. Xu, X. Chen, A. C. Wang, B. Zhang, P. Lin, Y. Yang, H. Zhao, Z. L. Wang, *Advanced Materials* **2019**, *31*, 1.

[230] S. Lin, L. Xu, L. Zhu, X. Chen, Z. L. Wang, *Advanced Materials* **2019**, *31*, 1.

[231] M. I. Kornfeld, *J Phys D Appl Phys* **1976**, *9*, 1183.

[232] M. Meunier, N. Quirke, *Journal of Chemical Physics* **2000**, *113*, 369.

[233] L. S. McCarty, G. M. Whitesides, *Angewandte Chemie - International Edition* **2008**, *47*, 2188.

[234] A. F. Diaz, *Journal of Adhesion* **1998**, *67*, 111.

[235] J. Lowell, *J Phys D Appl Phys* **1977**, *10*, DOI 10.1088/0022-3727/10/17/001.

[236] H. T. Baytekin, A. Z. Patashinski, M. Branicki, B. Baytekin, S. Soh, B. A. Grzybowski, *Science (1979)* **2011**, *333*, 308.

[237] B. Baytekin, H. T. Baytekin, B. A. Grzybowski, *J Am Chem Soc* **2012**, *134*, 7223.

[238] M. Sakaguchi, Y. Miwa, S. Hara, Y. Sugino, K. Yamamoto, S. Shimada, *J Electrostat* **2004**, *62*, 35.

[239] F. R. Fan, L. Lin, G. Zhu, W. Wu, R. Zhang, Z. L. Wang, *Nano Lett* **2012**, *12*, 3109.

[240] W. Zhong, B. Xu, Y. Gao, *Nano Energy* **2022**, *92*, DOI 10.1016/j.nanoen.2021.106782.

[241] H. S. Wang, C. K. Jeong, M. H. Seo, D. J. Joe, J. H. Han, J. B. Yoon, K. J. Lee, *Nano Energy* **2017**, *35*, 415.

[242] L. Liu, X. Yang, L. Zhao, W. Xu, J. Wang, Q. Yang, Q. Tang, *Nano Energy* **2020**, *73*, DOI 10.1016/j.nanoen.2020.104797.

[243] M. A. P. Mahmud, J. J. Lee, G. H. Kim, H. J. Lim, K. B. Choi, *Microelectron Eng* **2016**, *159*, 102.

[244] Z. Fang, K. H. Chan, X. Lu, C. F. Tan, G. W. Ho, *J Mater Chem A Mater* **2017**, *6*, 52.

[245] Y. Xi, F. Zhang, Y. Shi, *Nano Energy* **2021**, *79*, DOI 10.1016/j.nanoen.2020.105432.

[246] W. Yang, X. Wang, H. Li, J. Wu, Y. Hu, Z. Li, H. Liu, *Nano Energy* **2019**, *57*, 41.

[247] D. Tantraviwat, P. Buarin, S. Suntalelat, W. Sripumkhai, P. Pattamang, G. Rujijanagul, B. Inceesungvorn, *Nano Energy* **2020**, *67*, DOI 10.1016/j.nanoen.2019.104214.

[248] A. S. Bhavya, H. Varghese, A. Chandran, K. P. Surendran, *Nano Energy* **2021**, *90*, DOI 10.1016/j.nanoen.2021.106628.

[249] J. Ahn, Z. J. Zhao, J. Choi, Y. Jeong, S. Hwang, J. Ko, J. Gu, S. Jeon, J. Park, M. Kang, D. V. Del Orbe, I. Cho, H. Kang, M. Bok, J. H. Jeong, I. Park, *Nano Energy* **2021**, *85*, DOI 10.1016/j.nanoen.2021.105978.

[250] Y. Liu, J. Mo, Q. Fu, Y. Lu, N. Zhang, S. Wang, S. Nie, *Adv Funct Mater* **2020**, *30*, DOI 10.1002/adfm.202004714.

[251] S. Wang, Y. Zi, Y. S. Zhou, S. Li, F. Fan, L. Lin, Z. L. Wang, *J Mater Chem A Mater* **2016**, *4*, 3728.

[252] J. Xu, Y. Zou, A. Nashalian, J. Chen, *Front Chem* **2020**, *8*, DOI 10.3389/fchem.2020.577327.

[253] G. Song, Y. Kim, S. Yu, M. O. Kim, S. H. Park, S. M. Cho, D. B. Velusamy, S. H. Cho, K. L. Kim, J. Kim, E. Kim, C. Park, *Chemistry of Materials* **2015**, *27*, 4749.

[254] K. E. Byun, Y. Cho, M. Seol, S. Kim, S. W. Kim, H. J. Shin, S. Park, S. Hwang, *ACS Appl Mater Interfaces* **2016**, *8*, 18519.

[255] W. Sun, D. Yang, N. Luo, H. Li, D. Wang, *New Journal of Chemistry* **2022**, *46*, 15645.

[256] H. Feng, H. Li, J. Xu, Y. Yin, J. Cao, R. Yu, B. Wang, R. Li, G. Zhu, *Nano Energy* **2022**, *98*, DOI 10.1016/j.nanoen.2022.107279.

[257] S. H. Park, J. Lee, D. S. Kong, J. Choi, H. Jung, Y. J. Park, H. M. Park, J. H. Jung, M. Lee, *Small Methods* **2023**, *7*, DOI 10.1002/smtd.202300097.

[258] J. Seo, S. Hajra, M. Sahu, H. J. Kim, *Mater Lett* **2021**, *304*, DOI 10.1016/j.matlet.2021.130674.

[259] J. Wang, K. Xia, J. liu, T. Li, X. Zhao, B. Shu, H. Li, J. Guo, M. Yu, W. Tang, Z. Zhu, *Nano Energy* **2020**, *69*, DOI 10.1016/j.nanoen.2020.104461.

[260] Y. Fan, S. Li, X. Tao, Y. Wang, Z. Liu, H. Chen, Z. Wu, J. Zhang, F. Ren, X. Chen, E. Fu, *Nano Energy* **2021**, *90*, DOI 10.1016/j.nanoen.2021.106574.

[261] G. I. Dzhardimalieva, B. C. Yadav, T. V. Lifintseva, I. E. Uflyand, *Eur Polym J* **2021**, *142*, DOI 10.1016/j.eurpolymj.2020.110163.

[262] Y. Yu, X. Wang, *Extreme Mech Lett* **2016**, *9*, 514.

[263] H. Xiang, Y. Zeng, X. Huang, N. Wang, X. Cao, Z. L. Wang, *Small* **2022**, *18*, 2107222.

[264] K. P. Gregory, G. R. Elliott, H. Robertson, A. Kumar, E. J. Wanless, G. B. Webber, V. S. J. Craig, G. G. Andersson, A. J. Page, *Physical Chemistry Chemical Physics* **2022**, *24*, 12682.

[265] H. Ryu, J. H. Lee, T. Y. Kim, U. Khan, J. H. Lee, S. S. Kwak, H. J. Yoon, S. W. Kim, *Adv Energy Mater* **2017**, *7*, DOI 10.1002/aenm.201700289.

[266] J. Y. Cheong, J. S. C. Koay, R. Chen, K. C. Aw, T. S. Velayutham, B. Chen, J. Li, C. Y. Foo, W. C. Gan, *Nano Energy* **2021**, *90*, DOI 10.1016/j.nanoen.2021.106616.

[267] Y. Wu, Y. Mu, Y. Luo, C. Menon, Z. Zhou, P. K. Chu, S. P. Feng, *Adv Funct Mater* **2022**, *32*, DOI 10.1002/adfm.202110859.

[268] H. Park, S. J. Oh, D. Kim, M. Kim, C. Lee, H. Joo, I. Woo, J. W. Bae, J. H. Lee, *Advanced Science* **2022**, *9*, DOI 10.1002/advs.202201070.

[269] Y. Wu, T. J. Cuthbert, Y. Luo, P. K. Chu, C. Menon, *Small* **2023**, *19*, 2301381.

[270] K. Ghosh, C. Iffelsberger, M. Konečný, J. Vyskočil, J. Michalička, M. Pumera, *Adv Energy Mater* **2023**, *13*, 2203476.

[271] C. Park, M. Koo, G. Song, S. M. Cho, H. S. Kang, T. H. Park, E. H. Kim, C. Park, *ACS Nano* **2020**, *14*, 755.

[272] Y. Liu, J. Ping, Y. Ying, *Adv Funct Mater* **2021**, *31*, 2009994.

[273] R. Zhang, H. Olin, *ACS Nanoscience Au* **2022**, *2*, 12.

[274] R. Zhang, J. Örtegren, M. Hummelgård, M. Olsen, H. Andersson, H. Olin, *Nanotechnology* **2022**, *33*, 212003.

[275] H. Jiang, H. Lei, Z. Wen, J. Shi, D. Bao, C. Chen, J. Jiang, Q. Guan, X. Sun, S. T. Lee, *Nano Energy* **2020**, *75*, DOI 10.1016/j.nanoen.2020.105011.

[276] Y. Nan, X. Wang, H. Xu, Y. Wu, H. Zhou, Y. Sun, T. Yu, Y. Huang, *Nano Energy* **2023**, *110*, 108345.

[277] N. Wang, D. Yang, W. Zhang, M. Feng, Z. Li, E. Ye, X. J. Loh, D. Wang, *ACS Appl Mater Interfaces* **2023**, *15*, 997.

[278] S. A. Lone, K. C. Lim, K. Kaswan, S. Chatterjee, K.-P. Fan, D. Choi, S. Lee, H. Zhang, J. Cheng, Z.-H. Lin, *Nano Energy* **2022**, *99*, 107318.

[279] M. Kim, D. Park, M. M. Alam, S. Lee, P. Park, J. Nah, *ACS Nano* **2019**, *13*, 4640.

[280] J. Kim, H. Ryu, J. H. Lee, U. Khan, S. S. Kwak, H. J. Yoon, S. W. Kim, *Adv Energy Mater* **2020**, *10*, DOI 10.1002/aenm.201903524.

[281] J. Chen, H. Guo, X. He, G. Liu, Y. Xi, H. Shi, C. Hu, *ACS Appl Mater Interfaces* **2016**, *8*, 736.

[282] J. Chun, J. W. Kim, W. S. Jung, C. Y. Kang, S. W. Kim, Z. L. Wang, J. M. Baik, *Energy Environ Sci* **2015**, *8*, 3006.

[283] I. Appamato, W. Bunriw, V. Harnchana, C. Siriwong, W. Mongkolthanaruk, P. Thongbai, C. Chanthad, A. Chompoosor, S. Ruangchai, T. Prada, V. Amornkitbamrung, *ACS Appl Mater Interfaces* **2023**, *15*, 973.

[284] X. Liang, T. Zhao, W. Jiang, X. Yu, Y. Hu, P. Zhu, H. Zheng, R. Sun, C. P. Wong, *Nano Energy* **2019**, *59*, 508.

[285] D. Doganay, M. O. Cicek, M. B. Durukan, B. Altuntas, E. Agbahca, S. Coskun, H. E. Unalan, *Nano Energy* **2021**, *89*, DOI 10.1016/j.nanoen.2021.106412.

[286] X. Luo, L. Zhu, Y. C. Wang, J. Li, J. Nie, Z. L. Wang, *Adv Funct Mater* **2021**, *31*, DOI 10.1002/adfm.202104928.

[287] L. Shi, H. Jin, S. Dong, S. Huang, H. Kuang, H. Xu, J. Chen, W. Xuan, S. Zhang, S. Li, X. Wang, J. Luo, *Nano Energy* **2021**, *80*, DOI 10.1016/j.nanoen.2020.105599.

[288] Y. Qian, J. Yu, F. Zhang, Y. Kang, C. Su, H. Pang, *Nano Energy* **2021**, *88*, DOI 10.1016/j.nanoen.2021.106256.

[289] D. Tantraviwat, M. Ngamyingyoud, W. Sripumkhai, P. Pattamang, G. Rujijanagul, B. Inceesungvorn, *ACS Omega* **2021**, *6*, 29765.

[290] S. Sriphan, T. Charoonsuk, T. Maluangnont, N. Vittayakorn, *ACS Appl Energy Mater* **2019**, *2*, 3840.

[291] J. Wang, H. Wu, Z. Wang, W. He, C. Shan, S. Fu, Y. Du, H. Liu, C. Hu, *Adv Funct Mater* **2022**, *32*, DOI 10.1002/adfm.202204322.

[292] M. N. Biutty, J. M. Koo, M. Zakia, P. L. Handayani, U. H. Choi, S. Il Yoo, *RSC Adv* **2020**, *10*, 21309.

[293] P. Zhang, P. F. Li, H. H. Zhang, L. Deng, *Nanotechnology* **2022**, *33*, DOI 10.1088/1361-6528/ac8aa2.

[294] Q. Zhou, J. N. Kim, K. W. Han, S. W. Oh, S. Umrao, E. J. Chae, I. K. Oh, *Nano Energy* **2019**, *59*, 120.

[295] G. J. Choi, S. H. Baek, S. S. Lee, F. Khan, J. H. Kim, I. K. Park, *J Alloys Compd* **2019**, *797*, 945.

[296] A. Yar, Z. Kınas, A. Karabiber, A. Ozen, A. Okbaz, F. Ozel, *Renew Energy* **2021**, *179*, 1781.

[297] H. Kang, H. T. Kim, H. J. Woo, H. Kim, D. H. Kim, S. Lee, S. M. Kim, Y. J. Song, S. W. Kim, J. H. Cho, *Nano Energy* **2019**, *58*, 227.

[298] M. K. Kim, M. S. Kim, H. B. Kwon, S. E. Jo, Y. J. Kim, *RSC Adv* **2017**, *7*, 48368.

[299] X. Pu, J. W. Zha, C. L. Zhao, S. B. Gong, J. F. Gao, R. K. Y. Li, *Chemical Engineering Journal* **2020**, *398*, DOI 10.1016/j.cej.2020.125526.

[300] S. Kim, M. K. Gupta, K. Y. Lee, A. Sohn, T. Y. Kim, K. S. Shin, D. Kim, S. K. Kim, K. H. Lee, H. J. Shin, D. W. Kim, S. W. Kim, *Advanced Materials* **2014**, *26*, 3918.

[301] L. Shi, H. Jin, S. Dong, S. Huang, H. Kuang, H. Xu, J. Chen, W. Xuan, S. Zhang, S. Li, X. Wang, J. Luo, *Nano Energy* **2021**, *80*, DOI 10.1016/j.nanoen.2020.105599.

[302] Y. Chen, Z. Tian, X. Wang, N. Ran, C. Wang, A. Cui, H. Lu, M. Zhang, Z. Xue, Y. Mei, P. K. Chu, J. Liu, Z. Hu, Z. Di, *Advanced Materials* **2022**, *34*, DOI 10.1002/adma.202201630.

[303] T. Chekke, R. Narzary, S. Ngadong, B. Satpati, S. Bayan, U. Das, *J Electron Mater* **2023**, *52*, 2685.

[304] B. Hedau, B. C. Kang, T. J. Ha, *ACS Nano* **2022**, *16*, 18355.

[305] W. He, M. Sohn, R. Ma, D. J. Kang, *Nano Energy* **2020**, *78*, DOI 10.1016/j.nanoen.2020.105383.

[306] T. Bhatta, P. Maharjan, H. Cho, C. Park, S. H. Yoon, S. Sharma, M. Salauddin, M. T. Rahman, S. S. Rana, J. Y. Park, *Nano Energy* **2021**, *81*, DOI 10.1016/j.nanoen.2020.105670.

[307] Z. Chen, Y. Cao, W. Yang, L. An, H. Fan, Y. Guo, *J Mater Chem A Mater* **2022**, *10*, 799.

[308] Q. Zheng, Y. Zou, Y. Zhang, Z. Liu, B. Shi, X. Wang, Y. Jin, H. Ouyang, Z. Li, Z. L. Wang, *Sci Adv* **2016**, *2*, DOI 10.1126/sciadv.1501478.

[309] C. Wu, J. Jiang, H. Guo, X. Pu, L. Liu, W. Ding, P. A. Kohl, Z. L. Wang, *Adv Electron Mater* **2019**, *5*, DOI 10.1002/aelm.201900725.

[310] I. M. Imani, B. Kim, X. Xiao, N. Rubab, B. J. Park, Y. J. Kim, P. Zhao, M. Kang, S. W. Kim, *Advanced Science* **2023**, *10*, DOI 10.1002/advs.202204801.

[311] D.-M. Lee, N. Rubab, I. Hyun, W. Kang, Y.-J. Kim, M. Kang, B. O. Choi, S.-W. Kim, *Sci Adv* **2022**, *8*, 8423.

[312] X. Peng, K. Dong, C. Ning, R. Cheng, J. Yi, Y. Zhang, F. Sheng, Z. Wu, Z. L. Wang, *Adv Funct Mater* **2021**, *31*, 1.

[313] Z. Wu, T. Cheng, Z. L. Wang, *Sensors (Switzerland)* **2020**, *20*, DOI 10.3390/s20102925.

[314] J. Yi, K. Dong, S. Shen, Y. Jiang, X. Peng, C. Ye, Z. L. Wang, *Nanomicro Lett* **2021**, *13*, DOI 10.1007/s40820-021-00621-7.

[315] M. Wang, N. Zhang, Y. Tang, H. Zhang, C. Ning, L. Tian, W. Li, J. Zhang, Y. Mao, E. Liang, *J Mater Chem A Mater* **2017**, *5*, 12252.

[316] H. Patnam, B. Dudem, S. A. Graham, J. S. Yu, *Energy* **2021**, *223*, 120031.

[317] Y. Wang, L. Zhang, A. Lu, *J Mater Chem A Mater* **2020**, *8*, 13935.

[318] N. Gogurla, B. Roy, J. Y. Park, S. Kim, *Nano Energy* **2019**, *62*, 674.

[319] S. Jo, I. Kim, N. Jayababu, H. Roh, Y. Kim, D. Kim, *ACS Sustain Chem Eng* **2020**, *8*, 10786.

[320] R. Pan, W. Xuan, J. Chen, S. Dong, H. Jin, X. Wang, H. Li, J. Luo, *Nano Energy* **2018**, *45*, 193.

[321] X. Peng, K. Dong, C. Ye, Y. Jiang, S. Zhai, R. Cheng, D. Liu, X. Gao, J. Wang, Z. L. Wang, *Sci Adv* **2020**, *6*, DOI 10.1126/sciadv.aba9624.

[322] T. G. Zimmerman, J. Lanier, C. Blanchard, S. Bryson, Y. Harvill, *CHI + GI 1987 A HAND GESTURE INTERFACE DEVICE*, **n.d.**

[323] Nintendo, **n.d.**

[324] I. E. Sutherland, *A Head-Mounted Three Dimensional Display**, **n.d.**

[325] M. Peckham, **2016**.

[326] M. Ö. Çiçek, SENSITIVITY IMPROVEMENT STRATEGIES AND APPLICATIONS FOR FLEXIBLE AND WEARABLE CAPACITIVE PRESSURE SENSORS, M.Sc., Middle East Technical University, **n.d.**

[327] T. Yang, D. Xie, Z. Li, H. Zhu, *Materials Science and Engineering: R: Reports* **2017**, *115*, 1.

[328] Z. Sun, M. Zhu, X. Shan, C. Lee, *Nat Commun* **2022**, *13*, DOI 10.1038/s41467-022-32745-8.

[329] K. Tao, Z. Chen, J. Yu, H. Zeng, J. Wu, Z. Wu, Q. Jia, P. Li, Y. Fu, H. Chang, W. Yuan, *Advanced Science* **2022**, *9*, DOI 10.1002/advs.202104168.

[330] J. Xu, Z. Xie, H. Yue, Y. Lu, F. Yang, *Nano Energy* **2022**, *104*, DOI 10.1016/j.nanoen.2022.107845.

[331] X. Yu, Z. Xie, Y. Yu, J. Lee, A. Vazquez-Guardado, H. Luan, J. Ruban, X. Ning, A. Akhtar, D. Li, B. Ji, Y. Liu, R. Sun, J. Cao, Q. Huo, Y. Zhong, C. M. Lee, S. Y. Kim, P. Gutruf, C. Zhang, Y. Xue, Q. Guo, A. Chempakasseril, P. Tian, W. Lu, J. Y. Jeong, Y. J. Yu, J. Cornman, C. S.

Tan, B. H. Kim, K. H. Lee, X. Feng, Y. Huang, J. A. Rogers, *Nature* **2019**, *575*, 473.

[332] H. Niu, Y. Chen, E. S. Kim, W. Zhou, Y. Li, N. Y. Kim, *Chemical Engineering Journal* **2022**, *450*, DOI 10.1016/j.cej.2022.138258.

[333] P. Zhu, Y. Wang, Y. Wang, H. Mao, Q. Zhang, Y. Deng, *Adv Energy Mater* **2020**, *10*, DOI 10.1002/aenm.202001945.

[334] Y. Chang, L. Wang, R. Li, Z. Zhang, Q. Wang, J. Yang, C. F. Guo, T. Pan, *Advanced Materials* **2021**, *33*, 2003464.

[335] W. Chen, X. Yan, *J Mater Sci Technol* **2020**, *43*, 175.

[336] Bijender, A. Kumar, *Sens Actuators A Phys* **2022**, *344*, 113770.

[337] R. Paradiso, G. Loriga, N. Taccini, *IEEE Transactions on Information Technology in Biomedicine* **2005**, *9*, 337.

[338] H. Bin Yao, J. Ge, C. F. Wang, X. Wang, W. Hu, Z. J. Zheng, Y. Ni, S. H. Yu, *Advanced Materials* **2013**, *25*, 6692.

[339] H. Liu, X. Chen, Y. Zheng, D. Zhang, Y. Zhao, C. Wang, C. Pan, C. Liu, C. Shen, *Adv Funct Mater* **2021**, *31*, DOI 10.1002/adfm.202008006.

[340] G. Mogli, A. Chiappone, A. Sacco, C. F. Pirri, S. Stassi, *ACS Appl Electron Mater* **2023**, *5*, 205.

[341] S. Das Mahapatra, P. C. Mohapatra, A. I. Aria, G. Christie, Y. K. Mishra, S. Hofmann, V. K. Thakur, *Advanced Science* **2021**, *8*, 2100864.

[342] Y. Huang, X. Fan, S. Chen, N. Zhao, *Adv Funct Mater* **2019**, *29*, 1808509.

[343] J. Zhou, Y. Gu, P. Fei, W. Mai, Y. Gao, R. Yang, G. Bao, Z. L. Wang, *Nano Lett* **2008**, *8*, 3035.

[344] C. Dagdeviren, Y. Su, P. Joe, R. Yona, Y. Liu, Y. S. Kim, Y. Huang, A. R. Damadoran, J. Xia, L. W. Martin, Y. Huang, J. A. Rogers, *Nat Commun* **2014**, *5*, DOI 10.1038/ncomms5496.

[345] M. Ha, S. Lim, J. Park, D. S. Um, Y. Lee, H. Ko, *Adv Funct Mater* **2015**, *25*, 2841.

[346] X. Xiong, J. Liang, W. Wu, *Nano Energy* **2023**, *113*, 108542.

[347] F. R. Fan, L. Lin, G. Zhu, W. Wu, R. Zhang, Z. L. Wang, *Nano Lett* **2012**, *12*, 3109.

[348] P. Yi, X. Fu, Y. Liu, X. Zhang, C. Zhang, X. Li, *Nano Energy* **2023**, *113*, DOI 10.1016/j.nanoen.2023.108592.

[349] H. Wang, Z. Li, Z. Liu, J. Fu, T. Shan, X. Yang, Q. Lei, Y. Yang, D. Li, *J Mater Chem C Mater* **2022**, *10*, 1594.

[350] R. Li, Q. Zhou, Y. Bi, S. Cao, X. Xia, A. Yang, S. Li, X. Xiao, *Sens Actuators A Phys* **2021**, *321*, 112425.

[351] T. Li, H. Luo, L. Qin, X. Wang, Z. Xiong, H. Ding, Y. Gu, Z. Liu, T. Zhang, *Small* **2016**, *12*, 5042.

[352] K. H. Ha, W. Zhang, H. Jang, S. Kang, L. Wang, P. Tan, H. Hwang, N. Lu, *Advanced Materials* **2021**, *33*, DOI 10.1002/adma.202103320.

[353] A. Chhetry, S. Sharma, H. Yoon, S. Ko, J. Y. Park, *Adv Funct Mater* **2020**, *30*, DOI 10.1002/adfm.201910020.

[354] Y. Chang, L. Wang, R. Li, Z. Zhang, Q. Wang, J. Yang, C. F. Guo, T. Pan, *Advanced Materials* **2021**, *33*, 2003464.

[355] M. A. Brown, Z. Abbas, A. Kleibert, R. G. Green, A. Goel, S. May, T. M. Squires, *Phys Rev X* **2016**, *6*, 1.

[356] M. O. Cicek, M. B. Durukan, B. Yıldız, D. Keskin, D. Doganay, S. Çınar Aygün, M. P. Cakir, H. E. Unalan, *Adv Mater Technol* **2023**, DOI 10.1002/admt.202300322.

[357] M. O. Cicek, D. Doganay, M. B. Durukan, M. C. Gorur, H. E. Unalan, *Adv Mater Technol* **2021**, *6*, DOI 10.1002/admt.202001168.

[358] M. Li, J. Liang, X. Wang, M. Zhang, *Sensors (Switzerland)* **2020**, *20*, DOI 10.3390/s20020371.

[359] C. M. Boutry, Y. Kaizawa, B. C. Schroeder, A. Chortos, A. Legrand, Z. Wang, J. Chang, P. Fox, Z. Bao, *Nat Electron* **2018**, *1*, 314.

[360] L. Teng, S. Ye, S. Handschuh-Wang, X. Zhou, T. Gan, X. Zhou, *Adv Funct Mater* **2019**, *29*, DOI 10.1002/adfm.201808739.

[361] S. Wang, H. Ning, N. Hu, Y. Liu, F. Liu, R. Zou, K. Huang, X. Wu, S. Weng, Alamusi, *Adv Mater Interfaces* **2020**, *7*, 1.

[362] A. Atalay, V. Sanchez, O. Atalay, D. M. Vogt, F. Haufe, R. J. Wood, C. J. Walsh, *Adv Mater Technol* **2017**, *2*, 1.

[363] A. Atalay, V. Sanchez, O. Atalay, D. M. Vogt, F. Haufe, R. J. Wood, C. J. Walsh, *Adv Mater Technol* **2017**, *2*, 1.

[364] N. Bai, L. Wang, Q. Wang, J. Deng, Y. Wang, P. Lu, J. Huang, G. Li, Y. Zhang, J. Yang, K. Xie, X. Zhao, C. F. Guo, *Nat Commun* **2020**, *11*, 3.

[365] J. Huang, M. Zhao, Y. Cai, M. Zimniewska, D. Li, Q. Wei, **2020**, *1900934*, 1.

[366] Z. Jin, H. Zhou, J. Lai, X. Jin, H. Liu, P. Wu, W. Chen, A. Ma, *ACS Appl Polym Mater* **2021**, *3*, 2732.

[367] S. Wan, H. Bi, Y. Zhou, X. Xie, S. Su, K. Yin, L. Sun, *Carbon N Y* **2017**, *114*, 209.

[368] H. Kou, L. Zhang, Q. Tan, G. Liu, H. Dong, W. Zhang, J. Xiong, *Sci Rep* **2019**, *9*, 1.

[369] C. Hou, Z. Xu, W. Qiu, R. Wu, Y. Wang, Q. Xu, X. Y. Liu, W. Guo, *Small* **2019**, *15*, 1.

[370] C. M. Boutry, A. Nguyen, Q. O. Lawal, A. Chortos, S. Rondeau-Gagné, Z. Bao, *Advanced Materials* **2015**, *27*, 6954.

[371] A. Elsayes, V. Sharma, K. Yiannacou, A. Koivikko, A. Rasheed, V. Sariola, *Adv Sustain Syst* **2020**, *2000056*, DOI 10.1002/adsu.202000056.

[372] H. Cheng, V. Vepachedu, *Theoretical and Applied Mechanics Letters* **2016**, *6*, 21.

APPENDICES

A. Permission Licence

JOHN WILEY AND SONS ORDER DETAILS

Aug 02, 2023

This Agreement between Mete Batuhan Durukan ("You") and John Wiley and Sons ("John Wiley and Sons") consists of your order details and the terms and conditions provided by John Wiley and Sons and Copyright Clearance Center.

Order Number

501834645

Order date

Aug 02, 2023

Licensed Content Publisher

John Wiley and Sons

Licensed Content Publication

Advanced Functional Materials

Licensed Content Title

Multifunctional and Physically Transient Supercapacitors, Triboelectric Nanogenerators, and Capacitive Sensors

Licensed Content Author

Mete Batuhan Durukan, Melih Ogeday Cicek, Doga Doganay, et al

Licensed Content Date

Oct 3, 2021

Licensed Content Volume

32

Licensed Content Issue

1

Licensed Content Pages

12

Type of use

Dissertation/Thesis

Requestor type

Author of this Wiley article

Format

Print and electronic

Portion

Full article

Will you be translating?

No

Title

Multifunctional and Physically Transient Supercapacitors, Triboelectric Nanogenerators, and Capacitive Sensors

Institution name

Middle East Technical University

Expected presentation date

Aug 2023

Order reference number

ThesisRights

Requestor Location

METU
Orta Dogu Teknik Universitesi
Metalurji ve Malzeme Muh D-308
Cankaya
Ankara, 06800
Turkey
Attn: METU

Publisher Tax ID

EU826007151

Billing Type

Invoice

Billing Address

METU
Orta Dogu Teknik Universitesi
Metalurji ve Malzeme Muh D-308
Cankaya
Ankara, Turkey 06800
Attn: METU

Total

0.00 USD

Terms and Conditions

TERMS AND CONDITIONS

This copyrighted material is owned by or exclusively licensed to John Wiley & Sons, Inc. or one of its group companies (each a"Wiley Company") or handled on behalf of a society with which a Wiley Company has exclusive publishing rights in relation to a particular work (collectively "WILEY"). By clicking "accept" in connection with completing this licensing transaction, you agree that the following terms and conditions apply to this transaction (along with the billing and payment terms and conditions established by the Copyright Clearance Center Inc., ("CCC's Billing and Payment terms and conditions"), at the time that you opened your RightsLink account (these are available at any time at http://myaccount.copyright.com).

Terms and Conditions

- The materials you have requested permission to reproduce or reuse (the "Wiley Materials") are protected by copyright.
- You are hereby granted a personal, non-exclusive, non-sub licensable (on a stand-alone basis), non-transferable, worldwide, limited license to reproduce the Wiley Materials for the purpose specified in the licensing process. This license, **and any CONTENT (PDF or image file) purchased as part of your order,** is for a one-time use only and limited to any maximum distribution number specified in the license. The first instance of republication or reuse granted by this license must be completed within two years of the date of the grant of this license (although copies prepared before the end date may be distributed thereafter). The Wiley Materials shall not be used in any other manner or for any other purpose,

beyond what is granted in the license. Permission is granted subject to an appropriate acknowledgement given to the author, title of the material/book/journal and the publisher. You shall also duplicate the copyright notice that appears in the Wiley publication in your use of the Wiley Material. Permission is also granted on the understanding that nowhere in the text is a previously published source acknowledged for all or part of this Wiley Material. Any third party content is expressly excluded from this permission.

- With respect to the Wiley Materials, all rights are reserved. Except as expressly granted by the terms of the license, no part of the Wiley Materials may be copied, modified, adapted (except for minor reformatting required by the new Publication), translated, reproduced, transferred or distributed, in any form or by any means, and no derivative works may be made based on the Wiley Materials without the prior permission of the respective copyright owner.**For STM Signatory Publishers clearing permission under the terms of the STM Permissions Guidelines only, the terms of the license are extended to include subsequent editions and for editions in other languages, provided such editions are for the work as a whole in situ and does not involve the separate exploitation of the permitted figures or extracts,** You may not alter, remove or suppress in any manner any copyright, trademark or other notices displayed by the Wiley Materials. You may not license, rent, sell, loan, lease, pledge, offer as security, transfer or assign the Wiley Materials on a stand-alone basis, or any of the rights granted to you hereunder to any other person.
- The Wiley Materials and all of the intellectual property rights therein shall at all times remain the exclusive property of John Wiley & Sons Inc, the Wiley Companies, or their respective licensors, and your interest therein is only that of having possession of and the right to reproduce the Wiley

Materials pursuant to Section 2 herein during the continuance of this Agreement. You agree that you own no right, title or interest in or to the Wiley Materials or any of the intellectual property rights therein. You shall have no rights hereunder other than the license as provided for above in Section 2. No right, license or interest to any trademark, trade name, service mark or other branding ("Marks") of WILEY or its licensors is granted hereunder, and you agree that you shall not assert any such right, license or interest with respect thereto

- NEITHER WILEY NOR ITS LICENSORS MAKES ANY WARRANTY OR REPRESENTATION OF ANY KIND TO YOU OR ANY THIRD PARTY, EXPRESS, IMPLIED OR STATUTORY, WITH RESPECT TO THE MATERIALS OR THE ACCURACY OF ANY INFORMATION CONTAINED IN THE MATERIALS, INCLUDING, WITHOUT LIMITATION, ANY IMPLIED WARRANTY OF MERCHANTABILITY, ACCURACY, SATISFACTORY QUALITY, FITNESS FOR A PARTICULAR PURPOSE, USABILITY, INTEGRATION OR NON-INFRINGEMENT AND ALL SUCH WARRANTIES ARE HEREBY EXCLUDED BY WILEY AND ITS LICENSORS AND WAIVED BY YOU.
- WILEY shall have the right to terminate this Agreement immediately upon breach of this Agreement by you.
- You shall indemnify, defend and hold harmless WILEY, its Licensors and their respective directors, officers, agents and employees, from and against any actual or threatened claims, demands, causes of action or proceedings arising from any breach of this Agreement by you.
- IN NO EVENT SHALL WILEY OR ITS LICENSORS BE LIABLE TO YOU OR ANY OTHER PARTY OR ANY OTHER PERSON OR

ENTITY FOR ANY SPECIAL, CONSEQUENTIAL, INCIDENTAL, INDIRECT, EXEMPLARY OR PUNITIVE DAMAGES, HOWEVER CAUSED, ARISING OUT OF OR IN CONNECTION WITH THE DOWNLOADING, PROVISIONING, VIEWING OR USE OF THE MATERIALS REGARDLESS OF THE FORM OF ACTION, WHETHER FOR BREACH OF CONTRACT, BREACH OF WARRANTY, TORT, NEGLIGENCE, INFRINGEMENT OR OTHERWISE (INCLUDING, WITHOUT LIMITATION, DAMAGES BASED ON LOSS OF PROFITS, DATA, FILES, USE, BUSINESS OPPORTUNITY OR CLAIMS OF THIRD PARTIES), AND WHETHER OR NOT THE PARTY HAS BEEN ADVISED OF THE POSSIBILITY OF SUCH DAMAGES. THIS LIMITATION SHALL APPLY NOTWITHSTANDING ANY FAILURE OF ESSENTIAL PURPOSE OF ANY LIMITED REMEDY PROVIDED HEREIN.

- Should any provision of this Agreement be held by a court of competent jurisdiction to be illegal, invalid, or unenforceable, that provision shall be deemed amended to achieve as nearly as possible the same economic effect as the original provision, and the legality, validity and enforceability of the remaining provisions of this Agreement shall not be affected or impaired thereby.
- The failure of either party to enforce any term or condition of this Agreement shall not constitute a waiver of either party's right to enforce each and every term and condition of this Agreement. No breach under this agreement shall be deemed waived or excused by either party unless such waiver or consent is in writing signed by the party granting such waiver or consent. The waiver by or consent of a party to a breach of any provision of this Agreement shall not operate or be construed as a waiver of or consent to any other or subsequent breach by such other party.

- This Agreement may not be assigned (including by operation of law or otherwise) by you without WILEY's prior written consent.
- Any fee required for this permission shall be non-refundable after thirty (30) days from receipt by the CCC.
- These terms and conditions together with CCC's Billing and Payment terms and conditions (which are incorporated herein) form the entire agreement between you and WILEY concerning this licensing transaction and (in the absence of fraud) supersedes all prior agreements and representations of the parties, oral or written. This Agreement may not be amended except in writing signed by both parties. This Agreement shall be binding upon and inure to the benefit of the parties' successors, legal representatives, and authorized assigns.
- In the event of any conflict between your obligations established by these terms and conditions and those established by CCC's Billing and Payment terms and conditions, these terms and conditions shall prevail.
- WILEY expressly reserves all rights not specifically granted in the combination of (i) the license details provided by you and accepted in the course of this licensing transaction, (ii) these terms and conditions and (iii) CCC's Billing and Payment terms and conditions.
- This Agreement will be void if the Type of Use, Format, Circulation, or Requestor Type was misrepresented during the licensing process.
- This Agreement shall be governed by and construed in accordance with the laws of the State of New York, USA, without regards to such state's conflict of law rules. Any legal action, suit or proceeding arising out of or relating to these Terms and Conditions or the breach thereof shall be instituted in a court of competent jurisdiction in New York County in the State of New York in the United States of America and each party hereby consents and

submits to the personal jurisdiction of such court, waives any objection to venue in such court and consents to service of process by registered or certified mail, return receipt requested, at the last known address of such party.

WILEY OPEN ACCESS TERMS AND CONDITIONS

Wiley Publishes Open Access Articles in fully Open Access Journals and in Subscription journals offering Online Open. Although most of the fully Open Access journals publish open access articles under the terms of the Creative Commons Attribution (CC BY) License only, the subscription journals and a few of the Open Access Journals offer a choice of Creative Commons Licenses. The license type is clearly identified on the article.

The Creative Commons Attribution License

The Creative Commons Attribution License (CC-BY) allows users to copy, distribute and transmit an article, adapt the article and make commercial use of the article. The CC-BY license permits commercial and non-

Creative Commons Attribution Non-Commercial License

The Creative Commons Attribution Non-Commercial (CC-BY-NC)License permits use, distribution and reproduction in any medium, provided the original work is properly cited and is not used for commercial purposes.(see below)

Creative Commons Attribution-Non-Commercial-NoDerivs License

The Creative Commons Attribution Non-Commercial-NoDerivs License (CC-BY-NC-ND) permits use, distribution and reproduction in any medium, provided the original work is properly cited, is not used for commercial purposes and no modifications or adaptations are made. (see below)

Use by commercial "for-profit" organizations

Use of Wiley Open Access articles for commercial, promotional, or marketing purposes requires further explicit permission from Wiley and will be subject to a fee.

Further details can be found on Wiley Online Library http://olabout.wiley.com/WileyCDA/Section/id-410895.html

Other Terms and Conditions:

v1.10 Last updated September 2015

CURRICULUM VITAE

Mete Batuhan Durukan

Research Assistant
Department of Metallurgical and Materials Engineering
Middle East Technical University (METU)
06800, Ankara, TÜRKİYE

EDUCATION

Degree	Institution	Year of Graduation
MS	METU Metallurgical and Materials Engineering	2017
BS	METU Metallurgical and Materials Engineering	2015
High School	Ankara Atatürk Lisesi, Ankara	2009

FOREIGN LANGUAGES

Advanced English, Beginner Japanese

ACADEMIC RESEARCH EXPERIENCE

Research Assistant (2015 – Ongoing)

Nanomaterials and Devices Laboratory, Metallurgical and Materials Engineering, Middle East Technical University.

PUBLICATIONS (9) (Total Citations: 191, h-index:7 as of 01.08.2023)

1. Tutel, Y., **Durukan, M. B**., Hacioglu, S., Baskose, U. C., Toppare, L. Unalan, H. E. (2023) Cobalt-doped MoO_3 Thin Films and Dual-Band Electrochromic Devices with Excellent Cyclic Stability. Submitted to Applied Materials Today.
2. **Durukan, M. B.**, Keskin, D., Tufan, Y., Dincer, O., Cicek, M. O., Yildiz, B., Çınar Aygün, S., Ercan, B., Unalan, H. E. (2023) An Edible Supercapacitor Based on Zwitterionic Soy Sauce-Based Gel Electrolyte. Submitted to: Advanced Functional Materials.
3. Gorur, Muhammed. C., Doganay, D., **Durukan, M. B.,** Kınçal, C., Solak, N., Unalan, H. E. 3D Printing of Hexagonal Boron Nitride Nanosheets/Polylactic Acid Nanocomposites for Thermal Management of Electronic Devices. Submitted to: Composites Part: B
4. Cicek, M .O, **Durukan, M. B**., Yıldız, B., Keskin, D., Doganay , D., Aygün Çınar, S., Cakir, M. P., Unalan, H. E. (2023). Ultra-Sensitive Bio-Polymer Iontronic Sensor for Object Recognition from Tactile Feedback. Advanced Materials Technologies, 2300322
5. Yabas, E., Bicer, E., **Durukan, M. B.,** Keskin, D. & Unalan, H. E. (2022). Double-decker lutetium and europium phthalocyanine composites with reduced graphene oxide as supercapacitor electrode materials. Journal of Organometallic Chemistry, 980, 122509
6. Tutel, Y., **Durukan, M. B.,** Koc, S., Koylan, S., Cakmak, H., Kocak, Y., Hekmat, F., Ozensoy, E., Ozbay, E., Arslan Udum, Y., Toppare, L. & Unalan, H. E. (2021). Multichromic Vanadium Pentoxide Thin Films Through Ultrasonic Spray Deposition. Journal of the Electrochemical Society, 168, 106511.
7. **Durukan, M. B.,** Cicek, M. O., Doganay, D., Gorur, M. C., Çınar, S., & Unalan, H. E. (2021). Multifunctional and Physically Transient Supercapacitors, Triboelectric Nanogenerators, and Capacitive Sensors. Advanced Functional Materials, 2106066
8. Doganay, D., Cicek, M. O., **Durukan, M. B.,** Altuntas, B., Agbahca, E., Coskun, S., & Unalan, H. E. (2021). Fabric Based Wearable Triboelectric Nanogenerators for Human Machine Interface. Nano Energy, 89, 106412.
9. Cicek, M. O., Doganay, D., **Durukan, M. B.**, Gorur, M. C., & Unalan, H. E. (2021). Seamless Monolithic Design for Foam Based, Flexible, Parallel Plate Capacitive Sensors. Advanced Materials Technologies, 6(6), 2001168.
10. Koylan, S., Tunca, S., Polat, G., **Durukan, M. B.,** Kim, D., Kalay, Y. E., Ko, S. H., & Unalan, H. E. (2021). Highly Stable Silver-Platinum Core-Shell Nanowires for H_2O_2 Detection. Nanoscale, 13, 13129.
11. Dogru, I.B., **Durukan, M. B.,** Turel, O. & Unalan, H. E. (2016). Flexible Supercapacitor Electrodes with Vertically Aligned Carbon Nanotubes Grown on Aluminum Foils. Progress in Natural Science: Materials International, 26 (3), 232-236

12. **Durukan, M. B.,** Yuksel, R. & Unalan, H. E. (2016). Cobalt Oxide Nanoflakes on Single Walled Carbon Nanotube Thin Films for Supercapacitor Electrodes. Electrochimica Acta, 222, 1475-1482.

PROJECTS (7)

1. Assesment of the Capacitive Deionization Performance of the Microsupercapacitors Fabricated with Reduced Graphene Oxide/Molybdenum Disulfide Nanocomposites using Combinatorial Approach. TUBITAK 1001 Project (Research and Supervision) 2021-2023 (Ongoing)
2. Supercapacitor Powered Non-Invasive Glucose Monitoring Wearable Patch. TUBITAK International Cooperation Program (Research and Supervision). 2020 – 2023 (Ongoing)
3. Direct Ink Writing of 1T-Molybdenum Disulfide – Silver Nanowires Inks for Microsupercapacitor Fabrication. TUBITAK Project (Project Leader). 2020-2021
4. Development of Flexible Supercapacitors with Metal Nanowires with Enhanced Electrochemical Stability. TUBITAK International Cooperation Program (Researcher). 2018-2020
5. Production and Use of Molybdenum Sulfide/Graphene Nanocomposites in Supercapacitors. YOK Project (Researcher). 2018-2019
6. Development of Capacitors Using Metal Oxides to Increase the Ion Removal Efficiency of the Capacitive Deionization Process. YOK Project. (Researcher). 2017
7. Fabrication of Supercapacitors with Carbon Nanotubes. TUBITAK Project (Researcher). 2014-2016.

PRESENTATIONS (15)

1. 3D-Printed Hexagonal Boron Nitride/Polylactic Acid Nanocomposites. Gorur, M. C., Doganay, D., **Durukan, M. B.,** Unalan, H. E. e-MRS Fall'2022
2. Ultrasonic Spray Deposition of 1T-MoS2 for In-Plane Micro-Supercapacitors. Keskin, D., Gorur, C., **Durukan, M. B**., Unalan, H. E. e-MRS Fall'2022
3. Textile-Based Co-MOF//FexSy/Graphene Energy Devices for Wearable Technologies. Cetin, O., Bolukbasi, T., **Durukan, M. B**., Ozturk, G., Unalan, H. E. e-MRS Fall'2022.
4. Biodegradable and Biocompatible Gel Electrolyte for Edible Supercapacitors. Keskin, D., **Durukan, M. B.,** Cicek, M. O., Tufan, Y., Dincer, O., Ercan, B., Cinar-Aygun, S., Unalan, H. E. e-MRS Fall'2022.

5. Multifunctional and Physically transient Supercapacitors, Triboelectric Nanogenerators, and Capacitive Sensors. **Durukan, M. B.,** Cicek, M. O., Doganay, D., Gorur, M. C., Cinar Aygun, S., Unalan, H. E. e-MRS Fall'2022
6. Direct Ink Writing of 1T-MoS_2/Ag NW Inks for the Fabrication of Interdigitated Microsupercapacitors. **Durukan, M. B.,** Gorur, M. C., Ozturk, G., Keskin, D., Bolukbasi, T., Yildiz, B., Cinar Aygun, S., Unalan, H. E. e-MRS Fall'2022.
7. Facile Fabrication of Multifunctional and Transient All-PVA Based Green Electronics. **Durukan, M. B.,** Cicek, M. O., Doganay, D., Gorur, M. C., Unalan, H. E., MRS Fall'2021 USA.
8. Wearable Triboelectric Nanogenerators with Thermoplastic Polyurethane/Silver Nanowire Textiles for Human Machine Interface, Doganay, D., Cicek, M.Ö., **Durukan, M. B.,** Altuntas, B., Agbahca, E., Coskun, S., Unalan, H.E., MRS Fall'2021 USA.
9. Ultrasonic Spray Deposition of Cobalt Organic Frameworks for Textile-Based Supercapacitor Electrodes. **Durukan, M. B.,** Cetin, A., Bolukbasi, T., Unalan, H. E. mESC-IS 2021 (Virtual).
10. High Electrochemical Stability of Ag-Pt Core-Shell Nanowires in a Wide Potential Window. Tunca, S., Koylan, S., **Durukan, M. B.,** Kim, D., Ko, S. H., Unalan, H. E. MRS Fall' 2019 USA.
11. Silver Nanowire–Cobalt Hydroxide Textile Electrodes for Flexible and Wearable Energy Storage Applications, **Durukan, M. B.,** Hekmat, F., Doganay, D., Unalan, H.E., MRS Fall' 2019 USA.
12. Silver Nanowire Modified Fabrics for Wearable Triboelectric Nanogenerators, Doganay, D., **Durukan, M. B.,** Cicek, M.Ö., Guven, M.N., Unalan, H.E., MRS Fall' 2019 USA.
13. Coaxial Copper Nanowire Network Core – Polypyrrole Shell Nanocomposites as Supercapacitor Electrodes. **Durukan, M. B.,** Polat Genlik, S., Tigan, D., Unalan, H. E., MRS Fall' 2018
14. Microsupercapacitors from Laser Ablated Multi Walled Carbon Nanotube Films. **Durukan, M., B.,** Cinar, K., Bek, A., Unalan, H. E., MRS Fall' 2017 USA
15. Single Walled Carbon Nanotube Cobalt Oxide Nanocomposites as Supercapacitor Electrode Materials. **Durukan, M. B.,** Yuksel, R., Unalan, H. E., MRS Fall' 2015 USA.